Semiconductors, Vol. 39, No. 5, 2005, pp. 485–492. Translated from Fizika i Tekhnika Poluprovodnikov, Vol. 39, No. 5, 2005, pp. 513–520.

ELECTRONIC AND OPTICAL PROPERTIES OF SEMICONDUCTORS

The Effect of Oxygen on the ZnS Electronic Energy-Band Structure

N. K. Morozova*, I. A. Karetnikov*, K. V. Golub*, N. D. Danilevich*, V. M. Lisitsyn, and V. I. Oleshko****

**Moscow Power Institute (Technical University), ul. Krasnokazarmennaya 17, Moscow, 111250 Russia*

***Tomsk Polytechnical University, pr. Lenina 30, Tomsk, 634034 Russia*

Submitted July 13, 2004; accepted for publication August 9, 2004

Abstract—Experimental data indicating that the band gap of Zn–O–S solid solutions decreases appreciably in accordance with the theory of noncrossing energy bands are reported for the first time. It is shown that this effect is mainly characteristic of ZnS with an excess of Zn. The concentration of dissolved oxygen [O_S] has been determined from data taken using precision *X*-ray structure analysis and chemical phase analysis. The decrease in the band gap determined from the cathodoluminescence spectra is equal to 75 meV for sphalerite ZnS (*s*) and 90 meV for wurtzite ZnS (*w*) per 1 mol % and depends virtually linearly on the oxygen concentration [O_S]. An increase in [O_S], in addition to an intensification and shift of the free-exciton (FE) band, is also conducive to the formation of SA oxygen-containing complexes in ZnS. These complexes are responsible for emission in the visible region of the spectrum and for the band I_1 of excitons bound to these complexes. The binding energy is equal to ~61 and ~104 meV for ZnS (*s*) and ZnS (*w*), respectively. The band I_1 shifts as [O_S] varies, similarly to the shift of the FE band. The obtained dependences define the position of the FE band in oxygen-free ZnS and make it possible to assess the oxygen concentration in the compound from the shift of the FE band.

1. INTRODUCTION

II–O–VI semiconductor solid solutions were studied for the first time by Kroeger and Dikhoff [1]. At present, there is a large and fairly complex body of experimental data available in this field [1–20]. Recent theoretical studies (see, for example, [21]) have made it possible to understand and explain a large number of phenomena in a system of processes that are initiated by the presence of oxygen in II–VI compounds.

These phenomena include the effect of oxygen on the electronic structure of the energy bands, which brings about, in particular, a large decrease in the energy band gap under certain conditions. Oxygen is an isoelectronic impurity and exhibits the largest (among the elements of Subgroup VIB) distinction between its properties and those of substituted chalcogen. For such substitutional impurities, which introduce appreciable local distortions into the lattice, the model suggested by Shan *et al.* [21] implies a strong interaction between the localized impurity states and extended states in the conduction band. As a result, even a small amount of an isoelectronic impurity gives rise to a splitting of the conduction band into two noncrossing subbands. One of these subbands is formed of highly localized impurity states, while the second subband is formed of extended conduction-band states that experience the effect of the narrow resonance band introduced by the isoelectronic impurity. Optical transitions (E_- and E_+) to the valence band are related to the energy minima in the two subbands of the conduction band. It is noteworthy, however, that the valence band is not affected by the isoelectronic impurity. Since the strong effect of the impurities under consideration on the electronic properties of semiconductors is promising from the standpoint of the fabrication of a number of quantum structures in which nonlinear optical phenomena are used at room temperature, the corresponding studies are of great interest and have actively been pursued during the last decade.

We now turn our attention to a consideration of similar phenomena in the II–O–VI solid solutions. These phenomena are also related to the presence of substitutional oxygen (O_S) and should be discussed in combination with other previously reported facts [1–20]. Specifically, taking zinc sulfide as an example, we can note the following:

(i) The thermochemical characteristics (as well as the specific features of growth) of II–O–VI solid solutions, in particular, those based on ZnS, indicate that there is dissolved oxygen O_S at a concentration higher than 10^{17}–10^{18} cm^{-3} without any additional doping [2, 12].

(ii) The dissolved-oxygen concentration [O_S] varies (by approximately three orders of magnitude for ZnS) within the homogeneity domain in II–VI compounds: this concentration is at its highest if there is an excess of Zn, decreases nonlinearly as the sulfur content increases, and exhibits a step at the stoichiometry point [9, 15].

(iii) The phenomena related to a drastic decrease in the band gap as the dissolved-oxygen concentration increases are observed only if there was an excess of zinc and if $[O_S] \geq 10^{19}$ cm^{-3} [2].

(iv) The formation of oxygen complexes (with intrinsic point defects), as well as an increase in their concentration, is observed as $[O_S]$ increases. These complexes are responsible for the so-called "self-activated" emission [3, 17].

(v) The presumed recharging of the oxygen complexes as the departure from stoichiometry in high-purity compounds varies accounts for a change in the type of ZnS self-activated emission: from 445–400 nm, SA (I), in ZnS with an excess of Zn to ~365 nm, SAL (II), for the stoichiometric composition and to 505–510 nm, band III, if there is an excess of sulfur [3, 17].

(vi) Bands of bound excitons are observed for the studied SA (I) and SAL (II) complexes, and the spectral positions of these bands are consistent with the complexes' acceptor-level depth [4, 7, 16–19].

(vii) Various transitions are prevalent depending on temperature, excitation intensity, or exposure to pressure. This phenomenon has not, as yet, been adequately studied.

In this paper, we report the results of studying the effect of substitutional oxygen O_S on the optical properties of zinc sulfide. We compare the variation in the band gap under the effect of oxygen with some other phenomena also initiated by oxygen.

2. EXPERIMENTAL

We studied the effect of doping with oxygen on the ZnS energy-band structure using polycrystalline samples. Luminophor-grade powders were annealed in cells under an excess of zinc and then subjected to rapid cooling [2]. The initial compounds contained zinc sulfate, which decomposed during annealing, and doped ZnS. The dissolved-oxygen concentration $[O_S]$ was determined from the data of precision X-ray structure analysis using Vegard's law [2]. For comparison, the concentration $[O_S]$ was also estimated using the results of neutron-activation [22], gas-chromatographic [23], and chemical phase [24] analyses for samples treated in acetic acid after their annealing in order to remove the oxide. We determined the limiting solubility of oxygen in ZnS with an excess of zinc and the temperature dependence of this solubility for the sphalerite and wurtzite phases [2] as

$$[O_S]\ [\text{cm}^{-3}] = 2.5 \times 10^{22} \times \exp\left(-0.329\frac{10^4}{T\ [\text{K}]} - 1.744\right). \quad (1)$$

According to [24], the solubility of oxygen in wurtzite ZnS can be somewhat higher:

$$[O_S]\ [\text{cm}^{-3}] = 2.5 \times 10^{22} \times \exp\left(-0.307\frac{10^4}{T\ [\text{K}]} - 1.686\right). \quad (2)$$

We also used polycrystalline high-purity condensates (layers) obtained by chemical vapor deposition (CVD). It has been found [4, 16] that oxygen can be dissolved in these layers under high isostatic pressure [25]. Exposure to a pressure of ~10^3 atm at temperatures ≥1000°C is conducive to the additional incorporation of oxygen into the lattice sites and the resulting filling of sulfur vacancies and exit of interstitial zinc Zn_i from the grain bulk. As a result of a decrease in the number of intrinsic point defects, the crystal's composition approaches that of stoichiometric material [4, 16, 26]. The variation in the ZnS band gap is mainly determined from excitonic cathodoluminescence spectra, measured at 77–400 K; the excitation intensity 10^{22} cm^{-3} s^{-1}; and electron-beam penetration to a depth of ~(0.5–1) μm using a method developed at the Moscow Power Institute [2–4, 15–19]. In order to refine some of the data, we measured pulsed cathodoluminescence using a method developed at the Tomsk Polytechnical University [27]. The cathodoluminescence in the samples was excited by an pulsed electron beam with an electron energy of no higher than ~400 keV, a pulse width of ~20 ns, and an excitation level of 10^{22}–10^{26} cm^{-3} s^{-1}. The spectra of the pulsed cathodoluminescence were measured at 25, 77, and 300 K. The depth of penetration of the electron beam into ZnS was larger than 250 μm; i.e., the information was gained from the grain bulk.

3. RESULTS AND DISCUSSION

The experiment was carried out using zinc sulfide samples with cubic and hexagonal modifications. The cathodoluminescence spectra are consistent with the results obtained from measurements of the reflection and absorption of ZnS doped heavily with oxygen [2]. In the 1960s, similar data initiated a discussion about the precise value of the ZnS band gap.[1] However, the lack of theoretical studies meant that there was no way to explain the results at that time.

In Fig. 1, we show the cathodoluminescence spectra of the sphalerite ZnS (*s*) samples. The variations with temperature in the spectra are illustrated in Figs. 1a and 1b. As can be seen, a superposition of the edge emission on the region of the excitonic spectrum is observed at low temperatures (T = 80 K). After quenching of the intense edge emission (with the intensity $I_{EE} \sim 10^5$ arb. units), two bands, whose position and relative intensity depend on the oxygen concentration $[O_S]$, can be distinguished at T > 200 K as the temperature increases to 300 K.

[1] According to [5, 8], the binding energy of free excitons is equal to 40 meV in both ZnS (*s*) and ZnS (*w*).

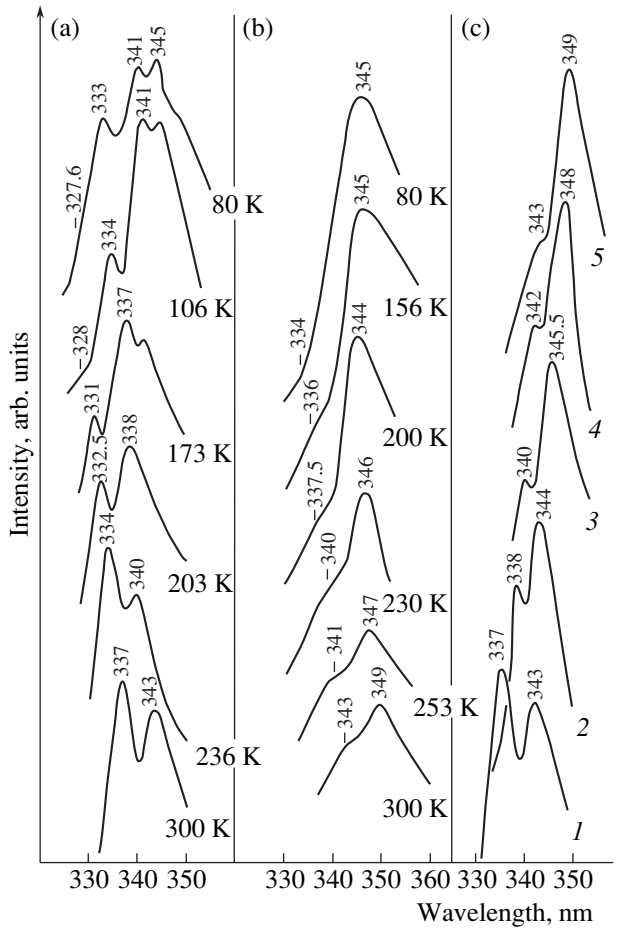

Fig. 1. Excitonic cathodoluminescence spectra of the Zn–O–S sphalerite powders: temperature dependences of the spectra at the substitutional-oxygen concentration $[O_S]$ = (a) 0.1 and (b) 1.0 mol %, and (c) the oxygen-concentration dependence of the spectra at 300 K. For (c), $[O_S]$ = (*1*) 0.1, (*2*) 0.3, (*3*) 0.5, (*4*) 0.8, and (*5*) 1.0 mol %. Precise values of the wavelengths (in nm) are indicated for the features in the spectra.

These dependences on $[O_S]$ are illustrated in Fig. 1c for excitonic spectra measured at 300 K. At a low oxygen concentration $[O_S]$, a short-wavelength band (with a half-width of ~55 meV) is prevalent. An increase in the oxygen concentration leads to an increase in the intensity of the long-wavelength band, whose half-width (70–80 meV) also increases. The intensities of these bands at 300 K decrease somewhat (from 10^3 to 10^2 arb. units) as $[O_S]$ increases. Defects may possibly contribute, to a certain degree, to the broadening of the bands. These defects are related to the excess zinc atoms in the samples grown in cells under zinc-vapor pressure of 2–5 atm at temperatures of 800–1000°C.

In Fig. 2, we show the energies of the bands' peaks E_{exc} in relation to the oxygen concentration. The range of $[O_S]$ is limited from above by the ultimate solubility of oxygen in sphalerite ZnS (*s*). This solubility corresponds to ~1.3 mol % if there is an excess of zinc and the phase-transition temperature is equal to ~(1020–1040)°C [2]. As can be seen from Fig. 2, the energies corresponding to the peaks of both bands shift to longer wavelengths almost linearly as $[O_S]$ increases, and the rate of this shift amounts to 75 meV per 1 mol % [2]. At $[O_S] \longrightarrow 0$, the short-wavelength band shifts to the well-known position for the band of a free *A* exciton (FE) 336.18 nm (3.688 eV) at 300 K [8]; i.e., the short-wavelength band corresponds to the free excitons and the shift of the band to lower energies correlates with a decrease in the band gap of ZnS (*s*).

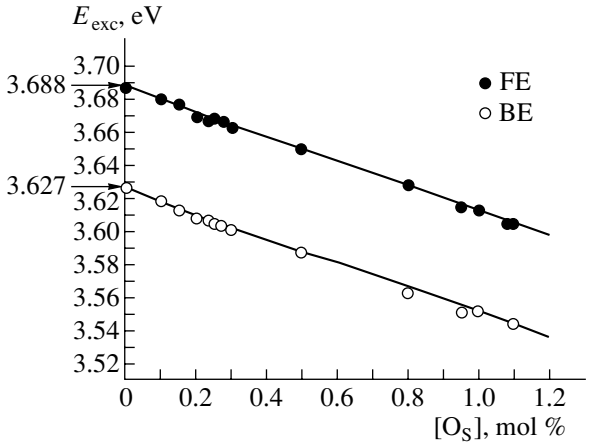

Fig. 2. Shifts of the cathodoluminescence bands related to the free (FE) and bound (BE) excitons in sphalerite ZnS in relation to the substitutional-oxygen concentration $[O_S]$ at a temperature of 300 K.

As the oxygen concentration increases ($[O_S] \geq$ 0.15 mol %), the intensity of the long-wavelength band in the cathodoluminescence spectrum increases, in addition to the shift of the FE band to longer wavelengths. The spectral position of the long-wavelength band makes it possible to relate it to bound excitons. This band is separated by ~61 meV from the FE band in ZnS (*s*) with an excess of zinc. If $[O_S] \longrightarrow 0$, the long-wavelength band shifts to the position of the band related to the bound excitons I_1 identified in [4, 16] with the excitons bound to the oxygen-containing SA complexes that are prevalent in high-purity ZnS with an excess of zinc.[2] This long-wavelength band controls the absorption-edge position in the spectra and specifies it for 350 nm (T = 300 K) at $[O_S]$ = 1.2 mol %. It is worth noting that the spectral position of this band is affected

[2] Some researchers [20] attempted unsuccessfully to detect (in ZnS samples with an excess of Zn and the SA band in the visible region of the luminescence spectrum) the bound-exciton band that is similar to the I_1^d band observed for zinc selenide. It was shown [3, 4] that this type of exciton is characteristic of ZnS with a stoichiometric composition or with an insignificant excess of sulfur, in which case the self-activated SAL band at a wavelength of ~365 nm is observed in the visible region of the corresponding luminescence spectrum.

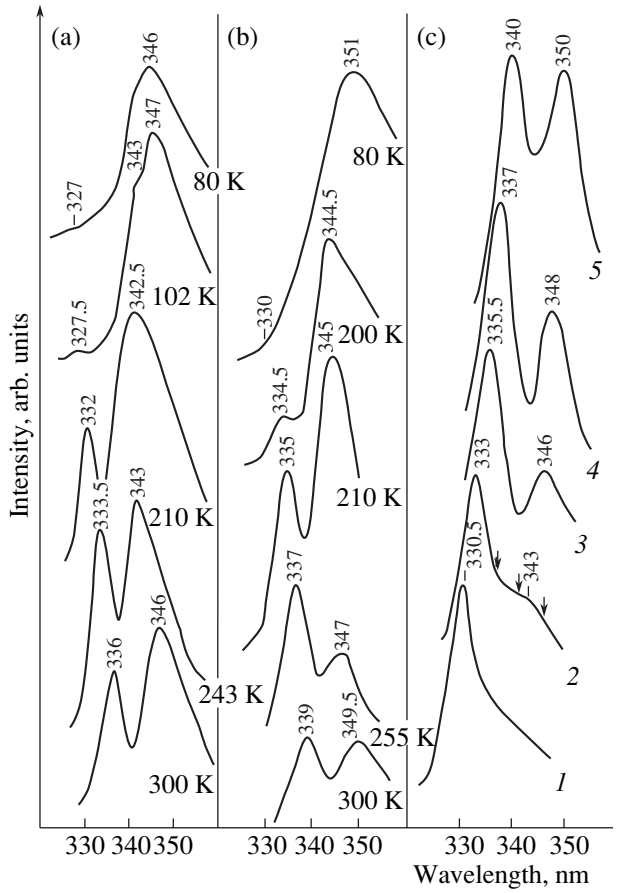

Fig. 3. Excitonic cathodoluminescence spectra of the Zn–O–S wurtzite powders: temperature dependences of the spectra at the substitutional-oxygen concentration $[O_S]$ = (a) 0.8 and (b) 1.1 mol %, and (c) the oxygen-concentration dependence of the spectra at 300 K. For (c), $[O_S]$ = (*1*) 0.06, (*2*) 0.4, (*3*) 0.8, (*4*) 1.0, and (*5*) 1.25 mol %. The arrows at curve *2* indicate the possible positions of LO replicas of the main cathodoluminescence band. Precise values of the wavelengths (in nm) corresponding to the features in the spectra are indicated.

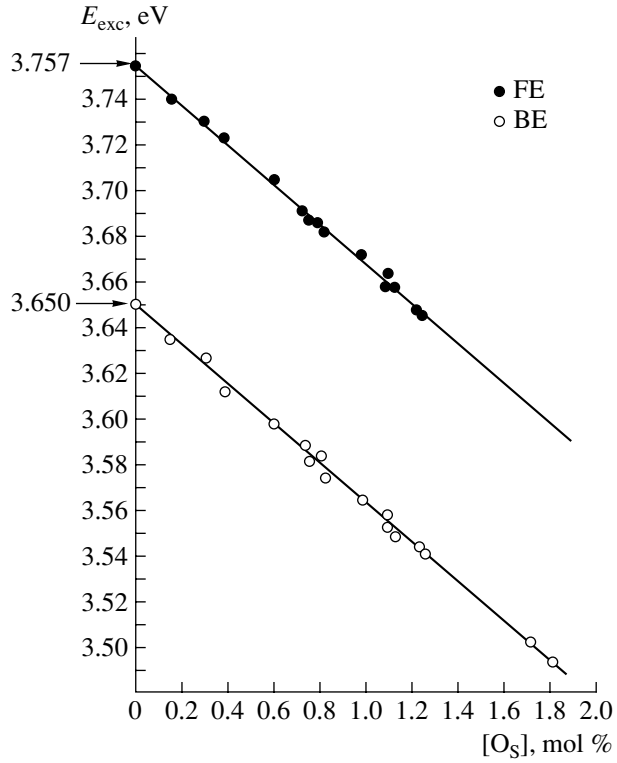

Fig. 4. The shift of cathodoluminescence bands related to the free (FE) and bound (BE) excitons in wurtzite ZnS as a function of the substitutional-oxygen concentration $[O_S]$ at a temperature of 300 K.

by an excess of Zn. The long-wavelength band is accompanied by a blue-emission SA band at ~445 nm in the visible region of the spectrum. At a low photoexcitation level, the SA band is prevalent while the excitonic bands are not detected. According to Fig. 2, the band corresponding to the bound exciton I_1 can be related to the lower subband of the split conduction band in ZnS [21].

In Fig. 3, we show the cathodoluminescence spectra that correspond to the samples of wurtzite ZnS (*w*). For this material, the oxygen solubility limit is higher; indeed, when there is an excess of zinc and at 1200°C, the limiting solubility is as high as 2 mol % according to [2] or 2.5 mol % according to [24]. As an example, Figs. 3a and 3b illustrate the temperature dependence of the cathodoluminescence spectra at oxygen concentrations of 0.8 and 1.1 mol %. The oxygen-concentration dependence of the spectra at 300 K is shown in Fig. 3c. The FE band is not observed in the cathodoluminescence spectrum at 80 K if the oxygen concentration $[O_S]$ is high (Figs. 3a, 3b). Two bands (as in the case of sphalerite) are observed in the spectrum as temperature increases and the featureless edge emission ($I_{EE} \sim 10^5$–10^4 arb. units) is quenched; the position and relative intensity of these bands depend on the oxygen concentration $[O_S]$. The intensity of the bands under consideration at 300 K decreases somewhat as $[O_S]$ increases, similarly to what is observed for sphalerite. If the oxygen-solubility limit is reached in ZnS (*w*), this intensity drops as low as $(1–5) \times 10^1$ arb. units. If $[O_S] <$ 0.1 mol %, the long-wavelength band decays to a greater extent than the short-wavelength band and is not detected (Fig. 3c).

In Fig. 4, we show the shift of the peaks of the wurtzite long-wavelength excitonic bands in relation to $[O_S]$. This shift is nearly linear (as in the case of ZnS (*s*)); however, the rate of this shift is now 90 meV per 1 mol % of $[O_S]$. If $[O_S] \longrightarrow 0$, the short-wavelength band is located at the position of the *A*-exciton band in the wurtzite ZnS (*w*) sample; this position corresponds to 330 nm (3.757 eV) at 300 K [2, 5].

At a low photoexcitation level, a blue-emission band with a peak at ~440 nm is prevalent in the spectrum [2], whereas excitonic bands are not detected. Thus, the pattern of the bands for wurtzite ZnS is basically similar to

that for sphalerite. This similarity suggests that the observed long-wavelength excitonic cathodoluminescence band corresponds to wurtzite as well to the excitons bound to the oxygen-containing SA complexes with a binding energy of ~104 meV. We observed the absorption-edge shift determined from this band up to 356 nm (300 K) at $[O_S] \approx 1.8$ mol %.

The above-considered appreciable shifts of excitonic spectra to longer wavelengths can be accounted for on the basis of theoretical studies concerned with III–V compounds doped with nitrogen (see, in particular, [21]). According to these studies, in the case of anionic substitution in solid solutions, an impurity that gives rise to an appreciable number of defects brings about a drastic decrease in the fundamental band gap. This decrease is related to a descent of one of the two noncrossing subbands that appear owing to the conduction-band splitting. Transitions (E_-) from the subband formed of extended states belonging to the conduction band are responsible for the band that is located at the longest wavelengths and exhibits the highest intensity. In the cathodoluminescence spectra we studied, this band corresponds to the FE emission that is accompanied by the band related to the I_1 bound exciton and has its origin in the oxygen-containing complexes (Figs. 1–4).

Phenomena similar to those considered above were also observed in the case of oxygen dissolution in CVD ZnS, with a composition close to stoichiometric, from which excess Zn was removed as a result of exposure to high isostatic pressure [4, 16]. In [16], the shift of excitonic bands to longer wavelengths, caused by a decrease in the band gap as a result of the dissolution of oxygen, was clearly detected in the cathodoluminescence spectra of these samples at 300 K. However, at 80 K, the free-exciton band is obscured by the high-intensity band I_2 with a peak at 327.5 nm (Fig. 5). The I_2 band is related to the excitons bound to interstitial zinc atoms [4, 8]. The cathodoluminescence spectra were measured at the depth of the informative layer (~0.3 μm) and corresponded to the surface layers of grains that apparently contained more Zn_i owing to the exit of zinc from the crystal as a result of exposure to high isostatic pressure.

In Fig. 6, in order to verify the results reported in [16], we show the spectra of pulsed cathodoluminescence for the same cleaved surfaces at an electron-beam energy of 400 keV. In this case, the data obtained correspond mainly to the deeper parts of a grain. As can be seen, the intensity of the I_2 band is appreciably reduced at the same liquid-nitrogen temperature. In addition, the free-exciton (FE) band for ZnS is observed; however, this band is shifted to longer wavelengths. The spectra corroborate the presence of several fractions formed as a result of recrystallization of the samples in the course of the exposure to high isostatic pressure [16]. In order to identify the fractions with different oxygen concentrations, we introduced into Fig. 6 the designations FE_0, FE_1, FE_2, and so on, where FE_0 corresponds to the *A* excitons in oxygen-free ZnS, and subscripts 1, 2, etc. correspond to the free excitons in solid solutions of various compositions. The LO phonon replicas (41–40 meV) have similar designations and confirm the spectral positions of the zero-phonon bands. The shifts to longer wavelengths for the prevalent fractions amount to ~(20–30) meV, which is consistent with the data reported in [16]. The dependence of the spectral position of the FE band on the oxygen concentration $[O_S]$ for sphalerite (see Fig. 2) makes it possible to determine $[O_S]$ from the shift of excitonic bands. For example, for a shift of ~30 meV, the dissolved-oxygen concentration corresponds to ~0.4 mol % (1×10^{20} cm^{-3}), which is lower than the limiting solubility of oxygen in sphalerite ZnS at the treatment temperature for high isostatic pressure ($(2–3) \times 10^{20}$ cm^{-3}) but is consistent with the solubility at the temperature of the CVD ZnS growth [16].[3] It is worth noting that the dependence of E_{exc} on $[O_S]$ (Figs. 2, 4) also governs the position of the excitonic bands themselves in oxygen-free ZnS.

The measurements of the pulsed-cathodoluminescence spectra were also aimed at refining the temperature dependence of the band of bound excitons I_1 [3, 4]. A detailed analysis shows that, at 25 K, (Fig. 6a) the band of excitons I_1 with a binding energy of ~60 meV is indistinguishable against the background of the phonon replicas, in particular, LOI_2. As the temperature of the measurements increases to 77 K, the intensity of the I_1 band increases and exceeds that of the LOI_2 band (Fig. 6a). However, this conclusion is only true for the "oxygen-free" fraction (FE_0), which is apparently present in a small amount, judging from the low intensity of the $LOFE_0$ band. For the prevalent fractions FE_2 and FE_1 (at the actual, i.e., experimentally refined, binding energy of 55–56 meV), the band I_1 should shift to longer wavelengths in correlation with variations in the band gap (Fig. 2). This band falls within the region of the phonon replicas $LOFE_3$ and $LOFE_4$; as a result, these replicas are broader than the other bands, for example, $LOFE_2$.

The pulsed-cathodoluminescence spectrum of the sample subjected to high isostatic pressure is shown in Fig. 6b; the spectrum was measured at 300 K. A single band is observed in the excitonic region of the spectrum. This band is accompanied by a number of phonon replicas on both the short- and long-wavelength sides of the peak. The energy of the phonons (14.4 meV) is close to that of the transverse acoustic (TA) phonons in sphalerite [5] and solid solutions based on ZnS [28]. The spectral position of the band under consideration (Fig. 6b) corresponds to the short-wavelength component of the bound-exciton doublet I_1 [4]. The binding

[3] The possibility of determining the value of $[O_S]$ from the shift of excitonic bands is very attractive, since the data of the X-ray structure analysis used to determine the dissolved-oxygen concentration from a decrease in the lattice constants cannot always be applied without reservations. These reservations are especially relevant in the case of ZnS (s) because, in this material, stacking faults and polytype inclusions can be formed, which affect (in addition to oxygen) the lattice constant [2].

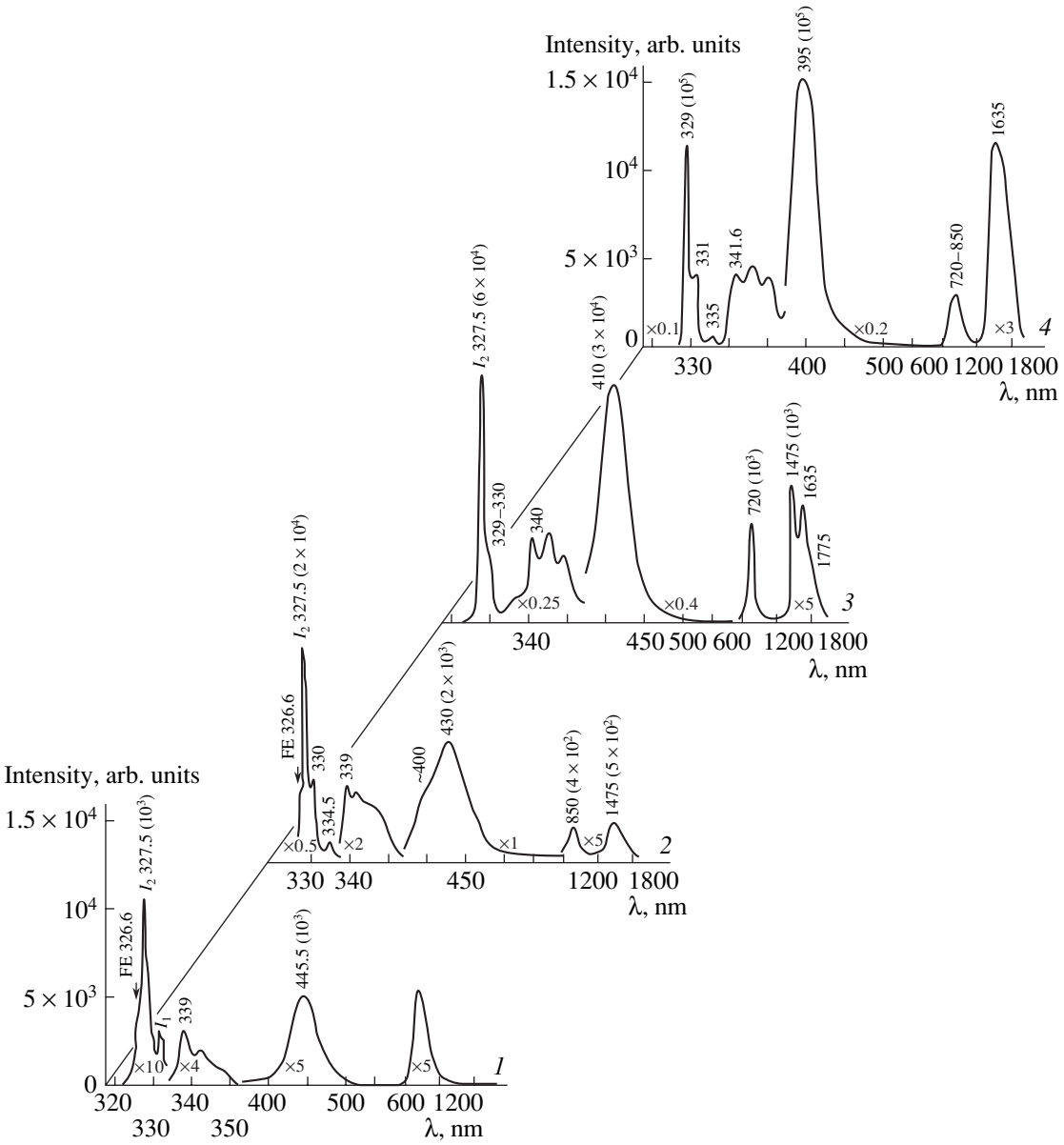

Fig. 5. Cathodoluminescence spectra measured at 80 K at the excitation intensity of 10^{22} cm^{-3} s^{-1} for the CVD ZnS samples: (*1*) the initial sample and (*2–4*) the samples subjected to high isostatic pressure at 1500 atm and temperatures of 940 ⟶ 1060°C (*2* ⟶ *4*). Spectrum *4* corresponds to the sample grown in an atmosphere of excess H_2S. Precise values of the wavelengths (in nm) corresponding to the features in the spectra and (in brackets) the relative intensities of the main bands are indicated.

energy, determined from a comparison of the position of this band to that of the excitonic band FE_0, is equal to ~55 meV.

For the sample under consideration, the short-wavelength component of the SA band at ~410 nm is observed in the visible region of the spectrum (Fig. 5, curve *3*). It is worth noting that the earlier assumption [3, 4] that the short-wavelength component of the SA band corresponds to a specific wavelength should be refined. As is found out, an exposure to high isostatic pressure results in different spectral positions of this band in relation to $[O_S]$; specifically, the band gradually shifts to shorter wavelengths as the dissolved-oxygen concentration increases and attains a position at 395 nm in the range of the compositions under study (Fig. 5, curve *4*). Taking into account previous publications [13, 14], we may assume that the position of the band under consideration can be found at even shorter wavelengths as $[O_S]$ increases and attains its limiting value for ZnS. Taking into consideration theoretical conclusions [21], according to which one of the two subbands (the E_- transitions) descends with respect to the valence band while the second subband (the E_+ transitions) ascends, we may assume that the short-wavelength

component of the SA emission is related to transitions from the second subband formed of highly localized impurity states to the acceptor level of the oxygen-containing SA complex. This consideration accounts for the gradual shift of the short-wavelength component of the SA band to higher energies. In this case, localized oxygen-related states should be found above the conduction-band bottom E_c. According to our experimental data, these states are located at $\lesssim 0.2$ eV from E_c (in oxygen-free ZnS) at comparatively small values of $[O_S]$, in which case the short-wavelength component of the SA luminescence becomes distinguishable. At a comparatively low concentration $[O_S]$, the probability of a transition from O_S to the acceptor level of the oxygen-containing complexes increases as the $Zn_i^{\bullet}$ atoms leave the crystal; these atoms are incorporated into the SA centers as donors and control the long-wavelength component of the emission. The effect of the dissolved oxygen on the energy-band states also endows this emission with certain specific features [17–19], which differentiate it from emission related to the typical donor–acceptor recombination.

The fact that the band I_1 is the only band observed in the spectrum of the ZnS:O crystal at 300 K confirms the prevalence of the corresponding transitions as both the temperature and the excitation intensity increase, as was noted in [4, 18]. In this study, we do not report the pulsed-cathodoluminescence spectra of the CVD ZnS samples at an excitation level of 10^{26} cm^{-3} s^{-1}, since we found that an appreciable increase in the excitation intensity gave rise to a certain broadening of the spectra, which was apparently caused by instability of the supersaturated ZnS:O solid solution. The available published data on the luminescence of "high-purity" ZnS samples grown using new technologies (see, for example, [8]) are typically obtained at a high excitation intensity. In this case, the excitonic bands (in particular, I_1) are prevalent but oxygen-initiated emission from the oxygen-containing complexes, which is enhanced at a low excitation level, is hardly observed [18]. Our studies indicate that both bands are related to the same oxygen-containing centers.

Finally, we note that the above-considered effect of an isoelectronic acceptor (oxygen) on the ZnS electronic energy-band structure can be reduced to a great extent by other impurities (isoelectronic donors). For example, tellurium can act as a compensating impurity for oxygen. Indeed, the effect of an isoelectronic impurity (oxygen in ZnS) gives rise to local distortions at the lattice sites due to the difference between the atoms' sizes and electronegativities (of sulfur and oxygen). Tellurium, when introduced into ZnS (ZnSe) that contains oxygen, gives rise to the completely opposite effect and undoubtedly forms a complex with oxygen. The interaction of these impurities suppresses the main effect on the lattice (the local short-range strains). Indeed, as was shown in [7, 9], the simultaneous introduction of Te_S and O_S did not give rise to the above-described effects; i.e., appreciable shifts of both the excitonic bands and the fundamental-absorption edge to longer wavelengths due to a decrease in the band gap, the emergence of the short-wavelength component in the SA emission, and other such effects were not observed.

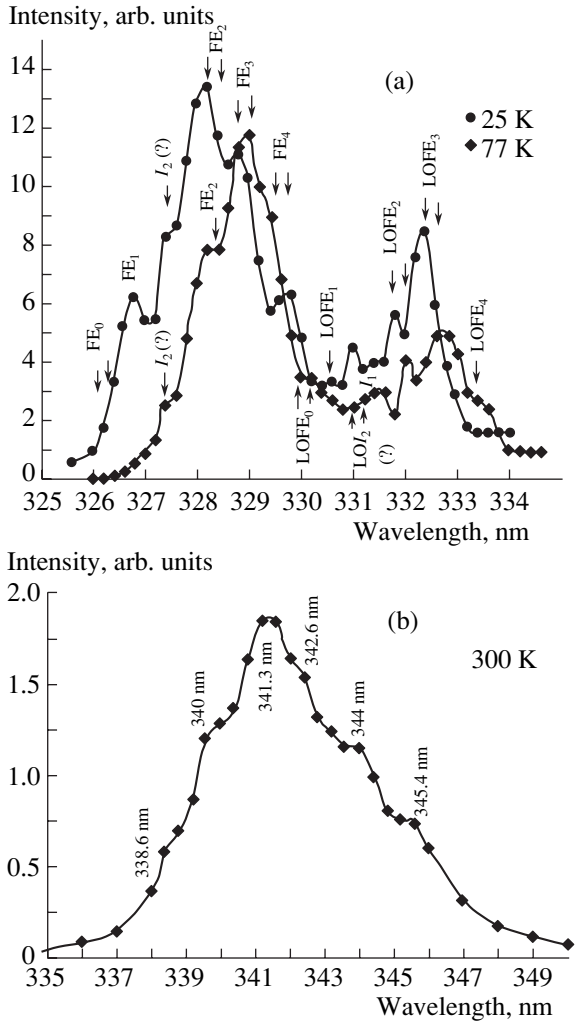

Fig. 6. Pulsed-cathodoluminescence spectra measured at (a) 25 and 77 K and (b) 300 K and at the excitation intensity $\leq 10^{24}$ cm^{-3} s^{-1}. The paired vertical arrows correspond to the position of a band at 25 and 77 K.

4. CONCLUSIONS

In conclusion, we note the following.

The results concerning a variation in the spectra of excitonic and self-activated luminescence, as well as in the Zn–O–S band gap, that have not been accounted for in earlier publications are consistent with the theory of noncrossing energy bands (this theory was developed for III–N–V solid solutions).

The observed shift of the excitonic bands to lower energies as the substitutional-oxygen concentration $[O_S]$

increases can be used to directly determine the dissolved-oxygen concentration in sphalerite and wurtzite modifications of ZnS.

We verified the role of oxygen in the formation of the centers of self-activated emission and the origination of the band related to the excitons I_1 bound to these centers in ZnS with an excess of Zn. We showed that the band related to the bound exciton I_1 is observed in ZnS at 300 K owing to the fact that the corresponding binding energy exceeds *kT*.

The obtained dependences of the energy positions E_{exc} of excitonic peaks on $[O_S]$ confirm the spectral positions of the excitonic bands observed in oxygen-free ZnS. However, it should be noted that the acceptability of these positions is still being debated in current publications.

REFERENCES

1. F. A. Kroeger and J. A. M. Dikhoff, J. Electrochem. Soc. **99** (4), 144 (1952).
2. N. K. Morozova and V. A. Kuznetsov, *Zinc Sulfide. Production and Optical Properties* (Nauka, Moscow, 1987) [in Russian].
3. N. K. Morozova, I. A. Karetnikov, V. V. Blinov, and E. M. Gavrishchuk, Fiz. Tekh. Poluprovodn. (St. Petersburg) **35**, 25 (2001) [Semiconductors **35**, 24 (2001)].
4. N. K. Morozova, I. A. Karetnikov, V. M. Plotnichenko, *et al.*, Fiz. Tekh. Poluprovodn. (St. Petersburg) **38**, 39 (2004) [Semiconductors **38**, 36 (2004)].
5. *Physics and Chemistry of II–VI Compounds*, Ed. by M. Aven and J. S. Prener (North-Holland, Amsterdam, 1967; Mir, Moscow, 1970).
6. K. Akimoto, T. Miyajima, and Y. Mori, Phys. Rev. B **39**, 3138 (1989).
7. N. K. Morozova, L. D. Nazarova, and N. D. Danilevich, Fiz. Tekh. Poluprovodn. (St. Petersburg) **28**, 1699 (1994) [Semiconductors **28**, 944 (1994)].
8. Nam Sungun, Rhee Jongkwang, O. Byungsung, and Ki-Seon Lee, J. Korean Phys. Soc. **32** (2), 156 (1998).
9. L. D. Nazarova, Candidate's Dissertation (Moscow Power Inst., Moscow, 1995).
10. N. K. Morozova, I. A. Karetnikov, V. V. Blinov, *et al.*, Fiz. Tekh. Poluprovodn. (St. Petersburg) **33**, 569 (1999) [Semiconductors **33**, 531 (1999)].
11. N. K. Morozova, A. V. Morozov, I. A. Karetnikov, *et al.*, Neorg. Mater. **30**, 731 (1994).
12. M. V. Fok and N. P. Golubeva, Zh. Prikl. Spektrosk. **17**, 261 (1972).
13. N. K. Morozova, V. D. Chernyĭ, T. P. Dolukhanyan, and Yu. A. Pashchenko, Izv. Vyssh. Uchebn. Zaved., Fiz., No. 2, 60 (1987).
14. N. K. Morozova, O. I. Korolev, M. M. Veselkova, and M. M. Malov, Zh. Prikl. Spektrosk. **23**, 81 (1975).
15. N. K. Morozova, V. S. Zimogorskiĭ, and A. V. Morozov, Neorg. Mater. **29**, 1014 (1993).
16. N. K. Morozova, I. A. Karetnikov, K. V. Golub, *et al.*, Neorg. Mater. **40** (11), 1299 (2004).
17. V. V. Blinov, Candidate's Dissertation (Moscow Power Inst., Moscow, 2003).
18. N. K. Morozova, V. V. Blinov, V. M. Lisitsyn, *et al.*, in *Proceedings of XXXIV International Scientific and Technical Workshop on Noise and Degradation Processes in Semiconductor Devices* (Mosk. Énerg. Inst., Moscow, 2004), p. 223.
19. N. K. Morozova, D. V. Zhukov, and V. E. Mashchenko, in *Proceedings of XXXII International Scientific and Technical Seminar on Noise and Degradation Processes in Semiconductor Devices* (Mosk. Énerg. Inst., Moscow, 2004), p. 234.
20. M. Yoneta, K. Ishino, and K. Yoshino, J. Cryst. Crowth **237–239**, 1731 (2002).
21. W. Shan, W. Walukiewicz, J. W. Ager, *et al.*, Phys. Rev. Lett. **82**, 1221 (1999).
22. E. A. Zakharov, I. V. Tolkachev, and D. Ya. Kovalenko, Neorg. Mater. **14**, 1389 (1978).
23. N. A. Yashtulov and V. S. Zimogorskiĭ, in *Proceedings of XXX International Scientific and Technical Seminar on Noise and Degradation Processes in Semiconductor Devices* (Mosk. Énerg. Inst., Moscow, 2000), p. 211.
24. E. A. Chechetkina, S. S. Galaktionov, and A. A. Bundel', Neorg. Mater. **14**, 1393 (1978).
25. US Patent, No. 6,083,561 (2000).
26. C. Rooymans, *Structural Investigations on Some Oxides and Other Chalcogenides at Normal and Very High Pressures* (North-Holland, Amsterdam, 1967; Mir, Moscow, 1969).
27. V. M. Lisitsyn, V. I. Korepanov, V. I. Oleshko, and V. Yu. Yakovlev, Izv. Vyssh. Uchebn. Zaved., Fiz., No. 11, 5 (1996).
28. D. Schmeltzer, R. Baserman, and D. Slamovits, Phys. Rev. B **22**, 4038 (1980).

Translated by A. Spitsyn

Semiconductors, Vol. 39, No. 5, 2005, pp. 493–498. Translated from Fizika i Tekhnika Poluprovodnikov, Vol. 39, No. 5, 2005, pp. 521–527.

ELECTRONIC AND OPTICAL PROPERTIES OF SEMICONDUCTORS

Magnetic Ordering Effects in Heavily Doped GaAs:Fe Crystals

B. P. Popov^, V. K. Sobolevskiĭ, E. G. Apushkinskiĭ, and V. P. Savel'ev

St. Petersburg State Polytechnical University, Politekhnicheskaya ul. 25, St. Petersburg, 195251 Russia

^e-mail: popov@tuexph.stu.neva.ru

Submitted September 6, 2004; accepted for publication September 15, 2004

Abstract—The exchange coupling of Fe centers in GaAs crystals is studied by electron spin resonance (ESR). Transitions to a superparamagnetic state and to an impurity ferromagnetism domain are analyzed. A study of a system of single-domain magnetically ordered regions in GaAs:Fe with the transition to a ferromagnetic state occurring at the temperature T_{C1} = 460 K is described. It is shown that impurity ferromagnetism with a transition temperature T_{C2} of 60 K in a disordered system of Fe centers randomly distributed among superparamagnetic regions exists in GaAs:Fe. © *2005 Pleiades Publishing, Inc.*

1. INTRODUCTION

Elements of the iron transition Group stand out as having a large magnetic moment of the unfilled 3*d* shell and deep energy states in the semiconductor band gap, whose wave functions are delocalized over the atoms of the host lattice within two to three coordination shells [1]. Extensive 3*d* electron delocalization permits the formation of various clusters of 3*d* elements. This circumstance is indicated by studies of the electron spin resonance (ESR) spectra, for example, *g*-factor shifts, large linewidths, and so on [1, 2]. Clusters of 3*d* centers should have "giant" magnetic moments and are capable of imparting unique properties to a material. The application and research potential of such materials is determined by the possibility of controlling their magnetic properties by properly varying the size and concentration of magnetic clusters at a high electrical resistivity.

Nasledov and Masterov *et al.* were the first to investigate the anomalous magnetic properties of GaAs [3–5]. Determination of the state of an Fe impurity in heavily doped GaAs has been a long-standing problem. The limiting solubility of Fe in this matrix is about 10^{18} cm^{-3}. Therefore, studies of samples with a high Fe concentration were performed under the assumption that the formation of magnetically ordered regions in III–V compounds is related to the presence of chemical compounds belonging to a second (magnetic) phase. In this case, complexes should preferably be formed by impurity atoms that can combine chemically with the atoms of the host lattice (FeAs or FeGa). X-ray analysis of heavily doped GaAs samples showed that they had a perfect crystal structure. The analysis revealed that the samples had second-phase inclusions, but these inclusions added up to no more than 1% of the sample volume. By properly varying the growth and doping conditions, it was possible to prepare GaAs⟨Fe⟩ crystals with the iron concentration $n_{Fe} = (10^{18}–10^{20})$ cm^{-3} [3, 4], which had anomalously high magnetic susceptibility ($\chi \approx 10^{-3}$). The temperature of the ferromagnetic phase transition of these samples was derived from studies of the temperature dependence of the static magnetic susceptibility [3]. Figure 1 shows the temperature dependences of the derivative of magnetic susceptibility $d\chi/dT$. Both paramagnetic and ferromagnetic samples, i.e., irrespective of the Fe concentration, exhibited a magnetic phase transition at the same temperature: T_{C1} = 460 K.

Studies of the magnetic phase transitions in Fe–Ga and Fe–As systems [3, 4] showed that neither of these compounds undergoes a phase transition at the temperature T = 460 K. Among all the Fe compounds with Ga, only Fe_8Ga_{11}, with the phase transition temperature T_C = 750 K, is ferromagnetic. Among the Fe compounds with As, Fe_2As undergoes antiferromagnetic ordering at the Curie temperature T_C = 850 K and FeAs undergoes ferromagnetic ordering at the transition temperature T_C = 130 K. It was assumed, in this context [3, 5], that heavily doped GaAs:Fe crystals can undergo

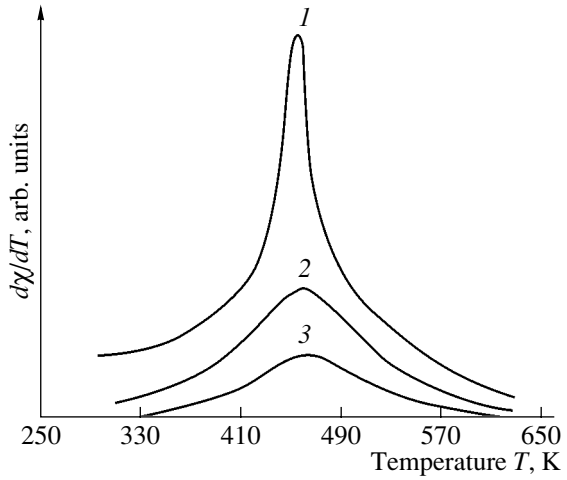

Fig. 1. The temperature dependence of the derivative of the magnetic susceptibility $d\chi/dT$ for GaAs:Fe crystals. n_{Fe} = (*1*) 10^{20}, (*2*) 10^{19}, and (*3*) 10^{18} cm^{-3}.

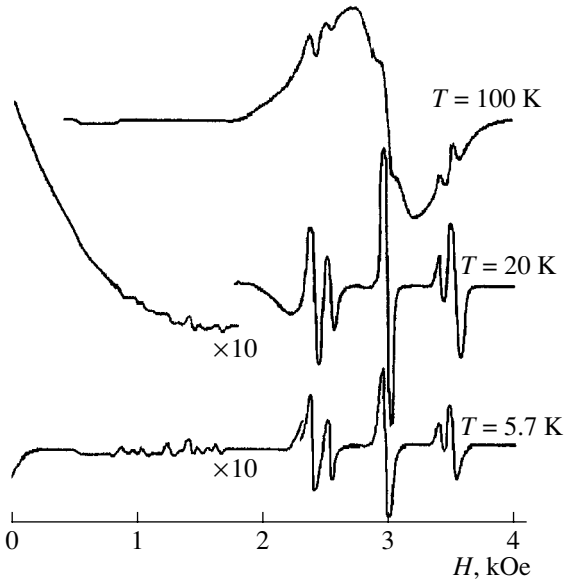

Fig. 2. ESR spectra of the exchange-coupled Fe–Fe pairs at the *X* band obtained for GaAs:Fe samples with $n_{Fe} = 3 \times 10^{18}$ cm^{-3} at various temperatures (specified at the spectra).

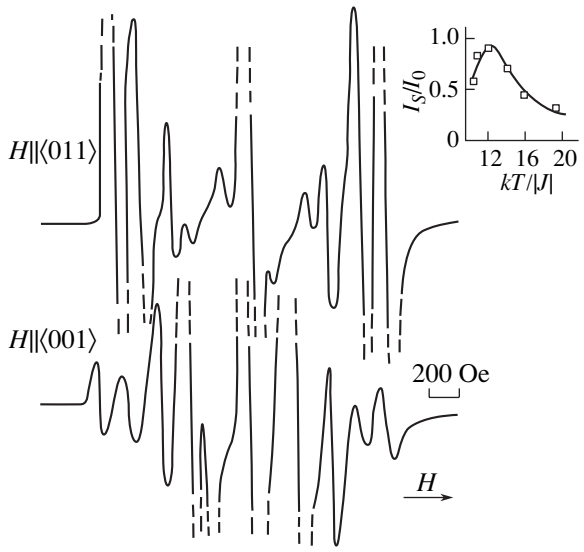

Fig. 3. ESR spectra of the exchange-coupled Fe–Fe pairs in GaAs:Fe samples with $n_{Fe} = 3 \times 10^{18}$ cm^{-3} obtained at the *Q* band at $T = 77$ K. The inset shows the temperature dependence of the signal I_S intensity resulting from pairs of neighboring magnetic centers for $S = 5$ and $J < 0$. I_0 is the largest experimental value of I_S.

the formation of single-domain, magnetically ordered (superparamagnetic) regions in which exchange interaction is mediated by the atoms of the host lattice.

The purpose of this study was to gain insight into the coupling of Fe impurity centers in a GaAs diamagnetic matrix and investigate the magnetic properties of the superparamagnetic regions.

2. INVESTIGATION OF EXCHANGE-COUPLED PAIRS

To clarify the nature of the magnetic coupling of iron atoms and determine the interaction constants of the impurity centers, we studied exchange-coupled Fe pairs in GaAs crystals. An ESR study was performed using GaAs:Fe crystals with the iron concentrations $n_{Fe} = 3 \times 10^{18}$–$10^{19}$ cm^{-3}. The samples were prepared by directed crystallization followed by successive impurity dilution and zone leveling of the impurity over the crystal [3, 4]. Figure 2 displays a characteristic ESR spectrum obtained at 9.6 GHz (the *X* band). The ESR spectrum obtained for $T \geq 100$ K consists of a broad line produced by groups of interacting magnetic centers and a fine structure due to separate Fe atoms. As the temperature is lowered, the broad line decreases in its intensity and splits into a number of narrow resonance peaks. In magnetic fields with $g \approx 2$, the spectrum of separate centers persists, and a spectrum produced by exchange-coupled iron pairs appears. The coincidence of the centers of the lines split into weak fields with the center of the separate iron atom line suggests that the weak-field transitions are actually forbidden transitions with $\Delta m = 2$ and 3. *X*-band microwave studies showed that the ESR spectrum of the exchange-coupled pairs does not permit the identification of individual transitions because they are poorly resolved. Thus, it does not appear to be possible to determine the value of the exchange integral from the temperature dependence of the ESR spectrum in this frequency range. Therefore, ESR measurements were conducted at 28 GHz (the *Q* band) [5]. The 28-GHz room-temperature spectrum of the same samples was found to be similar to that shown in Fig. 2. As the temperature is dropped to below 100 K, the spectrum, in addition to the fine-structure lines of the separate iron centers, features lines originating from the exchange-coupled pairs of magnetic centers with the total spin $S = 5$, whose ESR spectrum is shown in Fig. 3.

Assume that the line connecting the two iron atoms nearest to each other, A and B, occupying sites in the gallium sublattice of GaAs, i.e., the ⟨011⟩ axis, is the *z* axis. The spin part of the Hamiltonian for these two atoms in the case of strong exchange coupling can then be written as [6]

$$H = g\beta\mathbf{H}\mathbf{S} + J\mathbf{S}_A\mathbf{S}_B + D(S_{Ax}^2 - S_{By}^2) + \frac{B}{2}(\mathbf{S}_A\mathbf{S}_B - 3S_{Az}S_{Bz}), \quad (1)$$

where $\mathbf{S} = \mathbf{S}_A + \mathbf{S}_B$, *D* and *B* are the spin Hamiltonian parameters accounting for the exchange coupling anisotropy, β is the Bohr magneton, and **H** is the magnetic field vector. The exchange integral *J* is negative ($J < 0$) for ferromagnetic interaction. The quantity *B* determines the angular dependence of the spectrum and is defined as

$$B = g^2\beta^2 R^{-3}(3\cos^2\theta - 1),$$

where R is the size of the AB pair, g is the spectroscopic splitting factor for this pair, and θ is the angle between the axis of the AB pair and the **H** direction.

The angular dependence of the ESR spectrum can be used to derive the constant B and, hence, the distance between the Fe atoms nearest to each other. The size of the pair was found to be $R = (5 \pm 1)$ Å. For a gallium arsenide lattice parameter of 5.65 Å, the distance obtained corresponds to an Fe–As–Ga–As–Fe structure. Studies of the separate iron centers show [1–3] that the 3d electron wave function is delocalized over the atoms of at least two coordination spheres. Thus, the d electron wave functions of two neighboring magnetic centers overlap at the Ga atom, which accounts for the onset of indirect ferromagnetic interaction.

The value of the exchange integral J was derived from a study of the temperature dependence of the ESR signal intensity (see the inset in Fig. 3). According to [6], the resonance line intensity is proportional to the product of the transition probability

$$W_S = \frac{1}{2}\sum \langle M|S|M+1\rangle^2, \qquad (2)$$

where $\langle M$ and $M+1\rangle$ are states with the magnetic quantum numbers M and $M+1$, and by the exchange level population

$$P_S = \frac{\exp\left[-\frac{JS(S+1)}{2kT}\right]}{\sum(2S+1)\exp\left[-\frac{JS(S+1)}{2kT}\right]}. \qquad (3)$$

A comparison of Eqs. (2) and (3) with the experimental data permitted us to identify the exchange interaction as ferromagnetic in character, with the exchange integral $J = J_0 = -8.3$ cm^{-1}.

3. INVESTIGATION OF SUPERPARAMAGNETISM IN GaAs CRYSTALS

At higher iron doping levels ($n \approx 10^{20}$ cm^{-3}), the formation of macroscopic regions with uniform magnetization was observed [2, 3]. Transition to a superparamagnetic (SP) state is known [7] to occur in magnetic systems formed of single-domain ferromagnetic regions in which the thermal fluctuations exceed the remagnetization threshold set by magnetic anisotropy. The energy of a uniaxial uniformly magnetized region can be written as [7]

$$E = K_{\text{anis}} V \sin^2\alpha - \boldsymbol{\mu}\mathbf{H}\cos(\beta - \alpha),$$

where K_{anis} is the anisotropy constant, V is the volume of the region, and β and α are the angles produced between the easy-magnetization axis and the corresponding $\boldsymbol{\mu}$ and **H** vectors. Above a certain temperature, an ensemble of single-domain regions behaves similarly to a gas formed of paramagnetic molecules with a large magnetic moment μ. Note that, in strong magnetic fields, these regions behave paramagnetically at high temperatures but in a ferromagnetic manner at lower temperatures. The relaxation time τ is controlled by the probabilities of transition between two equilibrium magnetic moment orientations. The transition probability depends on both the anisotropy energy, $K_{\text{anis}}V$, and the energy of an SP region in a magnetic field μH. Hence, in the presence of SP regions, ESR spectra measured at different frequencies should be substantially different. The same magnetized regions behave similarly to superparamagnets at low frequencies ($f < 1/\tau$) and ferromagnets at high frequencies ($f > 1/\tau$).

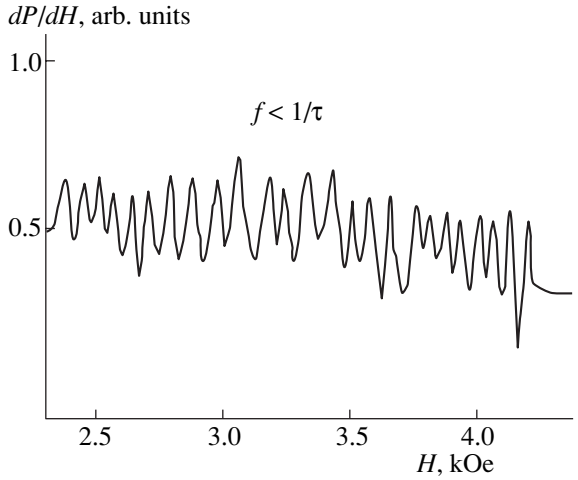

Fig. 4. ESR spectra of a GaAs sample with an Fe concentration of 10^{20} cm^{-3} obtained in the X band.

We studied the ESR spectra of GaAs samples with the iron concentration $n_{\text{Fe}} = 10^{20}$ cm^{-3} at the frequencies $f_X = 9.6$ GHz and $f_Q = 28$ GHz. The ESR spectrum obtained at 9.6 GHz ($f_X < 1/\tau$) (Fig. 4) consisted of a large number of fine-structure lines. This structure is caused by the possible components of the total magnetic moment of an SP region along magnetic field direction. At a frequency of 28 GHz ($f_Q > 1/\tau$), this spectrum disappeared and was replaced by a broad line and a spectrum of individual Fe^{3+} centers; the latter spectrum included five fine-structure lines. The large number of lines in the 9.6-GHz ESR spectrum and their small width imply a fairly uniform impurity distribution over an SP region. This specific behavior of the ESR spectra measured at different frequencies, as well as the absence of an ESR absorption signal in a zero magnetic field, are characteristic of a superparamagnet [6, 7]. The ESR spectra were used to derive the number of magnetic atoms in the regions, $N_{\text{Fe}} \approx 25$, the average distance between the magnetic centers, $\bar{r} \approx 10$ Å, and the lower limit of the parameter $\tau < 4 \times 10^{-11}$ s.

The GaAs samples used to study the parameters of SP regions had iron concentrations of $2 \times 10^{20} < n_{\text{Fe}} < 6 \times 10^{20}$ cm^{-3}. NMR measurements made on Ga and As

Parameters of the superparamagnetic regions

Sample	n_{Fe} in sample, 10^{20} cm^{-3}	V/V_0, %	$I_S(0)$, Oe	V, 10^{18} cm^{-3}	n_{Fe} in region, 10^{20} cm^{-3}
1	2	10	32	0.24	5.7
2	3	25	32	0.96	5.7
3	4	75	32	2.5	5.7
4	6	100	33	9.1	5.9

Note: V is the volume of superparamagnetic regions, V_0 is the sample volume, and $I_S(0)$ is the spontaneous magnetization at $T = 0$.

nuclei revealed that the relative volume V/V_0 occupied by the spontaneous magnetization regions in the crystals ranged from 10 to 100% (see table). X-ray structure microanalysis of the samples permitted the localization of the crystal regions with second-phase inclusions. These regions were removed from the samples and the ESR spectra measured again. The resulting ESR spectra were found to be identical to the spectra in Fig. 3. This circumstance suggests that the linear dimensions of the regions responsible for the broad ESR line are less than 100 Å (the limiting resolution of the X-ray analysis).

The field and temperature dependences of the magnetization were also investigated. According to the theory of Néel [7], the magnetization of an ensemble of SP particles can be presented in the form

$$I(T) = I_S\bar{V}\coth\left(\frac{\mu H}{kT} - \frac{kT}{\mu H}\right), \quad (4)$$

where I_S is the spontaneous magnetization at the temperature $T = 0$, and $\bar{V}$ is the average volume of the SP region. Assuming that I_S is independent of the volume of the region, the hyperbolic cotangent can be expanded in a series to yield

$$I = I_S^2\frac{\bar{V}H}{3kT} \text{ for } \mu H \ll kT, \quad (5)$$

$$I = I_s\left(1 - \frac{kT}{I_S\bar{V}H}\right) \text{ for } \mu H \gg kT. \quad (6)$$

Here, $\mu = \bar{\mu} = I_S\bar{V}$ is the average magnetic moment of an SP region. Taking into account the temperature dependence of the magnetization and using Eq. (6), we can easily find the average volume of SP regions and their magnetic moment $\bar{\mu}$. If a sample is not completely polarized, the magnetization $I_S(T)$ should be determined taking into account the part of the sample volume occupied by the SP regions.

Figure 5 displays the magnetization of GaAs (sample 2 in the table) as a function of the magnetic field strength for various temperatures. The solid lines are calculated using Langevin relation (4). The field dependences of the magnetization convincingly demonstrate that the sample is superparamagnetic. Setting the magnetizations $I_1 = 0.47$ Oe for $T_1 = 4$ K and $I_2 = 0.44$ Oe for $T_2 = 10$ K, and rewriting Eq. (6) in the form

$$\bar{\mu} = I_S\bar{V} = \frac{k(I_1T_2 - I_2T_1)}{H(I_1 - I_2)}, \quad (7)$$

we obtain the value of the average magnetic moment of an SP region for $T \longrightarrow 0$ K: $\bar{\mu} \approx 1.4 \times 10^{-18}$ erg/Oe. Then, using the values of I_S obtained at $T = 4$ K (Fig. 5) and $V/V_0 = 0.25$ from the NMR experiments for the polarized part of the sample volume, we obtain $I_S(0) = 32$ Oe for the magnetization of an SP region. The parameters of the spontaneous magnetization regions for GaAs:Fe crystals with different doping levels are listed in the table. When determining the iron atom concentration in the SP regions, the value of the magnetization was extrapolated to $T = 0$ and the value of the g factor was assumed to be 2.04, which corresponds to separate iron centers.

A comparison of the parameters of the SP regions suggests that an increase in the content of magnetic impurity in a sample brings about an increase in the average size of the regions while not noticeably changing their magnetic nature. This conclusion is confirmed by studies of the temperature behavior of the derivative of magnetic susceptibility $d\chi/dT = f(T)$ performed for samples with different iron concentrations (Fig. 1). All the samples exhibited a magnetic phase transition at the

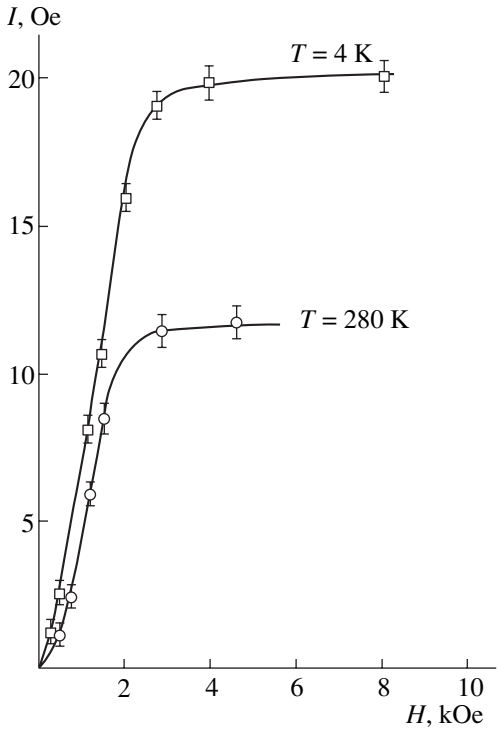

Fig. 5. Magnetization of a GaAs:Fe sample as a function of the magnetic field strength at various temperatures.

same temperature (T_{C1} = 460 K). This temperature corresponds to the phase transition inside the SP regions and is in good agreement with the value derived from straightforward molecular field theory [7]: $T_{C1} = 2ZJ_0S(S + 1)$. Using the exchange integral found in the ESR experiments, $|J_0| = 8.3$ cm^{-1}, the experimental value T_{C1} = 460 K is obtained assuming that the number of nearest neighbors $Z = 6$. This result suggests a noticeable correlation in the magnetic atom arrangement in the SP regions.

4. INVESTIGATION OF IMPURITY FERROMAGNETISM

An increase in the magnetic impurity concentration should bring about the onset (at a certain stage) of interaction among the magnetic atoms outside the SP regions. This conjecture has received direct substantiation from NMR measurements of intrinsic magnetic fields at the host lattice nuclei [4]. GaAs:Fe crystals with the iron concentration $n_{Fe} = 10^{18}$ cm^{-3} exhibited a decrease in the Ga and As NMR signals by about 0.1%. No NMR signals were observed at the resonance frequencies of Ga and As in crystals with $n_{Fe} = 6 \times 10^{20}$ cm^{-3}. Estimation of the magnetic fields for the case of a uniformly distributed impurity showed the presence of induced magnetic fields of about 10 Oe at the nuclei of the host lattice, which indicates that there is magnetic ordering in the material. The magnetic order extending over the crystal may be due to the Fe impurity atoms residing outside the SP regions. Thus, there should exist a second, low-temperature phase transition to a magnetically ordered state. This second ferromagnetic transition should take place at low temperatures ($T_{C2} < T_{C1}$) because of the low concentration and random distribution of the impurity atoms; i.e., this transition should be of a percolation nature.

Experimental observation of the second phase transition could provide a basis for using the concept of ferromagnetism in III–V semiconductors. We searched for the second phase transition in GaAs crystals with the iron concentration $n_{Fe} = (1–6) \times 10^{20}$ cm^{-3}. These samples were used to study the temperature behavior of ^{71}Ga NMR and Fe($3d^5$) ESR signal intensity. As follows from the NMR data, the spontaneous polarization regions occupied 10–75% of the total sample volume. If there exists a temperature T_{C2} below which the sample becomes completely polarized, the NMR signal produced by the host lattice nuclei should decrease substantially for $T < T_{C2}$ due to the shift and broadening of the NMR line in the nonuniform internal magnetic field. The results obtained in the study of the temperature behavior of the ^{71}Ga NMR signal are summarized in Fig. 6. We can clearly see that the NMR line intensity varies only weakly as the temperature decreases from room temperature level to 100 K, increases sharply at T = 60 K, and drops abruptly as the temperature is lowered still further. The slight increase in the NMR signal intensity observed to occur as the temperature

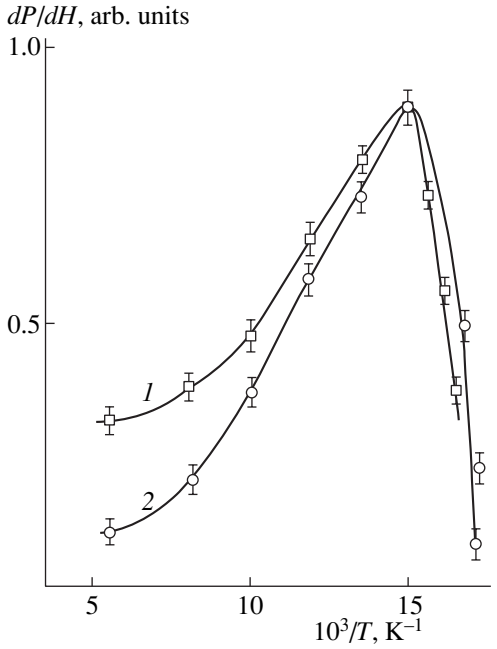

Fig. 6. Temperature dependences of the (*1*) NMR and (*2*) ESR signal intensities.

decreases for $T > 60$ K can apparently be assigned to two competing processes that take place in the sample: polarization of the ^{71}Ga magnetic moments in the external magnetic field, which causes a rise of the signal in accordance with the Curie law, and an increase in the magnetic moments of the SP regions. As the crystal magnetization monotonically increases, an ever increasing number of host lattice nuclei are affected by the internal nonuniform magnetic field. The sharp drop in the NMR signal intensity observed for $T < 60$ K indicates that the polarization of the crystal is complete.

The NMR studies do not, however, answer the question of whether the transition is induced by magnetic interaction among the SP regions or by the Fe atoms distributed outside them. To clarify this point, we studied the temperature dependence of the ESR signal (see Fig. 6). The ESR spectra of the GaAs:Fe samples with an Fe concentration of $n_{Fe} \approx 10^{20}$ cm^{-3} were similar in their pattern to those in Fig. 2. As has already been mentioned, these spectra essentially consist of a broad line of an irregular shape in the low-field domain, which is caused by resonance of the exchange-coupled 3*d* centers in the SP regions, and of fine-structure lines indicating separate iron centers (Fe^{3+}) located between the above regions. As the temperature is lowered to 60 K, the ESR line broadens in weak fields and, as a consequence, decreases in its intensity. At the same time, the ESR signal of the separate centers increases. Further lowering of the temperature brings about a sharp decrease in the ESR intensity of the separate centers and an increase in the broad-line amplitude. This observation is indicative of the existence of a second magnetic phase transition at $T \approx 60$ K. If the SP regions

are nonuniformly distributed in size and, accordingly, in magnetic moments, the ESR signal amplitude, due to the separate centers, should vary monotonically with temperature. Indeed, the centers affected by the internal magnetic field of the SP regions should primarily be those located between regions with large magnetic moments, followed by those with smaller moments, and so on. In the case of direct coupling between the SP regions [8], the phase transition should be diffuse; however, this is not observed experimentally. As can be seen from Fig. 5, as the temperature is decreased to 60 K, the Fe^{3+} ESR signal intensity grows and then drops sharply at $T > 60$ K. The wide variation in the ESR signal experimentally observed below 60 K can be assigned to the interaction between the iron atoms distributed randomly between the SP regions.

Considerations based on the theory of percolation in unordered systems [9, 10] permit the estimation of the temperature of the second ferromagnetic phase transition. Let us consider a system of randomly distributed 3*d* centers whose interaction is described by Hamiltonian (1) with an exchange interaction potential falling off exponentially at the distance *r*:

$$U(r) = U_0 \exp(-r/R), \tag{8}$$

where

$$U_0 = J_0 S(S+1),$$

and *R*, as in Eq. (1), determines the radius of the paramagnetic-ion potential. We now introduce the length $r(T)$ defined by the equality $U(r) = kT$, i.e.,

$$r(T) = R \ln \frac{U_0}{kT}. \tag{9}$$

Since the exchange energy depends exponentially on *r*, all the magnetic moments of individual centers with a separation of less than $r(T)$ may be considered as aligned at a given temperature. The moments spaced by $r > r(T)$ may be regarded as uncorrelated. A system is ferromagnetic if the coupled magnetic centers form an infinite cluster. Thus, determination of the Curie temperature is reduced to a geometric problem, namely, one of problems in percolation theory, the so-called continual problem. According to [11], the critical value of r_0 is given by

$$r_0 = 0.87 n^{-1/3} = 0.87 r_C,$$

where *n* is the magnetic-center concentration. The ferromagnetic-transition temperature is derived from the condition $r(T) = r_0$ which, on account of (9), yields

$$T_C = J_0 Z S(S+1) \exp\left(-\frac{0.87 r_C}{R}\right). \tag{10}$$

As is evident from expression (10), the temperature of the ferromagnetic transition corresponds, in its order of magnitude, to the interaction energy of centers spaced by the approximately average distance $r_C \propto n^{-1/3}$. It is noteworthy that this energy differs from the average interaction energy, which is proportional to the center concentration *n*.

Assuming that the average number of 3*d* centers whose interaction energy with a given center is of the order of kT_C is equal to the number of the nearest neighbors $Z = 3$, the spin of the magnetic center $S = 5/2$, the average center separation $r_C = n_{Fe}^{-1/3}$, and the exchange integral obtained in the ESR study of exchange-coupled pairs is $J_0 = 8.3$ cm^{-1} with the radius of the potential $R = 5$ Å, we find that the temperature of the second ferromagnetic transition is equal to $T_{C2} = 20$–60 K for the iron atom concentrations $n_{Fe} = 2 \times 10^{20}$–$6 \times 10^{20}$ cm^{-3}.

5. CONCLUSION

Heavily doped GaAs:Fe crystals may be considered as a two-phase system. One phase consists of superparamagnetic (SP) regions with the Curie temperature $T_{C1} = 460$ K, in which the iron atoms are arranged with a noticeable correlation. The second phase is formed of iron atoms distributed among the SP regions and represents a disordered magnetic system with the ferromagnetic transition temperature $T_{C2} = 60$ K. Thus, within the temperature interval $T_{C1} > T > T_{C2}$, the heavily doped gallium arsenide crystals are in an SP state. At $T = T_{C2}$, the system undergoes a transition induced by the interaction between Fe impurity atoms distributed randomly between the SP regions.

REFERENCES

1. N. P. Il'in, A. É. Vasil'ev, and V. F. Masterov, Fiz. Tekh. Poluprovodn. (St. Petersburg) **26**, 1878 (1992) [Sov. Phys. Semicond. **26**, 1052 (1992)].
2. B. P. Popov and D. Bois, Telecom, No. 78, 29 (1991).
3. V. V. Isaev-Ivanov, N. M. Kolchanova, V. F. Masterov, *et al.*, Fiz. Tekh. Poluprovodn. (Leningrad) **7**, 414 (1973) [Sov. Phys. Semicond. **7**, 299 (1973)].
4. V. P. Maslov, V. F. Masterov, D. N. Nasledov, and G. N. Talalakin, Fiz. Tverd. Tela (Leningrad) **17**, 2149 (1975) [Sov. Phys. Solid State **17**, 1418 (1975)].
5. V. F. Masterov and B. P. Popov, Fiz. Tekh. Poluprovodn. (Leningrad) **12**, 404 (1978) [Sov. Phys. Semicond. **12**, 234 (1978)].
6. A. Abragam and B. Bleaney, *Electron Paramagnetic Resonance of Transition Ions* (Clarendon, Oxford, 1970; Mir, Moscow, 1972).
7. R. M. White, *The Quantum Theory of Magnetism* (McGraw-Hill, New York, 1970; Mir, Moscow, 1972).
8. R. S. Iskhakov, G. I. Frolov, V. S. Zhigalov, and D. E. Prokof'ev, Pis'ma Zh. Tekh. Fiz. **30** (6), 51 (2004) [Tech. Phys. Lett. **30**, 687 (2004)].
9. I. Ya. Korenblit and E. F. Shender, Usp. Fiz. Nauk **126**, 233 (1978) [Sov. Phys. Usp. **21**, 832 (1978)].
10. B. P. Popov and V. P. Maslov, in *Proceedings of All-Union Conference on the Physics of III–V Compounds* (Leningrad, 1978), p. 37.
11. B. I. Shklovskiĭ and A. L. Éfros, *Electronic Properties of Doped Semiconductors* (Nauka, Moscow, 1979; Springer, New York, 1984).

Translated by G. Skrebtsov

Semiconductors, Vol. 39, No. 5, 2005, pp. 499–505. Translated from Fizika i Tekhnika Poluprovodnikov, Vol. 39, No. 5, 2005, pp. 528–534.

ELECTRONIC AND OPTICAL PROPERTIES OF SEMICONDUCTORS

The Electrical and Optical Properties of InP Irradiated with High Integrated Fluxes of Neutrons

V. N. Brudnyĭ*^, N. G. Kolin^^, D. I. Merkurisov**, and V. A. Novikov***

**Kuznetsov Physicotechnical Institute, Tomsk State University, ul. Revolyutsii 1, Tomsk, 634034 Russia*
^e-mail: brudnyi@ic.tsu.ru
***Karpov Research Physicochemical Institute (Obninsk Branch), Obninsk, Kaluga oblast, 249033 Russia*
^^e-mail: fci@meteo.ru

Submitted August 31, 2004; accepted for publication September 17, 2004

Abstract—The results of studying the electrical properties and optical-absorption spectra of InP irradiated with fast neutrons ($E > 0.1$ MeV and $D_{f.n} \le 10^{19}$ cm^{-2}) and full-spectrum reactor neutrons ($D_{th.n} \le 2.1 \times 10^{19}$ cm^{-2}; the ratio of the fluxes was $\varphi_{th.n}/\varphi_{f.n} \approx 1$) are reported. The variations in these properties resulting from postirradiation annealing at temperatures as high as 900°C are also studied. The results of the optical studies indicate that, in InP irradiated heavily with neutrons, free charge carriers appear only after annealing at temperatures higher than 500°C. The efficiency of neutron-initiated transmutational doping and the quality of transmutation-doped InP are assessed. © *2005 Pleiades Publishing, Inc.*

1. INTRODUCTION

The transmutation-induced doping of semiconductors accomplished by their irradiation with high-energy ions or reactor neutrons ensures a controlled introduction of the chemical impurity and makes it possible to obtain a material with a high degree of uniformity in its electrical and optical properties over the irradiated area [1]. Bombardment with protons or α particles is used for the doping of surface layers, whereas irradiation with reactor neutrons makes it possible, owing to the high penetrability of the neutrons, to accomplish the uniform doping of the material [2, 3]. The main disadvantage of neutron-transmutation doping is the formation of radiation defects in the lattice of a semiconductor. These defects introduce deep states of the donor and acceptor types into the band gap and define, to a great extent, the material's properties immediately after irradiation. This effect is especially pronounced at large the integrated bombarding-particle fluxes that are necessary for the attainment of heavily doped materials. Under these conditions, the removal of the radiation defects, by subjecting the irradiated material to high-temperature annealing or by irradiating this material at elevated temperatures, represents an essential component of transmutation-induced doping. In order to perform this procedure with confidence, it is necessary to have information about the behavior of the material under the conditions of high-temperature annealing; furthermore, experimental data on the thermal stability of the radiation defects are needed.

In this paper, we report the results of studying the electrical properties and optical-absorption spectra of InP irradiated with large integrated fluxes of fast neutrons and full-spectrum of reactor neutrons; in addition, we studied the variation in the above properties that resulted from a subsequent heat treatment of the irradiated material. A characteristic specific feature of InP is the high efficiency of nuclear-transmutation doping it provides under irradiation with neutrons. This feature a consequence of a large cross section ($\sigma \approx 190$ barn) for the absorption of thermal neutrons by In atoms. Stable Sn isotopes are introduced as a result of nuclear reactions initiated by the neutrons, and the electrical activity of these isotopes can be attained if the radiation defects are annealed out using a postirradiation heat treatment of the material [4, 5]. The choice of the optimal conditions under which the heat treatment is carried out is related not only to the determination of the thermal stability of radiation defects in InP but also to the processes of generation, in this compound, of quenched-in defects with deep levels. The latter defects compensate for the electrical activity of the material under consideration [6, 7]. In a number of studies devoted to these problems, the electrical properties of InP were mainly analyzed in the context of developing the technology of the nuclear-transmutation doping of this material by irradiating it with reactor neutrons [8–10]. In this paper, we pay the most attention to studying the optical characteristics of the material under consideration.

2. EXPERIMENTAL

Initial *n*-InP single crystals grown by the Czochralski method were irradiated with neutrons in a water-cooled and water-moderated reactor at the Karpov Research Physicochemical Institute (Obninsk Branch). The parameters of the studied materials and the irradiation conditions are given in Table 1.

Table 1. Electrical properties of the initial InP crystals at T_{test} = 295 K and the conditions under which these samples were irradiated

Sample	Doping impurity	Electron concentration n, 10^{17} cm^{-3}	The Hall electron mobility μ_H, cm^2/(V s)	Irradiation conditions
1	–	0.1–0.4	3800–5000	Fast neutrons
2	Te	1.0–2.0	2800–3200	Fast neutrons
3	Te	5.0–10.0	2200–2800	Fast neutrons
4	–	0.1–0.4	3800–5000	Reactor neutrons

The bombardment of InP with fast neutrons (f.n) was performed at temperatures of no higher than 70°C, and the samples were placed in Cd containers ($d \approx 1$ mm). The nuclear-transmutation doping of the InP wafers was carried out by irradiating these wafers with full-spectrum reactor neutrons at the flux density of thermal neutrons (th.n) $\varphi_{th.n} \approx 5 \times 10^{13}$ cm^{-2} s^{-1} and the ratio between the flux densities of the thermal and fast neutrons ($E > 0.1$ MeV) $\varphi_{th.n}/\varphi_{f.n} \approx 1$. The InP wafers' thickness was about 2 mm. In order to reduce the induced radioactivity, the irradiated samples were stored for 4–24 months before measurements were taken.

The heat treatment of the irradiated samples was carried out in vacuum at $T_{ann} < 600$°C and in sealed quartz cells under the equilibrium pressure of phosphorus vapors at $T_{ann} \geq 600$–900°C. In order to eliminate the influence of surface effects on the measured parameters, we removed layers with a thickness of ~50 μm from both sides of the wafers by grinding and subsequent chemical etching after the high-temperature annealing.

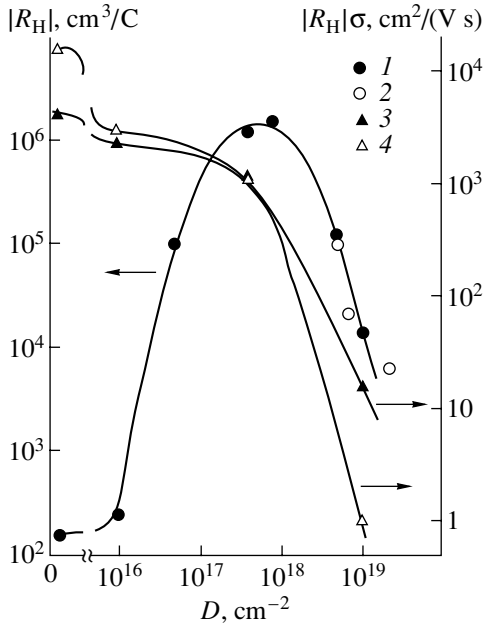

Fig. 1. Variations in the Hall coefficient $|R_H|$ (*1*, *2*) and the Hall mobility $|R_H|\sigma$ (*3*, *4*) in InP in relation to the radiation dose D (calculated for the fast neutrons) as a result of irradiation with (*1*, *3*, *4*) fast neutrons and (*2*) full-spectrum reactor neutrons. Curves *1*, *3*, and *4* correspond to sample 1, and curve *2* corresponds to sample 4 (see Table 1). The temperature of the measurements T_{test} = (*1*–*3*) 295 and (*4*) 200 K.

3. RESULTS AND ESTIMATES BASED ON THE MODEL

3.1. Electrical Properties

As a result of various types of high-energy irradiation, point or clustered radiation defects are introduced into the InP crystal lattice. These defects act as deep-level donors or acceptors, depending on the initial doping level and the conductivity type of the starting material [11–16]. The radiation-induced donors are more effective after irradiation if the initial doping level corresponds to $n_{st} < (2–3) \times 10^{12}$ cm^{-3}, while the radiation-induced acceptors are more effective if $n_{st} > (2–3) \times 10^{12}$ cm^{-3}. This circumstance makes it possible to use high-energy radiation to obtain a material with the highest resistivity of 10^7–10^9 Ω cm (at 295 K) in the case of initial *p*-InP and with a resistivity of about 10^3–10^4 Ω cm for the initial *n*-InP samples. A pronounced asymmetry of the removal rates for electrons ($\partial n/\partial D$ cm^{-1}) in *n*-InP and holes ($\partial p/\partial D$ cm^{-1}) in *p*-InP was observed in all the samples studied. For all the types of radiation used (electrons, protons, and neutrons), $\partial p/\partial D > \partial n/\partial D$. This behavior is accounted for by the fact that the Fermi level F in InP is pinned in the upper half of the band gap, close to the position $F_{lim} \approx E_V + 1.0$ eV, as a result of the introduction of radiation defects [17–19]. The electrical parameters of this material are independent of both its history and the irradiation conditions; i.e., these parameters are characteristics of the crystal itself rather than of the spectrum of the radiation defects introduced by irradiation with particles. It is noteworthy that, in the case of irradiation with reactor neutrons, both cluster-type and point defects can be formed. The former defects are produced as a result of the displacement of crystal-lattice atoms by fast neutrons or recoil atoms, whereas the latter defects are produced by the γ-ray component of the reactor radiation. In addition, when irradiated samples are cooled (stored for some time) in order to reduce the induced radioactivity, radiation defects can also be formed as a result of the irradiation of the material with β particles ("internal" irradiation) from the reactions $\text{In} \xrightarrow{\beta} \text{Sn}$.

In Fig. 1, we illustrate the variations in the Hall coefficient $|R_H|$ at 295 K (*1*, *2*) and the Hall electron mobility $\mu_H = |R_H|\sigma$ at 200 and 295 K (*3*, *4*) resulting from the irradiation of *n*-InP with fast neutrons (sample 1) and with the full-spectrum reactor neutrons (sample 4); in the latter case, the radiation dose also refers to the fast neutrons. The dose dependences $|R_H|(D)$ in the

region $D \lesssim (5–10) \times 10^{17}$ cm^{-2} indicate that the initial electrical conductivity of *n*-InP is compensated as a result of the irradiation with neutrons. Simultaneously, the InP resistivity ρ increases and attains a maximum $\rho_{max}(D) \approx (2–6) \times 10^3$ Ω cm at the integrated fast-neutron flux $D_{f.n} \approx (5–10) \times 10^{17}$ cm^{-2}. This maximum corresponds to *n*-InP in which the Fermi level is located in the upper half of the band gap (~0.35 eV below the conduction-band bottom), as it does in the samples irradiated with electrons or protons [18, 19]. Further irradiation of this material with neutrons (at $D > 10^{18}$ cm^{-2}) leads to a decrease in the Hall coefficient $|R_H|$ to 1.4×10^4 cm^3/C (to be compared with $|R_H|_{max}(D) \approx 2 \times 10^6$ cm^3/C) and in the resistivity to 7×10^2 Ω cm (295 K) at the integrated fast-neutron fluxes $D_{f.n} = 10^{19}$ cm^{-2}. It is noteworthy that the mobility $\mu_H = |R_H|/\rho$ measured at 295 K decreases by a factor of 4, whereas the value of $|R_H|$ varies by four orders of magnitude in the region where the initial conductivity is compensated as a result of the irradiation with neutrons. At the same time, in the region $D > 10^{18}$ cm^{-2}, where $|R_H|$ decreases by approximately three orders of magnitude, the value of $|R_H|/\rho$ at 295 K decreases by approximately two orders of magnitude. This behavior is related to the appearance of the impurity (hopping) conductivity of the electrons via the radiation-defect states whose levels are located in the vicinity of the Fermi level [8]. A sharp decrease in μ_H is observed in the region of low temperatures, especially in the samples irradiated with high neutron doses, in which case μ_H attains values characteristic of an unordered material (Fig. 1). At these neutron doses, the obtained values of μ_H are two orders of magnitude smaller than those in the samples irradiated with electrons at the integrated fluxes $D = 10^{19}$ cm^{-2} [18]. In general, the electrical properties of InP irradiated with fast neutrons vary similarly to those of InP irradiated with full-spectrum reactor neutrons; however, in the region of high doses, the resistivity of *n*-InP after irradiation with full-spectrum reactor neutrons (recalculated to the flux of fast neutrons) is somewhat lower than in the case of irradiation with fast neutrons. This circumstance can be related to the higher concentration of defects in InP irradiated with full-spectrum reactor neutrons due to the contribution of point defects formed as a result of the internal β-ray irradiation of InP during the storage of the irradiated samples and to the doping effect of the Sn impurity. Thus, the electrical properties of InP immediately after irradiation are almost completely controlled by the introduced radiation defects, both in the case of irradiation of InP with fast neutrons and for irradiation with full-spectrum reactor neutrons.

In order to remove the radiation defects and activate the Sn impurity, we subjected the InP samples irradiated with neutrons to isochronous annealing at temperatures as high as $T_{ann} \approx 900$°C. The variations in the electrical parameters of the samples irradiated with neutrons resulting from this postirradiation annealing

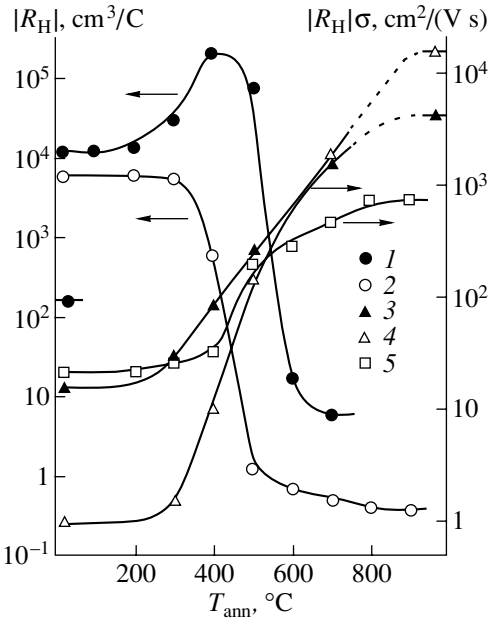

Fig. 2. Dependences of the (*1, 2*) Hall coefficient $|R_H|$ and (*3–5*) the Hall mobility $|R_H|\sigma$ in InP on the temperature T_{ann} of isochronous postirradiation annealing for $\Delta t = 20$ min after irradiation with (*1, 3, 4*) fast neutrons at $D_{f.n} = 10^{19}$ cm^{-2} (sample 1) and (*2, 5*) full-spectrum reactor neutrons at $D_{th.n} = 2.1 \times 10^{19}$ cm^{-2}. The temperature of the measurements was T_{test} = (*1–4*) 295 and (*5*) 200 K.

are illustrated in Fig. 2. An appreciable recovery of the electrical parameters of the heavily irradiated samples is observed at $T_{ann} > 250$°C and continues to $T_{ann} = 900$°C. Such annealing leads to the removal of the radiation defects, a decrease in the compensation factor in the material, and the appearance of free electrons as a result of the ionization of the Sn impurity atoms. We used the results of the electrical measurements to estimate the concentration of electrically active Sn introduced into InP as a result of nuclear reactions with thermal neutrons; this concentration was found to be equal to $N_{Sn} \approx 2.3 D_{th.n}$ [5]. If InP is irradiated with fast neutrons, Sn is also introduced; however, this introduction is caused by nuclear reactions with intermediate-energy neutrons at an efficiency of about 0.2 [5].

3.2. Model-Based Estimations of the Fermi Level Position in Irradiated InP

The variations in the electrical parameters of InP resulting from irradiation can be interpreted in the context of a model that implies the pinning of the Fermi level $F = F_{lim}$ in a semiconductor if the crystal lattice is saturated with intrinsic structural defects. Since the microscopic structure of radiation defects is still poorly known in the majority of semiconductors (except in Si), various heuristic models have gained wide recognition regarding calculation of the position F_{lim} in irradiated

Table 2. The limiting position of the Fermi level F_{lim} in irradiated InP (experiment) and the calculated values of E_{cnl}, E_{lnl}, E_{dl}, and $\langle E_G \rangle/2$ expressed in eV. The energies are measured from the valence-band top

F_{lim} [18, 19]	E_{cnl} [20]	E_{lnl} [21, 22]	E_{dl} [23, 24]	$\langle E_G \rangle/2$ [22]
1.0	0.72	0.89	1.03	0.90

semiconductors and estimation of the electrical characteristics of a material that correspond to this position of the Fermi level. In these models, the Fermi level position F_{lim} is identified with certain characteristic energies in a crystal. The following energies are used: the charge-neutrality level E_{cnl} [20, 21] or the local-neutrality level E_{lnl} [22] for the band-gap states of defects and the states of a material, and the level of the "deepest" (most localized) state of defects in a semiconductor E_{dl} in the energy interval close to the corresponding narrowest band gap [23, 24]. In addition, the Fermi level position F_{lim} can be identified with the energy $\langle E_G \rangle/2$, where $\langle E_G \rangle = 5.25$ eV (for InP) is the mean energy interval between the lower conduction band and the upper valence band within the first Brillouin zone; the value of this interval is close to that of the dielectric gap in InP (~5 eV) [22]. The results of the corresponding calculations of the quantities E_{cnl}, E_{lnl}, E_{dl}, and $\langle E_G \rangle/2$ are close to each other and are in satisfactory agreement with the experimental values of F_{lim} in InP (Table 2). These studies confirm both the fundamental character of the phenomenon that consists in the pinning of the Fermi level in semiconductors with defects and the fact that the value $F_{lim} \approx E_V + 1.0$ eV is a characteristic (canonical) parameter of InP and manifests itself in a situation where the crystal lattice is saturated with intrinsic structural defects. This circumstance makes it possible to estimate the interval of the variations in the concentrations of free electrons $n_{st} - n_{lim}$ and holes $p_{st} - p_{lim} = n_i^2/n_{lim}$ in InP for any kind of irradiation with high-energy particles (here, $n_{lim} \approx (2\text{–}3) \times 10^{12}$ cm^{-3} at 295 K) and, thus, predict the interval of the variations in electrical properties resulting from exposure to high-energy radiation.

3.3. The Spectra of Optical Absorption

Only a small fraction of the available publications concerned with the study of radiation defects in InP have been devoted to the optical properties of irradiated InP. Until now, the corresponding experimental data

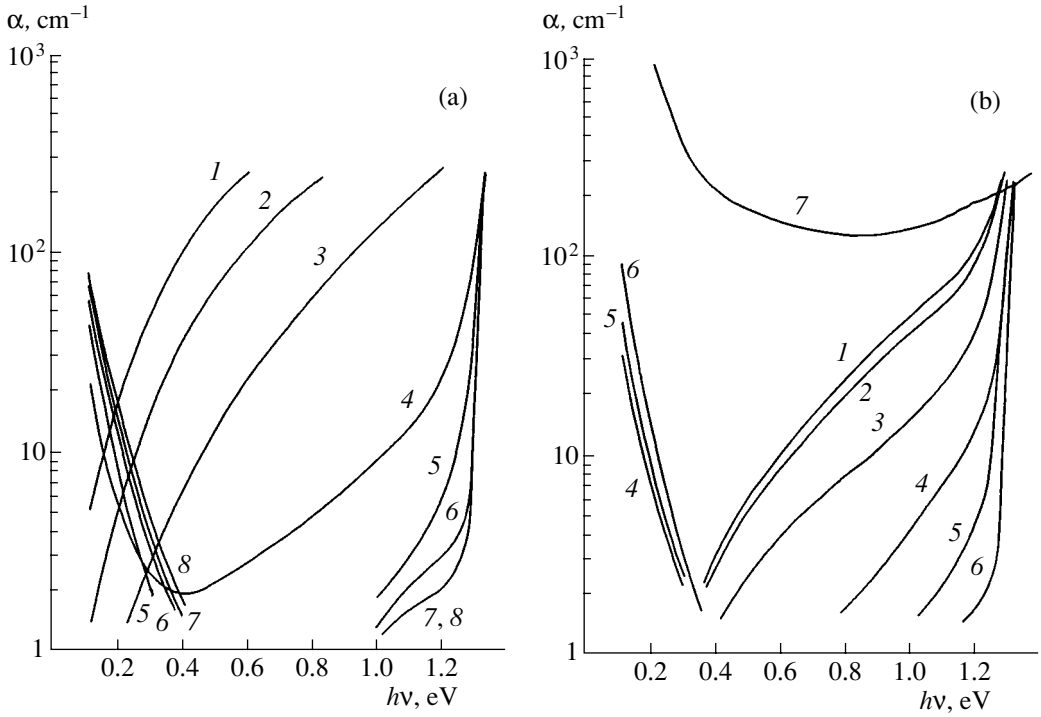

Fig. 3. Variations in the spectral dependences of the absorption coefficient in the *n*-InP samples irradiated with (a) fast neutrons and (b) full-spectrum reactor neutrons followed by isochronous annealing for $\Delta t = 20$ min. $T_{test} = 295$ K. (a) For sample 2, $D_{f.n} = 10^{19}$ cm^{-2} and T_{ann} = (*1*) 20, 100, 200°C; (*2*) 300°C; (*3*) 400°C; (*4*) 500°C; (*5*) 600°C; (*6*) 700°C; (*7*) 800°C; and (*8*) 900°C. (b) For sample 4, $D_{th.n}$ = (*1–6*) 4.8×10^{17} and (*7*) 2.1×10^{19} cm^{-2}. Here, curves *1–5* were obtained after annealing at the same temperatures as in the case of curves *1–5* in (a). T_{ann} = (*6*) 700 and 800°C, and (*7*) 900°C.

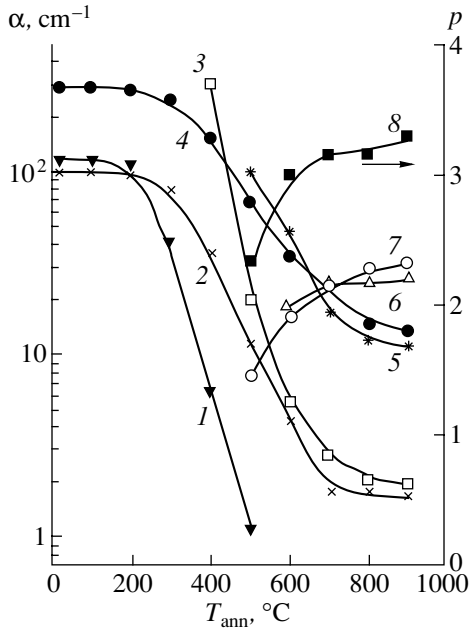

Fig. 4. (*1–7*) The absorption coefficient for various wavelengths and (*8*) the exponent p in the expression $a \propto 1/(h\nu)^p$ for the samples irradiated with (*1*, *3*, *5*, *7*, and *8*) fast neutrons at $D_{f.n} = 10^{19}$ cm^{-2} (sample 2) and (*2*, *4*, and *6*) full-spectrum reactor neutrons at $D_{th.n} = 4.8 \times 10^{17}$ cm^{-2} (sample 4) in relation to the isochronous-annealing temperature T_{ann} (Δt = 20 min). T_{test} = 295 K. $h\nu$ = (*1*) 0.4, (*2*, *3*) 1.18, (*4*, *5*) 1.3, and (*6*, *7*) 0.16 eV.

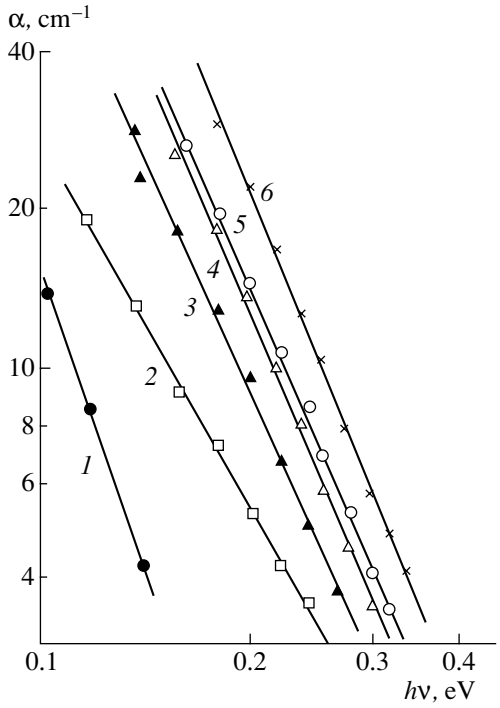

Fig. 5. Variations in the spectral dependences of the absorption coefficient α in sample 2 irradiated with fast neutrons and then annealed isochronously (Δt = 20 min) at T_{ann} = (*1*) 20, (*2*) 500, (*3*) 600, (*4*) 700, (*5*) 800, and (*6*) 900°C. The neutron dose was $D_{f.n}$ = (*1*) 0 and (*2–6*) 10^{19} cm^{-2}. The measurements were carried out at T_{test} = 295 K.

have mainly been obtained for samples irradiated with electrons. There are also a small number of publications concerned with studying the optical-absorption spectra of InP irradiated with protons or fast neutrons [8, 25, 26]. The optical-absorption spectra of InP irradiated with high integrated fluxes of reactor neutrons and then annealed have not been studied. In this study, we measured the optical-absorption spectra of InP irradiated with fast neutrons and full-spectrum reactor neutrons and subjected to subsequent annealing at temperatures as high as 900°C.

In the low-energy region ($h\nu < E_g$) of the optical-absorption spectrum of irradiated InP, we observe the additional optical absorption $\int_{h\nu}^{E_g} \alpha(h\nu) d(h\nu)$, whose value is proportional to the integrated neutron flux (Figs. 3a, 3b). In contrast to the results attained by irradiation with electrons, the spectral dependences $\alpha(h\nu)$ do not exhibit any special features caused by photoionization of the defects' deep levels; rather, these dependences are characteristic of unordered semiconductors with a high density of localized states in the band gap. Presumably, this circumstance is caused by the fact that irradiation with neutrons can lead to the formation of a "disordered alloy" in a binary semiconductor due to both the production of vacancy-type defects and stratification of the material (formation of antisite defects). For example, data on the electron spin resonance for irradiated InP substantiate the high efficiency exhibited in the formation of both the phosphorus vacancies V_P and P_{In}-type antisite defects [27, 28].

After an annealing of irradiated InP at $T_{ann} > 300$°C, we observe a decrease in the integrated additional absorption in the near-edge region of the spectrum; in addition, an increase of the optical absorption in the extrinsic region of the spectrum for the photon energies $h\nu < 0.4$ eV after annealing at temperatures higher than 500°C is observed (Figs. 3a, 3b). Such annealing-induced variations in the value of $\int_{h\nu}^{\varepsilon_g} \alpha(h\nu) d(h\nu)$ are related to a decrease in the concentration of deep-level radiation defects, which, in turn, leads to a decrease in the compensation factor of the irradiated material and to an increase in α in the region of $h\nu < 0.4$ eV. The latter tendency is a consequence of the appearance of free electrons in the conduction band due to the ionization of the Sn impurity. In Fig. 4, we illustrate, for various wavelengths, the variation in the absorption coefficient α resulting from the heat treatment of the samples irradiated with fast and reactor neutrons. Curves *1–5* illustrate the efficiency of the radiation-defect annealing, while curves *6* and *7* illustrate the efficiency of the appearance of free electrons in the material. It is worth

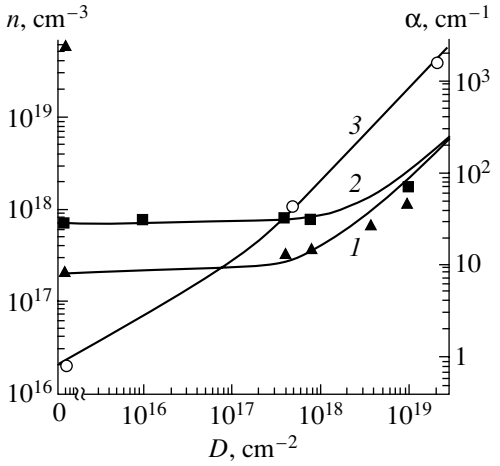

Fig. 6. The neutron-dose dependences of the absorption coefficient α (at $h\nu = 0.14$ eV) and free-electron concentration n in the samples irradiated with (*1*, *2*) fast neutrons and (*3*) reactor neutrons and then annealed at 900°C. The triangles and squares correspond to samples 2 and 3, respectively; the circles correspond to sample 4. The solid lines represent the calculated dependences for $n_D - n_0 = 0.2D$ (curves *1*, *2*) and $n_D - n_0 = 2.3D$ (curve *3*). The measurements were carried out at $T_{test} = 295$ K.

noting that the annealing temperature $T_{ann} \approx 500$°C is critical for InP, since it is in the vicinity of this temperature that the recovery of most of the parameters of defect-containing InP, including the recovery of the long-range order in *a*-InP, is observed [29].

A study of the spectral dependence $\alpha \propto 1/(h\nu)^p$ (Fig. 5) in the region of free-electron absorption in the irradiated samples shows that the exponent p increases from ~2.3 in the material immediately after irradiation to 3.0–3.4 if the temperature of the postirradiation annealing is increased to 700–900°C (Fig. 4, curve *8*). This value of p is characteristic of InP in the case of free-electron scattering by ionized hydrogen-like impurities. Using the known values of the cross section for optical absorption by free electrons $S_n = \Delta\alpha/\Delta n \approx 4.7 \times 10^{-17}$ cm^2 at $h\nu \approx 0.14$ eV in InP doped with hydrogen-like impurities [30], we can estimate the free-electron concentration n_D and the efficiency K of the transmutational doping of this material from the expression

$$K \approx \Delta\alpha/S_n D,$$

where

$$\Delta\alpha = (\alpha_0 - \alpha_D), \quad \Delta n = (n_D - n_0).$$

Here, α_0 (α_D) and n_0 (n_D) are the absorption coefficients and free-electron concentrations before (after) the irradiation and annealing, respectively.

In Fig. 6, we show the values of $\alpha(h\nu = 0.14$ eV) in the InP samples irradiated with fast neutrons and with full-spectrum reactor neutrons after these samples were annealed at 900°C. The corresponding values of the free-electron concentration were calculated taking into account the efficiency K of the InP transmutational doping: $K = 0.2$ in the case of irradiation with fast neutrons and $K = 2.3$ in the case of irradiation with reactor neutrons [5]. These estimates are close to the corresponding data obtained in the optical measurements performed in this study. Thus, the results of the optical measurements are, in general, consistent with the electrical data on the high efficiency of transmutational doping of InP as a result of irradiation with neutrons.

4. CONCLUSION

The irradiation of *n*-InP with fast neutrons or full-spectrum reactor neutrons at integrated fluxes of as high as ~10^{18} cm^{-2} (with respect to the fast neutrons) leads to the formation of a high-resistivity material with *n*-type conductivity and $\rho \approx (2–6) \times 10^3$ Ω cm at 295 K and to the pinning of the Fermi level in the vicinity of $E_V + 1.0$ eV. At higher doses of neutrons, extrinsic conductivity comes into effect, manifesting itself in a decrease of both the resistivity of the irradiated material and the conductivity activation energy as the integrated flux of particles increases. It is important that appreciable featureless absorption, characteristic of unordered semiconductors, is observed in the spectral region of ~E_g – 0.1 eV for InP crystals irradiated with neutrons. Annealing at temperatures higher than 300°C leads to a decrease in this absorption and, at annealing temperatures higher than 500°C, to an increase in the optical-absorption coefficient in the extrinsic region of the spectrum (for $h\nu < 0.4$ eV) as a result of the activation of the Sn impurity introduced into the InP crystal lattice. We estimated the efficiency of transmutational doping and assessed the quality of the obtained material.

ACKNOWLEDGMENTS

This study was supported by the International Science & Technology Center (project no. 1630, Highly Stable Radiation-Resistant Semiconductors) and the federal scientific and technological programs “New Materials” and “Neutron-assisted Studies of Materials” of the Ministry of Industry and Science of the Russian Federation.

REFERENCES

1. L. S. Smirnov, S. P. Solov’ev, V. F. Stas’, and V. A. Kharchenko, *The Doping of Semiconductors Using the Method of Nuclear Reactions*, Ed. by L. S. Smirnov (Nauka, Novosibirsk, 1982) [in Russian].
2. L. F. Zakharenkov, V. V. Kozlovskii, and B. A. Shustrov, Phys. Status Solidi A **117**, 85 (1990).
3. N. G. Kolin, Izv. Vyssh. Uchebn. Zaved., Fiz. **46** (6), 12 (2003).
4. B. Lee, N. Pan, G. E. Stillman, and K. L. Hiess, J. Appl. Phys. **62**, 1129 (1987).
5. N. G. Kolin, D. I. Merkurisov, and S. P. Solov’ev, Fiz. Tekh. Poluprovodn. (St. Petersburg) **34**, 157 (2000) [Semiconductors **34**, 150 (2000)].

6. H. Y. Bardeleben, J. C. Bourgoin, K. Kainosho, and O. Oda, Appl. Phys. Lett. **57**, 2464 (1990).
7. D. Hoffman, G. Muller, and N. Streckfuss, Appl. Phys. A **48**, 315 (1988).
8. V. N. Brudnyi, V. A. Charchenko, N. G. Kolin, *et al.*, Phys. Status Solidi A **93**, 195 (1986).
9. V. N. Brudnyi, N. G. Kolin, and V. A. Novikov, Phys. Status Solidi A **132**, 35 (1992).
10. N. G. Kolin, D. I. Merkurisov, and S. P. Solov'ev, Fiz. Tekh. Poluprovodn. (St. Petersburg) **34**, 153 (2000) [Semiconductors **34**, 146 (2000)].
11. M. Kitagawa, T. Endo, J. Dei, *et al.*, Annu. Rep. Radiat. Center Osaka Prefecture **26**, 75 (1985).
12. B. E. Samorukov and S. V. Slobodchikov, Fiz. Tekh. Poluprovodn. (Leningrad) **23**, 921 (1989) [Sov. Phys. Semicond. **23**, 581 (1989)].
13. J. D. Woodhouse, J. P. Donnely, and G. W. Iseler, Solid-State Electron. **31**, 13 (1988).
14. V. V. Kozlovskiĭ, T. I. Kol'chenko, and V. M. Lomako, Fiz. Tekh. Poluprovodn. (Leningrad) **24**, 1123 (1990) [Sov. Phys. Semicond. **24**, 710 (1990)].
15. A. Sibille, J. Suski, and M. Gileron, J. Appl. Phys. **60**, 595 (1986).
16. K. Tadamasa, K. Makato, Ji-Kui Luo, *et al.*, Nucl. Instrum. Methods Phys. Res. **37–38**, 321 (1989).
17. P. E. Tompson, S. C. Binary, and H. B. Dietrich, Solid-State Electron. **26**, 805 (1983).
18. V. N. Brudnyĭ and V. A. Novikov, Fiz. Tekh. Poluprovodn. (Leningrad) **16**, 1880 (1982) [Sov. Phys. Semicond. **16**, 1211 (1982)].
19. V. N. Brudnyĭ, P. N. Drobot, and V. A. Novikov, Available from VINITI, No. 6584-B87.
20. J. Tersoff, Phys. Rev. Lett. **52**, 465 (1984).
21. V. N. Brudnyĭ and S. N. Grinyaev, Fiz. Tekh. Poluprovodn. (St. Petersburg) **32**, 315 (1998) [Semiconductors **32**, 284 (1998)].
22. V. N. Brudnyĭ, S. N. Grinyaev, and V. E. Stepanov, Physica B (Amsterdam) **212**, 429 (1995).
23. V. N. Brudnyĭ, S. N. Grinyaev, and N. G. Kolin, Materialovedenie **72** (3), 17 (2003).
24. V. N. Brudnyĭ, S. N. Grinyaev, and N. G. Kolin, Physica B (Amsterdam) **348**, 213 (1995).
25. E. Yu. Brailovski, G. N. Eritsyan, and N. E. Grigoryan, Phys. Status Solidi A **78**, K113 (1983).
26. F. F. Leonberger, J. N. Walpole, and J. P. Donnelly, IEEE J. Quantum Electron. **17**, 830 (1981).
27. H. J. Bardeleben, Solid State Commun. **57**, 137 (1986).
28. A. Goltzene, B. Meyer, and C. Schwab, J. Appl. Phys. **62**, 4406 (1987).
29. E. Wender, T. Opferman, and P. I. Gaiduk, J. Appl. Phys. **82**, 5965 (1997).
30. *Semiconductors and Semimetals*, Ed. by R. K. Willardson and A. C. Beer (Academic, New York, 1967; Mir, Moscow, 1970).

Translated by A. Spitsyn

Semiconductors, Vol. 39, No. 5, 2005, pp. 506–513. Translated from Fizika i Tekhnika Poluprovodnikov, Vol. 39, No. 5, 2005, pp. 535–542.

ELECTRONIC AND OPTICAL PROPERTIES OF SEMICONDUCTORS

The Conductivity and Hall Effect in CdF_2:In and CdF_2:Y

I. I. Saĭdashev*, E. Yu. Perlin, A. I. Ryskin**, and A. S. Shcheulin****

**Ioffe Physicotechnical Institute, Russian Academy of Sciences, Politekhnicheskaya ul. 26, St. Petersburg, 194021 Russia*

***Vavilov State Optical Institute, Birzhevaya liniya 12, St. Petersburg, 199034 Russia*

Submitted June 7, 2004; accepted for publication September 30, 2004

Abstract—Temperature dependences of the static conductivity σ and Hall coefficient R_H in CdF_2 crystals doped with bistable indium and donor yttrium impurities have been measured. It is shown that this material contains different types of free carriers, i.e., electrons and polarons. A comparison of the calculated temperature dependences of σ and R_H with the experimental data also shows that the impurity-band conductivity makes a significant contribution (due to hops of bound polarons or holes) to σ and R_H. © *2005 Pleiades Publishing, Inc.*

1. INTRODUCTION

Cadmium fluoride is a wide-gap (~7.8 eV) insulator. However, CdF_2 crystals doped with donor impurities and annealed in a reduction hydrogen or cadmium vapor atmosphere transform into a semiconductor state [1]. During this procedure, referred to as additive coloration, interstitial fluorine ions F^-, which compensate for the excess (+1) charge of the impurity core in this ionic crystal, diffuse to the surface and recombine with a reduction agent. In this case, charge neutrality is maintained by the electron counterflow carried by this agent. As these electrons are localized at the donor impurities or in the conduction band, they transform the CdF_2 crystal into an *n*-type semiconductor. Cadmium fluoride is a unique crystal with high ionicity; moreover, it features a fundamental property of extrinsic semiconductors: the existence of hydrogen-like levels whose parameters only marginally depend on the chemical properties of a certain impurity. Its uniqueness in this respect is caused by its high electron affinity (~4 eV), which results in the *s* states of donor impurities being rather close to the conduction band (cadmium *s* band) and collectivized with it, forming hydrogen-like states.

Two donor impurities, Ga and In, form *DX* centers in CdF_2, which, in addition to a hydrogen-like donor state that operates as a metastable ("shallow") state for the impurities, have a highly relaxed ground state with a negative correlation energy ("deep" state). At the center in this state, a pair of electrons with oppositely directed spins is localized [2–4].

The CdF_2 ionic semiconductor features an extended energy scale (the band gap and binding energies of its local levels, etc.) in comparison with typical covalent and ionic-covalent semiconductors. Furthermore, the electrical and optical properties of this material are substantially controlled by the coupling of free and bound electrons with polarization phonons. In particular, a significant manifestation of polaron effects can be expected in the Hall conductivity of CdF_2 crystals containing both donor (Y) and bistable (In) impurities. In this paper, we report the results of studying these effects. The electrical properties of CdF_2:Y were previously studied in [5]. The interpretation of the experimental data suggested in this paper significantly complements the concepts developed in [5].

2. EXPERIMENTAL

The CdF_2 crystals under study were grown using a modified Stockbarger–Bridgman method in graphite crucibles. Dopants (In and Y) were introduced into the initial material at concentrations of 0.05 and 0.02 mol %, respectively, and grown in the form of fluorides. These values correspond to the average donor concentrations of 1.25×10^{19} (In) and 5.0×10^{18} cm^{-3} (Y).

The grown crystals were subjected to additive coloration in cadmium vapor. As was shown in [6], this procedure, as a rule, does not result in the total substitution of interstitial F^- ions with electrons. Therefore, the number of electrons introduced into the crystal during the coloration procedure is smaller than the number of donor impurities. Thus, F^- ions play the role of acceptors in this unipolar semiconductor, and the electronic properties of CdF_2 are described by the following two parameters: the concentration of donors and the degree of their compensation. The electron concentrations in the crystals under study were determined from the intensity of the photoionization band of the shallow centers and were found to be 5.0×10^{18} and 2.0×10^{18} cm^{-3} for In and Y, respectively [7, 8]. These values correspond to a compensation factor for both impurities that is approximately equal to 60%. This value should be considered as an upper estimate, since impurity ions locally compensated by fluorine [9, 10] and impurity–fluorine clusters with more complex compositions [11] reduce the effective concentration of statistically distributed ("isolated") impurities, which control the electrical properties of crystals. An analysis of the Hall data in the CdF_2:Y sample under study shows that its degree of compensation is lower than 50% (see below). Here-

after, we assume that the degrees of compensation are 40% and 50% for Y and In, respectively. These values are the conduction-model parameters used to approximate the experimental data. Accurate values for these parameters, taking into account the above comment, have almost no effect on qualitative conclusions about the conduction mechanisms in CdF_2.

The Hall and specific resistances of the cadmium fluoride samples were measured using the dc Van der Pauw method. The samples were shaped as square plates $8.0 \times 8.0 \times 1.1$ mm in size and had deposited ohmic indium contacts. The sample temperature was set and maintained in the range 95–350 K using an electronic stabilizer in a flow-type cryostat placed between the poles of an electromagnet with the induction $B = 0.9$ T. The low carrier mobility in the material under study results in a weak Hall signal, which is observed against a background of rather strong spurious signals. The latter are due to an imperfect sample configuration and contact arrangement, as well as the crystal's inhomogeneity. In order to eliminate the above-listed and other spurious signals, and to obtain reliable Hall resistances, the Hall voltage was measured on both diagonals of the samples. The direction of the current through the samples and that of the magnetic field were commutated at each temperature. Thus, the Hall resistance was determined by averaging over 12 measurements. The measurement results are presented in Section 4.

3. ENERGY STATES AND STATISTICS OF THE ELECTRONS IN THE SEMICONDUCTOR CdF_2

The energy spectrum of free and bound states in ionic materials, to which CdF_2 belongs, is significantly modified owing to the coupling of electrons with longitudinal optical phonons and the formation of polarons. The polaron binding energy is given by (see [12, 13])

$$E_{\text{pol-}s} = -\frac{\alpha^2\hbar\omega_0}{3\pi} - 3\hbar\omega_0(\ln 2 + 1/4)\coth\beta/2 + 3\hbar\omega_0(\ln 2 - 1/4)\frac{\beta/2}{\sinh^2\beta/2}, \quad (1)$$

where

$$\beta = \lambda\hbar\omega_0, \quad \lambda = \frac{1}{k_B T}, \quad \alpha = \frac{e^2 c_p}{2\hbar}\sqrt{\frac{2m_c}{\hbar\omega_0}}, \quad c_p = \frac{1}{n^2} - \frac{1}{\varepsilon_0}, \quad (2)$$

ω_0 is the cutoff frequency of the longitudinal optical phonons, ε_0 is the static permittivity, n is the refractive index in the material transparency range, and m_c is the electron effective mass in the conduction band. Formula (1), which is valid for the tight-binding approximation, yields polaron binding energies for CdF_2 that are approximately 20% larger in magnitude than the formula

$$E_{\text{pol-}w} = -\alpha\hbar\omega_0\left(1 - \frac{9}{32\beta^2}\right) - \frac{\alpha^2\hbar\omega_0}{81}\left(1 - \frac{2.034}{\beta^2}\right), \quad (3)$$

which is used in the case of weak binding and moderate temperatures.

The polaron effective mass in the case of tight binding is given by the relation

$$m_{\text{pol}} = \frac{16}{81\pi^2}\alpha^4 m_c. \quad (4)$$

For weak binding, the relation

$$m_{\text{pol}} = \left(1 + \frac{1}{6}\alpha + \frac{1}{40}\alpha^2\right)m_c, \quad (5)$$

which yields polaron effective masses 20–30% smaller than those given by formula (4), is valid.

The ground state energy for a shallow hydrogen-like impurity, taking into account the coupling of electrons with longitudinal optical phonons (the bound polaron problem), was derived in [14] using the variational method within the Lagrangian formalism of quantum mechanics in the following form:

$$E_1 = -\hbar\omega_0\frac{\alpha^2}{3\pi}\left[\left(1 + \frac{2\sqrt{2}}{\varepsilon_0 c_p}\right)^2 + 3\ln 2\left(1 + \frac{2\sqrt{2}}{\varepsilon_0 c_p}\right)^{-1}\frac{\sinh\beta - \beta}{2\sinh^2\beta/2}\right]. \quad (6)$$

As was shown in [15], in the limit of low temperatures, the problem is reduced to a minimization of the expression

$$E_1(\nu) = -\hbar\omega_0\left[\frac{2\sqrt{2}\alpha}{\sqrt{\pi}\varepsilon_0 c}\nu^{1/2} + \alpha\nu^{-1/2}\frac{\Gamma(1/\nu)}{\Gamma(1/2 + 1/\nu)} + \frac{3\nu}{4}\right] \quad (7)$$

with respect to the parameter ν. As a result (see [15]), ν is obtained as a root of the equation

$$\frac{3}{4\alpha}\left(\nu^{1/2} - \frac{4\sqrt{2}}{\sqrt{\pi}}\frac{\alpha}{\varepsilon_0 c}\right) = \frac{\Gamma(1/\nu)}{\Gamma(1/2 + 1/\nu)} \times\left\{\frac{1}{\nu}[\psi(1/2 + 1/\nu) - \psi(1/\nu)] - \frac{1}{2}\right\}, \quad (8)$$

where $\psi(z)$ is the logarithmic derivative of the Γ function.

The ionization energy E_2 of the shallow doubly charged centers (bound bipolarons) in ionic semiconductors was calculated in [16]. In [16], the following expres-

sion was derived for the case of weak polaron binding and weak local binding in the low-temperature limit:

$$E_{2w} = -2\hbar\omega_0\left[\alpha + 2\frac{(2\sqrt{2}-1)^2}{2\pi}\left(\frac{\alpha}{\varepsilon_0 c}\right)^2\left(1-\frac{\alpha}{6}\right)^{-1}\right]. \quad (9)$$

In [16], the following expression was derived for the case of a tight binding of localized electrons to the lattice defects and strong electron–phonon coupling:

$$E_{2s} = -\hbar\omega_0\left[\frac{2\alpha^2}{3\pi}\left(\frac{c'}{c_p}+\frac{2\sqrt{2}}{\varepsilon_0 c_p}\right)^2\alpha + \frac{6\ln 2}{\frac{c'}{c_p}+\frac{2\sqrt{2}}{\varepsilon_0 c_p}}\frac{\sinh\beta-\beta/2}{\cosh\beta-1}\right], \quad (10)$$

where

$$c' = \frac{1}{n^2}-\frac{2}{\varepsilon_0}. \quad (11)$$

In the CdF_2 crystal, the binding is intermediate. For low temperatures, formulas (9) and (10) both yield almost identical ionization energies (~0.47 eV). However, it should be kept in mind that the energy calculated using formula (10) noticeably decreases in magnitude with temperature (by approximately 9% in the range 150–300 K).

In addition to "ordinary" polarons, bipolarons can also exist in ionic semiconductors under certain conditions. In [17], the condition for bipolaron stability was obtained for the first time, $\eta_v \gtrsim 0.95$, where $\eta_v = n^2 c_p$. For CdF_2, $\eta_v \approx 0.69$; hence, this condition is not satisfied. However, as has been shown in further studies, the bipolaron stability is specified by a softer condition, which can be reduced to the inequality $\alpha > \alpha_{cr}$. The values of α_{cr} at various values of the parameter $\eta = \varepsilon_\infty/\varepsilon_0$ are given in review [18]. For CdF_2 at $T = 100$ K, we have $\eta = 0.306$, $\alpha_{cr}(\eta) \approx 2.85$, and $\alpha \approx 3.205$. For CdF_2 at $T = 350$ K, we have $\eta = 0.283$, $\alpha_{cr}(\eta) \approx 2.6$, and $\alpha \approx 3.13$. We can see that, in the entire temperature range for the measurements, the condition $\alpha > \alpha_{cr}$ is met. At high temperatures, it is satisfied with a larger safety margin than at low temperatures.

The Fermi level μ of the system is determined from the condition for crystal electrical neutrality, which is written as

$$n_c + n_{pol} + 2n_{bip} = N_{sh}^+ - N_d^- - N_F, \quad (12)$$

where n_c, n_{pol}, and n_{bip} are the concentrations of free electrons, polarons, and bipolarons, respectively; N_{sh}^+ is the concentration of ionized (shallow) impurities; N_d^- is the concentration of deep centers with amphoteric and donor–acceptor properties (during thermoionization, they supply electrons to the conduction band; at the same time, they decrease the population of shallow donor centers, playing, in a sense, the role of acceptors), and N_F is the concentration of compensating acceptors (F^- ions). The parameters appearing in Eq. (12) are given by

$$N_{sh}^+ = N_m f^{(0)}(\mu),$$
$$N_d^- = N_m f^{(0)}(\mu)\exp[\lambda(2\mu - E_1 - E_2)], \quad (13)$$
$$N_F = \gamma N_m,$$

where N_m is the total number of impurity atoms, γ is the compensation factor, and

$$f^{(0)}(\mu) = \{1 + 2\exp[\lambda(\mu - E_1)] + \exp[\lambda(2\mu - E_1 - E_2)]\}^{-1}. \quad (14)$$

Following [19, 20], let us introduce the electron localization volume V_0 and the highest phonon group velocity u, as well as the momenta p_0 and p_1 given by

$$p_0 = \hbar(6\pi^2/V_0)^{1/3}, \quad p_1 = m_c u \quad (15)$$

with $p_0 \gg p_1$. According to the concepts developed in [19–23], the average carrier momentum in a polaron cannot exceed p_1, and the highest total concentration of polarons and "cold" electrons with momenta $p \le p_0$ cannot exceed $2/V_0$. Free electrons with momenta smaller than p_1 cannot exist either. Let us introduce

$$A = \frac{V_0}{2\pi^2\hbar^3}\left\{\int_0^{p_1} p^2\exp[-\lambda(E_{pol} + p^2/2m_{pol})]dp + \int_{p_1}^{p_0} p^2\exp(-\lambda p^2/2m_c)dp\right\}. \quad (16)$$

Then, writing the free electron concentrations as

$$n_c + n_{pol} = n_{cold} + n_{hot} = n_{pol} + n_{c\text{-cold}} + n_{c\text{-hot}}, \quad (17)$$

the total number of "cold" carriers (polarons and free electrons with momenta $p < p_0$) is written as (see [19, 20])

$$n_{cold} = \frac{A\exp(\lambda\mu)}{V_0\left[1+\frac{1}{2}A\exp(\lambda\mu)\right]}, \quad (18)$$

$$n_{hot} = \frac{1}{\pi^2\hbar^3}\int_{p_0}^{\infty}\frac{p^2}{\exp\left[\lambda\left(\frac{p^2}{2m_c}-\mu\right)+1\right]}dp. \quad (19)$$

The polaron concentration is given by

$$n_{pol} = n_{cold}\frac{V_0}{2\pi^2\hbar^2 A} \times \int_0^{p_1} \exp[-\lambda(E_{pol} + p^2/2m_{pol})]p^2 dp. \quad (20)$$

The concentration of "cold" free electrons with momenta $p_1 < p < p_0$ is given by

$$n_{c\text{-cold}} = n_{cold}\frac{V_0}{2\pi^2\hbar^3 A}\int_{p_1}^{p_0} \exp(-\lambda p^2/2m_c)p^2 dp. \quad (21)$$

The concentration of bipolarons is given by (see [19])

$$n_{bip} = \frac{1}{2\pi^2\hbar^3 A} \times \int_0^{m_{bip}u} \frac{p^2 dp}{\exp[\lambda(E_{bip} - p^2 m_{bip}/8m_c^2 - 2\mu)] - 1}, \quad (22)$$

where m_{bip} is the bipolaron effective mass and E_{bip} is the position of the bipolaron band bottom

$$E_{bip} = 2E_{pol} + \delta E_{bip}. \quad (23)$$

We consider the bipolaron binding energy δE_{bip} as a negative value with $|\delta E_{bip}| \ll |E_{pol}|$. The polaron binding energy in expressions (16), (20), and (23) is given by formulas (1) or (3).

When calculating the energy level positions and state populations in the systems under study, we used the following material parameters: $V_0 = 2 \times 10^{-18}$ cm^{-3}, $m_c = 0.45m_0$, $u = 10^6$ cm s^{-1}, $\varepsilon_\infty \simeq 2.4$, and $\hbar\omega_0 \simeq$ 0.05 eV. The calculated results are listed in the table and shown in Fig. 1. Figure 2 shows the state populations in CdF_2:In with the indium concentration $N_m = 1.25 \times 10^{19}$ cm^{-3}, which was calculated using formulas (12)–(21). The calculation of the populations in CdF_2:Y crystals with $N_m = 5 \times 10^{18}$ cm^{-3} differs from that for CdF_2:In in that there are no *DX*-center states in the crystal with yttrium; hence, we should set $N_d^- = 0$ in Eq. (12) and the term $\exp[\lambda(2\mu - E_1 - E_2)]$ does not appear on the right-hand side of Eq. (14).

Temperature dependences of the static permittivity ε_0, electron–phonon coupling constant α, and polaron effective mass m_{pol}

T, K	ε_0	α	m_{pol}/m_0
100	7.84	3.205	0.950
150	7.97	3.228	0.978
200	8.10	3.250	1.005
250	8.23	3.272	1.032
300	8.36	3.293	1.059
350	8.49	3.313	1.085

The state populations in CdF_2:Y with the yttrium concentration $N_m = 5 \times 10^{18}$ cm^{-3} are shown in Fig. 3. As expected, in the case of CdF_2:In, the Fermi level is almost in the middle of the binding energies of the bound polarons and bound bipolarons; in contrast, in the case of CdF_2:Y, the Fermi level is slightly lower than the bound polaron level E_1. As we show below, this

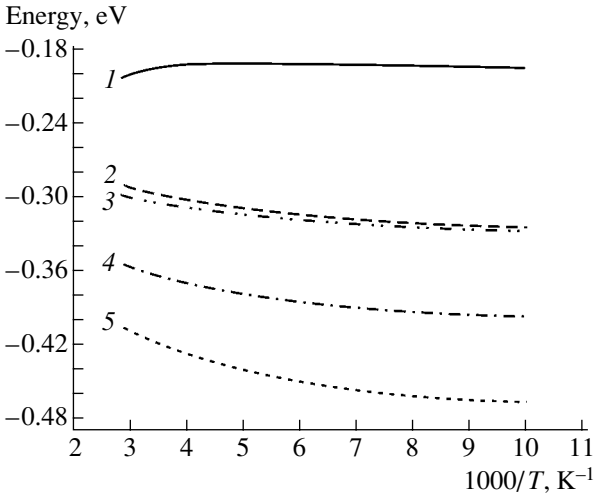

Fig. 1. Temperature dependences of the energy $E_{pol\text{-}s}$ of the free-polaron band bottom (*1*), the bound polaron energy E_1 (*2*), and the bipolaron energy E_{2s} (*5*), as well as the positions of Fermi levels $\mu^{(In)}$ (*4*) and $\mu^{(Y)}$ (*3*) for the CdF_2:In and CdF_2:Y crystals, respectively.

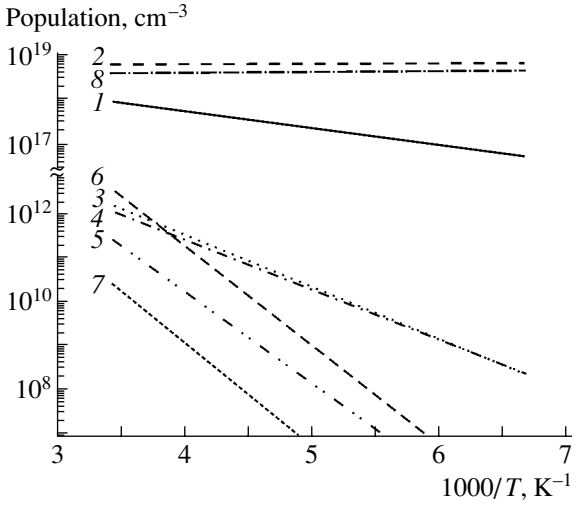

Fig. 2. Temperature dependences of the state population for "cold" carriers n_{cold} (*3*), "cold" $n_{c\text{-cold}}$ (*5*) and "hot" n_{hot} (*6*) electrons, free polarons n_{pol} (*4*), and free bipolarons n_{bip} (*7*), as well as the concentrations of ionized (shallow) impurities N_{sh}^+ (*2*), bound polarons N_{sh}^0 (*1*), and bound bipolarons N_d^- (*8*) in the CdF_2:In crystal.

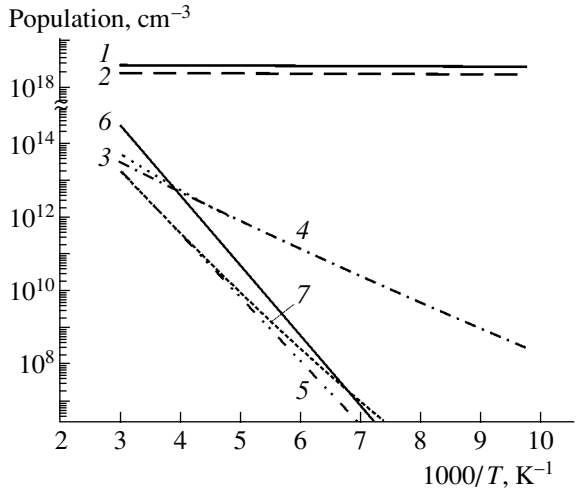

Fig. 3. Temperature dependences of the state population for "cold" carriers, n_{cold} (*3*), "cold" $n_{c\text{-cold}}$ (*5*) and "hot" $n_{c\text{-hot}}$ (*6*) electrons, free polarons n_{pol} (*4*), and free bipolarons n_{bip} (*7*), as well as the concentrations of ionized (shallow) impurities N_{sh}^{+} (*2*) and bound polarons N_{sh}^{0} (*1*) in the CdF_2:Y crystals.

difference is very significant in the analysis of experimental data on the conductivity and Hall effect in CdF_2:In and CdF_2:Y.

We note that energy gaps between the free-polaron band bottom and energy levels of the bound polarons and bipolarons in CdF_2:In are close to the corresponding activation energies determined for this crystal using several different experimental techniques (e.g., [24]), as well as determined in the ab initio calculation of an In deep center (bound bipolaron [25]).

4. THE CONDUCTIVITY AND HALL EFFECT

When analyzing the experimental data described in Section 2, it should be kept in mind that the material contains several carrier groups, which can all contribute to the conductivity σ and Hall coefficient R_{H}. In this case, the corresponding expressions take the form

$$\sigma = e\sum_i n_i\mu_i, \tag{24}$$

$$R_{\text{H}} = \frac{\sum_i e^i n_i\mu_i^2}{c\left(e\sum_i n_i\mu_i\right)^2}, \tag{25}$$

where μ_i are the mobilities of the ith-type carriers, and $e_i = -|e|$ and $e_i = |e|$ if the carriers are electrons and holes, respectively. In order to compare the theoretical and experimental data, it is convenient to use the reduced Hall coefficient

$$\tilde{R}_{\text{H}} \equiv cR_{\text{H}}\sigma^2 = \sum_i e_i n_i\mu_i^2. \tag{26}$$

The following temperature dependences of the mobility were used:

(i) For free electrons, $\mu_{\text{el}} = \sqrt{\beta}\,\mu_{\text{el0}}$ (see formulas (2)), which is characteristic of scattering by polarization phonons or piezoelectric scattering by acoustic phonons. Since the minimum kinetic energy of "hot" electrons is only 8 meV at a chosen value of V_0, we can consider "cold" and "hot" electrons as a single carrier group. We note that, in the case of mechanisms characterized by a power temperature dependence of the mobility, determination of the exponent becomes complicated when comparing the theoretical and experimental data in this study.

(ii) The free-polaron mobility μ_{pol} is determined from the relation $\mu_{\text{pol}}^{-1} = = \mu_{\text{pol-1}}^{-1} + \mu_{\text{pol-2}}^{-1}$, where $\mu_{\text{pol-1}} = \mu_{\text{pol-10}}\sqrt{2}\,[\exp(\beta) - 1]$ corresponds to scattering by optical phonons (see, e.g., [13]) and $\mu_{\text{pol-2}} = \sqrt{\beta}\,\mu_{\text{pol-20}}$ corresponds to scattering by acoustic phonons [26] or impurities [27].

(iii) The mobility corresponding to impurity-band conduction features various temperature dependences when it is caused by the hops of bound polarons or drift of holes. In the former case, the mobility mechanism is of an activation type: $\mu_{tp} = \mu_{0tp}\exp[-\lambda\varepsilon_{tp}]$. When considering the latter case, it should be kept in mind that there exists a significant energy spread of holes, which is primarily due to their interaction with charged impurities. At low temperatures, the holes become bound to acceptors (see, e.g., [28], Section 26). Only the holes that can be detached from the acceptors are involved in conduction. The number n_{hc} of such holes at low T is defined by the activation exponential function $\exp(-\lambda\varepsilon_a)$. Accordingly, we will refer to these holes to as activated holes. As the temperature is elevated, the increase in n_{hc} drops off, and n_{hc} tends to a constant value. This effect corresponds to the approximation we accepted,

$$n_{hc} \approx \chi_h N_{sh}^{+}\frac{\exp(-\lambda\varepsilon_a)}{\exp(-\lambda\varepsilon_a) + a_{hc}}, \tag{27}$$

where χ_h is a constant close to unity. The temperature dependence of the mobility μ_h of activated holes can be disregarded. It is assumed that the hole motion in the impurity band is not accompanied by lattice polarization. The reason for this assumption is that the state of the electronic subsystem in which a donor is ionized and an electron is in the conduction band exactly corresponds to a specific arrangement of lattice atoms; in this case, the configuration coordinate characterizing the lattice relaxation during the formation of a free polaron

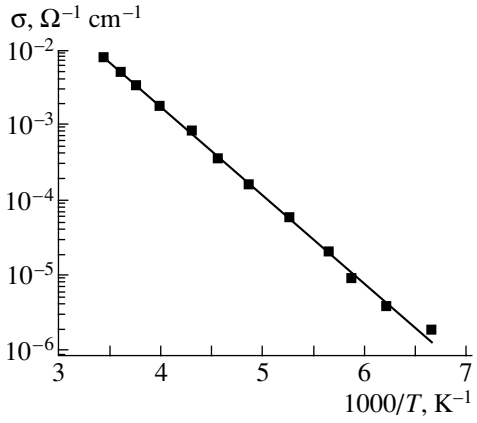

Fig. 4. The temperature dependence of the static conductivity σ in CdF_2:In.

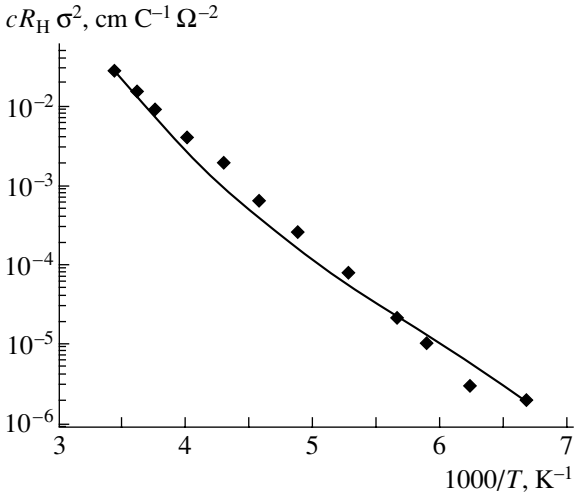

Fig. 5. The temperature dependence of the reduced Hall coefficient $\tilde{R}_H \equiv cR_H\sigma^2$ in CdF_2:In.

and during electron trapping by a donor (bound polaron) becomes equal to zero.

We can see in Fig. 2 that the concentration of free bipolarons (if they actually exist) is insignificant in the case of CdF_2:In, and their contribution to σ and R_H can be disregarded. The concentration of bound bipolarons (deep centers) is high in the entire temperature range under study; nevertheless, there is no reason to believe that their contribution to σ and R_H is significant. There are no bound bipolarons in the CdF_2:Y crystals; however, since the Fermi level μ is located higher than in CdF_2:In (see Fig. 1), the concentration of free bipolarons is much higher and they can, in principle, affect σ and R_H. The impurity-band conduction at a weak compensation can be effected by holes.

When calculating the temperature dependences of σ and $\tilde{R}_H$, we used the theoretical energies of the states of free and bound polarons and bipolarons, as well as the concentrations of various carriers, obtained in this study. The parameters $\mu_{el\text{-}0}$, $\mu_{pol\text{-}10}$, $\mu_{pol\text{-}20}$, $\mu_{0\text{-}tr}$, ε_{tp}, $\varepsilon_a\mu_h$, a_{hc}, and χ_h were selected so that the theoretical curves $\sigma(1000/T)$ and $\tilde{R}_H(1000/T)$ would best approximate the experimental dependences. The necessity to describe two different experimental curves using a single set of parameters imposes very severe constraints on the values of these parameters.

Figures 4 and 5 show the experimental and calculated curves $\sigma(1000/T)$ and $\tilde{R}_H(1000/T)$ for CdF_2:In. The following parameters were used: $\mu_{0tp} = 24$ cm^2 V^{-1} s^{-1}, $\varepsilon_{tp} = 0.15$ eV, $\mu_{pol\text{-}10} = 0.64 \times 10^2$ cm^2 V^{-1} s^{-1}, $\mu_{pol\text{-}20} = 1.26 \times 10^2$ cm^2 V^{-1} s^{-1}, and $\mu_{e10} = 1.6 \times 10^2$ cm^2 V^{-1} s^{-1}. The Arrhenius plot for the CdF_2:In conductivity in the studied temperature range is a straight line corresponding to the effective conductivity activation energy 0.231 eV.

As is known (see, e.g., [29, 30]), the probability of bound polaron hopping is defined by the quantity

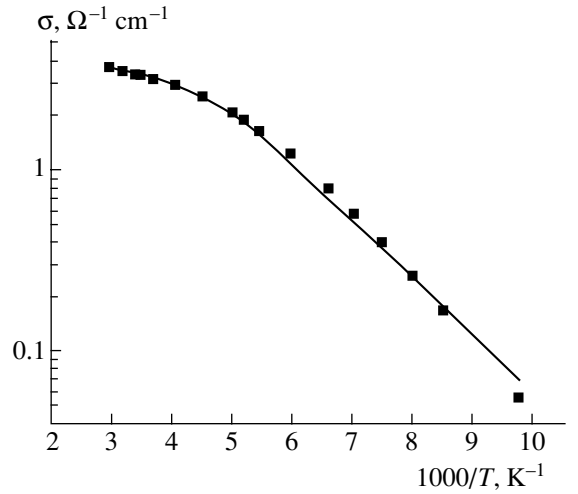

Fig. 6. The temperature dependence of the static conductivity σ in CdF_2:Y.

$\exp(-\lambda W_H)$, where the activation energy $W_H = \frac{1}{2}U_p$. In the case under consideration, the lattice polarization energy is $U_p \approx -2E_{pol\text{-}s} \approx 0.4$ eV. The value $\varepsilon_{tp} \approx \frac{3}{4}W_H$, obtained from a comparison of the calculated curves with the experimental data, corresponds to a situation (typical of hopping mobility) where the activation energy is lower than W_H.

Figures 6 and 7 show the experimental data and theoretical curves $\sigma(1000/T)$ and $\tilde{R}_H(1000/T)$ for CdF_2:Y. When plotting the theoretical curves, the following parameters were used: $\varepsilon_a = 0.0775$ eV, $a_{hc} = 0.011$, $\chi_h = 0.666$, $\mu_{pol\text{-}10} = 1.71 \times 10^2$ cm^2 V^{-1} s^{-1}, $\mu_{pol\text{-}20} =$

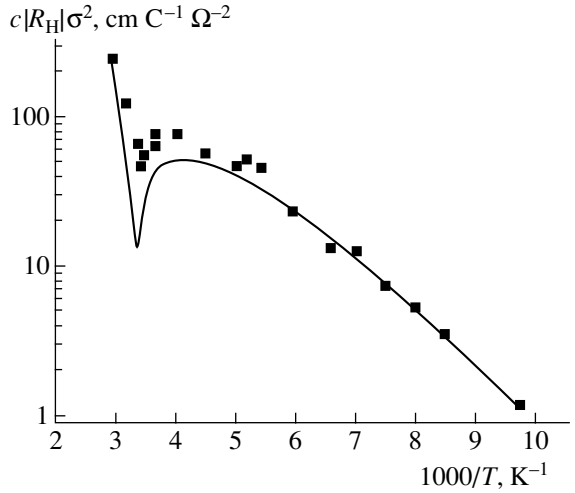

Fig. 7. The temperature dependence of the reduced Hall coefficient in CdF_2:Y.

0.95 cm^2 V^{-1} s^{-1}, and $\mu_{e10} = 1.9 \times 10^3$ cm^2 V^{-1} s^{-1}. Let us take into account the fact that bipolarons do not significantly contribute to σ and $\tilde{R}_H$ at least until their mobilities μ_{bip} are lower than 10^3 cm^2 V^{-1} s^{-1}. The activation energy ε_a corresponds to the compensation factor $\gamma = 0.25$, which is slightly smaller than in the sample under study, if the estimate from [31, 32] is used:

$$\varepsilon_a \simeq 0.61\varepsilon_D(1 - 0.29\gamma^{1/4}),$$
$$\varepsilon_D = e^2/(\varepsilon_0 r_D), \quad r_D = \left(\frac{4\pi}{3}N_m\right)^{-1/3}. \qquad (28)$$

When applying this formula, the following two points should be taken into account: First, (28) is valid for very small γ and the extrapolation of Eq. (28) to the range $\gamma \approx 0.2$–0.4 can yield incorrect results. Second, the actual degree of compensation in the sample cannot be determined with confidence. Therefore, it can be concluded that the obtained value ε_a does not contradict the available concepts on the hopping mobility of bound polarons.

Let us take into consideration the fact that the Hall coefficient sign in CdF_2:Y (Fig. 7) changes at the curve knee point at $1000/T \approx 3.4$. In the low-temperature region (to the right of the knee), the activated holes mainly contribute to $\tilde{R}_H$ (its sign is positive); in the high-temperature region, free carriers, electrons, and polarons mainly contribute to R_H (its sign is negative). At $\gamma \geq 0.5$, this sign change in the Hall coefficient could not take place, and the dependence $c|R_H|/\sigma$ on $1000/T$ would be monotonic. Therefore, it can be concluded that, in fact, the degree of compensation is $\gamma < 0.5$ in the CdH_2:Y samples under study, and the contribution to the conductivity is made not only by the electrons and polarons but also by the *p*-type impurity-band conductivity (see the discussion of this problem above). It is important that a simultaneous matching of the theoretical and experimental curves $\sigma(1000/T)$ and $\tilde{R}_H(1000/T)$ is impossible for both materials (CdF_2:In and CdF_2:Y) if the impurity-band conduction is to be disregarded. Furthermore, the contribution of the free electrons to $\tilde{R}_H$ plays an important role, which, if it is disregarded, does not allow the attainment of satisfactory agreement between the theoretical and experimental data in the near-room temperature range.

A reasonable variation of the theory [19–23] parameters u and V_0 results in an appreciable redistribution of the free carrier populations, but only slightly affects the curves in Figs. 4–7 when calculated using the same values of the other parameters.

5. CONCLUSION

We measured the temperature dependences of the static conductivity σ and Hall coefficient R_H in semiconductor CdF_2:In and CdF_2:Y crystals.

The obtained dependences were theoretically analyzed taking into account free electrons, free polarons and bipolarons, and bound polarons and bipolarons (the latter exist in CdF_2:In). The energies and occupancies of these states were calculated. The mobilities for various carrier groups were estimated from a comparison of the theoretical curves with the experimental data.

We show that the impurity-band conduction significantly contributes to σ and R_H due to the hops of bound polarons (CdF_2:In) or to activated holes (CdF_2:Y). In addition, free polarons and free electrons also contribute to σ and R_H.

ACKNOWLEDGMENTS

This study was supported by the International Science and Technology Center, project no. 2136.

REFERENCES

1. J. D. Kingsley and J. S. Prener, Phys. Rev. Lett. **8**, 315 (1962).
2. A. S. Shcheulin, A. I. Ryskin, K. Swiatek, and J. M. Langer, Phys. Lett. A **222**, 107 (1996).
3. A. I. Ryskin and P. P. Fedorov, Fiz. Tverd. Tela (St. Petersburg) **39**, 1050 (1997) [Phys. Solid State **39**, 943 (1997)].
4. D. E. Onopko and A. I. Ryskin, Phys. Rev. B **61**, 12952 (2000).
5. R. P. Hosla, Phys. Rev. **183**, 695 (1969).
6. S. A. Kazanskii, D. S. Rumyantsev, and A. I. Ryskin, Phys. Rev. B **65**, 165214 (2002).
7. F. Moser, D. Matz, and S. Luy, Phys. Rev. **182**, 808 (1969).
8. J. M. Langer, T. Langer, G. L. Pearson, *et al.*, Phys. Status Solidi B **66**, 537 (1974).
9. A. Kessler and J. E. Kaffin, J. Phys. C: Solid State Phys. **5**, 1134 (1972).

10. A. Kessler, J. Phys. C: Solid State Phys. **6**, 1594 (1973).
11. S. A. Kazanskiĭ and A. I. Ryskin, Fiz. Tverd. Tela (St. Petersburg) **44**, 1356 (2002) [Phys. Solid State **44**, 1415 (2002)].
12. M. A. Krivoglaz and S. I. Pekar, Izv. Akad. Nauk SSSR, Ser. Fiz. **21**, 16 (1957).
13. S. I. Pekar, *Selected Works* (Naukova Dumka, Kiev, 1988), p. 204 [in Russian].
14. Yu. E. Perlin and I. Ya. Ogurtsov, Fiz. Tverd. Tela (Leningrad) **7**, 1468 (1965) [Sov. Phys. Solid State **7**, 1180 (1965)].
15. Yu. E. Perlin and Sh. N. Gifeĭsman, Fiz. Tverd. Tela (Leningrad) **9**, 2752 (1967) [Sov. Phys. Solid State **9**, 2165 (1967)].
16. Yu. E. Perlin and Sh. N. Gifeĭsman, Fiz. Tekh. Poluprovodn. (Leningrad) **12**, 459 (1978) [Sov. Phys. Semicond. **12**, 266 (1978)].
17. V. L. Vinetskiĭ, Zh. Éksp. Teor. Fiz. **40**, 1459 (1961) [Sov. Phys. JETP **13**, 1023 (1961)].
18. V. D. Lakhno and G. N. Chuev, Usp. Fiz. Nauk **165**, 285 (1995) [Phys. Usp. **38**, 273 (1995)].
19. É. N. Myasnikov and A. É. Myasnikova, Zh. Éksp. Teor. Fiz. **116**, 1386 (1999) [JETP **89**, 746 (1999)].
20. A. E. Myasnikova, Phys. Lett. A **291**, 439 (2001).
21. A. É. Myasnikova and É. N. Myasnikov, Zh. Éksp. Teor. Fiz. **112**, 278 (1997) [JETP **85**, 152 (1997)].
22. A. É. Myasnikova, Zh. Éksp. Teor. Fiz. **115**, 180 (1999) [JETP **88**, 101 (1999)].
23. A. É. Myasnikova and É. N. Myasnikov, Phys. Rev. B **56**, 5316 (1997).
24. U. Piekara, J. M. Langer, and B. Krukowska-Fulde, Solid State Commun. **23**, 583 (1977).
25. C. H. Park and J. D. Chadi, Phys. Rev. Lett. **82**, 113 (1999).
26. Yu. E. Perlin, Zh. Éksp. Teor. Fiz. **21**, 547 (1951).
27. Yu. E. Perlin and V. A. Kovarskiĭ, Uch. Zap. Kishinev. Gos. Univ. **11**, 81 (1954).
28. B. I. Shklovskiĭ and A. L. Éfros, *Electronic Properties of Doped Semiconductors* (Nauka, Moscow, 1979; Springer, New York, 1984).
29. N. F. Mott and E. A. Davis, *Electronic Processes in Non-Crystalline Materials* (Clarendon, Oxford, 1979; Mir, Moscow, 1982).
30. V. L. Bonch-Bruevich, I. P. Zvyagin, R. Keiper, A. G. Mironov, R. Enderlein, and B. Esser, *Electronic Theory of Disordered Semiconductors* (Nauka, Moscow, 1981) [in Russian].
31. B. I. Shklovskiĭ, A. L. Éfros, and I. Ya. Yanchev, Pis'ma Zh. Éksp. Teor. Fiz. **14**, 348 (1971) [JETP Lett. **14**, 233 (1971)].
32. A. L. Éfros, B. I. Shklovskiĭ, and I. Y. Yanchev, Phys. Status Solidi B **50**, 45 (1972).

Translated by A. Kazantsev

Semiconductors, Vol. 39, No. 5, 2005, pp. 514–520. Translated from Fizika i Tekhnika Poluprovodnikov, Vol. 39, No. 5, 2005, pp. 543–549.

ELECTRONIC AND OPTICAL PROPERTIES OF SEMICONDUCTORS

The Conductivity Tensor and Frequency of Electron Momentum Relaxation in the Case of Scattering by Ionized Impurities in a Magnetic Field: The Density Matrix Method

V. E. Kaminskii

Institute of UHF Semiconductor Electronics, Russian Academy of Sciences, Moscow, 117105 Russia
e-mail: kamin@zelnet.ru

Submitted June 21, 2004; accepted for publication October 8, 2004

Abstract—A solution to the Liouville equation for a one-electron density matrix in relation to a homogeneous semiconductor in a magnetic field is obtained using perturbation theory. Expressions for the conductivity tensor and electron-momentum relaxation rate are obtained for the case of scattering by ionized impurities. These expressions provide a sufficiently accurate description of the concentration and magnetic field dependences of the longitudinal conductivity of a nondegenerate electron gas in the quantum limit that have been observed in some studies. No explanation for these dependences is found in the context of the current theory of magnetoresistivity. An explanation of the temperature dependences of the components of the conductivity tensor is suggested for a degenerate electron gas in magnetic fields that correspond to the quantum limit. © *2005 Pleiades Publishing, Inc.*

1. INTRODUCTION

It is known that, in a magnetic field, the electron energy spectrum of semiconductors is quantized. However, for $\alpha = \hbar\omega/kT \ll 1$, where $\omega = qB/m$ is the cyclotron frequency, the effect of quantization appears, in most cases, to be small and electron transport can be described using the Boltzmann transport equation. It follows from this equation that a magnetic field substantially affects transverse (with respect to the field) transport phenomena if $\omega\tau = \mu B > 1$, where μ is the electron mobility. In the longitudinal direction, transport effects are independent of a magnetic field.

In a quantizing magnetic field, for $\alpha \gg 1$, the use of the transport equation for the electron distribution function cannot be applied to a description of transverse galvanomagnetic effects in semiconductors (for which the magnetic field vector **B** is perpendicular to the current-density vector **j**). Moreover, this approach cannot, in principle, describe a number of specific effects related to quantization. The problem of transverse galvanomagnetic effects has been exactly solved by Adams and Holstein using the density matrix method [1]. According to [1–3], the character of conductivity in the presence of a magnetic field in the quantum limit does not substantially differ from the case of classical high fields. The only difference is that the density of states at the Fermi level and the relaxation times depend on the magnetic field [4, 5]. According to [1], the longitudinal conductivity of electron gas σ_{zz} ($\mathbf{B} \parallel \mathbf{j} \parallel z$) does not differ from the classical expression.

However, further studies have shown that in the case of scattering by ionized impurities, the expressions for σ_{xx} and σ_{zz} obtained in [1–3] are not quite exact in the quantum limit [4]. It was assumed that this circumstance is related to the fact that it is necessary to take into account the effects of screening and the quasi-one-dimensional character of electron motion in the field of a charged impurity. However, in the traditional approach, a consistent consideration of these effects [1] does not describe a number of features of magnetotransport. With regard to these effects, the longitudinal conductivity $\sigma_{zz}(B_z)$ for a nondegenerate electron gas increases with the magnetic field in the ultra-quantum limit when only the lowest Landau level is occupied, due to the suppression of small-angle scattering [4]; moreover, the greater the increase in conductivity, the smaller the electron concentration. In InSb, this pattern in the dependence of $\sigma_{zz}(B_z)$ was observed at a temperature of $T = 30$ K only for a relatively high electron concentration ($n \approx 10^{15}$ cm^{-3}). At lower electron concentrations, the opposite field dependence was observed [6]. For electron concentrations of $n \approx 10^{13}$ cm^{-3}, the disagreement between theory and experiment can be up to a factor of 40. In the context of the existing theories, this fact has no explanation. For a degenerate electron gas in doped semiconductors in a temperature range from 0.05 to 15 K in the ultra-quantum limit, a rather strong temperature dependence of the diagonal components of the conductivity was observed (see review [4] and the references therein). Longitudinal resistivity $\rho_{zz}(B_z)$ monotonically decreases with increasing temperature, whereas transverse conductivity $\sigma_{xx}(B_z)$ and resistivity $\rho_{xx}(B_z)$ ($\mathbf{j} \parallel x$, $\mathbf{B} \parallel z$) depend nonmonotonically on temperature. At the same time, the Hall conductivity $\sigma_{xy}(B_z)$ varies only very slightly with temper-

ature. It is impossible to explain these temperature dependences in the context of the theory developed in [1].

Recently, it has been shown that, in some cases, a consistent consideration of quantization in a magnetic field is important when formulating an adequate description of galvanomagnetic effects [7, 8]. However, in [7, 8], the case of scattering by ionized impurities, which is very important from the experimental point of view, was not analyzed. In this study, the transport equation for a density matrix in arbitrary magnetic fields is solved for scattering by ionized impurities, assuming that the departure from equilibrium is small. Expressions for the momentum relaxation rate are also obtained and compared with the available experimental results.

2. THEORY

It is known that, in a magnetic field, the matrices of electron momentum components normal to the field have no diagonal elements. Due to this fact, the electron transport in a quantizing magnetic field cannot in principle be described using the Boltzmann transport equation. Generally, the most complete microscopic description of a state in a quantum system is a description using the statistical operator (the density matrix) R. In the Schrödinger representation, it obeys the Liouville equation

$$i\hbar\frac{\partial R}{\partial t} = [H, R]. \quad (1)$$

In what follows, we restrict the analysis to a one-electron approximation. We assume that the magnetic field B is directed along the z axis, $\mathbf{j} \parallel x$, and the electric field E_x is also directed along the x axis.

The properties of a system considered in the one-electron approximation are described by the Hamiltonian operator

$$H = H_0 + W + U = H_e + W + U, \quad (2)$$

where H_e is the Hamiltonian of an electron in a magnetic field, W is the operator of the interaction of electrons with phonons or impurities, and $U = -qE_x x$ is the potential-energy operator. Generally, the electric current density can be calculated using the relation

$$\mathbf{j} = \mathrm{Tr}(R\mathbf{J}), \quad (3)$$

where Tr(…) denotes the trace of an operator and $\mathbf{J}$ is the current-density operator in a magnetic field. To calculate the current, we must find the statistical operator using Eq. (1). To solve this equation, we treat the sum $W + U$ in expression (2) as a perturbation.

If we choose the vector potential of the magnetic field in the gage $\mathbf{A} = (0, Bx, 0)$, then the wave functions of the operator H_0 and of the electron energy for a homogeneous semiconductor are described by the well-known relations in the Landau representation [9]. In this representation, an electron state $|i\rangle$ is described by a set of quantum numbers (n, k_y, k_z, and s).

We solve Eq. (1) using the method of successive approximations. A justification of this method and the procedure for deriving an approximate equation are described in detail in [10]. For steady-state conditions, using the chosen basis of wave functions, we obtain from Eq. (1)

$$(E_1 - E_2)R_{12} + U_{13}R_{32} - R_{13}U_{32} + i\pi S_{12} = 0, \quad (4)$$

where

$$S_{12} = 2\sum_3 \{\delta(E_2 - E_3)[M^+_{14}(\delta_{43} - R_{43})M_{35}R_{52} - (\delta_{14} - R_{14})M_{43}R_{35}M^+_{52}] + \delta(E_1 - E_3) \quad (5)$$

$$\times [R_{14}M^+_{45}(\delta_{53} - R_{53})M_{32} - M_{13}R_{34}M^+_{45}(\delta_{52} - R_{52})]\}.$$

Here, M_{ij} are the matrix elements of the interaction of electrons with charged impurities; the form of these elements depends on the method used to describe this interaction.

It is well known that, strictly speaking, Eq. (1) does not describe the irreversible behavior of an electron system. To obtain irreversible behavior, we must use additional arguments [1]. For this purpose, we may either modify the Hamiltonian or take advantage of some artificial mathematical method that permits us to describe the interaction of the system with the medium. The most common method is derived from the assumption on an initial approximation for the diagonal part of the density matrix, i.e., for the distribution function. We represent the density matrix as

$$R_{12} = F_1\delta_{12} + G_{12}\delta(k_{y1} - k_{y2}), \quad (6)$$

where $G_{12} = G_{n_1 n_2}(k_{z1}, k_{z2})$. If the electric field does not affect the spatial uniformity of the electron system, the quantity $F_1 = F(E_1)$ is usually chosen in the form of the Fermi–Dirac distribution function, which depends on the energy and quasi–Fermi level E_F. The choice of F_1 is actually based on the principle of local equilibrium, widely used in the theory of semiconductors. At high temperatures, this approximation is quite satisfactory. However, at low temperatures, it is necessary to take into account corrections to the distribution function related to the combined effect of the electric field and relaxation processes. Such a correction was obtained in [1] for the first nonvanishing order in scattering,. However, it can only be applied to high fields. A general procedure for obtaining the corrections is described in [10]. It consists in expansion of the Gibbs statistical operator in the interaction potential treated as a perturbation. In the approximation linear in an electric field, the distribution function can be written as

$$F_1 + \frac{\partial F_1}{\partial E}U_{11}Z, \quad (7)$$

where U_{11} is the potential-energy matrix element and Z is the function representing the result of summation

over all the high-order scattering terms. Generally, this function depends on the magnetic field, relaxation parameters, and the distribution function and can be determined by solving Eq. (1) for the diagonal elements of the density matrix. Then, from (6), we obtain

$$R_{12} = \left(F_1 + \frac{\partial F_1}{\partial E}U_{11}Z\right)\delta_{12} + G_{12}\delta(k_{y1} - k_{y2}). \quad (8)$$

In this study, we do not analyze the exact form of the function Z. Instead, we restrict the analysis to first approximation in magnetic field. A standard solution to the Boltzmann transport equation for the distribution function shows that its nonequilibrium part can be written as [11]

$$\Delta f = \frac{\mathbf{f}_1\mathbf{k}}{k}.$$

In the case of a magnetic field, we find

$$\mathbf{f}_1 = -q\frac{\hbar k}{m}\frac{\partial F}{\partial E}\frac{\omega[\mathbf{BE}] + \nu B\mathbf{E}}{B(\nu^2 + \omega^2)},$$

where ν is the momentum relaxation frequency. We omit the term proportional to $\mathbf{E}$. The consideration of this term improves the accuracy of the calculation of the function P_{nm}, which is determined below. However, in this study, we disregard this problem. Then, we obtain

$$\begin{aligned}\Delta f &= -\frac{\hbar q}{m}\frac{\partial F}{\partial E}\frac{\omega(\mathbf{k}[\mathbf{BE}])}{B(\nu^2 + \omega^2)} \\ &= -qk_y\lambda^2 E_x\frac{\partial F}{\partial E}\frac{\omega^2}{\nu^2 + \omega^2} = U_{11}\frac{\partial F}{\partial E}\frac{\omega^2}{\nu^2 + \omega^2}.\end{aligned} \quad (9)$$

Comparing this expression with (7), we obtain

$$Z = \frac{\omega^2}{\nu^2 + \omega^2}.$$

We see that $Z = 0$ for $B = 0$ and, in the high-field limit, $Z = 1$. In fact, in [1], the distribution function was written (although not explicitly) in form (9) with $Z = 1$. The divergence of the solutions in the low-field region [1] is mainly related to the fact that the field dependence of Z is disregarded.

We now search for a solution of Eq. (4) linear in G. We restrict further consideration of the interaction of electrons with a charged impurity to the case of a screened Coulomb potential. Then, we use (4), (5), and (8) to obtain

$$\begin{aligned}&(E_n - E_m + i\hbar\nu_{nm}^{(0)})G_{nm} + U_{nm}(F_m - F_n) \\ &- i\sqrt{2(n+1)}q\lambda E_x P_{nm} - i\hbar B_{nm} = 0,\end{aligned} \quad (10)$$

where

$$\begin{aligned}\nu_{nm}^{(0)} &= \nu_0\int_0^\infty dy\left\{\sum_{l=0}^{l_m}[(1 - F_m)K_{nl} + F_m K_{ml}]A_{ml}\right. \\ &\left. + \sum_{l=0}^{l_n}[(1 - F_n)K_{ml} + F_n K_{nl}]A_{nl}\right\},\end{aligned} \quad (11)$$

$$\begin{aligned}P_{nm} &= \frac{\hbar\nu_i}{\sqrt{n+1}}Z\int_0^\infty\sqrt{y}dy\left[(1 - F_n + F_m)\left(-\frac{\partial F_m}{\partial E_m}\right)\right. \\ &\times\sum_{l=0}^{l_m}\left|C_{n,l}^{m,m-n+l}\right|A_{ml} + (1 + F_n - F_n)\left(-\frac{\partial F_n}{\partial E_n}\right) \\ &\left.\times\sum_{l=0}^{l_n}\left|C_{m,l}^{n,n-m+l}\right|A_{ml}\right](\delta_{m,n+1} + \delta_{m,n-1}),\end{aligned} \quad (12)$$

$$\begin{aligned}B_{nm} &= \nu_i\int_0^\infty dy\left\{\sum_{l=0}^{l_m}[(1 - F_n)C_{nl}^{m,m-n+l}G_{l,m-n+l}\right. \\ &+ F_m C_{ml}^{n,n-m+l}G_{n-m+l,l}]A_{ml} \\ &+ \sum_{l=0}^{l_n}[(1 - F_m)C_{ml}^{n,n-m+l}G_{l,n-m+l} \\ &\left. + F_n C_{nl}^{m,m-n+l}G_{m-n+l,l}]A_{nl}\right\},\end{aligned}$$

$$\begin{aligned}A_{nl} &= \frac{1}{2b_{nl}}\{[2y + a^2 + (x + b_{nl})^2]^{-2} \\ &+ [2y + a^2 + (x - b_{nl})^2]^{-2}\},\end{aligned}$$

$$x = k_z\lambda, \quad a = k_s\lambda, \quad l_n = n + \left[\frac{x^2}{2}\right],$$

$$b_{nl}^2 = x^2 + 2(n - l),$$

$$\nu_i = \frac{mq^4N^+\lambda^3}{2\pi^2\kappa^2\hbar^3},$$

N^+ is the concentration of ionized impurities, $k_s = 1/r_s$, r_s is the screening radius, and κ is the permittivity of the semiconductor. The functions $K_{nl}(y)$ and $C_{n,l}^{m,p}(y)$, as well as the method of integration applied to the matrix elements, are described in the Appendix. We see that the required function G appears in Eq. (10) as a sum. Therefore, in contrast to scattering by phonons [7, 8], it

is impossible to obtain a simple solution for G. However, the solution to Eq. (10) can be always written as

$$G_{nm} = \frac{U_{nm}(F_n - F_m) + i\sqrt{2(n+1)}qE_x\lambda P_{nm}}{E_n - E_m + i\hbar\nu_{nm}}. \quad (13)$$

The accuracy of the calculation of ν_{nm} depends on a number of parameters and on the chosen procedure for the solution to Eq. (10). Using the results obtained in the Appendix, we can show that $\nu_{nm}^{(0)}G_{nm} > B_{nm}$. Using this inequality, we can solve Eq. (10), e.g., by the method of successive approximations. In the first approximation, we may set $B_{nm} = 0$. These questions will be considered in more detail below. The result for the components of the conductivity tensor is

$$\sigma_{xx} = \frac{q^2\omega}{(2\pi)^2\hbar}\sum_{s,n}(n+1) \times \int dk_z\left[\frac{\nu_{n,n+1}(F_n - F_{n+1}) + \omega P_{n,n+1}}{\omega^2 + \nu_{n,n+1}^2}\right], \quad (14)$$

$$\sigma_{xy} = \frac{q^2\omega}{(2\pi)^2\hbar}\sum_{s,n}(n+1) \times \int dk_z\left[\frac{\omega(F_n - F_{n+1}) - \nu_{n,n+1}P_{n,n+1}}{\omega^2 + \nu_{n,n+1}^2}\right], \quad (15)$$

where $F_n \equiv F(E_n)$. We see that the structure of these equations coincides with that of the equations describing scattering by phonons [7, 8]. Therefore, to account for the combined effect of different relaxation mechanisms, we have to represent ν and P as sums over these mechanisms. In addition, the obtained expressions indicate that the function Z depends on the magnetic-level number n and can be written more correctly in the form

$$Z_{n,n+1} = \frac{\omega^2}{\omega^2 + \nu_{n,n+1}^2}.$$

Using these results, we can easily show that the longitudinal conductivity $\sigma_{zz}(B_z)$ is described by a standard expression [11].

For high magnetic fields ($\omega \gg \nu$), Eq. (13) formally transforms into the expression obtained in [1]. However, a substantial difference is that, in contrast to [1], in the low-field limit, this equation transforms into the well-known expressions for the conductivity tensor in a semiconductor [11]. Furthermore, in this study, we obtain a more exact expression than (11) for the frequency of ionized impurity scattering ν_{nm} in high magnetic fields (see below).

3. CALCULATION OF THE FREQUENCY OF ELECTRON SCATTERING

Equation (10) is Fredholm's equation of the second kind, which satisfies all the conditions for absolute convergence. Therefore, we use the method of successive approximations in the calculations. In first approximation, we set $B_{nm} = 0$. To obtain the second approximation, we take the fact that G_{nm} is a generalized (symbolic) function into account. In Eq. (10), we replace $\nu_{nm}^{(0)}$ by μ_{nm} and omit the term proportional to P_{nm}. This term corresponds to scattering effects that are quadratic in frequency. The consideration of these effects can be important in an analysis of magnetotransport in semiconductors with a low charge-carrier mobility. Taking into account the δ functions in the collision integral, we derive the following equality from the integrand in (10):

$$G_{l,m-n+l}(k_{z3}; k_{z4}) = G_{nm}\frac{\partial K_{z2}}{\partial k_{z3}} = G_{nm}\frac{k_{z3}}{k_{z2}}.$$

Using this equality in the collision integral, we obtain the following approximation for the scattering frequency:

$$\nu_{nm} = \frac{q^4\hbar\omega N^+}{16\pi\kappa^2\sqrt{2m}} \times \int_0^\infty dy\left[\sum_{l=0}^{l_m}\frac{K_{nl}}{b_{ml}(p_2)}D_{mnl}(p_2) + \sum_{l=0}^{l_n}\frac{K_{ml}}{b_{nl}(p_1)}D_{nml}(p_1)\right]. \quad (16)$$

Here,

$$b_{nm}^2(p_i) = \hbar\omega(n-m) + p_i^2, \quad i = 1, 2,$$

$$p_i^2 = \frac{\hbar^2 k_{zi}^2}{2m}, \quad l_n = n + \left[\frac{p_1^2}{\hbar\omega}\right], \quad E_s = \frac{\hbar^2 k_s^2}{2m},$$

$$D_{nml}(p_i) = \left[\frac{[p_i - b_{nl}(p_i)](1 + F_n - F_m)}{p_i[\hbar\omega y + (b_{nl} - p_i)^2 + E_s]^2} + \frac{[p_i + b_{nl}(p_i)](1 + F_n - F_m)}{p_i[\hbar\omega y + (b_{nl} + p_i)^2 + E_s]^2}\right].$$

For a nondegenerate electron gas, we replace the summation in (16) by integration and, in the limit of a zero magnetic field, obtain

$$\nu = \frac{q^4 N^+}{8\pi\kappa^2\sqrt{2m}p} \times \left[\frac{1}{(\sqrt{E} - p)^2 + E_s} - \frac{1}{(\sqrt{E} + p)^2 + E_s}\right], \quad (17)$$

where $p = p_1 = p_2$.

Now, we calculate the scattering frequency in the absence of a magnetic field directly from Eq. (5). In this

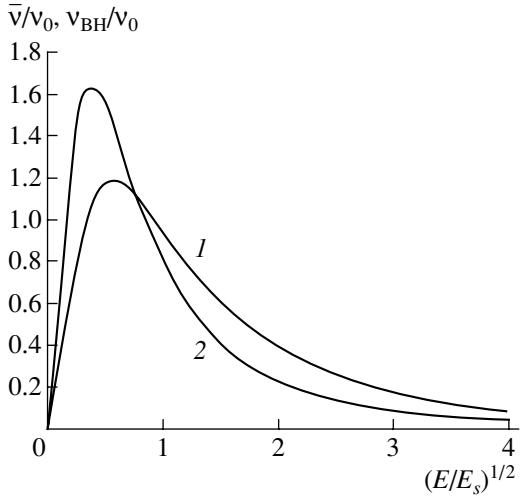

Fig. 1. The energy dependence of the rate of momentum relaxation induced by ionized impurities when (*1*) calculated using formula (18) and (*2*) calculated using the Brooks–Herring theory.

case, the electron state $|i\rangle$ is described by a set of quantum numbers (k_x, k_y, k_z, and s). An equation similar to Eq. (10) is obtained from Eq. (5). In the absence of a magnetic field, the frequency of the momentum relaxation depends only on the total electron energy. The iterative procedure of the solution converges well, and, in the second approximation, the well-known Brooks–Herring formula for the frequency of momentum relaxation ν_{BH} is obtained. We note here that further iterations only slightly improve the accuracy of the calculations.

We can see that frequency (16) depends on energy and k_z. However, the frequency ν_{BH} depends only on energy. This circumstance is due to the difference in the sets of quantum numbers used in the analysis in the absence and in the presence of a magnetic field. In order to obtain an expression for the scattering frequency from (16) that is equivalent to ν_{BH}, it is necessary to take into account that $p = \sqrt{E}\cos\Theta$ and average over the angle. The average frequency is given by

$$\bar{\nu} = \left(\int_0^\pi d\Theta \frac{\sin\Theta}{\nu(\Theta)}\right)^{-1}.$$

After simple calculations, we obtain the following expression from (16):

$$\bar{\nu} = \frac{60x}{15 + 40x^2 + 8x^4}\nu_0. \qquad (18)$$

Here,

$$x^2 = \frac{E}{E_s}, \quad \nu_0 = \frac{q^4 N^+}{16\pi\kappa^2\sqrt{2m}E_s^{3/2}}.$$

The obtained expression differs from the Brooks–Herring formula. The disagreement is caused by a difference in the convergence of the iterative procedure for the calculations with different sets of quantum numbers. Figure 1 shows the results of the calculation of the relaxation frequencies $\bar{\nu}$ and ν_{BH}. We can see that the difference in the results is nevertheless not very large.

4. CALCULATION OF THE CONDUCTIVITY OF ELECTRON GAS AND COMPARISON WITH THE EXPERIMENTAL RESULTS

First, we consider the temperature dependence of the conductivity of a degenerate electron gas in the ultra-quantum limit. In this case, for the transverse conductivity, $\omega \gg \nu$ and (13) can be used to obtain

$$\sigma_{xx} = \frac{q^2}{(2\pi)^2\hbar}\int dk_z P_{01}. \qquad (19)$$

Using this formula in the calculations, we must take into account that, for a degenerate electron gas in a semiconductor, the Fermi energy in high magnetic fields is low. For example, for InSb with an electron concentration of $n = 10^{16}$ cm^{-3} at $B = 5$ T, the Fermi energy is $E_F = 1.5$ meV and the ratio E_F/kT is small if the temperature is not too low. Therefore, the procedure in which the derivative of the distribution function is replaced by the δ function is not quite exact. Taking this circumstance into account, we use (12) to obtain the following approximate expression for the function $P_{n,n+1}$:

$$P_{01} = (1 + F_0)\left(-\frac{\partial F_0}{\partial E}\right)V_{01}(E_F).$$

Here,

$$V_{01} = \frac{\hbar\omega q^4 N^+}{8\pi^2\kappa^2\sqrt{2m}}\int_0^\infty \sqrt{y}C_{00}^{11}dy$$
$$\times\left[\frac{1}{(\hbar\omega\nu + 4E_F + E_s)^2} + \frac{1}{(\hbar\omega\nu + E_s)^2}\right].$$

Substituting this expression into (19) and then integrating, we find that the conductivity σ_{xx} in the ultra-quantum limit is

$$\sigma_{xx} = \frac{\sigma_{xx0}}{\left[1 + \exp\left(-\frac{E_F}{kT}\right)\right]^2},$$

where σ_{xx0} is the conductivity at a temperature of zero. Thus, for $n = 10^{16}$ cm^{-3}, σ_{xx} decreases by a factor of 1.4 as the temperature changes from 3 to 10 K. Since σ_{xy} is virtually independent of temperature and in the ultra-quantum limit, $\sigma_{xy} \gg \sigma_{xx}$, it follows that ρ_{xx} also decreases with temperature, in good agreement with the

experimental results [4]. Using (16), we can obtain a similar dependence of σ_{zz}.

From this analysis, we can see that, for a degenerate electron gas in a semiconductor, the temperature corrections for the diagonal components of the conductivity tensor are not large and do not modify the main form of the magnetic field dependence. At the same time, the obtained results allow us to interpret the experimentally observed dependences.

For nondegenerate semiconductors, the situation is different. As was noted in Section 1, the existing theory cannot explain the experimentally observed dependences of the longitudinal resistivity ρ_{zz} on the electron concentration n and magnetic field B_z. Therefore, we need to analyze this case in more detail. The desired dependences can be obtained using expression (16). However, to improve the accuracy of the calculations, we must take into account a number of factors that were not discussed above.

First, it is necessary to take into account the dependence of the concentration of activated impurities and, accordingly, the electron concentration on the magnetic field. Second, if not all the impurity atoms are ionized or the semiconductor is compensated, the electron concentration n_{eff}, which is used for the calculation of the screening radius, can differ from the concentration of free carriers $n = N^+$. In this case, screening can be also due to localized carriers moving between the centers [12]. For example, if, in an n-type semiconductor with the donor concentration N_D, there are some acceptors, whose concentration is $N_A \ll N_D$, then

$$n_{\text{eff}} = n + (N_D - N_A - n)(N_A + n)/N_D.$$

It follows from this relation that, in our case, when calculating the Debye radius r_s, we should replace n by n_{eff}. We should note that taking this fact into account does not strongly affect the calculated dependences. Third, we must take into account the relatively weak scattering by the deformation potential of acoustic phonons (DA), for which the frequency of momentum relaxation in a magnetic field was calculated in [7, 8].

Figure 2 shows the magnetic-field dependence of the longitudinal magnetoresistivity $\rho_{zz}(B_z)$ for doped InSb (for two different electron concentrations) calculated taking into account the above factors. This dependence is expected to be observed in the low-field limit. For the calculations, we used the following parameters from [5]: the Lande factor $g = -40$ and the momentum relaxation time $\tau_{DA}(300\ \text{K}) = 40$ ps. The impurity ionization energy was taken to be $E_d = 5$ meV. The calculation shows that the shape of the curves for the relative longitudinal magnetoresistivity weakly depends on E_d in a fairly wide range of E_d. The calculated curves agree with the experimental results [13] at an accuracy of no worse than 20% in the entire range of field variation. We note here that no decrease in resistivity was observed in the experimental curve for $n = 10^{13}$ cm^{-3} in the region of low fields. Under the specified conditions,

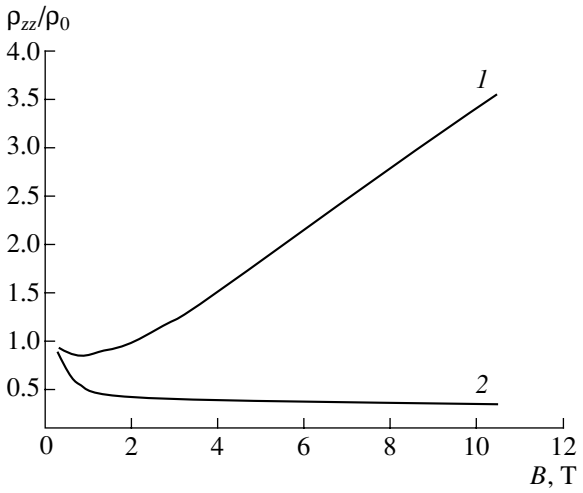

Fig. 2. The magnetic field dependence of the longitudinal resistivity at $T = 30$ K for semiconductors with the electron concentrations $n = (1)\ 10^{13}$ and $(2)\ 10^{15}$ cm^{-3}.

at an average thermal energy, the parameter $(E/E_s)^{1/2}$ in Fig. 1 is equal to 1.1 for the higher electron concentration and to 11 for the lower concentration. We can see from Fig. 1 that the scattering frequencies calculated using the two formulas are approximately equal. Therefore, the presence of a region of decreasing resistivity in the calculated curves may indicate that, for weak magnetic fields, it is necessary to take into account other scattering mechanisms.

5. CONCLUSIONS

Thus, the results obtained in this study allow us to describe the frequency of electron-momentum relaxation by ionized impurities in arbitrary magnetic fields much more precisely. These results also make it possible to describe the temperature dependences of the diagonal components σ_{xx} and σ_{zz} of the conductivity tensor of a degenerate electron gas in the ultra-quantum limit, without taking localization effects into account. In a nondegenerate electron gas, the obtained expressions satisfactorily describe the dependence of the longitudinal conductivity σ_{zz} on the electron concentration and magnetic field over a wide range of variation in these parameters.

APPENDIX

Integration of Matrix Elements and Orthogonal Polynomials

Using the equality $k_{y1} = k_{y2}$, we can represent the screened Coulomb potential as follows:

$$\frac{\exp(-k_s r)}{4\pi r} = \frac{1}{(2\pi)^3}\int \frac{d^3q}{q^2 + k_s^2}\exp(i\mathbf{qr}).$$

Then, the product of the matrix elements in (5) can be reduced to the integral

$$M_{14}^{+}M_{32} = 2\pi\left(\frac{q^2}{\kappa}\right)^2 N^{+}\int\frac{d^3q}{(q^2+k_s^2)^2}\delta(k_{y3}-k_{y1}+q_y)$$
$$\times\delta(k_{z3}-k_{z1}+q_z)\delta(k_{y2}-k_{y4}+k_{y3}-k_{y1})$$
$$\times\delta(k_{z2}-k_{z4}+k_{z3}-k_{z1})I_s,$$

where

$$I_s = \int dx_1dx_2 f_n\left(x_2-\frac{q_y}{2}\lambda^2\right)f_p\left(x_2+\frac{q_y}{2}\lambda^2\right)$$
$$\times f_l\left(x_2+\frac{q_y}{2}\lambda^2\right)f_m\left(x_1-\frac{q_y}{2}\lambda^2\right)\exp[iq_x(x_1-x_2)].$$

If we introduce the definition

$$I_{nl} = \int_{-\infty}^{\infty} dy\, f_n\left(y-\frac{q_y}{2}\lambda^2\right)f_l\left(y+\frac{q_y}{2}\lambda^2\right)$$
$$\times\exp(iq_xy) = \exp\left(-\frac{x}{2}\right)z_{nl},$$

then we obtain

$$I_s = \exp(-x)z_{ml}z_{np}^*,$$

where

$$q_r = \sqrt{q_x^2+q_y^2},\quad x = (q_r\lambda)^2/2,$$
$$z_{nl} = \frac{1}{\sqrt{\pi n!l!2^{n+l}}}$$
$$\times\int_{-\infty}^{\infty} dy\exp(-y^2)H_n\left(y+\frac{z_{10}}{\sqrt{2}}\right)H_l\left(y+\frac{z_{01}}{\sqrt{2}}\right).$$

Using these relations, we can easily show that

$$\int_0^{\pi} d\varphi I_{lm}I_{pn} = 2\pi\delta_{p,\,n-m+l}C_{m,\,l}^{n,\,n-m+l},$$

$$C_{m,\,l}^{n,\,n-m+l} = \exp(-x)z_{ml}z_{n,\,n-m+l}^*,$$

$$C_{m,\,l}^{m,\,l} = K_{ml} = K_{ln} = \exp(-x)z_{ml}z_{ml}^*,$$

$$\int_0^{\infty} C_{ml}^{n,\,n-m+l}dx = \delta_{nm}.$$

REFERENCES

1. E. N. Adams and T. D. Holstein, J. Phys. Chem. **10**, 254 (1959); in *Problems in Quantum Theory of Irreversible Processes* (Inostrannaya Literatura, Moscow, 1961), p. 255.
2. R. Kubo, H. Hesegawa, and N. Hashitdume, J. Phys. Soc. Jpn. **14**, 56 (1959); in *Problems in Quantum Theory of Irreversible Processes* (Inostrannaya Literatura, Moscow, 1961), p. 89.
3. P. N. Agryes and L. M. Roth, Phys. Chem. Solids **12**, 89 (1959).
4. S. S. Murzin, Usp. Fiz. Nauk **170**, 387 (2000) [Phys. Usp. **43**, 349 (2000)].
5. V. F. Gantmakher and I. B. Levinson, *Scattering of Carriers in Metals and Semiconductors* (Nauka, Moscow, 1984; North-Holland, Amsterdam, 1987), Chap. 14.
6. S. S. Murzin and P. V. Popov, Pis'ma Zh. Éksp. Teor. Fiz. **58**, 280 (1993) [JETP Lett. **58**, 289 (1993)].
7. V. É. Kaminskiĭ, Fiz. Tekh. Poluprovodn. (St. Petersburg) **36**, 1360 (2002) [Semiconductors **36**, 1276 (2002)].
8. V. É. Kaminskiĭ, Phys. Rev. B **67**, 085201 (2003).
9. L. D. Landau and E. M. Lifshitz, *Course of Theoretical Physics*, Vol. 3: *Quantum Mechanics: Non-Relativistic Theory*, 4th ed. (Nauka, Moscow, 1989; Pergamon, Oxford, 1977), Chap. 15.
10. A. I. Akhiezer and S. V. Peletminskiĭ, *Methods of Statistical Physics* (Nauka, Moscow, 1977; Pergamon, Oxford, 1981), Chaps. 3–5.
11. A. I. Ansel'm, *Introduction to the Theory of Semiconductors* (Nauka, Moscow, 1977), Chap. 7.
12. L. M. Falicov and M. Quevas, Phys. Rev. **164**, 1025 (1967).

Translated by I. Zvyagin

Semiconductors, Vol. 39, No. 5, 2005, pp. 521–522. Translated from Fizika i Tekhnika Poluprovodnikov, Vol. 39, No. 5, 2005, pp. 550–551.

ELECTRONIC AND OPTICAL PROPERTIES OF SEMICONDUCTORS

The Extrinsic Photoconductivity of Chalcogens in $Ge_{1-x}Si_x$ Solid Solutions

N. B. Radchuk and A. Yu. Ushakov^

St. Petersburg State Polytechnical University, ul. Politekhnicheskaya 29, St. Petersburg, 195251 Russia

^e-mail: ushakov@twonet.stu.neva.ru

Submitted September 9, 2004; accepted for publication October 14, 2004

Abstract—The effect of ~3% of silicon additive on the energy spectra of selenium and tellurium impurities in germanium is studied. The photoconductivity spectra are measured at 80 K in a spectral range from 2.5 to 5 μm. Narrow lines corresponding to the excited states of chalcogen ions are observed against the background of the extrinsic-photoconductivity band. It is found that the spectrum of excited states is not affected by silicon at the concentration used. An increase in the energy gaps between the conduction band and impurity states of the chalcogens is detected. © *2005 Pleiades Publishing, Inc.*

Tellurium and selenium act as substitutional impurities in germanium and silicon and introduce deep doubly charged donor states into the band gap. These states correspond to the neutral and ionized states of chalcogen atoms. The known energies of impurity ionization for germanium are

Te [1]: 0.095 and 0.28 eV,

Se [2]: 0.24 and 0.372 eV,

while, for silicon, we have

Te [3]: 0.199 and 0.411 eV,

Se [4]: 0.3 and 0.52 eV.

The given energies correspond to atmospheric windows in the infrared spectral region, which makes Ge:Te(Se) and Si:Te(Se) promising as materials for the fabrication of photodetectors. In $Ge_{1-x}Si_x$ solid solutions, the band gap varies as the Si fraction increases [5]; simultaneously, the impurities' ionization energy increases, which additionally makes it possible to control the photosensitivity range.

Narrow peaks corresponding to transitions to the excited states of chalcogen ions are observed against the background of conventional impurity bands in the photoconductivity spectra of germanium doped with chalcogens. It is noteworthy that a single peak with a positive polarity is observed in the spectra of the samples doped with tellurium, whereas three negative peaks correspond to the selenium impurity [6, 7]. In order to obtain data on the origin of the differences between the behavior of the chalcogen impurities, we studied the photoconductivity spectra of the $Ge_{1-x}Si_x$ solid solutions doped with Te and Se.

We used the method of horizontal recrystallization in a graphite boat to grow single crystals of a Ge–Si alloy that had an Si content of no higher than 3% and was doped with chalcogens. Since the initial material had *p*-type conductivity and the Ga concentration was ~10^{15} cm^{-3}, the donors were partly compensated. If the compensation factor $K \approx 0.5$, features related to the transitions of the impurity ions to an excited state were observed in the photoconductivity spectra of Ge doped with chalcogens [8]. The addition of silicon led to an increase in the ionization energy.

In Fig. 1, we show the spectral dependence of the photoeffect for $Ge_{0.98}Si_{0.02}$:Te at a temperature of 80 K (curve *2*). The spectrum of a Ge:Te semiconductor without the addition of Si is also shown for comparison. It can be seen that the peak corresponding to the electron transitions from a singly charged ionized state to

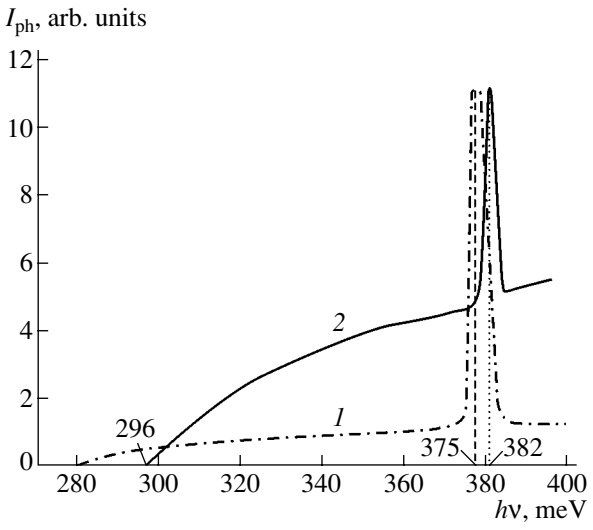

Fig. 1. The photoconductivity spectra for the (*1*) Ge:Te and (*2*) $Ge_{0.98}Si_{0.02}$:Te samples. The spectra were measured at 80 K. For all the samples, the compensation factor was equal to $K \approx 0.5$.

1063-7826/05/3905-0521$26.00 © 2005 Pleiades Publishing, Inc.

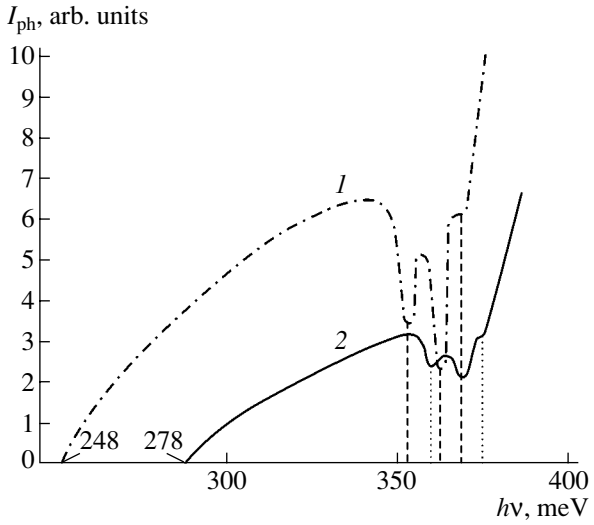

Fig. 2. The photoconductivity spectra for the (*1*) Ge:Se and (*2*) $Ge_{0.985}Si_{0.015}$:Se samples. The spectra were measured at 80 K. The compensation factor was equal to $K \approx 0.5$ for all the samples. The vertical dashed and dotted straight lines indicate the energies that correspond to features in the spectra (from left to right) at $h\nu$ = 353, 360, 362, 368, and 373 meV.

an excited state is shifted by 7 meV to higher energies for the sample with Si (curve *2*), whereas the long-wavelength edge corresponding to the electron transitions from a neutral state to the conduction band is shifted by 16 meV. The introduction of 4.5% of Si into germanium leads to an increase of 30 meV in the ionization energy and, simultaneously, to a shift of the peak by 16 meV with respect to the position of the peak in Ge:Te. Thus, the ionization energy for a neutral tellurium atom changes by 7–8 meV as a result of a 1% variation in the Si content, whereas the variation in the bonding energy amounts to 3.5 meV per 1% of Si.

In Fig. 2, we show the photoconductivity spectrum of $Ge_{0.985}Si_{0.015}$:Se at 80 K (curve *2*). In contrast to tellurium, the electron transitions from the Se^+ ion to excited states manifest themselves as three dips in the spectrum [8]. It can be seen that the introduction of Si leads to a shift of the spectrum to shorter wavelengths and to an increase in the ionization and bonding energies by 30 meV and 7 meV, respectively (cf. curves *1* and *2*); i.e., the ionization energy varies at the rate of (20 meV)/(1% Si), while the bonding energy varies at the rate of approximately (5 meV)/(1% Si).

Thus, the replacement of germanium atoms with silicon atoms does not lead to a radical transformation of the photoconductivity spectrum; rather, only quantitative changes are observed. At the same time, the rate of variation in the transition energy resulting from the introduction of Si into Ge with the selenium impurity is approximately twofold higher than in Ge with the tellurium impurity. This behavior is indicative of structural differences between the impurity centers formed by the chalcogens and can be also caused by the previously ascertained relation of the excited states of selenium ions to the *L* point of the conduction band and those of tellurium ions to the Γ point [2].

REFERENCES

1. H. G. Grimmeiss, L. Montelius, and K. Larsson, Phys. Rev. B **37**, 6916 (1988).
2. A. Yu. Ushakov, N. B. Radchuk, and R. M. Shterengas, Fiz. Tekh. Poluprovodn. (St. Petersburg) **29**, 754 (1995) [Semiconductors **29**, 392 (1995)].
3. H. G. Grimmeiss, Helv. Phys. Acta **56**, 317 (1983).
4. H. G. Grimmeiss, E. Janzen, and B. Skarstam, J. Appl. Phys. **51**, 3740 (1980).
5. E. R. Johnson and S. M. Christian, Phys. Rev. **95**, 560 (1954).
6. N. B. Radchuk and A. Yu. Ushakov, Fiz. Tekh. Poluprovodn. (Leningrad) **16**, 1855 (1982) [Sov. Phys. Semicond. **16**, 1192 (1982)].
7. N. B. Radchuk and A. Yu. Ushakov, Fiz. Tekh. Poluprovodn. (Leningrad) **19**, 749 (1985) [Sov. Phys. Semicond. **19**, 462 (1985)].
8. A. Yu. Ushakov, P. M. Shterengas, L. M. Shterengas, and N. B. Radchuk, Fiz. Tekh. Poluprovodn. (St. Petersburg) **32**, 155 (1998) [Semiconductors **32**, 140 (1998)].

Translated by A. Spitsyn

Semiconductors, Vol. 39, No. 5, 2005, pp. 523–527. Translated from Fizika i Tekhnika Poluprovodnikov, Vol. 39, No. 5, 2005, pp. 552–556.

SEMICONDUCTOR STRUCTURES, INTERFACES, AND SURFACES

Specific Features of Epitaxial-Film Formation on Porous III–V Substrates

A. A. Sitnikova, A. V. Bobyl, S. G. Konnikov, and V. P. Ulin

Ioffe Physicotechnical Institute, Russian Academy of Sciences, Politekhnicheskaya ul. 26, St. Petersburg, 194021 Russia

Submitted September 15, 2004; accepted for publication September 29, 2004

Abstract—Porous GaAs (100) and (111) substrates with nanostructured (~10 nm) surface profiles are obtained in which pores branching in the ⟨111⟩ direction form a dense network with a volume density of ~60% under the surface at a depth of ~(50–100) nm. The surface of the substrates and the structure of GaSb layers grown on these substrates are studied. A decrease of 22% in the lattice-parameter mismatch at the GaSb/GaAs(porous) interface compared with that at the GaSb/GaAs(monolithic) interface is observed. Ideas about the chemical mechanisms of pore formation in III–V crystals are developed, and relations connecting the structure of porous layers to the composition of electrolytes and anodization conditions are established. It is shown that the dependence of the layers' growth rate on lattice elastic strain can be conducive to an enhanced overgrowth of pores and to a transition to planar growth. © *2005 Pleiades Publishing, Inc.*

The use of porous substrates in homoepitaxial and heteroepitaxial technology makes it possible to appreciably reduce internal stresses in the layers grown [1]. At small crystal-lattice mismatches ($f_m = \Delta a/a < 2\%$), it is possible, in a number of cases, to completely localize the mismatch strains arising in a heterostructure within the bulk of the porous material [2]. In this context, it is of interest to study the potential of using porous substrates consisting of silicon and III–V compounds for the epitaxial growth of device-grade heterostructures under conditions in which there is an appreciable mismatch between the crystal-lattice parameters of the substrate and the layer to be grown. An assessment of this potential requires the special features of both the surface structure and the volume of porous substrates to be taken into account when the growth processes and the conditions and character of defect formation in the epitaxial layers are analyzed.

The simplest quantitative model for calculating the distribution of strains in a structure that consists of an epitaxial layer grown on a porous substrate is represented by a film strip with a finite width $2l$. An analytical calculation shows that the stress relaxes appreciably if the ratio between the strip width and its height h is small, $2l/h < 3$ [1, 3]. Moreover, it follows from theoretical calculations that a film with fairly small dimensions in both horizontal directions ($l < l_{\min}$) can be grown to an infinitely large thickness without any dislocations occurring in this film at all. It is important that the substrate takes over most of the strain of the film at the initial stage of growth. This circumstance is confirmed by a comparative calculation for monolithic and porous substrates (see [4]).

In this study, we analyze the effect of porous substrates on an interface structure, strains, and the type and density of extended crystal-lattice defects in the region of a highly mismatched epitaxial heteroboundary ($f_m > 7\%$). In our investigation, we used transmission electron microscopy (TEM). The structures under study were epitaxial GaSb layers grown by MOC-hydride epitaxy (vapor-phase epitaxy from metal–organic compounds) on porous and monolithic GaAs substrates. When analyzing the dynamics of the pores' overgrowth and the transition to planar growth, we took into account the strain dependence of the lateral growth rates for the layer on the pore–film side planes. The porous substrates used in this study were obtained using anodic etching of chemically polished *n*-GaAs wafers with orientations (100), (111)A, and (111)B (here, A stands for Ga and B stands for As). This chemical polishing was accomplished using aqueous HF solutions and similar (in their concentration of HF (2–3 M)) solutions with the addition of iodides [2, 5].

We also studied the anodic behavior of various III–V compounds in aqueous and nonaqueous chalcogenide electrolytes and electrolytes with oxyanions. We studied the microstructure of porous layers that were formed under similar conditions on the surface of crystals oriented differently with respect to the crystallographic axes. In addition, we theoretically studied variations, caused by an increase in the anode bias, in the chemical (the composition and density of adsorption-related coatings) and electrical states (the spatial distribution of the potential) in the region of the semiconductor–electrolyte interphase boundary. A combined analysis of the results obtained allowed us to suggest a new model for the process of anodic pore formation in semiconductors. The main mechanism of this process involves the nucleophilic-substitution reactions that occur between coordination-saturated atoms in the surface layer and anions adsorbed chemically by the surface. Figure 1 illustrates the course of the recurring

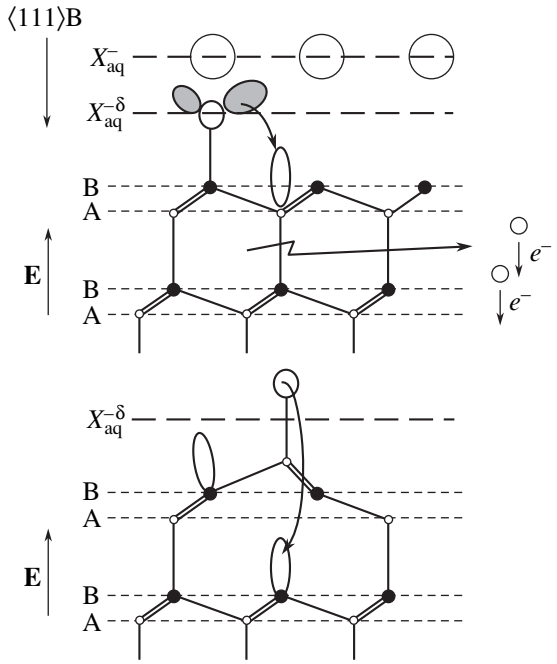

Fig. 1. A schematic representation of the cycles of the nucleophilic-attack reactions that lead to the formation of the porous-layer spatial structure.

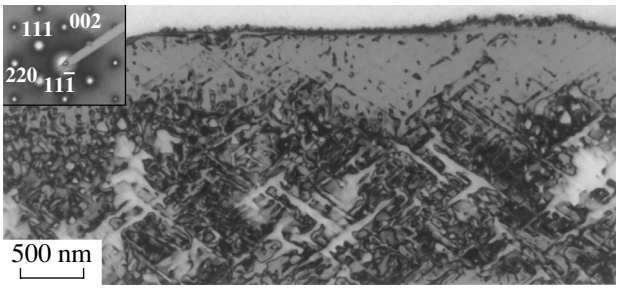

Fig. 2. An image of the section of a porous GaAs (110) layer with the pores aligned along the [111] direction. The image was obtained using a transmission electron microscope (TEM). The electron-microdiffraction pattern is shown in the inset, and the indices of the diffraction reflections are indicated.

cycles of the above reactions, which include the nucleophilic attack of the anions adsorbed at the outer atomic layer on the antibonding $(sp^3)^*$ orbitals of the crystal lattice. The transport of the nucleophilic particles (anions) from the solution to the newly formed crystal surface occurs through a layer of separated reaction products, which act as a solid electrolyte. The role of an electric field **E** in the initiation of heterogeneous reactions amounts to bringing the energy levels of electrons at the occupied antibonding orbitals of the adsorbed anions and at unoccupied orbitals of the atoms in the lattice of a semiconductor crystal into proximity. Since the network of chemical bonds is continuous at the crystal surfaces, the probability of nucleophilic-substitution reactions occurring on these surfaces as a set of separate and independent events is found to be lower than the probability of the same reactions occurring according to a cooperative mechanism of synchronous activation within fairly large areas of a continuous adsorption layer with a closed and compact contour. It is this circumstance that accounts for the fluctuating character of the distribution of the primary etching areas over the homogeneous crystal surfaces (the entries to the pores) and the relation of these areas to the anode bias. The fraction of the surface area that is unaffected in the initial stage of the electrochemical process is found to be electrically shunted by current channels of the pores and is not involved in further interaction with the solution. The involvement of the antibonding $(sp^3)^*$ orbitals of the III–V atomic lattice in the formation of transitional complexes accounts for the observed anisotropy of the pore propagation along the ⟨111⟩ directions. In Fig. 2, we show a TEM image of the section, transverse to the (110) plane, of the porous GaAs substrate. It can easily be seen that the channels along which the front of the pore-formation reaction propagates into the crystal bulk are oriented along the ⟨111⟩ directions. The pores propagating along these directions have a triangular cross section and are bounded by surfaces that are close to the (211) orientation. The inset in Fig. 2 shows the corresponding microdiffraction pattern, in which only the reflections related to point defects are seen. This observation indicates that the sample is a single crystal and that it contains no polycrystalline or mosaic inclusions. Two sets of four equivalent directions (⟨111⟩A and ⟨111⟩B) exist in polar crystals with a sphalerite structure. Porous layers with a pronounced anisotropic structure are formed by pores that propagate only along the directions of one of the above types in accordance with the direction corresponding to the lowest activation energy of the nucleophilic attack. The use of the effect of selective adsorption of various anions by the atoms of III and V sublattices made it possible, in the case of GaAs, to arbitrarily vary the polarity of the ⟨111⟩ pores that propagate in the crystal by varying the electrolyte composition. By selecting the electrolyte composition and polarization conditions, we can also affect the size and density of the pore openings and vary the intensity of their branching beneath the crystal surface. By varying the anionic composition of the solution or increasing the voltage across the cell, we can achieve a transition from anisotropic pore propagation along the ⟨111⟩ directions to the propagation of pores along the electric-field lines without any pronounced relation to the crystallographic direction (this is the case for InP in chloride and bromide aqueous solutions and for GaP in fluoride electrolytes). This effect is probably caused by the fact that the probabilities of the pores branching along the different polar directions ⟨111⟩ become nearly equal to each other, which leads to superposition of the pore motion along the A and B directions. An exception is porous layers that are formed as a result of

the anodization of lightly doped GaP crystals in fluoride electrolytes at voltages > 25 V. In the context of the model suggested, this effect is attributed to a variation in the electronic structure of the transitional complexes that are involved in nucleophilic-substitution reactions and acquire the d^2sp^3 configuration.

The possibility of forming a specific geometric pattern of pores opens up new opportunities for the use of porous materials as "soft" substrates in the epitaxial growth of heterostructures by various methods [6–8]. As an example, Fig. 3 shows TEM comparative data on the structure of GaSb/GaAs epitaxial layers that have a thickness of 1.5–2 μm and are grown under identical conditions on (Fig. 3a) monolithic (100) substrates, (Fig. 3b) porous (100) substrates that have slightly branching pores with large (~150 nm) high-density (10^9 cm^{-2}) entrance holes, and (Fig. 3c) porous (111)B substrates that have a surface with a regular microprofile and a low density (10^7–10^8 cm^{-2}) of small-diameter (60–80 nm) pores that branch intensely along the ⟨111⟩A directions under the crystal surface. According to measurements of the microdiffraction patterns in the heteroboundary region, the mismatch between the lattice parameters of the film and the substrate amounts to 7.4, 7.0, and 5.8%. Thus, in the case of growth on the porous substrate, we observe a 22% decrease in the mismatch between the lattice parameters of the film and substrate compared with the value of the mismatch when the film is grown on the monolithic substrate. This result can be indicative of the appearance of distributed elastic strains in a fairly wide region of the substrate's porous material where it adjoins the heteroboundary. The main technological achievement consists in an appreciable decrease in the concentration of extended defects in the epitaxial film grown on the substrate with a high density of relatively small-diameter pores forming a regular three-dimensional network with branching along the ⟨111⟩A directions. The evident advantage of porous substrates stimulated a more detailed consideration of the elastic mechanisms joining the surfaces of the modified substrates to those of the growing film. An axonometric image of the porous GaAs surface is shown in Fig. 4. The image was obtained using atomic-force microscopy and reveals a complex profile that exhibits a spread in height of ~10 nm and consists of joined homogeneous hillocks with dimensions of ~100 nm in tangential directions. In addition, deep craters with diameters of 60–80 nm, which correspond to regions of stable development of the chemical interactions (openings of the pores), can be recognized in the images. An overgrowth of this epitaxial-film profile can be divided into two independent processes: (i) joining of the crystal planes above the pore openings and (ii) formation of a continuous layer with a low concentration of defects on the surface with a nanoprofile.

It is evident from the results reported that the growth of a continuous film becomes possible if the lateral overgrowth of both the shallow profile and deep openings of

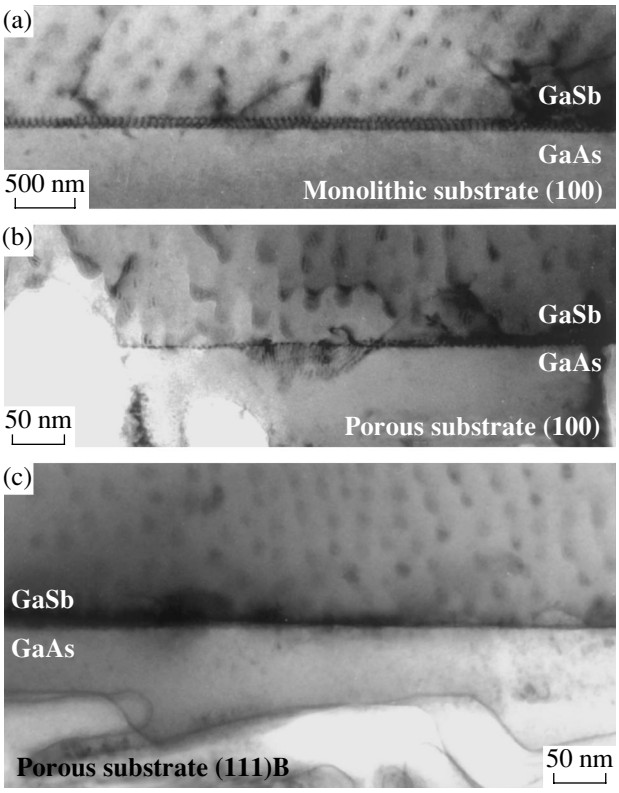

Fig. 3. TEM images of the (110) section for the epitaxial GaSb/GaAs(100) structures grown on (a) a monolithic (100) substrate, (b) a porous (100) substrate with large-diameter openings (~150 nm) to the weakly branching pores with a density of ~10^9 cm^{-2}, and (c) a porous (111)B substrate with a regular surface nanoprofile and a low density (~10^7 cm^{-2}) of small-diameter (~(60–80) nm) pores that branch actively along the [111]A direction beneath the surface.

the pores take place in the initial stage of the epitaxial process. There is a trivial process that is related to the arrival of the growth components from the front surface to the lateral faces of the pores. We can use a model of two-component diffusion from a source that occurs over a plane and is accompanied by the formation of immobile complexes to describe the growth process [9].

We now consider the strain dependence of the normal-growth parameters if the atoms arrive from a gaseous medium or melt. In [10], the following expression was derived for the rate V of growth on a crystal surface that exhibits kinks separated by the distance λ:

$$V \approx \frac{\Delta T}{A}\left(\frac{a}{\lambda}\right)^2 a\nu\frac{\Delta H}{kT_{ml}}\exp\left(-\frac{\Delta H}{kT_{ml}}\right)\exp\left(-\frac{E}{kT}\right). \quad (1)$$

Here, ΔT is the supercooling at the crystallization front, E is the potential barrier at the phase boundary, ΔH is the heat of the phase transition, a is the lattice constant, and ν is the frequency of the atoms' vibrations ($\nu \approx 10^{13}$ cm^{-1}). Since $\Delta H \gg E$, it can be assumed, in the simplest case, that the heat of the phase transition

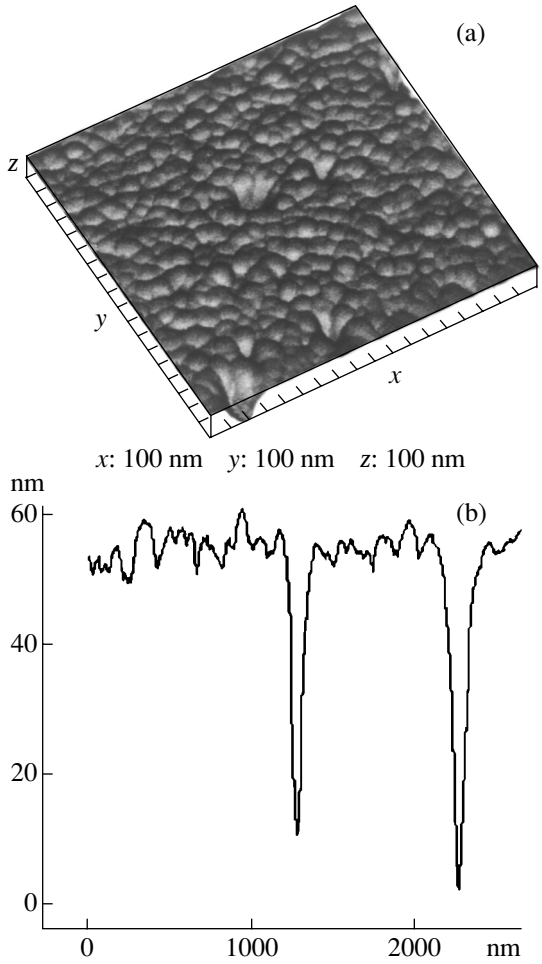

Fig. 4. (a) An axonometric TEM image of the surface of the porous GaAs (100) substrate and (b) the depth profile of the surface. The data were obtained using an atomic-force microscope.

depends linearly on the strain ε: $\Delta H = \Delta H_0 + A\varepsilon$, where $\varepsilon = \Delta a/a$ and the value of A can range from several electronvolts to tens of electronvolts [11]. The value of $\Delta H/kT$ varies from 3 to 20, depending on the type of deposited material, the phase and chemical composition of the growth medium, and the parameters of the epitaxial process. Since the crystallization front bends during growth, the value of λ depends on the angle φ of a surface with closely packed lattice planes. For small values of φ, we have

$$\lambda = [1 - 1/2(\lambda_0/a)^2\varphi^2]\lambda_0. \quad (2)$$

Here, λ_0 is the distance between the kinks at $\varphi = 0$ (these kinks arise owing to thermal fluctuations) and $\lambda_0 = a[\exp(\omega/kT) + 2]/2$, where ω is the formation energy of a kink. For large values of φ,

$$\lambda = \alpha(\sin\varphi)^{-1}. \quad (3)$$

Concerning the value of ω, we note that, at $\omega/kT < 0.7$, the surface is represented by a random assembly of

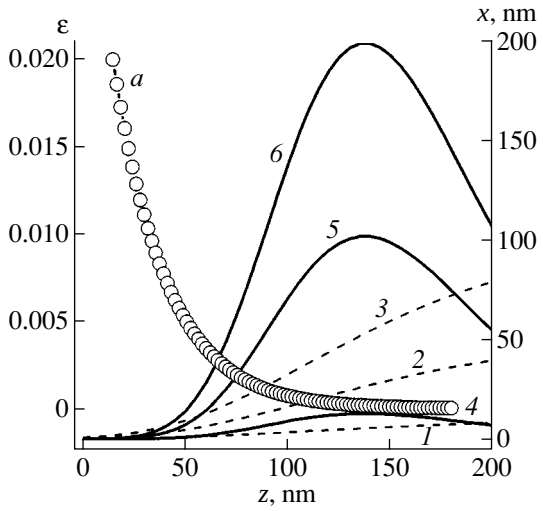

Fig. 5. (*a*) Distributions of the strain ε over the side plane of the strip and positions of the lateral-growth front after (*1*) 2, (*2*) 10, and (*3*) 30 s at $a/\lambda = 30$ and in (*4*) 2, (*5*) 4, and (*6*) 5 s with the dependence of λ on φ taken into account.

clusters. At the same time, at large values of ω/kT, the mean free path of the adatoms becomes smaller than λ; as a result, the island growth mechanism, for which expression (1) is not valid, comes into effect.

In order to describe the distribution of strain in a strip with the width $2l$, we use the following expression derived in the context of the two-dimensional model:

$$\varepsilon = f_m \exp\left(-\frac{\pi\gamma^{1/2}z}{2l}\right)\cos(\pi x/2l). \quad (4)$$

Here, z and x are the distances from the heteroboundary and from the midplane of the strip, respectively; $\gamma = C_{11}/C_{44} \approx 2$; and f_m is the mismatch parameter ($f_m = (a_f - a_{sub})/a_{sub}$, where a_f and a_{sub} are the lattice parameters of the film and substrate). The last multiplier in (4) is caused by the boundary condition, i.e., the absence of strain at the side planes. However, since this condition is violated at the growth temperature, owing to appreciable thermal fluctuations and a high density of kinks, this multiplier does not vanish at $x = l$. In Fig. 5, we show the results of calculations of both the strain distribution at the side of the strip and the position of the lateral-growth front. The value of the last multiplier in (4) was taken as being equal to 0.2, which corresponds to its averaged value at $0.1l$ of the layer from the side plane. We used the following values for the other parameters: $\Delta T/T = 1/30$, $a = 0.6$ nm, $\Delta H/kT_{ml} = 20$, $A = 25$ eV, $f_m = 0.1$, and $2l = 300$ nm. At $\varepsilon = 0$, we can use expression (1) to find that $V = 5$ nm/s. It can be seen from Fig. 5 that, in the case of growth on porous substrates of the (111)B type, the position of the lateral-growth front (curve *6*) is in good qualitative agreement with the profile of the pore dome shown in Fig. 3. It is worth noting that the performed analysis is, in our opinion, very important in the consideration of the mecha-

nism of growth on a porous substrate; however, this mechanism should be considered only as the first stage. The next stages should include the following:

(i) an analysis of the local inhomogeneities in the field of elastic stresses in thin epitaxial layers crystallized on the surface with vicinal hillocks of submicrometer sizes;

(ii) an estimation of the effects of the stresses' modulation on the formation and structure of the network of misfit dislocations at the heteroboundary; and

(iii) an analysis of the elastic stresses in a system that consists of a ~50-nm-thick slightly damaged surface layer that covers the loose volume of a porous substrate (with the porosity amounting to ~60%) and an epitaxial layer with a thickness equal to or smaller than the critical thickness.

Thus, the use of porous substrates brings about an appreciable decrease in the density of extended defects at the heteroboundary. The optimal porous substrates are those with a homogeneous nanostructured surface and a low density of pore openings (10^7 cm^{-2}) in combination with a high density network of small-diameter pores (20–60 nm) formed at a depth of ~(50–100) nm owing to an active branching along the ⟨111⟩A directions. In order to interpret the process of pore overgrowth and the transition to planar growth, we should take into account the strain dependence of the layer's lateral-growth rate at the pore–film boundaries. The results obtained make it possible to conclude that control over the structure parameters of porous crystals opens up new prospects for using porous materials in the heteroepitaxial growth of layers by various methods (molecular-beam epitaxy, MOC-hydride epitaxy, and so on) in the presence of an appreciable mismatch between the corresponding lattice parameters.

REFERENCES

1. S. Luryi and E. Suhir, Appl. Phys. Lett. **49**, 140 (1986).
2. V. V. Mamutin, V. P. Ulin, V. V. Tret'yakov, *et al.*, Pis'ma Zh. Tekh. Fiz. **25** (1), 3 (1999) [Tech. Phys. Lett. **25**, 1 (1999)].
3. A. Atkinson, S. C. Jain, and A. H. Harker, J. Appl. Phys. **77**, 1907 (1995).
4. A. Fischer and H. Richter, J. Appl. Phys. **75**, 657 (1994).
5. I. N. Arsent'ev, M. V. Baĭdakova, A. V. Bobyl', *et al.*, Pis'ma Zh. Tekh. Fiz. **28** (17), 57 (2002) [Tech. Phys. Lett. **28**, 735 (2002)].
6. S. Guha, A. Madhukar, and Li Chen, Appl. Phys. Lett. **56**, 2304 (1990).
7. M. Mynbaeva, S. E. Saddow, G. Melnychuk, *et al.*, Appl. Phys. Lett. **78**, 117 (2001).
8. S. Jin, H. Bender, L. Stalmans, *et al.*, J. Cryst. Growth **212**, 119 (2000).
9. S. V. Bulyarskiĭ and V. I. Fistul', *Thermodynamics and Kinetics of Interacting Defects in Semiconductors* (Nauka, Moscow, 1997), Chap. 6, p. 254 [in Russian].
10. A. A. Chernov, E. I. Givargizov, Kh. S. Bagdasarov, *et al.*, in *Modern Crystallography*, Vol. 3: *Crystal Growth*, Ed. by B. K. Vaĭnshteĭn, A. A. Chernov, and L. A. Shuvalov (Nauka, Moscow, 1980; Springer, Berlin, 1984), Chap. 1.
11. A. V. Bobyl, M. E. Gaevskii, S. F. Karmanenko, *et al.*, J. Appl. Phys. **82**, 1274 (1997).

Translated by A. Spitsyn

Semiconductors, Vol. 39, No. 5, 2005, pp. 528–532. Translated from Fizika i Tekhnika Poluprovodnikov, Vol. 39, No. 5, 2005, pp. 557–562.

SEMICONDUCTOR STRUCTURES, INTERFACES, AND SURFACES

p^+-Si–n-CdF_2 Heterojunctions

N. T. Bagraev*^, L. E. Klyachkin*, A. M. Malyarenko*, A. I. Ryskin, and A. S. Shcheulin****

**Ioffe Physicotechnical Institute, Russian Academy of Sciences, Politekhnicheskaya ul. 26, St. Petersburg, 194021 Russia*

^e-mail: impurity.dipole@mail.ioffe.ru

***Vavilov State Optical Institute, Birzhevaya liniya 12, St. Petersburg, 199034 Russia*

Submitted November 4, 2004; accepted for publication November 25, 2004

Abstract—Boron diffusion and the vapor-phase deposition of silicon layers are used to prepare ultrashallow p^+–n junctions and p^+-Si–n-CdF_2 heterostructures on an n-CdF_2 crystal surface. Forward portions of the I–V characteristics of the p^+–n junctions and p^+-Si–n-CdF_2 heterojunctions reveal the CdF_2 band gap (7.8 eV), as well as allow the identification of the valence-band structure of cadmium fluoride crystals. Under conditions in which forward bias is applied to the p^+-Si–n-CdF_2 heterojunctions, electroluminescence spectra are measured for the first time in the visible spectral region. *© 2005 Pleiades Publishing, Inc.*

1. INTRODUCTION

The production of wide-gap semiconductor materials and heterostructures for developing emitters and photodetectors in wide ultraviolet and visible spectral ranges, as well as high-speed logic units for computer facilities and next-generation displays, is an important area of semiconductor nanoelectronics and optoelectronics. A promising wide-gap semiconductor for these purposes is cadmium fluoride (CdF_2), whose band gap (7.8 eV) is wider than that of diamond by a factor of 1.5 [1–5]. Nevertheless, despite the technology's simplicity and reproducibility, crystalline CdF_2 has remained, until recently, out of view of semiconductor physics due to its unipolar (*n*-type) conductivity. In this study, the possibility of overcoming this restriction using boron diffusion is shown for the first time. This process allows the production of ultrashallow p^+–n junctions on the n-CdF_2 crystal surface. Boron diffusion is also used to produce p^+-Si–n-CdF_2 heterostructures under the conditions of vapor-phase polysilicon deposition onto the n-CdF_2 crystal surface, which is facilitated by the close lattice constants of silicon and cadmium fluoride (5.43 and 5.46 Å, respectively) and their identical electron affinities (4 eV) [1–5].

2. EXPERIMENTAL

Ultrashallow p^+–n junctions on the surface of an n-CdF_2 crystal 1.0 mm thick were prepared by vapor-phase doping with boron. Since CdF_2 crystals are wide-gap insulators, *n*-type conductivity is attained by preliminary doping with Group III impurities, e.g., yttrium, gallium, or indium, followed by thermochemical coloration [6, 7]. It should be noted that this introduction of Group III impurities is not sufficient for producing *n*-type conductivity, since shallow donors are compensated by excess interstitial fluorine atoms.

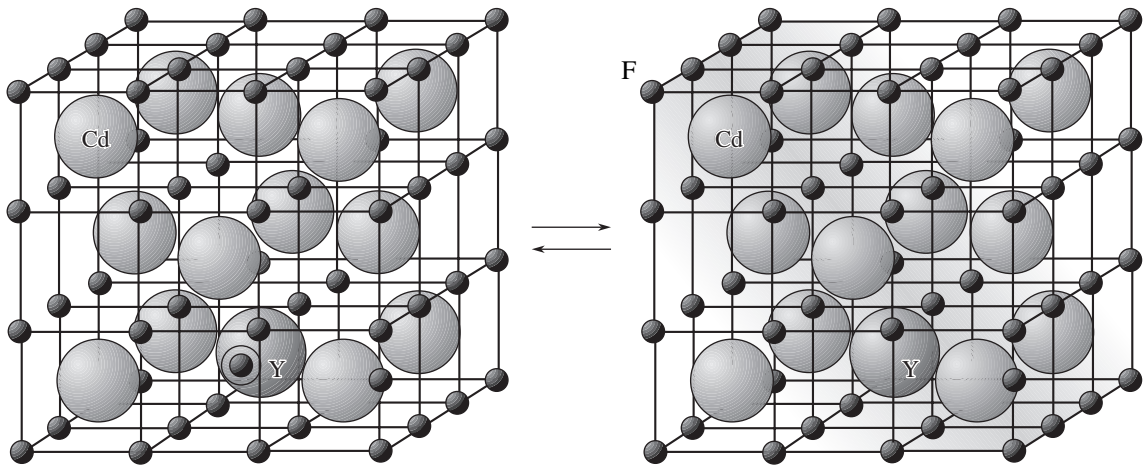

Fig. 1. The crystallographic structure of CdF_2. The arrows relate to thermochemical coloration and the subsequent by decoloration due to yttrium donor centers, which are accompanied by the removal and arrival of excess fluorine atoms, respectively.

1063-7826/05/3905-0528$26.00 © 2005 Pleiades Publishing, Inc.

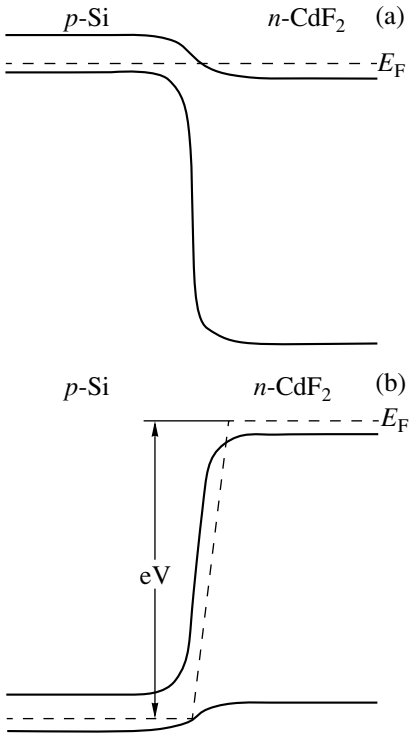

Fig. 2. A band diagram of the p^+-Si–n-CdF_2 heterojunction at zero (a) and forward (b) biases.

Therefore, further thermochemical treatment in a reduction atmosphere of metal vapor or hydrogen is required to remove these atoms, which results in crystal coloration due to local donor levels arising in the CdF_2 band gap (Fig. 1).

One of the optimum ways to achieve the p-type conductivity of CdF_2 crystals seems to be the substitution of lattice-site fluorine with boron, which, in this study, was carried out using vapor-phase boron diffusion. We note that a partial decoloration of the n-CdF_2 crystal during the doping with boron, accompanied by its transition to a semi-insulating state, was observed. Therefore, to restore the n-type conductivity of the CdF_2 crystal, additional thermochemical coloration was used after the vapor-phase doping. This technique made it possible to produce, for the first time, ultrashallow p^+ diffusion boron profiles at the surface of an n-CdF_2 crystal.

The p^+-Si–n-CdF_2 heterostructures were produced by the vapor-phase deposition of boron-doped silicon layers on the n-CdF_2 crystal surface. Variation in the deposition time made it possible to grow silicon layers 0.1–0.25 μm thick. The deposition temperature depended on the hydrogen and nitrogen contents in the chamber. It was found that thermally colored CdF_2 crystals were annealed during the deposition of p-type silicon layers, as in the case of vapor-phase doping with boron. This process transformed the crystals from the n-type conductivity to a semi-insulating state. Therefore, the above-described additional thermochemical coloration of the produced structures was carried out,

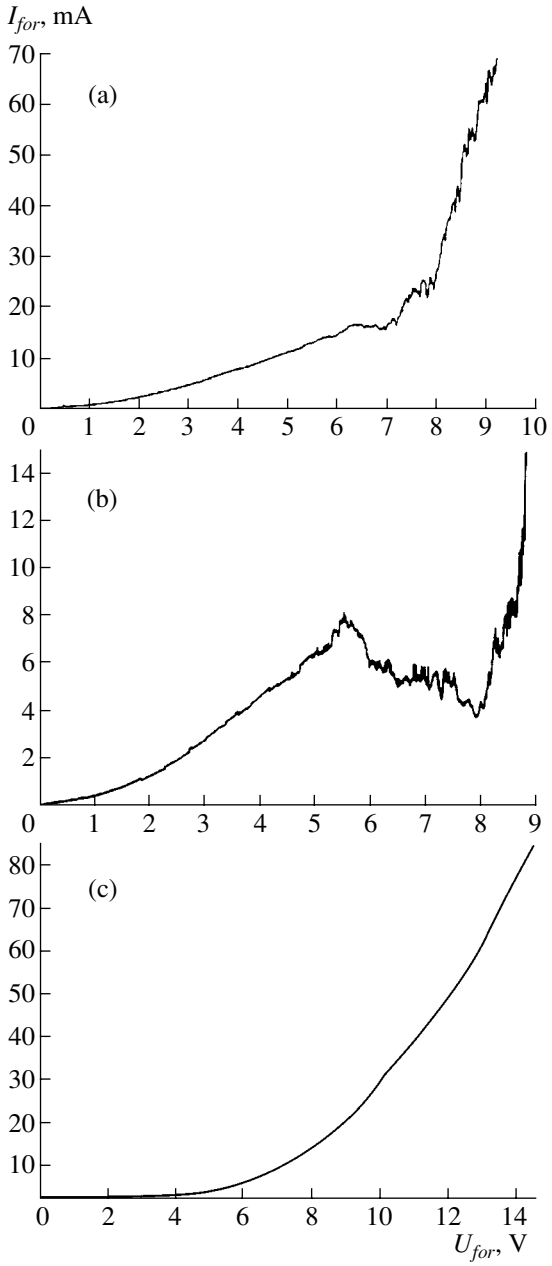

Fig. 3. Forward portions of the I–V characteristic of the p^+–n junction on (a) the CdF_2 surface and (b, c) p^+-Si–n-CdF_2 heterojunctions at T = 300 (a, b) and 77 K (c).

which led to the CdF_2 crystals being transformed from the intrinsic conductivity into the n-type state. The above-listed sequential operations allowed the production of p^+-Si–n-CdF_2 heterostructures (Fig. 2a) for the first time.

Contacts to the boron-doped n-CdF_2 crystal surface and heavily boron-doped silicon layers grown by vapor-phase deposition were formed using gold deposition. A study of the I–V characteristics showed that the surface barriers were almost completely absent in the ohmic contacts [8]. Contacts to the rear surface of the n-CdF_2 crystal were formed by a low-temperature

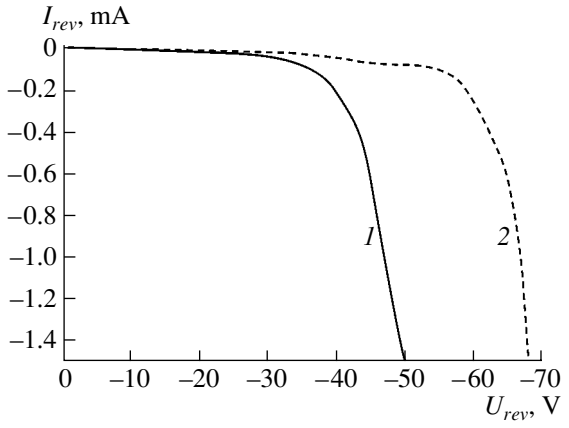

Fig. 4. Reverse portions of the *I–V* characteristic of the p^+-Si–*n*-CdF_2 heterojunctions grown by the vapor-phase deposition of doped polycrystalline silicon onto (*1*) weakly and (*2*) strongly colored cadmium fluoride substrates.

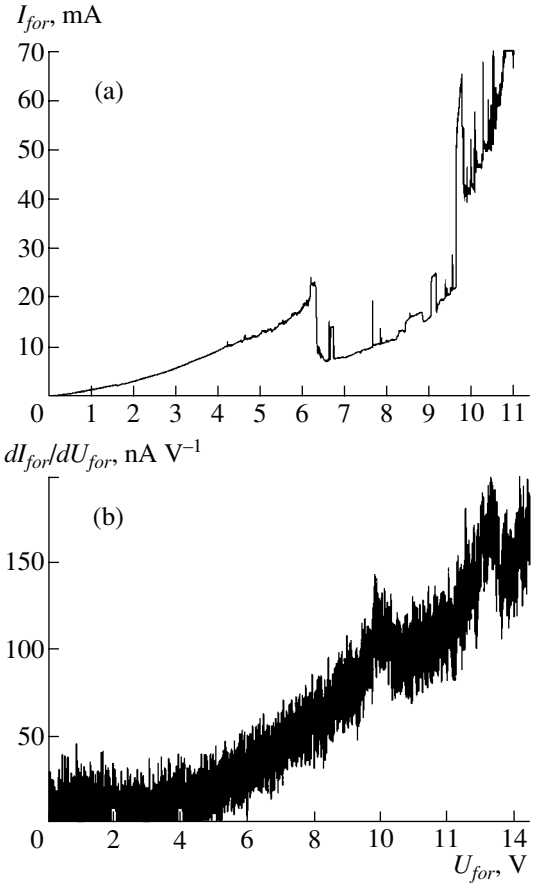

Fig. 5. Forward portions of the *I–V* characteristic of the p^+-Si–*n*-CdF_2 heterojunction, measured after a preliminary exposure to light in the IR wavelength range (1–27 μm), which demonstrate the structure of the CdF_2 valence band. T = 300 (a) and 77 K (b).

vapor-phase deposition of ytterbium silicide. The existence of p^+–*n* junctions on the CdF_2 surface and p^+-Si–*n*-CdF_2 heterojunctions was revealed by analyzing the *I–V* characteristics (Figs. 3a, 3b). The forward portions of the *I–V* characteristics are indicative of the existence of the CdF_2 band gap (7.8 eV), which controls the formation of the p^+–*n* junction and heterojunction. The stability of the electrical characteristics of the produced p^+–*n* junctions and heterojunctions was studied in relation to the temperature and duration of the vapor-phase doping and deposition, as well as the atmosphere composition (vacuum, argon, and nitrogen). It was found that pronounced thermal coloration of *n*-CdF_2, in comparison to weakly pronounced coloration, results in the lowest leakage current of the grown structures (Fig. 4).

3. RESULTS AND DISCUSSION

Not only are the forward portions of the *I–V* characteristics of p^+-Si–*n*-CdF_2 heterojunctions indicative of the CdF_2 band gap (7.8 eV), but they also exhibit a region of negative differential resistivity (Fig. 3b). The latter is apparently caused by a decrease in the probability of hole tunneling from the silicon valence band to the CdF_2 conduction band as the forward voltage increases (Fig. 2b). This assumption is confirmed by a change in the shape of the *I–V* characteristic as the temperature decreases, which demonstrates the suppression of the negative differential resistivity due to electron freezing at the donor levels in *n*-CdF_2 (Fig. 3c).

The use of preliminary exposure to light in the IR wavelength range (1–27 μm) made it possible to increase the slope of the negative differential resistivity, which is associated with ionization of the shallow donors in the *n*-CdF_2 crystal (Fig. 5a) [4, 5]. Furthermore, the photoionization of the shallow donors results in a sharp increase in the current at a forward bias due to an increase in the lifetime of the injected holes passing through the 1.0-mm-thick CdF_2 crystal (Fig. 5a). As a result of this increase in *p*-type conductivity and the identical electron affinities of silicon and cadmium fluoride (4 eV) [8], the study of the forward portions of the *I–V* characteristic made it possible to determine the valence band structure of the CdF_2 crystal (Figs. 5a, 5b).

The measured high-resolution *I–V* characteristics are consistent with the calculated energy structure of the valence band of cadmium fluoride [9–11], as well as with the density of states in this band, determined using optical [12] and photoelectron spectroscopy [13–15] (Fig. 6). In particular, the excitonic peak and direct transitions Γ_{15}–Γ_1 and Γ_{25}–Γ_1 manifest themselves at 7.87, 8.5, and 9.98 eV, respectively, whereas the X_5–Γ_1 transition occurs at 8.05 eV. Despite the fact that the excitonic peak is observed at somewhat higher energies than could be expected from the data of optical measurements and photoelectron spectroscopy [12, 14], the results obtained are consistent with the polaron model if the measured Γ_{15}–Γ_1 energies are taken into account.

The peaks at 9.78, 10.12, and 10.19 eV are apparently caused by the contribution of the L_3, L_2, and L_1

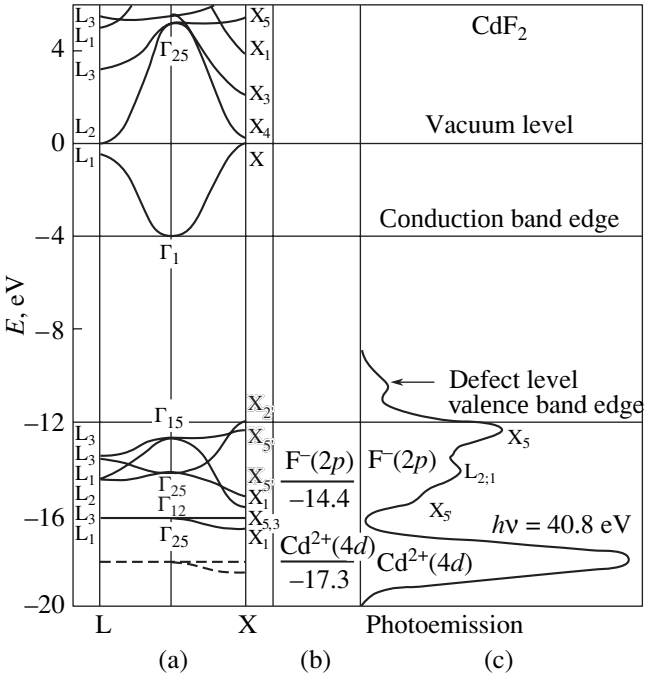

Fig. 6. A band diagram of the cadmium fluoride crystal [13]: (a, b) states of the CdF_2 valence band and (c) the density of states according to the photoemission measurement data [13].

states of the CdF_2 valence band, while the transitions arising due to the X_5 and X_1 states of the CdF_2 valence band are resolved in the energy range 10.9–11.2 eV. In turn, $Cd^{2+}(4d)$ states are observed at the forward biases of 13.27 and 13.75 eV (Fig. 5b). The observed *d*-state splitting is probably due to spin–orbit splitting or splitting induced by the crystal field [12, 14, 15].

The feasibility of tunnel spectroscopy in relation to the CdF_2 valence band in the produced heterojunctions and p^+–n junctions is apparently indicative of a ballistic transport mechanism for the holes injected into n-CdF_2. To determine the parameters of this hole transport, we studied the *I–V* characteristics over the p^+–n junction plane and Si–CdF_2 interface. The measurements yielded an unexpected result: the metal conductivity of quasi-two-dimensional hole gas (Fig. 7). These data indicate the formation of a two-dimensional layer, whose properties are close to those of a hypothetical CdB_2 compound, which should apparently feature *p*-type conductivity. Quasi-one-dimensional fluctuations of this compound toward n-CdF_2 promote the formation of short quantum wires, along which the electric field is localized as a forward voltage is applied. This effect is responsible for the induction of the ballistic transport of holes in the naturally formed anionic sublattice (Fig. 8). Hole tunneling into the valence band of cadmium fluoride through a two-dimensional metal depends on the band structure of the latter, which results in peaks at 6.84 and 6.92 eV in the forward portion of the *I–V* characteristic at energies lower than the CdF_2 band gap (Fig. 5a).

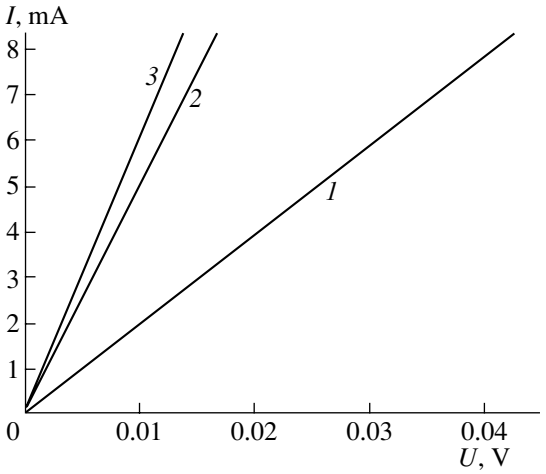

Fig. 7. *I–V* characteristics in the p^+–n junction plane on the n-CdF_2 surface at (*1*) 300, (*2*) 77, and (*3*) 4.2 K.

Studies of the photoluminescence and electroluminescence of the produced p^+-Si–n-CdF_2 heterojunctions in the infrared spectral region, carried out using an IFS-115 IR Fourier spectrometer, indicated the formation of microcavities embedded into the system of self-assembled silicon nanostructures that form the p^+-Si layer deposited from the vapor phase. Under the conditions in which a forward bias is applied to the produced p^+-Si–n-CdF_2 heterojunctions, the electroluminescence spectra in the visible wavelength region were measured for the first time (Fig. 9). These spectra arise due to radiative recombination of the holes and electrons injected at the Si–CdF_2 interface.

4. CONCLUSION

Ultrashallow p^+–n junctions on the surface of n-CdF_2 crystals and p^+-Si–n-CdF_2 heterostructures were produced using boron diffusion and the vapor-phase deposition of silicon layers onto the n-CdF_2 surface. It is shown that thermally colored CdF_2 crystals were annealed during vapor-phase doping and deposition, which transformed them from *n*-type conductivity into a semi-insulating state. Due to a subsequent coloration, CdF_2 crystals were again transformed from the intrinsic conductivity into *n*-type conductivity.

The study of the reverse and forward portions of the *I–V* characteristics made it possible to establish the formation of ohmic contacts on the surface of heavily doped *p*-type silicon layers and n-CdF_2, which exhibit an almost total absence of surface barriers.

The forward portions of the *I–V* characteristics of the p^+–n junctions and p^+-Si–n-CdF_2 heterojunctions indicate the presence of the CdF_2 band gap (7.8 eV). The *I–V* characteristics of the p^+-Si–n-CdF_2 heterojunctions also exhibit a region of negative differential resistivity, which is caused by the existence of a degenerate hole gas at the Si–CdF_2 interface.

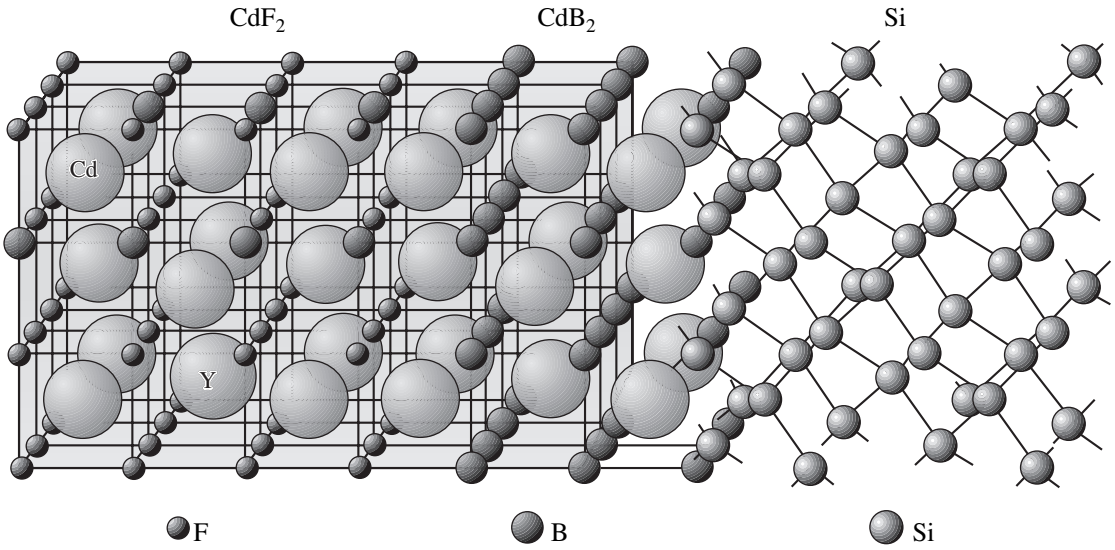

Fig. 8. The structure of the p^+-Si–n-CdF_2 heterojunction with a two-dimensional CdB_2 layer, whose fluctuations penetrate into n-CdF_2.

The study of the forward portions of the *I–V* characteristics of the p^+–n junctions and p^+-Si–n-CdF_2 heterojunctions made it possible to clarify the valence-band structure of cadmium fluoride crystals, which seems to manifest itself due to the ballistic transport of holes injected in the n-CdF_2 volume. The observed high-resolution *I–V* characteristic is in good agreement with the data on the CdF_2 valence-band structure, which were obtained using optical [12] and photoelectron [13–15] spectroscopy.

Under conditions in which a forward bias was applied to the grown p^+-Si–n-CdF_2 heterojunctions, electroluminescence spectra were measured in the visible wavelength region for the first time. This luminescence arises due to radiative recombination of the holes and electrons injected from the Si–CdF_2 interface.

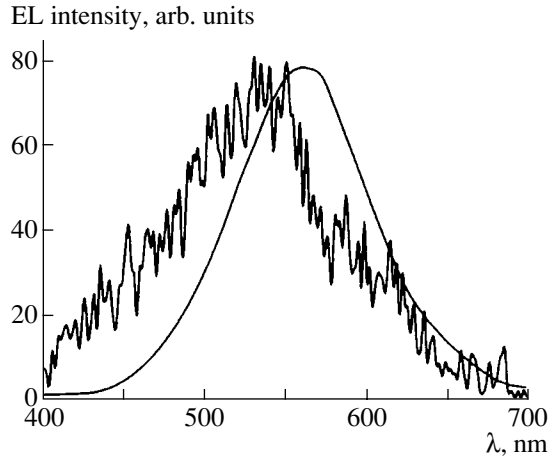

Fig. 9. The electroluminescence spectrum at a forward bias of the p^+-Si–n-CdF_2 heterojunction (the forward current is ~90 mA). The solid curve is the spectral characteristic of the human eye.

ACKNOWLEDGMENTS

This study was supported by the International Science and Technology Center, project no. 2136.

REFERENCES

1. F. Trautweiler, F. Moser, and R. P. Khosla, J. Phys. Chem. Solids **29**, 1869 (1968).
2. F. Moser, D. Matz, and S. Lyu, Phys. Rev. **182**, 808 (1969).
3. J. M. Langer, T. Langer, G. L. Pearson, *et al.*, Phys. Status Solidi B **66**, 537 (1974).
4. S. A. Kazanskii, D. S. Rumyantsev, and A. I. Ryskin, Phys. Rev. B **65**, 165214 (2002).
5. A. I. Ryskin, A. S. Shcheulin, B. Koziarska, *et al.*, Appl. Phys. Lett. **67**, 31 (1995).
6. J. D. Kingsley and J. S. Prener, Phys. Rev. Lett. **8**, 315 (1962).
7. J. S. Prener and J. D. Kingsley, J. Chem. Phys. **38**, 667 (1963).
8. J. Garbarczyk, B. Krukowska-Fulde, T. Langer, and J. M. Langer, J. Phys. D **11**, L17 (1978).
9. J. P. Albert, C. Jouanin, and G. Gout, Phys. Rev. B **16**, 4619 (1977).
10. N. V. Starostin and M. P. Shepilov, Fiz. Tverd. Tela (Leningrad) **17**, 822 (1975) [Sov. Phys. Solid State **17**, 523 (1975)].
11. V. K. Bashenov, I. Bauman, and V. V. Timofeenko, Phys. Status Solidi B **81**, K55 (1977).
12. C. Raisin, J. M. Berger, S. Robin-Kandare, *et al.*, J. Phys. C **13**, 1835 (1980).
13. B. A. Orlowdki and J. M. Langer, Acta Phys. Pol. A **63**, 107 (1983).
14. B. A. Orlowski and J. M. Langer, Phys. Status Solidi B **91**, K53 (1979).
15. R. T. Poole, J. A. Nicholson, J. Liesegang, *et al.*, Phys. Rev. B **20**, 1733 (1979).

Translated by A. Kazantsev

Semiconductors, Vol. 39, No. 5, 2005, pp. 533–538. Translated from Fizika i Tekhnika Poluprovodnikov, Vol. 39, No. 5, 2005, pp. 563–568.

SEMICONDUCTOR STRUCTURES, INTERFACES, AND SURFACES

Injection Currents in Narrow-Gap ($Pb_{1-x}Sn_xTe$):In Insulators

A. N. Akimov, V. G. Erkov, A. E. Klimov^, E. L. Molodtsova, S. P. Suprun, and V. N. Shumsky

Institute of Semiconductor Physics, Siberian Division, Russian Academy of Sciences, Novosibirsk, 630090 Russia

^e-mail: klimov@thermo.isp.nsc.ru

Submitted September 7, 2004; accepted for publication September 17, 2004

Abstract—The low-temperature current–voltage characteristics of narrow-gap ($Pb_{1-x}Sn_xTe$):In have been studied experimentally and calculated for a wide range of electric fields. It is shown that the obtained data are satisfactorily described in terms of a space-charge-limited current model in the presence of traps. The concentration and energy depth of the traps have been estimated. © *2005 Pleiades Publishing, Inc.*

1. INTRODUCTION

There have been a number of studies of ($Pb_{1-x}Sn_xTe$):In (lead tin telluride LTT:In) solid solutions over the years. In particular, a great deal of attention has been paid to the study of the so-called insulator state, which is observed in a certain range of LTT:⟨In⟩ compositions, and the persistent photoconductivity observed at low temperatures ($T \lesssim 20$–30 K). The insulator state is related to Fermi level stabilization at the In level, which, in this case, lies near the mid-gap. Several models have been offered to explain the long-term relaxation of the photoconductivity. They are generally based on the assumption that, in the vicinity of a charged impurity, the crystal lattice is transformed in accordance with the charge state of this impurity. The Jahn–Teller effect, structural phase transition, dielectric constant, etc. have been suggested as the possible mechanisms of such a structural rearrangement (for a detailed description of these concepts, see [1–5]).

At the same time, it is evident that, at low temperatures and for compositions in which the equilibrium Fermi level position provides low carrier density in the allowed bands, the transport of carriers, both equilibrium and nonequilibrium (including those excited by light), can be described in terms of the theory of space-charge-limited current (SCLC). As was stated in [4], the shape of the current–voltage (*I–V*) characteristics in LTT:In is determined by the space charge; however, no detailed analysis of these characteristics was made. It is also necessary to note that, in the presence of carrier traps, their filling should affect not only the *I–V* characteristics but also the photoconductivity relaxation in LTT:In.

The aim of this study is to investigate the *I–V* characteristics of LTT:In films with $x = 0.25$ and 0.27 in the temperature range $4.2\ \text{K} < T < 35\ \text{K}$ and to reveal the mechanism of dark current transport.

2. EXPERIMENT

Epitaxial ($Pb_{1-x}Sn_xTe$):In films of ~1 μm in thickness, with a tin content of $x \approx 0.25$ and 0.27 and In content of 1–3 at %, were grown by MBE on BaF_2 substrates [6, 7].

Under study were structures formed between two 0.5- to 1.5-cm silver contacts spaced 16–64 μm from each other. Standard measurement circuits were used to determine the capacitive and resistive components of the structure conductance.

The *I–V* characteristics were directly measured in liquid helium. At voltages below $U = 7$–8 V, they were measured in the standard way with a dc voltage source. At voltages above this limit, sample heating was observed. Therefore, the *I–V* characteristics at higher voltages were recorded in a pulsed mode with a generator of rectangular pulses. The generator, a sample, and a load resistor with $R = 11\ \Omega$ were connected in series. The signal voltage from the load was applied to an oscilloscope input; in the entire measurement range, the signal voltage was much lower than the generator voltage. The pulse spacing was 3×10^{-4} s, and, for different voltage ranges, a pulse width of 1, 4, or 8 μs was used. The pulse width was chosen according to the signal shape. At high voltages and long pulse widths, as a result of the sample heating, a specific deviation from the rectangular shape appeared at the end of the pulses. Transient regions of several tenths of a microsecond, related to stray capacitance in the measurement circuit, were observed both at the beginning and end of the pulses. Therefore, the measurement precision decreased if the pulse width was less than 1 μs.

The technique we used for capacitance measurement was described in detail in [8]. Two lock-in amplifiers were used, with their phases adjusted to measure the capacitive and active components of the load current. The frequency dependence of the capacitive current component was also measured.

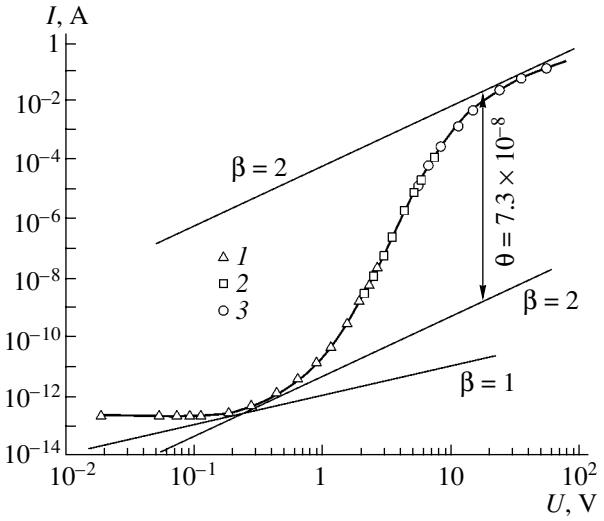

Fig. 1. The *I–V* characteristic of the $(Pb_{0.75}Sn_{0.25}Te)$:In structure at $T = 4.2$ K measured with the use of (*1*, *2*) dc bias and (*3*) in a pulsed mode. β is the exponent in the relation $I \propto U^{\beta}$.

The temperature dependences of the current were studied for the samples after they had been placed in a metallic chamber, which screened the studied structure from uncontrolled external background illumination. The sample temperature could be varied from 4.2 to 80 K.

3. EXPERIMENTAL RESULTS AND DISCUSSION

3.1. The I–V Characteristics at T = 4.2 K

Figure 1 shows an *I–V* characteristic recorded at $T = 4.2$ K. The following portions can clearly be seen: (a) a weak rise in current at a level of $(2–3) \times 10^{-13}$ A as the voltage increases from 0.02 to 0.2 V, (b) short portions along the voltage axis with linear ($\beta = 1$ in $I \propto U^{\beta}$) and quadratic ($\beta = 2$) dependences of the current at $U >$ 0.2 V, (c) a transition portion in which the slope of the *I–V* characteristic markedly changes, and (d) a portion with a quadratic *I–V* dependence at $U = 20–60$ V.

Portion *a* is most probably related to polarization (depolarization) currents or to leakage. The rest of the *I–V* characteristics can be described in terms of the theoretical concept of SCLC [9]. The presence of two quadratic portions separated by the transition range and with a strong dependence of the current on the voltage suggests that, at $0.2 \lesssim U \lesssim 0.7$ V, shallow traps start to intensively capture carriers injected from the contact into the film. At $U > 20$ V, these traps become completely filled.

As follows from SCLC theory, the transition of an *I–V* characteristic from ohmic to quadratic dependence occurs at

$$U_c \approx \frac{qn_0L^2}{\varepsilon\varepsilon_0\theta}, \qquad (1)$$

where n_0 is the equilibrium (at $U = 0$) electron density, $\theta = (gN_c/N_t)\exp[(E_t - E_c)/kT]$ determines the ratio of SCLCs before and after the trap filling, and L is the interelectrode distance. U_c has been experimentally determined as the point of intersection of the extrapolated linear and quadratic portions of an *I–V* characteristic. In the last expression, g is the spin degeneracy factor; E_t and E_c are the energies of the traps and the conduction band bottom, respectively; and N_t and N_c are the concentration of traps and the effective density of states in the conduction band, which can be determined from the relation [10]

$$N_c = \left(\frac{kTE_g}{\pi}\right)^{3/2}\left[\left(E_g\frac{\hbar^2}{2m_t^-} + P_t^2\right)^{-1}\left(E_g\frac{\hbar^2}{2m_l^-} + P_l^2\right)\right]^{-1/2}.$$

Here, E_g is the band gap; m_t^- and m_l^- are the transverse and longitudinal effective mass in the conduction band, respectively; and P_t and P_l are the corresponding interband matrix elements in the **kp** method of band structure calculation. The numerical values of these quantities were also taken from [10]. For $T = 4.2$ K, the calculated value of $N_c = 4 \times 10^{14}$ cm^{-3}.

For the dependence shown in Fig. 1, $\theta = 7.3 \times 10^{-8}$, and the voltage at the intersection of the $I \propto U$ ($\beta = 1$) and $I \propto U^2$ ($\beta = 2$) straight lines is $U_c \gtrsim 0.25$ V. The true voltage of the transition from the ohmic to SCLC mode may be significantly lower because of the poor experimental precision at $U < 0.2$ V and the existence of currents related to the spontaneous polarization of the samples, which govern the behavior of the *I–V* characteristic in this voltage range. If we assume that $\varepsilon = 2000$ [8], the equilibrium electron density in the film at $T = 4.2$ K can be estimated from Eq. (1) and is found to be $n_0 \lesssim 1.8 \times 10^6$ cm^{-3}. This value of n_0 implies that the spacing between the conduction band bottom and the Fermi level is $E_c - E_F \gtrsim 7$ meV. Since, at a low bias, the traps are virtually empty, their levels must lie above E_F.

If we assume that only one level of traps exists in the sample, we obtain

$$N_t\exp\frac{E_c - E_t}{kT} = N_c\frac{g}{\theta} = 2 \times 10^{22}\ \text{cm}^{-3}.$$

The concentration of traps can be estimated from the capacitance when measured at a zero bias, $C_{4.2\,K} = 5 \times 10^{-12}\,\Phi$ [8], and from the voltage of the transition to the complete filling of the traps (CFT). At a bias U, the charge injected into the film is $Q = CU$. At the same time, at the transition to the CFT mode, this charge is determined by the concentration of traps as $Q = qN_t\nu$, where ν is the volume of the film between the contacts, $\nu = 4.5 \times 10^{-7}$ cm^3. As can be seen in Fig. 1, the transition to the CFT occurs at the bias $U_{FFT} = 20–30$ V. Therefore, the concentration of traps $N_t = CU_{FFT}/q\nu =$

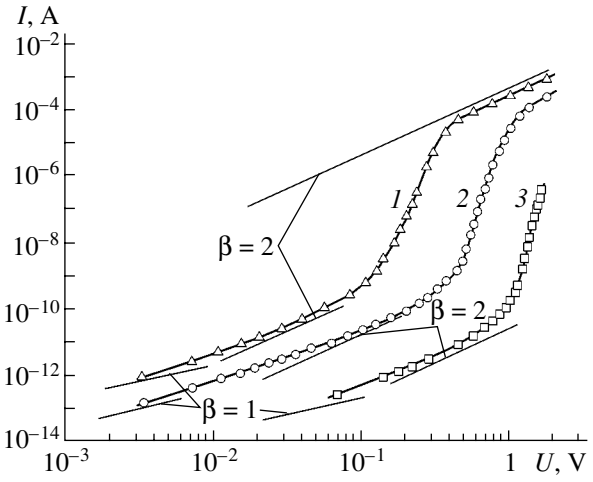

Fig. 2. The *I–V* characteristic of the ($Pb_{0.73}Sn_{0.27}Te$):In structure at $T = 4.2$ K. The interelectrode distance L: (*1*) 16, (*2*) 32, and (*3*) 64 μm. β is as described in Fig. 1.

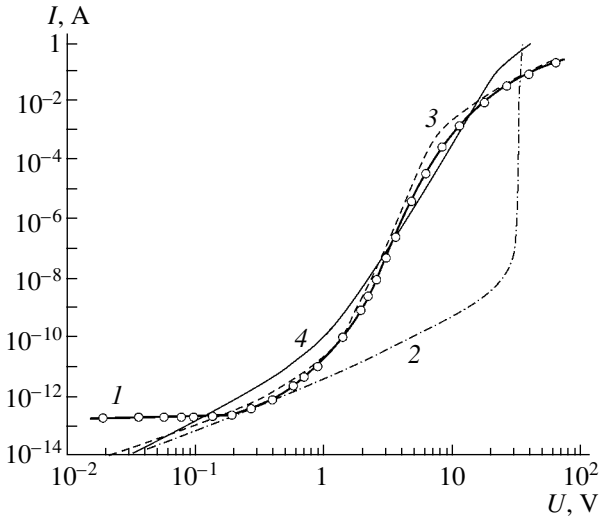

Fig. 3. The experimental and calculated *I–V* characteristics of the ($Pb_{0.75}Sn_{0.25}Te$):In film at $T = 4.2$ K for (*1*) the experiment, (*2*) the calculation in terms of a model with a single level, (*3*) the calculation involving five levels, and (*4*) the calculation with one level and the Poole–Frenkel effect taken into account.

(1.4–2.1) × 10^{15} cm^{-3}. Then, the energy depth of the traps $E_c - E_t = kT\ln(g/\theta N_t) \approx 6$ meV, in agreement with the above-made estimate.

At the quadratic portion of the characteristic, before the transition to the CFT mode, the SCLC is expressed by [9]

$$I = I_0\theta = \varepsilon\varepsilon_0\mu\frac{U^2}{L^3}\frac{gN_c}{N_t}\exp\frac{E_t - E_c}{kT}. \qquad (2)$$

It can be seen from (2) that, at a fixed bias, the current is inversely proportional to the cubed interelectrode gap L^3.

Figure 2 shows the *I–V* characteristics for a sample with the Sn content $x = 0.27$ for three different distances between the silver contacts: $L = 16$, 32, and 64 μm. As can be seen, the behavior of the *I–V* characteristics is similar to that shown in Fig. 1 for the sample with $x = 0.25$; however, in Fig. 2, the portions of linear dependence are more clearly pronounced. In the portions with quadratic dependence, the experimental ratio between the currents in the different samples (curves *1*, *2*, and *3*) are $I_1 : I_2 : I_3 \approx 700 : 40 : 1$, which does not coincide with the ratio $I_1 : I_2 : I_3 \approx 64 : 8 : 1$ calculated from (2) for $L = 16$, 32, and 64 mm, respectively. The reason for this discrepancy may be as follows. The interelectrode distance L was assumed to be equal to the corresponding parameter in the photomasks used in the structure's fabrication. It can be assumed that, in spite of the rather low temperature of the sample during the deposition of silver (about 150–200°C), the diffusion of silver occurred during the deposition and subsequent cooling of the substrate, which resulted in a decrease in the effective interelectrode distance. Our estimates show that, for the silver diffusion parameters presented in [11], the average length of the silver diffusion from the contacts is about 4–5 μm, which can cause the reduction of the effective distance in the structures by δL = 9–10 μm. In this case, the experimentally observed ratios of SCLC estimated from (2) should be 620 : 41 : 1 or 730 : 49 : 1 for $\delta L = 9.5$ or 10 μm, respectively, in good agreement with the experimental data.

Based on these estimates, we performed calculations of the *I–V* characteristics of the structure within the framework of a phenomenological analysis that disregards the spatial distributions of both the electric field between the contacts and the densities of free and trapped carriers, with only their average values being used. The results are shown in Fig. 3. The calculation made under the assumption that there is only a single trap level failed to provide satisfactory agreement with the experiment. For agreement, a steep rise in current should be observed at biases close to that of the transition to the CFT mode (curve *2*). Good agreement with the experiment is obtained in the calculations considering the existence of several trap levels with different energies. Curve *3* shows the results of a calculation made under the assumption that there are five trap levels with equal concentrations ($N_t = 1.3 \times 10^{14}$ cm^{-3} for each level) and energy depths of 1, 2, 3, 4, and 6 meV, respectively. The calculation procedure was as follows. The equilibrium electron density was assumed to be approximately n_0, as was estimated earlier from (1), and the equilibrium Fermi level position was calculated. In addition, different positions of quasi-Fermi level (related to the electron injection from the contacts) were set, the filling of the traps was calculated for

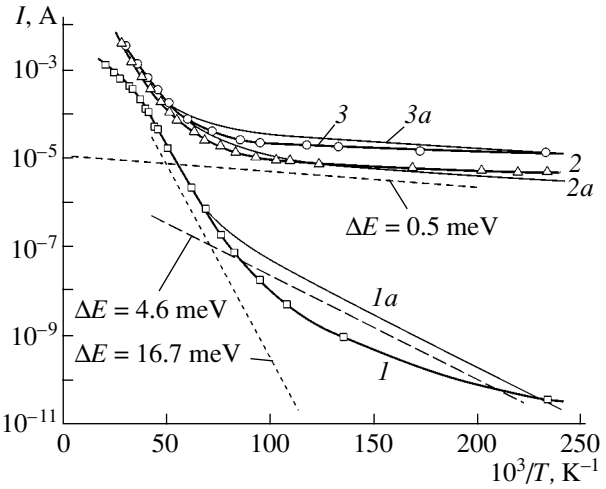

Fig. 4. The temperature dependences of the current I for the $(Pb_{0.75}Sn_{0.25}Te)$:In film from (*1–3*) the experiment, (*1a–3a*) the calculations. Bias U: (*1*, *1a*) 1.55, (*2*, *2a*) 4.65, and (*3*, *3a*) 5.6 V.

each position, and the voltage and current were calculated from the relations

$$U(E_F) = \frac{qL_s^2}{\varepsilon\varepsilon_0}[n_t(E_F) + n(E_F) - n_{t0} - n_0],$$
$$I(E_F) = q\mu_n n(E_F)\frac{wdU(E_F)}{L'}. \quad (3)$$

Here, $U(E_F)$ and $I(E_F)$ are the voltage and current at a given position of the quasi-Fermi level; $n_t(E_F)$ and $n(E_F)$ are the electron densities at the traps and in the conduction band, respectively; n_{t0} and n_0 are the equilibrium electron densities at the traps and in the conduction band; μ_n is the electron mobility; and d, w, and L' are the thickness, width, and length of the structure under study.

As can be seen in Fig. 3, good agreement is achieved between the calculation (*3*) and experiment (*1*). This result means that the total concentration of traps in the film under study (which defines the current in the SCLC mode) and their characteristic energy (which defines the range of transition from the quadratic portion of the *I–V* characteristic to the CFT mode) fall within the range of values used in the calculation. However, the equilibrium Fermi level is fixed arbitrarily rather than being determined from the known set of local centers. Therefore, traps with this concentration and energy depth do not necessarily exist in the real film, and the chosen position of the equilibrium Fermi level may be provided by some other set of local levels in the film.

In principle, a uniform energy distribution of traps (this is, in fact, the assumption made when there are five levels with the same concentration) is possible. For example, independently of the nature of these centers, the difference in activation energies can be related to inhomogeneity in the film composition. However, along with the energy distribution of the traps, an alternative explanation of the absence of the sharp current rise that should be observed at the transition to the CFT mode can be presented. When the interelectrode distance is 30 μm, the electric field is high even at relatively low biases, and the Coulomb potential barrier around the center can be reduced by the Poole–Frenkel effect. The reduction of the barrier height is $\Delta E = (qU/\varepsilon_\infty\varepsilon_0 L)^{1/2}$, where ε_∞ is the high-frequency dielectric constant. In other calculations, this reduction has been taken into account as the reduction of the thermal ionization energy for the traps [12]. Figure 3 shows the SCLC calculated for the film with $x = 0.25$ at $E_t = E_c - 6.5$ meV and $E_F = E_c - 9.0$ meV, which corresponds to the above-made estimates, with the Poole–Frenkel effect either disregarded (curve *2*), or taken into account (curve *4*). As can be seen from this figure, the *I–V* characteristic calculated with the Coulomb barrier reduction disregarded agrees with the experiment only below biases of 0.4–0.5 V, i.e., before the transition to the CFT mode. When the Poole–Frenkel effect is taken into account, the experiment is satisfactorily described at biases of up to 20 V; nevertheless, at larger biases, the calculated current exceeds the experimental one.

3.2. Temperature Dependence of Current

Figure 4 shows the current as function of the inverse temperature at different biases for the sample with $x = 0.25$. At temperatures above ~20 K, the slopes of all the curves are nearly the same and close to the energy $\Delta E = 17$ meV in the dependence $I(T) = I_0\exp(-\Delta E/kT)$.

It is worth noting that the slope of the curves at low temperatures decreases as the bias increases. This observation can be explained as follows. In the quadratic portion of the *I–V* characteristic, below the transition to the CFT mode (small biases, curve *1*), the current is described by relation (2). In this case, the rise in current as temperature increases is determined by the terms $\exp[(E_t - E_c)/kT]$ and N_c. In addition, ε and μ may also be temperature-dependent.

After the transition to the CFT mode (curves *2* and *3*), the current may increase as the temperature increases, as long as the injection-induced electron concentration in the conduction band remains higher than the equilibrium concentration, due to the increase of ε or μ on the condition that these quantities are temperature-dependent.

Therefore, if the temperature dependence of the current is recorded at a bias corresponding to the quadratic portion of the *I–V* characteristic below the transition to CFT mode, the slope of the $\log I = f(10^3/T)$ dependences are determined by the depth of the trap levels. In a comparatively narrow temperature range ($4.2 \lesssim T \lesssim 30$ K), the carrier mobility in LTT varies insignificantly,

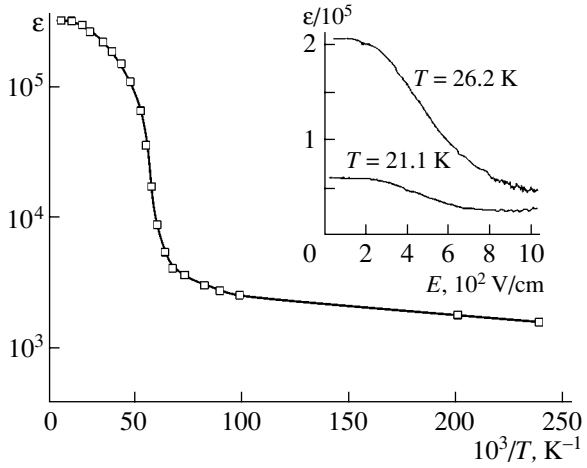

Fig. 5. The temperature dependence of the dielectric constant ε for ($Pb_{0.75}Sn_{0.25}Te$):In. In the inset, ε vs. the electric field E for the same sample is shown.

whereas the dielectric constant may change by a factor of up to 10^3 in the same temperature range and, thereby, define the temperature behavior of the SCLC in the CFT mode. Figure 5 shows the dependence of the low-frequency dielectric constant on the inverse temperature for the amplitude of a probing signal of about 50 mV [8].

This kind of temperature dependence of the dielectric constant is typical of LTT:In films at temperatures of ~30 K and lower. As was shown in [8, 13, 14], the decrease in the dielectric constant (and the corresponding decrease in the structure's capacitance) as the temperature decreases is related to a ferroelectric phase transition, which is confirmed, among other factors, by the emergence of spontaneous stress [14]. The dependence of the capacitance on the electric field is weak at temperatures below 15–20 K. The inset in Fig. 5 shows the field dependences of ε for T = 21.1 and 26.2 K.

Therefore, the dielectric constant increases as the temperature increases, but, at a fixed temperature, the constant decreases while the bias increases. This fact was taken into account in the calculation of the temperature dependences of the current for three different bias values, which was performed in the same approximation as that used in the estimation of the *I–V* characteristics at T = 4.2 K.

As can be seen in Fig. 4, the agreement between the calculated and experimental curves is satisfactory, particularly for high bias voltages. The discrepancy between the calculation (*1a*) and experiment (*1*) for U = 1.55 V at T = 5–17 K may be related, in particular, to the precision of the capacitance measurement in this temperature range. Similar results, with somewhat different slopes of the curves, were obtained in the study of the temperature dependences of the current for the film with x = 0.27.

4. CONCLUSION

(1) The current–voltage and capacitance–voltage characteristics of structures based on ($Pb_{1-x}Sn_xTe$):In/BaF_2 films with x = 0.25 and 0.27 were studied at 4.2–35 K in electric fields of (1–2) × 10^4 V/cm. The behavior of the *I–V* characteristics corresponds to that observed in the case of space-charge-limited current (SCLC).

Calculations for estimating the *I–V* characteristics of ($Pb_{0.75}Sn_{0.25}Te$):In/BaF_2 at T = 4.2 K were performed assuming the presence of trap levels uniformly distributed in the energy range 1–6 meV below the conduction band bottom. The calculated data agree well with the experiment. Good qualitative agreement with the experiment is also obtained for calculations in terms of a model with a single level of traps when the Poole–Frenkel effect is taken into account.

Thus, in PbSnTe:In, in which the "transition to an insulator state" is observed, the current at the electric field $E \geq$ 10–100 V/cm is not ohmic; rather, it is limited by space charge injected into the samples from the contacts.

(2) The study of the temperature dependences of the current I at different biases has shown that, in the temperature range 4.2–35 K, the slope of the curves plotted in the $\log I = f(10^3/T)$ coordinates is strongly dependent on bias. The temperature dependences of the current, calculated under the assumptions used in earlier calculations of the *I–V* characteristics, agree with the experiment only when the temperature and field dependences of the dielectric constant of $Pb_{0.75}Sn_{0.2}Te\langle In\rangle$, which were determined in the experiment, are taken into account.

Thus, it is shown that the temperature dependences of the current in the SCLC mode are determined by the electric field strength. At low temperatures, they can be determined by the activation energy of the centers only for a low electric field, $E \leq 10$ V/cm.

(3) The question of the inconsistency between the large concentration of introduced In and relatively low concentration of traps, which was estimated from the experiment and confirmed by calculations of the *I–V* characteristics remains open. A possible explanation is that the In atoms are incorporated into the film structure mostly in the electrically inactive phase.

ACKNOWLEDGMENTS

The study was supported by the Russian Foundation for Basic Research (project no. 02-02-17802).

REFERENCES

1. B. A. Volkov, V. V. Osipov, and O. A. Pankratov, Fiz. Tekh. Poluprovodn. (Leningrad) **14**, 1387 (1980) [Sov. Phys. Semicond. **14**, 820 (1980)].
2. B. A. Volkov and O. A. Pankratov, Dokl. Akad. Nauk SSSR **255**, 93 (1980) [Sov. Phys. Dokl. **25**, 922 (1980)].

3. V. I. Kaĭdanov and S. A. Nemov, Fiz. Tekh. Poluprovodn. (Leningrad) **15**, 542 (1981) [Sov. Phys. Semicond. **15**, 306 (1981)].
4. I. A. Drabkin and B. Ya. Moĭzhes, Fiz. Tekh. Poluprovodn. (Leningrad) **15**, 625 (1981) [Sov. Phys. Semicond. **15**, 357 (1981)].
5. Yu. Kagan and K. A. Kikoin, Pis'ma Zh. Éksp. Teor. Fiz. **31**, 367 (1980) [JETP Lett. **31**, 335 (1980)].
6. A. E. Klimov, D. V. Krivopalov, I. G. Neizvestny, *et al.*, Appl. Surf. Sci. **78**, 413 (1994).
7. L. F. Vasil'eva, A. É. Klimov, N. I. Petikov, and V. N. Shumskiĭ, Neorg. Mater. **37**, 193 (2001).
8. A. É. Klimov and V. N. Shumskiĭ, Avtometriya **3**, 65 (2001).
9. M. A. Lampert and P. Mark, *Current Injection in Solids* (Academic, New York, 1970; Mir, Moscow, 1973).
10. W. W. Anderson, IEEE J. Quantum Electron. **13**, 532 (1977).
11. F. A. Zaitov, A. V. Gorshkov, G. M. Malyashina, *et al.*, Neorg. Mater. **15**, 2077 (1979).
12. A. G. Milnes, *Deep Impurities in Semiconductors* (Wiley, New York, 1973; Mir, Moscow, 1977).
13. K. H. Herrmann and K.-P. Mollmann, Phys. Status Solidi A **80**, K101 (1983).
14. V. S. Vinogradov and I. V. Kucherenko, Fiz. Tverd. Tela (Leningrad) **33**, 2572 (1991) [Sov. Phys. Solid State **33**, 1453 (1991)].

Translated by D. Mashovets

Semiconductors, Vol. 39, No. 5, 2005, pp. 539–542. Translated from Fizika i Tekhnika Poluprovodnikov, Vol. 39, No. 5, 2005, pp. 569–572.

SEMICONDUCTOR STRUCTURES, INTERFACES, AND SURFACES

The Generation–Recombination Mechanism of Charge Transport in a Thin-Film CdS/CdTe Heterojunction

L. A. Kosyachenko*^, X. Mathew, V. V. Motushchuk*, and V. M. Sclyarchuk***

**Chernovtsy National University, Chernovtsy, 58012 Ukraine*

^e-mail: lakos@chv.ukrpack.net

***Centro de Investigacion en Energia-UNAM, 62580 Temixco, Morelos, Mexico*

Submitted September 7, 2004; accepted for publication October 6, 2004

Abstract—An *n*-CdS/*p*-CdTe heterostructure is studied. The heterostructure is obtained using the sequential growth of CdS and CdTe layers by electrochemical deposition and closed-space sublimation, respectively. The measured current–voltage characteristics are interpreted in the context of the Sah–Noyce–Shokley generation–recombination model for the depletion layer of a diode structure. The theory quantitatively agrees with the experimental results. *© 2005 Pleiades Publishing, Inc.*

1. INTRODUCTION

Numerous studies during recent decades have shown that the *n*-CdS/*p*-CdTe structure is a promising element for thin-film solar cells [1]. In this structure, CdTe is the absorbing layer, while CdS, which is the second component of the heterostructure, serves as a window for effective radiation input. For small-area CdS/CdTe photovoltaic structures (~1 cm^2), photovoltaic conversion of solar energy is attained at an efficiency of 16.5% [2]. For large-area modules (~1400 cm^2), which are being developed for large-scale production, the attained efficiency is 10.5% [3]. At present, it is not clear why the efficiency is so low as compared to the theoretical limit, which is 29–30% for a CdTe-based cell [4].

The key parameters of a solar cell (the short-circuit current, open-circuit voltage, fill factor, and efficiency) depend mainly on the mechanism of charge transport. However, in most reports, a description of the electrical characteristics of the CdS/CdTe heterostructure is reduced to the suggestion that the transport mechanism is thermionic emission (the Richardson effect) or recombination in the depletion region, i.e., in the space-charge region. For the current, the following formula is used [1, 5, 6]:

$$I = I_0\left[\exp\left(\frac{qV}{nkT}\right) - 1\right]. \quad (1)$$

Here, I_0 is a quantity considered as independent of voltage and is often referred to as the saturation current; q is the elementary charge; V is the voltage; k is the Boltzmann constant; and T is the temperature. The ideality factor n for thermionic emission and recombination in the depletion layer equals 1 and 2, respectively, and, in the general case, the value of n is between unity and two; occasionally, n is larger than two.

The results reported below indicate that the current–voltage (I–V) characteristic of the CdS/CdTe structure is described by the Sah–Noyce–Shokley generation–recombination theory [7] if we take into account special features of the processes in the heterojunction and do not use semiempirical formula(1).

2. EXPERIMENT AND RESULTS

For the purpose of measurement, we employed CdS/CdTe heterostructures fabricated using the most widespread technology [1, 8]. The substrates were glass wafers coated with a SnO_2 + In_2O_3 semitransparent layer (ITO) (Fig. 1). A CdS layer 0.1–0.15 μm thick was obtained by electrodeposition, while a CdTe layer 4–6 μm thick was obtained by closed-space sublimation (CSS). No subsequent thermal treatment in oxygen

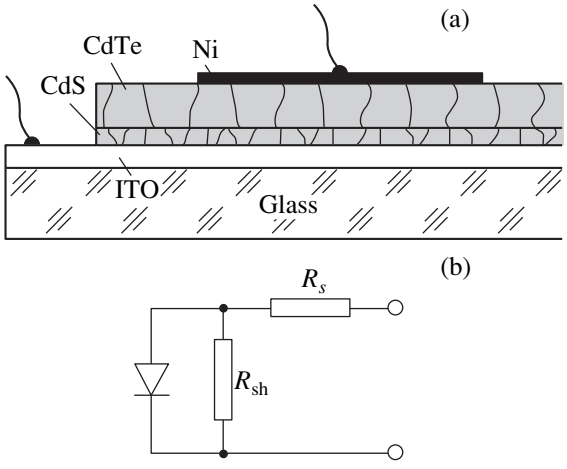

Fig. 1. (a) The cross section and (b) equivalent circuit of a photovoltaic cell with a CdS/CdTe heterojunction.

1063-7826/05/3905-0539$26.00 © 2005 Pleiades Publishing, Inc.

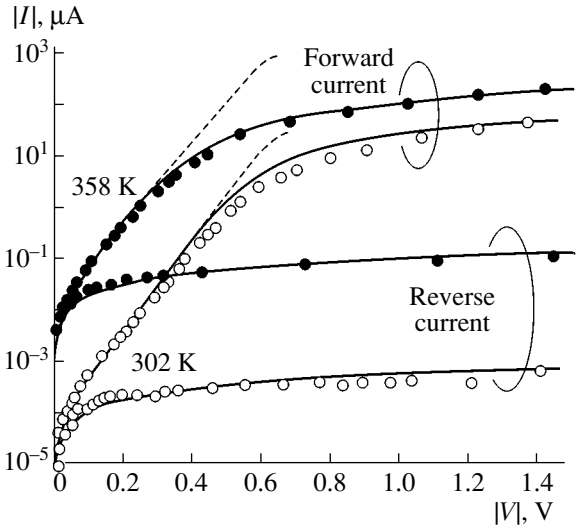

Fig. 2. Current–voltage characteristics of the CdS/CdTe heterostructure at 302 and 358 K. The circles correspond to the experiment, and the solid curves correspond to the calculation by formula (7). The dashed line corresponds to the calculation where the voltage drop across the resistance R_s of the bulk part of the CdTe film was disregarded.

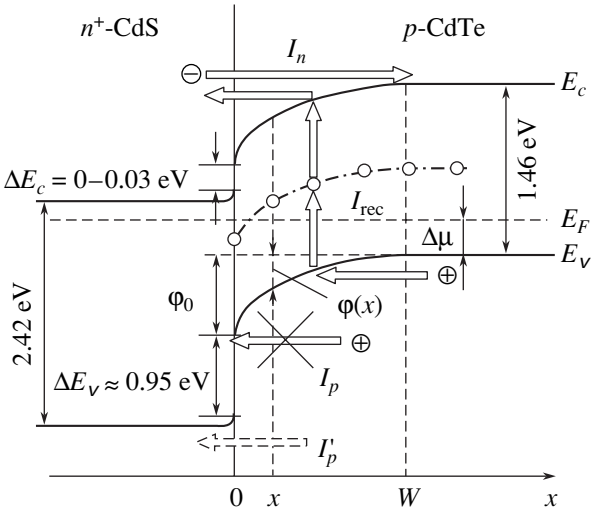

Fig. 3. The energy-band diagram of the CdS/CdTe heterojunction. Various transitions for the forward bias are shown. These transitions correspond to the recombination current I_{rec}, the above-barrier hole current I'_p, and the above-barrier electron (minority carrier) current I_n. For the reverse bias, when generation is dominant in the depletion region, the transition directions are opposite to those indicated. ΔE_c and ΔE_v are the offsets of the conduction band (E_c) and valence band (E_v), respectively, and E_F is the Fermi level.

and/or chlorine, which is often used to coarsen the grains in the CdTe layer, was carried out. It is believed that the CdS and CdTe layers have the columnar structure illustrated in Fig. 1. A contact to the CdTe layer, with an area of 0.3×0.3 mm^2, was formed by a vacuum thermal deposition (at 10^{-6} Torr) of Ni at a substrate temperature ranging from 150–200°C after preliminary irradiation of the CdTe surface with ~500-eV argon ions. The electrical characteristics of two neighboring Ni contacts on the CdTe surface were linear over the entire range of measured currents.

Figure 2 shows the typical *I–V* characteristics of the heterostructures under study at 302 and 358 K. The currents traveling through the shunting resistance R_{sh} (Fig. 1b) are subtracted from the measured currents. This shunting, as well as the voltage drop across the series resistance R_s, is usually taken into account in the equivalent circuit of the photovoltaic device [1, 5, 6]. For both temperatures, the values of $R_{sh} = 2.1 \times 10^9$ and 1×10^8 Ω were determined from the initial (linear) portions of the *I–V* characteristics ($V < 0.1$ V). The corrections for the current traveling through the shunt R_{sh} were found to be insignificant.

We can see from Fig. 2 that the shape of obtained dependences is complex. At 302 K, the curve $I(V)$ follows the dependence, which is close to $I \propto \exp(qV/2kT)$, in the current-variation range slightly exceeding two orders of magnitude and only at low voltages ($V < 0.4$ V). At an elevated temperature (358 K), this dependence is barely observed.

The reverse current at $|V| < 0.1$ V increases rather abruptly as the voltage increases, and, at larger *V*, the corresponding dependence becomes sublinear in a wide range of *V* up to the onset of the electric breakdown at $|V| > 10$–15 V. It is noteworthy that the electrical characteristics of the CdS/CdTe heterojunctions under study are reproducible and stable over time.

3. DISCUSSION

Let us consider the energy-band diagram of a thin-film *n*-CdS/*p*-CdTe heterojunction, which is accepted by most researchers (Fig. 3) [1, 9]. The diagram is shown without ohmic contacts, which can be diverse. However, these contacts do not relate directly to the question under consideration. Let us first of all pay attention to the fact that, due to the high conductivity of CdS (the electron concentration is ~10^{17} cm^{-3} [8]), the depletion layer of the diode structure is located virtually within CdTe; in addition, band bending (φ_0 in Fig. 3) is also observed in CdTe. Thus, the potential energy distribution in the heterojunction can be described, similarly to the Schottky diode, by the parabolic law [10]

$$\varphi(x, V) = (\varphi_0 - qV)\left(1 - \frac{x}{W}\right)^2, \qquad (2)$$

where *W* is the width of the depletion layer,

$$W = \sqrt{\frac{2\varepsilon\varepsilon_0(\varphi_0 - qV)}{q^2(N_a - N_d)}}, \qquad (3)$$

ε is the relative permittivity of the semiconductor, ε_0 is the permittivity of free space, and $(N_a - N_d)$ is the concentration of uncompensated acceptors in the CdTe layer. The energy is measured from the valence-band top E_v in the semiconductor bulk.

The main mechanism of charge transport in the Schottky diode is a diffusion (above-barrier) flow of majority carriers [10]. For the heterojunction under consideration, a "normal" hole above-barrier current (I_p in Fig. 3, crossed arrow) is impossible. The concentration of holes that can enter the valence band of CdS is several orders of magnitude lower. Therefore, the corresponding current I_p' is negligible. The energy barrier for electrons (minority carriers) is also very high (the current I_n in Fig. 3). Thus, the most probable mechanism of charge transport for the forward bias is recombination in the depletion layer with the involvement of the levels located in the vicinity of the CdTe midgap. These levels are the most efficient recombination centers (the current I_{rec}). For the reverse bias, the direction of all the transitions should be changed to the opposite one. In this case, generation, rather than recombination, occurs in the depleted layer. Note that the direction of the hole transitions is shown in Fig. 3.

According to the above, the generation and recombination in the depletion layer of the *n*-CdS/*p*-CdTe heterostructure are similar to those in the Schottky diode. Therefore, the current can be calculated similarly to the calculation in [11]. The generation–recombination rate in the section x of the depletion layer for the voltage V is determined by the expression [7]

$$U(x, V) = \frac{n(x, V)p(x, V) - n_i^2}{\tau_{p0}[n(x, V) + n_1] + \tau_{n0}[p(x, V) + p_1]}, \quad (4)$$

where $n(x, V)$ and $p(x, V)$ are the carrier concentrations in the conduction band and valence band, respectively; n_0 and p_0 are the equilibrium concentrations; n_i is the intrinsic carrier concentration; τ_{n0} and τ_{p0} are, respectively, the effective lifetimes of the electrons and holes in the depletion layer; and the quantities n_1 and p_1 are determined by the expressions

$$n_1 = N_c \exp\left(\frac{-E_t}{kT}\right), \quad (5)$$

$$p_1 = N_v \exp\left(\frac{E_t - E_g}{kT}\right). \quad (6)$$

Here, $N_c = 2(m_n kT/2\pi\hbar^2)^{3/2}$ and $N_v = 2(m_p kT/2\pi\hbar^2)^{3/2}$ are the effective density of states in the conduction and valence bands, respectively; m_n and m_p are the effective mass of an electron and hole, respectively; E_t is the energy spacing between the recombination level and the conduction band bottom E_c; and E_g is the band gap.

The generation current for the forward bias and the recombination current for the reverse bias can be found by integrating $U(x, V)$ over the entire depletion layer:

$$I = Aq\int_0^W U(x, V)dx, \quad (7)$$

where A is the diode area. In the selected set of coordinates, the expressions for the hole and electron concentrations take the form

$$p(x, V) = N_c \exp\left[-\frac{\Delta\mu + \varphi(x, V)}{kT}\right], \quad (8)$$

$$n(x, V) = N_v \exp\left[-\frac{E_g - \Delta\mu - \varphi(x, V) - qV}{kT}\right]. \quad (9)$$

The results of the calculation of the *I–V* characteristic using formula (7) and taking into account expressions (3)–(6), (8), and (9) are shown by the solid lines in Fig. 2. In the calculation, we assumed that $\Delta\mu$ = 0.314 eV, taking into consideration that the resistivity of the CdTe film equals 2×10^4 Ω cm and the concentration of uncompensated acceptors equals 10^{16} cm^{-3} [12]. The depth of the generation–recombination level E_t = 0.7 eV. To attain the best agreement between the calculation and experiment, we assumed that the electron and hole lifetimes are equal to 4×10^{-11} s. In the calculation, we made an allowance for the voltage drop across the series resistance of the bulk part of the CdTe film $R_s = 5 \times 10^4$ and 1.9×10^5 Ω at 302 and 358 K, respectively (Fig. 1b). The values of R_s are found from the voltage dependence of the differential resistance of a diode. The run of curves with the voltage drop disregarded for this resistance (this drop manifests itself only for high forward currents) is shown by the dashed lines in Fig. 2.

Figure 2 indicates that there is good agreement between the calculation and the experiment, which confirms the correctness of the decision to choose the physical model for processes in the *n*-CdS/*p*-CdTe heterostructure. It is noteworthy that the only adjustable parameter, specifically, the lifetime of the carriers, which is identical at both temperatures, was used in the calculation. Thus, the chosen model also accurately describes both the temperature variations in the *I–V* characteristic of the diode and the voltage dependence of the current for both voltage polarities.

To improve the quality of the heterointerfaces and photoelectric characteristics, the CdS/CdTe structure is usually annealed at 450–550°C. For this reason, the energy diagram of the junction varies somewhat, especially in the layer adjoining the interface. However, this circumstance could not substantially affect the results of the calculation of the *I–V* characteristic, since the magnitude of the current is the result of integrating the generation–recombination rate over the entire depletion layer, and a concrete potential run is of no importance [13].

4. CONCLUSIONS

We studied the voltage dependences of the forward current $I \propto \exp(qV/nkT)$, where n is the diode ideality factor, characteristic of a thin-film n-CdS/p-CdTe heterojunction. These dependences are observed in a narrow current range. They are not observed at elevated temperatures at all. The analysis of the energy diagram of the n-CdS/p-CdTe heterojunction shows that the above-barrier (diffusion) current of majority carriers is negligible, and the main charge transport mechanism is the generation and recombination occurring in the depletion layer, i.e., in the space-charge region. The observed I–V characteristic and its temperature variation can be described mathematically in the context of the Sah–Noyce–Shokley model. Allowance should be made for the special features of the heterojunction under study and for the effect of the indispensable elements of the equivalent circuit of the photovoltaic structure, specifically, the shunting and series resistances.

REFERENCES

1. R. W. Birkmire and E. Eser, Annu. Rev. Mater. Sci. **27**, 625 (1997).
2. M. A. Green, K. Emery, D. L. King, *et al.*, Prog. Photovolt. Res. **11**, 347 (2003).
3. A. Hanafusa, T. Aramoto, M. Tsuji, *et al.*, Sol. Energy Mater. Sol. Cells **67**, 21 (2001).
4. A. De Vos, J. E. Parrot, P. Baruch, and P. T. Landsberg, in *Proceedings of 12th European Photovoltaic Solar Energy Conference* (Amsterdam, 1994), p. 1315.
5. N. Romeo, A. Bosio, R. Tedeschi, *et al.*, Sol. Energy Mater. Sol. Cells **58**, 209 (1999).
6. G. Agostinelli, D. L. Batzner, and M. Burgelman, Thin Solid Films **431–432**, 407 (2003).
7. C. Sah, R. Noyce, and W. Shokley, Proc. IRE **45**, 1228 (1957).
8. K. Durose, P. R. Edwards, and D. P. Halliday, J. Cryst. Growth **197**, 733 (1999).
9. J. Fritsche, D. Kraft, A. Thissen, *et al.*, Thin Solid Films **403–404**, 252 (2002).
10. S. Sze, *Physics of Semiconductor Devices*, 2nd ed. (Wiley, New York, 1981; Mir, Moscow, 1984).
11. L. A. Kosyachenko, I. M. Rarenko, Z. I. Zakharchuk, *et al.*, Fiz. Tekh. Poluprovodn. (St. Petersburg) **37**, 238 (2003) [Semiconductors **37**, 227 (2003)].
12. L. A. Kosyachenko, O. L. Maslyanchuk, I. M. Rarenko, and V. M. Sklyarchuk, Phys. Status Solidi C **1**, 925 (2004).
13. G. E. Pikus, *Fundamentals of the Theory of Semiconductor Devices* (Nauka, Moscow, 1965), p. 189 [in Russian].

Translated by N. Korovin

Semiconductors, Vol. 39, No. 5, 2005, pp. 543–546. Translated from Fizika i Tekhnika Poluprovodnikov, Vol. 39, No. 5, 2005, pp. 573–576.

LOW-DIMENSIONAL SYSTEMS

The Resonant Tunneling of Holes through Double-Barrier Structures with InAs QDs at the Center of a GaAs Quantum Well

E. N. Morozova*^, O. N. Makarovskiĭ, V. A. Volkov***, Yu. V. Dubrovskiĭ*^^†, L. Turyanska**, E. E. Vdovin*, A. Patané**, L. Eaves**, and M. Henini****

**Institute of Microelectronics Technology and High Purity Materials, Russian Academy of Sciences, Chernogolovka, 142432 Russia*

^e-mail: morel@ipmt-hpm.ac.ru

^^e-mail: dubrovsk@ipmt-hpm.ac.ru

***The School of Physics and Astronomy, University of Nottingham, Nottingham, NG7 2RD, UK*

****Institute of Radio Engineering and Electronics, Russian Academy of Sciences, Moscow, 125009 Russia*

Submitted August 11, 2004; accepted for publication September 9, 2004

Abstract—The effect of InAs quantum dots (QDs) grown in the center of a GaAs quantum well on the tunneling characteristics of resonant-tunneling diodes based on *p*-AlAs/GaAs/AlAs heterostructures is studied. The introduction of QDs results in a shift and broadening of resonance peaks in the current–voltage characteristics of the diodes; however, this effect is found to be strongly dependent on the number of the 2D subband involved in the tunneling. The obtained dependence is attributed to origination of the fluctuation potential in the vicinity of the QD layer. © *2005 Pleiades Publishing, Inc.*

1. INTRODUCTION

The properties of self-organized quantum dots (QD) obtained by epitaxial growth according to the Stranski–Krastanow mechanism have attracted attention owing to their potential application in lasers [1], single-electron transistors [2], optical memory devices [3].

Generally, these devices are based on multilayer heterostructures, where QD layers can be located either within quantum wells (QWs) or in their vicinity. A complicated potential profile is formed in the region of a QD due to the local mechanical stresses and charges they contain. This fluctuation potential can exert a considerable effect on the 2D electron states in QWs. Earlier studies [4] have shown that, when InAs QDs are introduced into the region of a 2D electron gas in GaAlAs/GaAs heterostructures, the electron mobility is significantly reduced. The effect of InAs QDs located at the center of a QW on the tunneling characteristics of *n*-GaAlAs/GaAs/GaAlAs double-barrier resonant-tunneling diodes was studied in [5]. It was found that, in this case, peaks on the current–voltage characteristics related to the resonant tunneling of electrons via the states of the ground 2D subband E_0 in the QW disappear. At the same time, peaks related to resonant tunneling via the subbands E_1 and E_2, which have higher energies, are not radically changed. Now, we present the results obtained during a study of the tunneling spectra of double-barrier resonant-tunneling *p*-AlAs/GaAs/AlAs structures with InAs QDs in the QW center.

†Deceased.

2. SAMPLE FABRICATION

AlAs/GaAs/AlAs structures were grown by MBE on heavily doped (311) *p*-GaAs substrates. The distinction between these and standard resonant-tunneling structures is the presence of InAs QDs in the center of the GaAs QW. It is important that, along with the QD layer, an InAs monolayer, the so-called wetting layer, is formed.

The structure, hereafter denoted by QD, contains the following set of layers:

GaAs ($p = 2 \times 10^{18}$ cm^{-3}, with a thickness of 2 μm);

GaAs ($p = 10^{18}$ cm^{-3}, 100 nm);

GaAs ($p = 5 \times 10^{17}$ cm^{-3}, 100 nm);

undoped GaAs (5.1 nm);

an undoped AlAs barrier (5.1 nm);

undoped GaAs (2.1 nm);

an InAs layer (1.8 monolayer) with QDs;

undoped GaAs (2.1 nm);

an undoped AlAs barrier (5.1 nm);

undoped GaAs (5.1 nm);

GaAs ($p = 5 \times 10^{17}$ cm^{-3}, 100 nm);

GaAs ($p = 10^{18}$ cm^{-3}, 100 nm);

a top contact layer of GaAs ($p = 2 \times 10^{18}$ cm^{-3}, 1 μm);

In addition, for comparison, we used control structures that did not include the InAs layer and structures with a thinner InAs layer (1 monolayer) where only a wetting layer was formed (denoted by WL); i.e., it was without QDs.

1063-7826/05/3905-0543$26.00 © 2005 Pleiades Publishing, Inc.

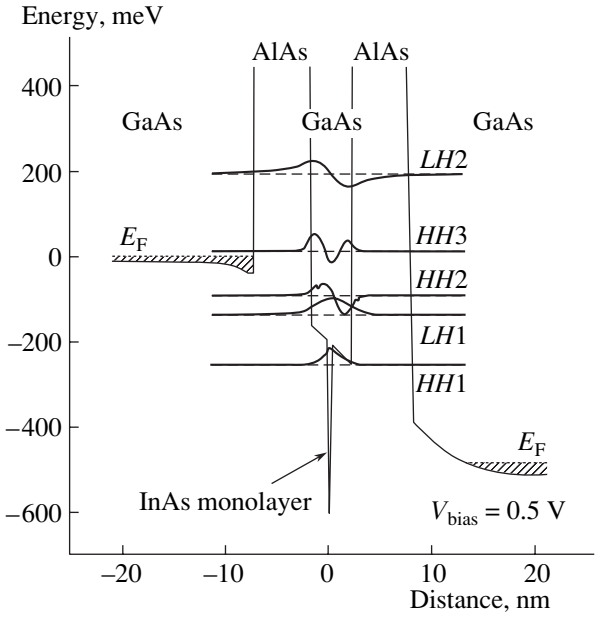

Fig. 1. Energy diagram of the valence band of a resonant-tunneling diode with an InAs wetting layer (sample WL) at a 0.5-V bias. The horizontal dashed lines show the energies of the bottoms of the 2D hole subbands in the QW, and the solid lines indicate the corresponding wave functions for the transverse motion. The scale for the wave functions along the ordinate axis is arbitrary. Notation: *HH* denotes the heavy-hole subband and *LH*, the light-hole subband. The energy is measured from the Fermi level in the emitter.

The samples under study were mesa structures of 50 and 100 μm in diameter with standard ohmic contacts on the top contact layer and *p*-GaAs substrate. The presence of QDs and the wetting layer was confirmed by studies of the photoluminescence spectra.

3. RESULTS AND DISCUSSION

In order to demonstrate the complex spectrum of 2D hole subbands in the QW, we present a band diagram of the resonant-tunneling diode with an InAs wetting layer (sample WL) at a 0.5-V bias (Fig. 1). In this diagram, the hole energy increases from the bottom upwards. The band diagram was calculated with self-consistent solutions of the Poisson and Schrödinger equations in the effective mass approximation. The effect of charge accumulation in the QW was disregarded. The energies of the bottoms of the 2D hole subbands in the QW and the corresponding wave functions for the transverse motion are shown. The following notation is used: *HH* denotes the heavy-hole subband and *LH*, light-hole subband. As is known [6], a pseudomorphic (wetting) InAs layer grown in the center of a GaAs QW strongly reduces the energy of the ground 2D subband. QDs are formed when the thickness of the wetting layer exceeds the critical value. This results, on the one hand, in a splitting of localized states from the 2D subband and, on the other hand, in the formation of chaotic potential, which strongly affects the properties of the 2D states.

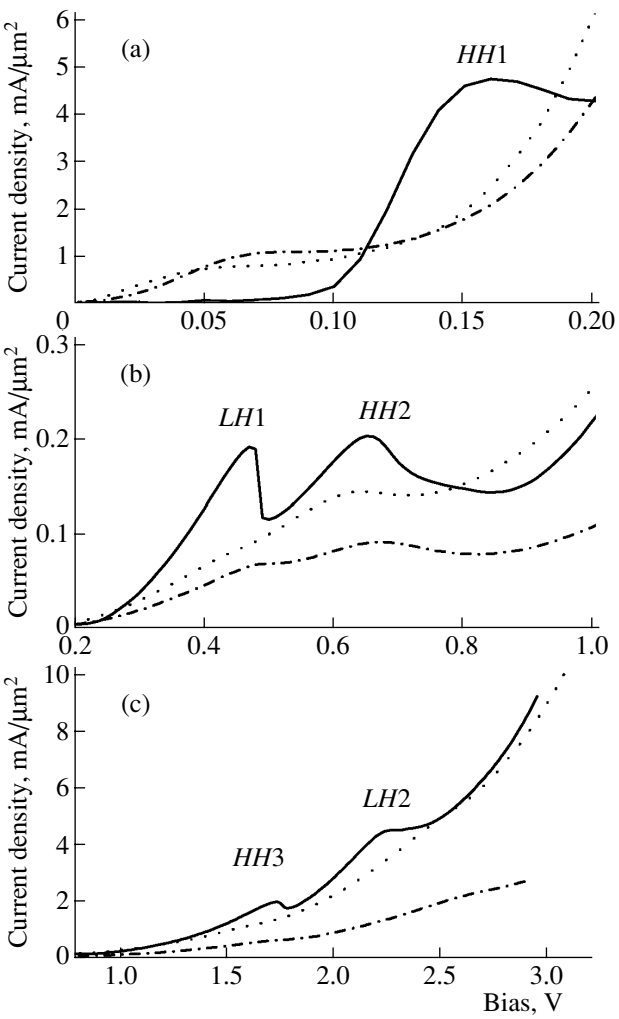

Fig. 2. Tunnel current *I* vs. the bias *V*. The solid lines indicate the control sample; the dot-dashed lines, the sample containing only the wetting layer (WL); the dashed lines, the sample with QDs (QD). Different scales are used in the three plots for current and voltage. The characteristics are shown (a) in the range of resonant tunneling via the ground quantum-confinement subband in the QW, i.e., heavy-hole subband *HH*1; (b) in the range of resonances *LH*1 and *HH*2; (c) in the range of resonances *HH*3 and *LH*2.

Figure 2 shows the dependences of the tunnel current *I* on bias *V* for all the samples under study at the temperature $T = 4.2$ K. Figures 2a–2c differ only in their scale. The control samples demonstrate distinct resonances that are related to tunneling from the emitter to the collector via subbands *HH*1, *LH*1, *HH*2, *HH*3, and *LH*2. The subbands were identified by comparing *I*(*V*) dependences measured in the magnetic field parallel to the interface (this method allows the reconstruction of the 2D dispersion of hole energy [7]) with the

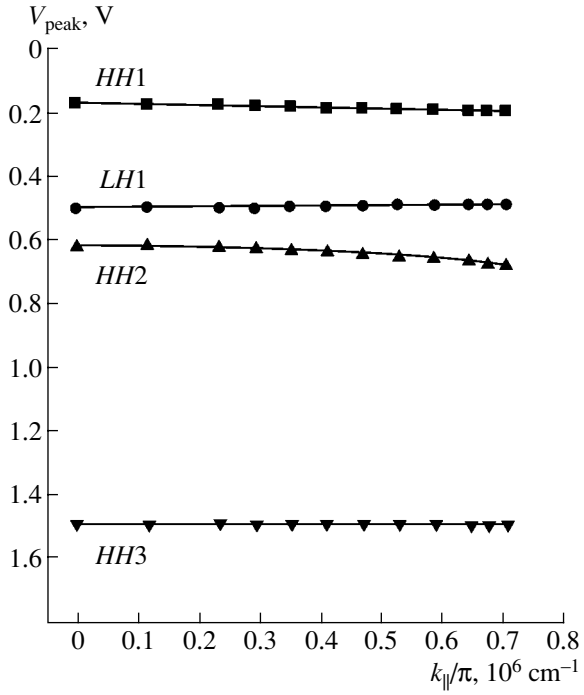

Fig. 3. Voltages corresponding to different resonance peaks in the *I–V* characteristics as function of $k_\parallel = eBd/\hbar$ at different magnitudes of the magnetic field parallel to the heterolayers.

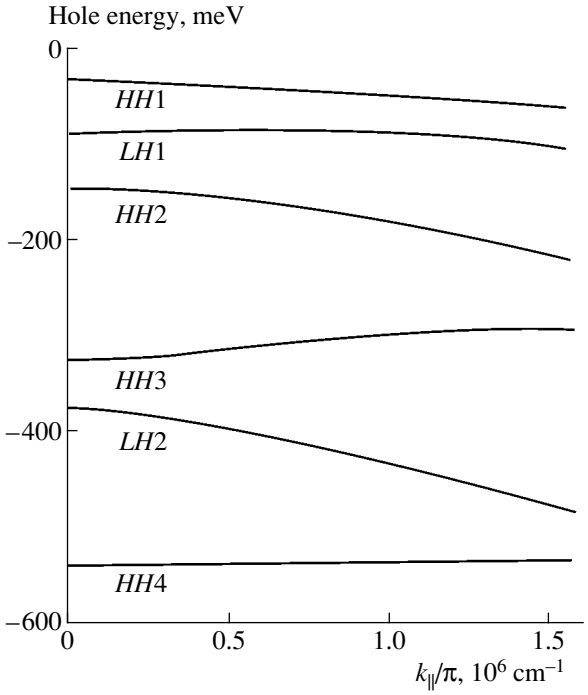

Fig. 4. The calculated dispersion of 2D hole states in the QW, $E_{hole} = f(k_\parallel)$, for a structure that has parameters coinciding with those in the structure under study [7].

hole spectrum calculated for a similar structure. Now, we discuss this method in more detail. Upon tunneling the distance d in the magnetic field B parallel to the interface, a hole acquires an additional 2D momentum ($\hbar k_\parallel = eBd$). In this respect, variation in B is equivalent to a variation in the 2D momentum of the hole. Having measured the $I(V)$ dependences at different magnitudes of the parallel magnetic field, we obtain the dependences of the resonance positions as functions of the magnetic field, $V_{peak} = f(B)$ (Fig. 3). These dependences can be interpreted as the dependences of the hole energy on the 2D momentum within a QW, $E_{hole} = f(k_\parallel)$. Now, we can use the calculations for $E_{hole} = f(k_\parallel)$ for a structure that coincides with our structure in its thickness and in the composition of its heterolayers [7] (Fig. 4). Comparison of the experimental and calculated data allows us to identify different peaks in relation to the structures under study, with resonant tunneling via the corresponding hole subbands in the QW.

We now return to the discussion of Fig. 2. In the WL and QD structures, the resonances are broadened. The shift of the *HH*1 resonance to a lower bias is the most pronounced, which correlates with the results of the simple calculations of hole spectra in the QW in the presence of a wetting layer. It is noteworthy that, in similar *n*-type samples with a wetting layer, the resonance via the ground electron quantum-confinement level in the QW is shifted to $V = 0$ [5]. In the case of the *p*-type resonant-tunneling structures under study, the resonance is not shifted to $V = 0$. In addition, no significant shift of the *LH*1 resonance is observed. The resonance peaks are more strongly broadened in the QD structure than in the WL structure. This effect was expected because of the presence of fluctuation potential in the vicinity of the QD layer. Somewhat unexpected was the strong broadening of the resonance peaks in the WL structure as compared to the control samples. Such strong broadening is not observed in *n*-type samples containing only a wetting layer. A possible source of this broadening may be that the wetting layer formed in during the growth of a pseudomorphic layer on the (311) surface in the WL samples is not solid but consists of islands, which results in a strong inhomogeneous broadening of the levels.

In addition, it can be seen that the negative differential conductivity in the QD structures is observed only near the *HH*2 resonance. The weaker effect of QDs on the *HH*2 resonance by contrast with the neighboring *LH*1 resonance is more clearly illustrated in Fig. 5, which shows the second derivative of the current in respect to voltage as a function of bias. In this plot, minima of the second derivative correspond to current peaks.

Indeed, as can be seen in Fig. 1, the wave function of the *HH*2 subband has a node in the center of the QW; therefore, its perturbation in the presence of QDs, which are also situated in the center of the QW, is the weakest [6]. It was, however, expected that specific resonance features related to tunneling via the *LH*2 subband would also be more clearly manifested in the presence of QDs, but this was not observed in the experiment.

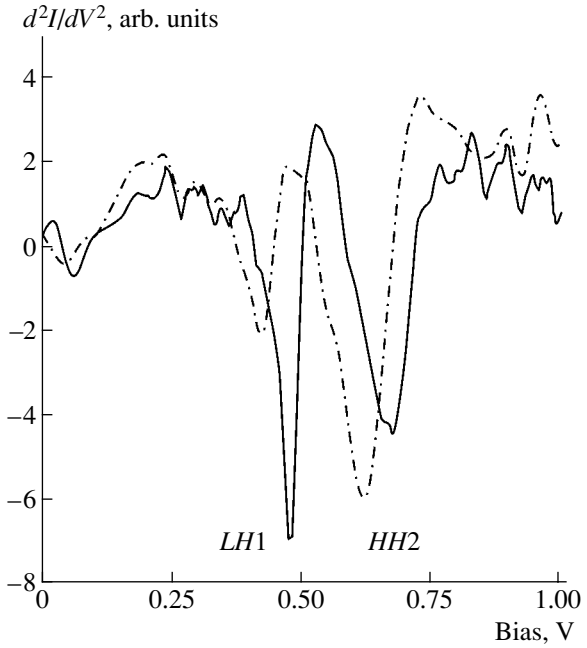

Fig. 5. The second derivative of the tunnel *I–V* characteristics in the range of resonances *LH*1and *HH*2. The solid line indicates sample WL and the dot-dashed line, sample QD.

A QD can be regarded as a local fluctuation of the QW thickness. Now, we discuss the effect of this fluctuation on the energy of the bottom of a 2D subband, which, in terms of the model of an infinitely deep QW, has the form

$$E_{n_{l,h}} = \frac{\hbar^2 n_{l,h}^2}{2m_{l,h}d^2}.$$

Here, n is the number of the subband; m is the transverse effective hole mass; and indices l and h refer to light and heavy holes, respectively. Let the QW width fluctuate: $d \longrightarrow d + \Delta d$ (where Δd is a random function). For the lowest order in the small parameter $\Delta d/d$, we obtain

$$E_{n_{l,h}} \approx \frac{\hbar^2 n_{l,h}^2}{2m_{l,h}d^2} - \frac{\hbar^2 n_{l,h}^2}{2m_{l,h}d^2}\frac{2\Delta d}{d} = E^0_{n_{l,h}} - \Delta E.$$

It can be seen that the energy levels of the subbands are inhomogeneously broadened due to fluctuations of the bandwidth; moreover, this broadening increases as the number of the subband increases and as the effective hole mass decreases:

$$\Delta E = \frac{\hbar^2 n_{l,h}^2}{2m_{l,h}d^2}\frac{2\Delta d}{d}.$$

Thus, the less pronounced specific resonance features near the *LH*2 peak in the presence of QDs, when compared with the *HH*2 peak, have a reasonable explanation in terms of this model calculation.

4. CONCLUSION

We studied the effect of InAs QDs introduced in the center of a QW on the tunneling characteristics of double-barrier resonant-tunneling *p*-AlAs/GaAs/AlAs diodes that were grown by MBE on (311) substrates. The presence of QDs results in a considerable broadening of the resonance peaks on the current–voltage characteristics of the diodes. As was expected, QDs situated in the center of the QW exert a smaller effect on resonance tunneling via the subbands whose wave functions have nodes in the center of the QW.

ACKNOWLEDGMENTS

We are grateful to Yu.N. Khanin for his participation in valuable discussions and to V.V. Sirotkin for the development of software for a self-consistent solution of the Schrödinger and Poisson equations.

The study was supported by the Russian Foundation for Basic Research, INTAS (grant no. 01-2362), target programs of the Presidium of Russian Academy of Sciences, and EPRSC (Engineering and Physical Sciences Research Council) (UK).

REFERENCES

1. D. Bimberg and N. Ledentsov, J. Phys.: Condens. Matter **15**, R1063 (2003).
2. M. H. Devoret and R. J. Schoelkopf, Nature **406**, 1039 (2000).
3. Y. Sugiyama, Y. Nakata, S. Muto, *et al.*, Physica E (Amsterdam) **7**, 503 (2000).
4. H. Sakaki, G. Yusa, T. Someya, *et al.*, Appl. Phys. Lett. **67**, 3444 (1995).
5. Yu. V. Dubrovskii, E. E. Vdovin, A. Patané, *et al.*, Nanotechnology **12**, 441 (2001).
6. A. Patané, A. Polimeni, L. Eaves, *et al.*, J. Appl. Phys. **88**, 2005 (2000).
7. R. K. Hayden, D. K. Maude, L. Eaves, *et al.*, Phys. Rev. Lett. **66**, 1749 (1991).

Translated by D. Mashovets

Semiconductors, Vol. 39, No. 5, 2005, pp. 547–551. Translated from Fizika i Tekhnika Poluprovodnikov, Vol. 39, No. 5, 2005, pp. 577–581.

LOW-DIMENSIONAL SYSTEMS

Threshold Behavior of the Formation of Nanometer Islands in a Ge/Si(100) System in the Presence of Sb

G. E. Cirlin*^, V. G. Dubrovskiĭ, A. A. Tonkikh*, N. V. Sibirev, V. M. Ustinov**, and P. Werner*****

**Institute for Analytical Instrumentation, Russian Academy of Sciences, Rizhskii pr. 26, St. Petersburg, 190103 Russia*
^e-mail: cirlin@beam.ioffe.ru
***Ioffe Physicotechnical Institute, Russian Academy of Sciences, Politekhnicheskaya ul. 26, St. Petersburg, 194021 Russia*
****Max-Planck Institut für Mikrostrukturphysik, Weinberg 2, D-06120 Halle, Germany*
Submitted September 14, 2004; accepted for publication September 29, 2004

Abstract—Atomic-force microscopy is used to study the behavior of an array of Ge islands formed by molecular-beam epitaxy on an Si (100) surface in the presence of an antimony flux incident on the surface. It is shown that, as the Sb flux increases to a certain critical level, the surface density of the islands increases; however, if this critical level is exceeded, nucleation of the islands is suppressed and mesoscopic small-height clusters are observed on the surface. This effect is explained qualitatively in the context of a kinetic model of the islands' formation in heteroepitaxial systems mismatched with respect to their lattice parameters. © *2005 Pleiades Publishing, Inc.*

1. INTRODUCTION

A large number of publications have been devoted to the physical properties and formation methods of nanodimensional Ge inclusions in an Si matrix. The interest of researchers in this field is caused, to a great extent, by the potential of using these inclusions as active elements of light-emitting and detecting devices based on silicon. For device applications, it is necessary to obtain a dense array of nanodimensional Ge islands on the Si surface, which can be accomplished, for example, using epitaxial technologies, in particular, molecular-beam epitaxy (MBE). An array of elastically stressed islands with nanometer-scale sizes is formed according to the Stranski–Krastanov mechanism as a result of the deposition of several Ge monolayers onto the surface of a single-crystal Si substrate using MBE. In general, the disadvantages of this method consist in a fairly large spread of the islands in relation to their shape and size. For example, in a temperature range from 550 to 600°C, two types of islands can be formed, i.e., multifaceted dome-shaped islands and pyramidal hut-shaped islands [1]. It has previously been shown [2] that, in growing the Ge islands on an Si substrate in a temperature range of 550–600°C, one can reduce the spread in the islands' sizes by exposing the surface simultaneously to fluxes of Sb_4 molecules and Ge atoms.

In this paper, we report the results of experiments with the growth of Ge islands at various Sb_4 fluxes incident on the substrate surface. The results obtained are discussed from the standpoint of the kinetic theory of formation of islands in systems that are mismatched with respect to their lattice parameters.

2. EXPERIMENT AND RESULTS

We used atomic-force microscopy (AFM) to experimentally study the effect of Sb surface concentration on the properties of an array of Ge islands on the Si (100) surface of the samples obtained as a result of growth experiments in an MBE system.

The samples under study were grown in a Riber SIVA-45 epitaxial system. A 100-nm-thick Si buffer layer was grown on the Si (100) surface for each sample. A Ge layer with an effective thickness of 0.8 nm was then deposited onto the Si buffer layer at a substrate temperature of 550°C; in all the cases, the deposition of Ge was accompanied by exposure of the surface to an antimony flux. The Ge growth rate was 0.016 nm/s. The Sb_4 flux was varied by adjusting the temperature of the antimony effusion source in a range from 450 to 550°C. In the course of the Ge deposition, the state of the surface was monitored using a system for reflection high-energy electron diffraction (RHEED). For samples 1–4 (see table), the RHEED pattern changed (the line reflections were replaced by point reflections) in the course of the formation of the Ge islands. This observation indicates that the elastically stressed Ge layer transforms into a system consisting of islands and a wetting layer. For sample 5, grown at the highest temperature of the antimony source, the RHEED pattern remained mainly linelike, and the lines corresponding to the most important reflections became thicker. Upon completion of the growth process, the samples were cooled to room temperature, removed from the growth chamber, and exposed to air. The samples' surfaces were then studied in a contactless mode using a Digital Instruments Inc. (USA) atomic-force microscope (AFM). NSC15/NoAl tips, produced by MicroMasch, were used in the AFM measurements.

1063-7826/05/3905-0547$26.00

The results of AFM measurements

Sample no.	Sb source temperature, °C	Multifaceted islands			Pyramidal islands		
		Base, nm	Height, nm	Density, cm^{-2}	Base, nm	Height, nm	Density, 10^{10} cm^{-2}
1	450	64.0	9.3	2.4×10^9	39.3	3.38	1.1
2	475				38.5	2.90	1.8
3	500				35.1	2.99	3.4
4	525				29.6	1.15	6.7
5	550	–	–	–	–	–	–

The main parameters of the growth experiments and the results of the AFM measurements are listed in the table.

In Fig. 1a, we show the AFM image of sample 1. It can be seen that pyramidal islands are present on the sample surface; the dome-shaped islands, which are not observed on other samples, are also present. This circumstance indicates that the effect of Sb on the formation of Ge islands is insignificant at a Sb source temperature of 450°C. Furthermore, the distributions in the shape and size of the islands are bimodal, as in the case of the deposition of pure Ge on the Si (100) surface [1]. Comparing this result with those reported in [2], we note that, in the case of the deposition of pure Ge on the Si surface at a substrate temperature of 450°C, the formation of the dome-shaped islands is accompanied by the formation of hut-shaped islands with rectangular or square bases; at the same time, the presence of even a small amount of Sb on the surface leads to the disappearance of the hut-shaped islands with the rectangular bases. In Fig. 1b, we show the AFM image of a surface area for sample 4. In this case, the size distribution of the islands is more uniform, their density is much higher, and their sizes are smaller than for sample 1. As the temperature of the Sb source is further increased to 550°C (sample 5), the structure changes radically. It follows from Fig. 1c that mesoscopic surface roughness with a characteristic height of less than 1 nm is observed for sample 5. This observation is consistent with the RHEED pattern obtained in situ. Thus, the nucleation of the islands at the surface becomes suppressed at a certain threshold value of the antimony flux. Experimental dependences of the surface density and the average lateral size of the islands on the temperature of the antimony source are shown in Fig. 2. As can be seen, the formation of islands in a Ge/Si(100) system exhibits threshold behavior in the presence of antimony; i.e., as the Sb concentration increases, the density of the islands' array first increases and then tends to zero as a certain threshold value of Sb concentration is exceeded. At the highest antimony flux used in this study, the suppression of the islands' formation and a transition to two-dimensional growth are observed. This effect is typically related to a decrease in the system's surface energy (the surfactant-mediated growth) [3]. In order to clarify the origin of the observed effect, we undertook an additional theoretical study of Ge/Si growth processes with the involvement of Sb.

3. THEORETICAL MODEL AND DISCUSSION OF THE RESULTS

As was shown in [4–7], the kinetic stage of the formation of quantum dots, according to the Stranski–Krastanov mechanism in heteroepitaxial systems, can be described in terms of classical nucleation theory [8]. The following expression was derived for the critical layer thickness that corresponds to a transition from two-dimensional to three-dimensional growth on the basis of the model suggested by Dubrovskii *et al.* [5] for the free energy of the islands' formation:

$$h_c = h_{eq}\left[1 + \left(\frac{2}{5}\frac{T_e}{T\ln Q}\right)^{1/2}\right]. \quad (1)$$

Here, h_{eq} is the equilibrium thickness of the wetting layer (h_{eq} is determined from the balance between the elastic and wetting forces [9] and is independent of the growth kinetics); T is the substrate temperature during the growth of the layer with quantum dots (this temperature is assumed to be constant); T_e is a quasi-equilibrium parameter that has the dimensions of temperature and is controlled by the surface energy, the islands' shape, and the lattice mismatch; and Q is a dimensionless kinetic parameter that depends on the conditions of epitaxial growth. As was shown in [5–7], the physical meaning of the parameter Q is the following: Q is the ratio between the characteristic time for the deposition of a material onto the surface and that for the growth of coherent islands from the atoms of the wetting layer. As a consequence, the dependence of Q on temperature T and the deposition rate V of the material is given by

$$Q \propto \frac{1}{V}\exp\left(-\frac{E_D}{k_B T}\right), \quad (2)$$

where k_B is the Boltzmann constant. The activation barrier E_D affects the rate at which the atom diffusion, caused by elastic stresses [4] and directed from the wetting layer to the islands, occurs.

We now consider the most important results of theoretical studies concerned with the formation kinetics of supercritical quantum dots (at an effective deposited-layer thickness H_0 that appreciably exceeds h_c). These results were reported in [5–7]. The nucleation of the islands occurs in the time period from $t_c - \Delta t$ to $t_c + \Delta t$, where $t_c = h_c/V$ is the time interval for growing a critical-thickness layer under the given conditions of heteroepitaxial growth. Upon completion of the nucleation

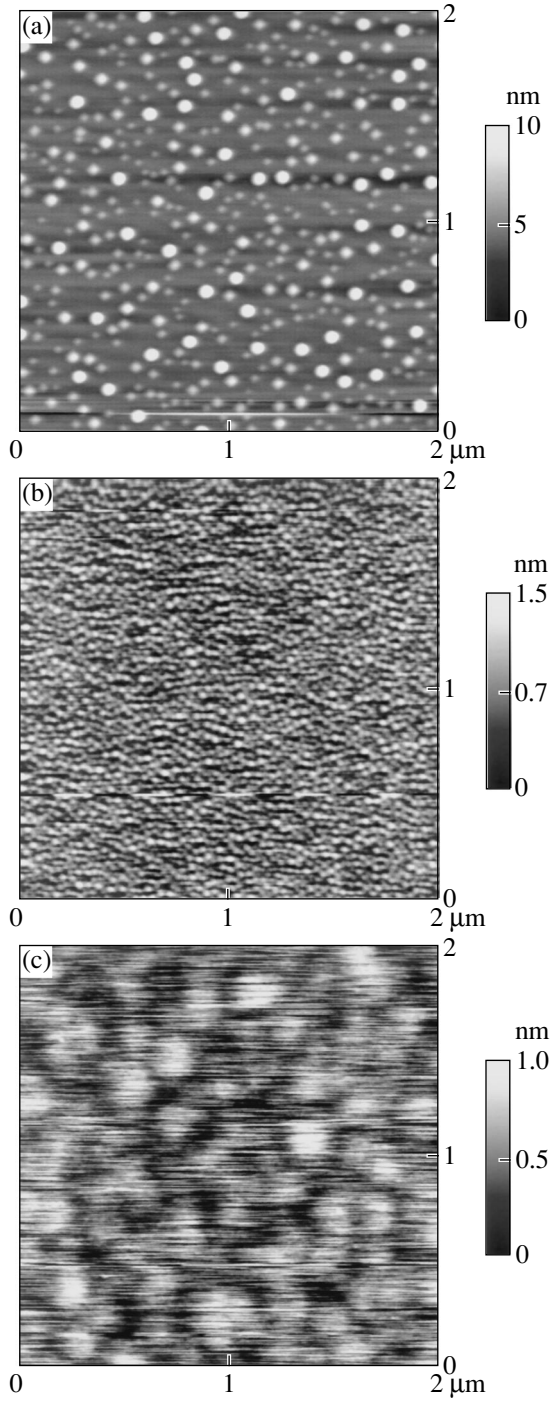

Fig. 1. AFM images of the surface for (a) sample 1, (b) sample 4, and (c) sample 5. The scanned area is 2×2 μm^2 for all the samples.

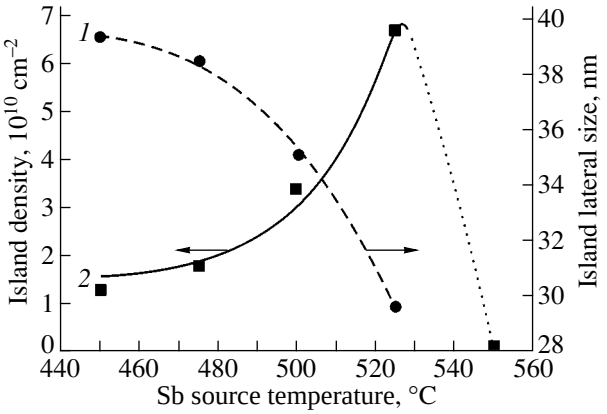

Fig. 2. Experimental dependences of (*1*) the average lateral size and (*2*) the density of islands on the Sb source temperature for samples 1–5.

stage (at $t > t_c + \Delta t$), the surface density of the islands N attains the constant value

$$N = N_0 \frac{T}{T_e}\left(\frac{\ln Q}{Q}\right)^{3/2}. \quad (3)$$

Here, N_0 is a known constant that is independent of the growth conditions. Upon completion of the nucleation stage, a longer stage sets in during which relaxation of the islands' sizes occurs. The average lateral size L of the islands increases to its quasi-stationary value L_R at $t \approx t_c + 3t_R$, where t_R is the characteristic time of the islands' size relaxation. The quasi-stationary average size of the islands depends on their surface density and also on the effective thickness of the deposited layer:

$$L_R = C_0\left(\frac{H_0 - h_{eq}}{N}\right)^{1/3}. \quad (4)$$

Here, C_0 is a dimensionless constant controlled by the shape of the islands. This shape is assumed to be independent of the growth conditions in the kinetic stage of the islands' formation.

In the case where the structure was not exposed to the antimony flux (for example, if the surface was immediately cooled or the structure was overgrown at a low temperature after interruption of the growth of the layer with quantum dots), the experimental value of the islands' average size can be much smaller than L_R. The time dependence of the average size is given by $L = L_R f[(t - t_c)/t_R]$, where $f(x)$ is an ascending function of x (this function was defined in [7]; it is important that $f(0) = 0$ and $f(3) \approx 1$). In the absence of exposure of the surface to the antimony flux, the islands' size $L(t_0)$ at the instant ($t_0 = H_0/V$) when the growth was interrupted after the deposition of the H_0 Ge monolayers is given by

$$L(t_0) = L_R f\left(\frac{H_0 - h_c}{V t_R}\right). \quad (5)$$

An analysis of recent results [5–7] suggests that the dependences of the characteristic durations of the nucleation stage and the stage in which the size relaxation on Q occurs can be written as

$$\Delta t \propto \frac{1}{(\ln Q)^{3/2}}, \quad t_R \propto \frac{1}{(\ln Q)^{5/6}}. \quad (6)$$

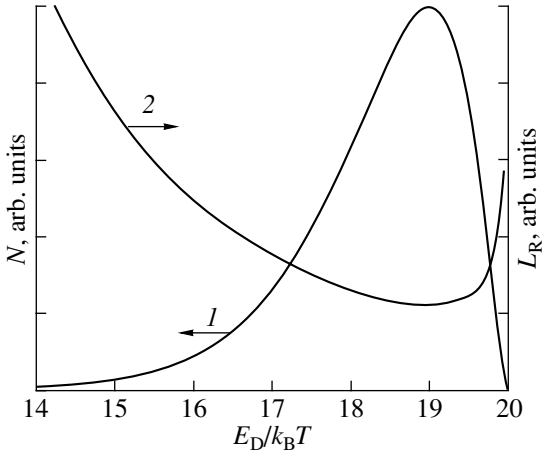

Fig. 3. Dependences of (*1*) the surface density of islands N and (*2*) their quasi-stationary lateral size L_R on the parameter E_D/k_BT; this parameter increases as the Sb flux increases.

Further evolution of the system requires a long-term exposure of the structure and occurs at time instants that appreciably exceed $t_c + 3t_R$.

The condition for the applicability of classical nucleation theory consists in the smallness of the thermodynamic fluctuation in the subcritical region: $\exp(F) \gg 1$, where F is the nucleation-activation barrier height expressed in thermal units [10]. In the model under consideration, it is this condition that makes it possible to derive a relation between the lowest activation barrier for the islands' nucleation at the largest thickness $h = h_c$ of the wetting layer and the kinetic parameter Q [5]:

$$F(h_c) = (5/2)\ln Q. \qquad (7)$$

Formula (1), describing the critical thickness, is a consequence of expression (7), which represents a specific form of the free energy for coherent-island formation. Evidently, the condition for the applicability of nucleation theory is satisfied with confidence in the case of $Q \gg 1$, which was analyzed in detail in [5–7].

However, as follows from expression (2), the value of the kinetic parameter Q decreases exponentially as the surface temperature T decreases and the height of the activation barrier E_D for the diffusion of atoms from the wetting layer to an island increases. The physical cause of this phenomenon is a retardation of the diffusion processes at the surface due to either a decrease in temperature or the use of impurities that restrict the diffusive motion. As has been shown recently (see, for example, [2]), one such diffusion-restricting impurity for a Ge/Si system is Sb. In the context of a simplified model, we assume that an increase in the Sb source temperature and the corresponding increases in the Sb concentration on the surface appreciably increase the effective barrier height E_D for the diffusion of Ge atoms from the wetting layer into an island (the quantity E_D appears in Q in formula (3) for N) and affects, to a lesser extent, the surface energy of the system (this energy appears in T_e in the same formula). Considering N and L_R as functions of Q for the constants T, T_e, and H_0, we ascertain that, in accordance with formulas (3) and (4), the density of the islands invariably exhibits a maximum, whereas their quasi-stationary size exhibits a minimum at $Q = e$. At the instant of growth interruption t_0, the islands' size $L(t_0)$, in accordance with formula (5), decreases progressively in comparison with L_R. This decrease is caused by both an increase in the critical thickness h_c (see formula (1)) and an increase in the size-relaxation time t_R (see formula (6)). Thus, as Q decreases to the threshold value $Q \sim e$, the suppression of nucleation in the heteroepitaxial system sets in. The height of the activation barrier for nucleation is small according to formula (7); consequently, there are no thermodynamic obstacles to the formation of islands. However, in this case, the nucleation rate and the islands' surface density are profoundly affected by the preexponential kinetic factor in the corresponding expression [8], which is proportional to the diffusion rate. The islands just cannot form, since the mechanism by which materials are transported from the wetting layer to an island is lacking under the conditions of an almost complete suppression of diffusion; at the same time, the probability of atoms arriving directly from the molecular flux is low. Theoretical dependences of the islands' surface density N and their lateral size L_R upon completion of the relaxation stage on the height of the diffusion-activation barrier, expressed in the thermal units E_D/k_BT, are shown in Fig. 3.

We should note the satisfactory qualitative agreement existing between the experimental data (Fig. 2) and the results of the theoretical calculations (Fig. 3) in the context of the application of the model under consideration to an interpretation of the reported experimental data on the dependences of the density and average size of quantum dots in a Ge/Si(100) system on a Sb flux. Figures 2 and 3 both indicate that the dependence of the islands' formation on Sb concentration is of a threshold type. However, owing to the following reasons, we should not expect good quantitative agreement between the theory and experiment. First, a quantitative relation between the Sb source temperature and the surface concentration of the adsorbed Sb atoms is not clear. The same is also true for the relation between the Sb concentration and the value of the activation-barrier height for the diffusion of Ge atoms. Second, an increase in the Sb concentration brings about an increase in the surface energy of the islands' lateral faces and, consequently, also affects the height of the activation barrier for nucleation. Finally, nucleation theory itself is on the verge of the applicability domain at small values of the parameter $Q \sim e$; therefore, this theory holds only qualitatively in this case.

4. CONCLUSION

The results obtained in this study indicate unambiguously that the behavior of the structural characteristics of quantum dots in a heteroepitaxial Ge/Si(100) system is nonmonotonic and threshold-like as the antimony concentration on the surface increases. This effect can be qualitatively explained as follows. At first, as the Sb flux increases, the surface density of the Ge islands increases significantly while, simultaneously, their lateral sizes decrease. This behavior is completely consistent with the mechanism that was outlined in [10] and described theoretically in [5–7]. The presence of Sb retards the diffusive supply of Ge atoms to the growing islands; as a result, the size of the islands decreases. The height of the activation barrier for the islands' nucleation also decreases; consequently, the nucleation rate for the islands and their surface density increase. However, a further inhibition of diffusion leads to quenching of the islands' nucleation in the system; therefore, the islands' density decreases drastically after a certain maximum value of this density has been attained. The time required for the nucleation and growth of the islands increases appreciably, and, as a result, their lateral size cannot attain the corresponding quasi-equilibrium value. As was shown, the threshold effect of quenching for nucleation can be qualitatively explained in the context of the kinetic model of coherent-island formation in heteroepitaxial systems [5–7]. However, quantitative studies require further development of the theory; in addition, more detailed experiments are needed.

ACKNOWLEDGMENTS

This study was supported in part by the scientific program Low-Dimensional Quantum Structures of the Russian Academy of Sciences.

G.E. Cirlin acknowledges the support of Alexander von Humboldt Stiftung. A.A. Tonkikh thanks the Deutsche Forschungsgemeinschaft.

REFERENCES

1. O. P. Pchelyakov, Yu. B. Bolkhovityanov, A. V. Dvurechenskiĭ, *et al.*, Fiz. Tekh. Poluprovodn. (St. Petersburg) **34**, 1281 (2000) [Semiconductors **34**, 1229 (2000)].
2. A. A. Tonkikh, G. E. Cirlin, V. G. Dubrovskiĭ, *et al.*, Fiz. Tekh. Poluprovodn. (St. Petersburg) **38**, 1239 (2004) [Semiconductors **38**, 1202 (2004)].
3. I. Berbezier, A. Ronda, A. Portavoce, and N. Motta, Appl. Phys. Lett. **83**, 4833 (2003).
4. A. V. Osipov, F. Schmitt, S. A. Kukushkin, and P. Hess, Appl. Surf. Sci. **188**, 156 (2002).
5. V. G. Dubrovskiĭ, G. E. Cirlin, and V. M. Ustinov, Phys. Rev. B **68**, 075409 (2003).
6. V. G. Dubrovskiĭ, Yu. G. Musikhin, G. E. Cirlin, *et al.*, Fiz. Tekh. Poluprovodn. (St. Petersburg) **38**, 342 (2004) [Semiconductors **38**, 329 (2004)].
7. V. G. Dubrovskiĭ, G. E. Cirlin, Yu. G. Musikhin, *et al.*, J. Cryst. Growth **267**, 47 (2004).
8. D. Kashchiev, *Nucleation: Basic Theory with Applications* (Butterworth Heinemann, Oxford, 2000).
9. P. Müller and R. Kern, Appl. Surf. Sci. **102**, 6 (1996).
10. F. M. Kuni, Preprint No. 84-178.E (ITP, Kiev, 1984).

Translated by A. Spitsyn

Semiconductors, Vol. 39, No. 5, 2005, pp. 552–556. Translated from Fizika i Tekhnika Poluprovodnikov, Vol. 39, No. 5, 2005, pp. 582–586.

LOW-DIMENSIONAL SYSTEMS

The Formation of Silicon Nanocrystals in SiO_2 Layers by the Implantation of Si Ions with Intermediate Heat Treatments

G. A. Kachurin*, V. A. Volodin*, D. I. Tetel'baum, D. V. Marin*, A. F. Leĭer*, A. K. Gutakovskiĭ*, A. G. Cherkov*, and A. N. Mikhaĭlov****

**Institute of Semiconductor Physics, Siberian Division, Russian Academy of Sciences, pr. Akademika Lavrent'eva 13, Novosibirsk, 630090 Russia*

***Nizhni Novgorod State University, pr. Gagarina 23, Nizhni Novgorod, 603950 Russia*

Submitted June 22, 2004; accepted for publication October 6, 2004

Abstract—The effect of heat treatments at 1100°C on an ion-beam synthesis of Si nanocrystals in SiO_2 layers is studied. The ion-implanted samples are subjected either to a single heat treatment after the total ion dose (10^{17} cm^{-2}) has been implanted, two heat treatments (a heat treatment after the ion implantation of each half of the total dose), or three heat treatments (a heat treatment after each third of the dose). The total duration of the heat treatments is maintained at 2 h. It is found that the intermediate heat treatments lead to a shift of the Raman spectrum of the nanocrystals to longer wavelengths and to a shift of the photoluminescence spectrum to shorter wavelengths. Study using electron microscopy shows that the size of the nanoprecipitates decreases, which is accompanied by the disappearance of the characteristic features of crystallinity; however, the features of photoluminescence remain characteristic of the nanocrystals. The experimental data obtained are accounted for by a preferential drain of Si atoms to newly formed clusters, which is consistent with the results of a corresponding numerical simulation. It is believed that small nanocrystals make the main contribution to photoluminescence, whereas the Raman scattering and electron microscopy are more sensitive to larger nanocrystals.

1. INTRODUCTION

Studies of the formation of silicon nanostructures and modification of the properties of these structures are important for the following three reasons: First, silicon is (and will remain in the near future) the main material used in microelectronics. Second, the central tendency in microelectronics, a progressive decrease in the sizes of device components leading to an eventual transition to the nanometer range, persists. Third, the discovered ability of silicon nanocrystals to emit intense visible light opens up fresh opportunities for the fabrication of silicon integrated circuits with the electrical and optical processing of information. At present, Si nanocrystals are typically formed by taking advantage of their self-organization after the decomposition of a supersaturated Si solid solution in SiO_2. It is believed that ion implantation is the most promising method for such a synthesis of Si nanocrystals [1–5]. The synthesis conditions have been found to be rather severe: an Si ion dose of ~10^{17} cm^{-2} and postimplantation-annealing temperature of ~1100°C are required. Recently, methods that can stimulate the formation of nanostructures or intentionally modify their properties have been under development. These methods include the doping of nanocrystals [6, 7], use of pulsed heat treatments [4], introduction of additional precipitation centers [8, 9], high-temperature implantation [10], heat treatments of samples subjected to pressure [11], and so on. Variation of the conditions of the self-organization of nanocrystals is another possible method for affecting their properties. It is well known that the decomposition of solid solutions proceeds in three stages: (i) the formation of stable nuclei, (ii) a diffusion-limited (or reaction-limited) increase in the nanocrystals' sizes, and (iii) Ostwald's ripening. In order to control the sizes of CdS nanocrystals in glass and Ge nanocrystals in SiO_2, the use of intermediate heat treatments that stimulate nucleation but are insufficient to cause an increase in the nanoparticles' sizes, due to the diffusive drain and Ostwald's ripening, has been suggested [12, 13]. We believe that intermediate heat treatments in the course of a synthesis induced by ion implantation may not only affect the formation of nanocrystals but can also clarify the mechanism of their formation. This consideration encouraged us to undertake this study.

2. EXPERIMENTAL

Si ions with an energy of 140 keV were implanted into SiO_2 layers that had a thickness of ~0.6 μm and were grown thermally on silicon substrates. The ion-current density was no higher than 5 $\mu A/cm^2$. We used three variants of ion-implantation synthesis; in each case, the total ion dose and total duration of the heat treatments were kept constant. As a result, we obtained samples of three types in accordance with the following conditions:

(1) samples implanted with an ion dose of 10^{17} cm^{-2} and then annealed once for 2 h at 1100°C;

(2) samples implanted with an ion dose of 5×10^{16} cm^{-2} and subsequently annealed for 1 h at 1100°C followed by a second implantation at the same dose and by the same annealing procedure; and

(3) implantation with a dose of 3.3×10^{16} cm^{-2} and subsequent annealing for 40 min at 1100°C; this procedure was then repeated twice.

All the heat treatments were carried out in a nitrogen atmosphere. According to computations of the ion ranges using the TRIM-95 software package, the content of excess Si atoms at the peak of its distribution amounted to ~10 at. %. In order to study the samples, we analyzed the photoluminescence (PL) and Raman spectra and examined images obtained by high-resolution electron microscopy (HREM) at transverse sections of the samples. The PL was excited using a nitrogen laser with the radiation wavelength $\lambda = 337$ nm and was detected using an FÉU-79 photomultiplier. All the spectra were normalized, taking into account the spectral sensitivity of the instrumentation. The emission of an argon laser with $\lambda = 514$ nm was used as a pump for the Raman scattering. In order to suppress the signal from the silicon substrate, we chose the quasi-backscattering geometry of the Raman process $Z(XX)\bar{Z}$, where Z corresponds to the $\langle 001 \rangle$ direction and X corresponds to the $\langle 100 \rangle$ direction. Both the Raman and PL spectra were measured at room temperature. The transverse cuts were prepared using the standard method. The electron microscopy studies were carried out using a JEM-4000EX microscope (the JEOL Co.).

3. RESULTS

In Fig. 1, we show the Raman spectra of the samples obtained using the three above-described modes of ion-beam synthesis of nanoprecipitates. A clearly pronounced additional peak at about 510 cm^{-1} appeared near a band peaked at 520 cm^{-1} and caused by the scattering from the crystalline silicon substrate after implantation of the total dose of Si ions and the subsequent annealing (Fig. 1*a*). The additional peak indicates that Si nanocrystals have formed. In addition, a low-intensity broad Raman band can be seen in the region 480 cm^{-1}; the Si–Si bonds in amorphous silicon are effective scatterers in this region. The transition to the implantation mode with an intermediate annealing changes the spectrum radically (Fig. 1*b*). The intensity of the additional peaks becomes much lower, and the peak itself is found to be shifted to longer wavelengths (to ~507 cm^{-1}). The mentioned tendencies became even more pronounced after the ion-beam synthesis with two intermediate heat treatments. As can be seen from Fig. 1*c*, the additional scattering characteristic of small silicon nanocrystals disappears almost completely. Only a trace of additional scattering can be observed at about 504 cm^{-1}; however, the intensity of this scattering

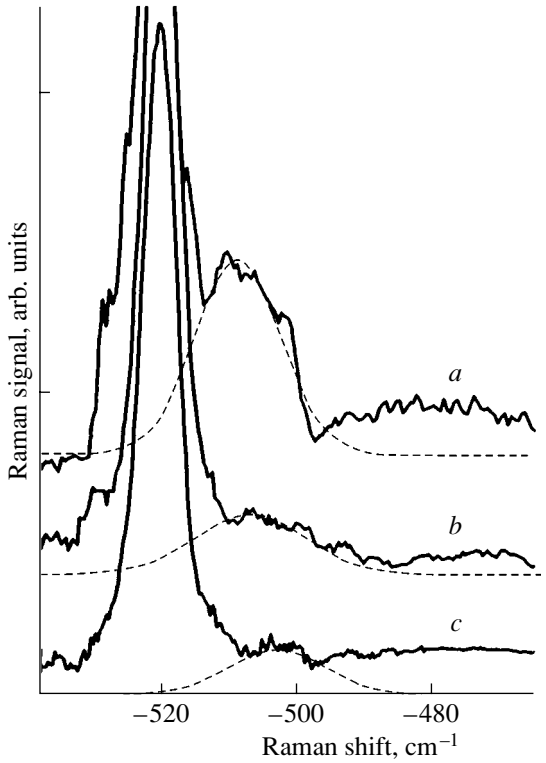

Fig. 1. The Raman spectra of the samples obtained in (*a*) mode 1, (*b*) mode 2, and (*c*) mode 3 of the implantation and annealing.

is comparable to that of noise. For clarity of presentation, the changes in the spectra related to nanocrystals are illustrated by the drawn Gaussian curves.

According to the data provided by high-resolution electron microscopy at the transverse cut, a single implantation with a dose of 10^{17} cm^{-2} and subsequent annealing lead to the formation of silicon nanoprecipitates with crystalline structures (Fig. 2a). The nanocrystals' sizes are 4–5 nm, and their density is ~(10^{11}–10^{12}) cm^{-2}. If the ions were implanted in portions with intermediate heat treatments, the nanoprecipitates could be seen (as dark spots) in the HREM images of the SiO_2 cleaved surfaces. We failed to detect any specific features of crystalline structure for these nanoprecipitates. Similar spots have been observed previously and repeatedly by several researchers in cases where the conditions of synthesis were found to be insufficient for the formation of distinct nanocrystals [5, 14–16]. Intermediate heat treatments lead to a decrease in the average sizes of the precipitates to ~(3–4) nm and to a slight decrease in their concentration (Figs. 2b, 2c). Any quantitative comparisons are hardly justified here owing to the small size of the scanned area.

The PL spectra after the ion-beam synthesis in each of the three modes of implantation and annealing are shown in Fig. 3. In this case, in contrast to the data obtained by the Raman scattering and electron microscopy, in which the attributes of the silicon nanocrystals

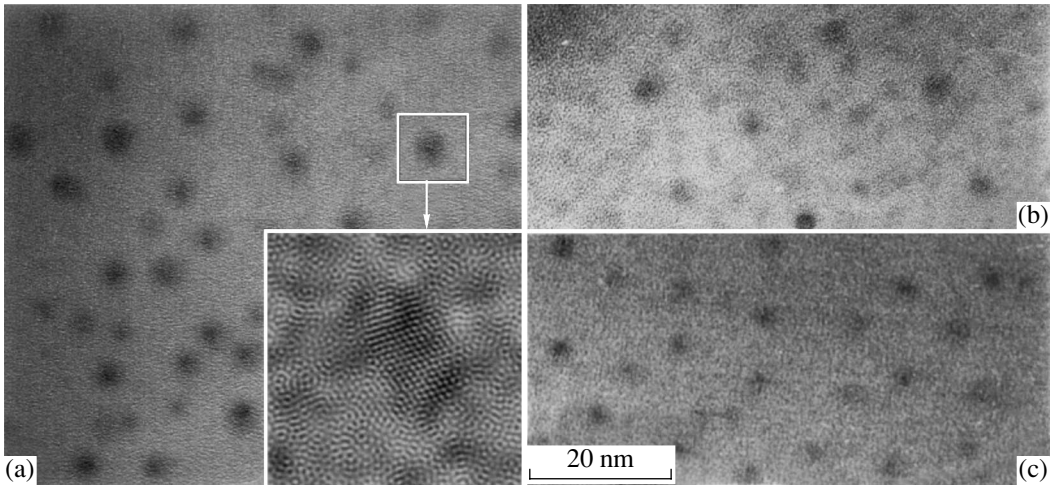

Fig. 2. Images of transverse sections of the samples prepared using (a) mode 1, (b) mode 2, and (c) mode 3 of the implantation and annealing. The images were obtained by high-resolution electron microscopy. The inset in (a) illustrates that the crystallinity of the inclusions is revealed within a selected area after the Fourier filtering.

were much less pronounced if intermediate heat treatments were used, the luminescence of the nanocrystals was affected by the intermediate heat treatments to a lesser extent. In the case of a single implantation of the total dose and subsequent annealing, a high-intensity band with the peak at about 795 nm was observed in the PL spectrum. At present, almost all researchers relate this band to radiative recombination in the formed silicon nanocrystals. The implantation with a single intermediate annealing led to a slight decrease in the emission intensity; however, no significant shift of the peak was observed. If the dose of 10^{17} cm^{-2} was built up in three portions, a further decrease in the PL intensity was observed; in addition, a shift of the peak to shorter wavelengths (to ~785 nm) becomes apparent. Thus, the use of two intermediate heat treatments reduced the nanocrystal-related PL intensity only by a factor slightly exceeding 2. At the same time, it was practically impossible to detect the attributes of the nanocrystals using the Raman scattering or high-resolution electron microscopy after this mode of implantation and annealing.

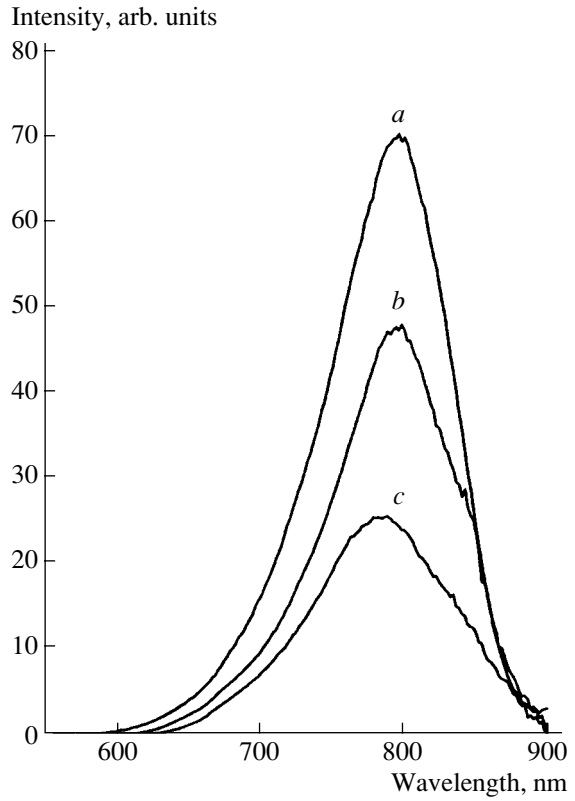

Fig. 3. The photoluminescence spectra of the samples obtained in (*a*) mode 1, (*b*) mode 2, and (*c*) mode 3 of the implantation and annealing.

4. DISCUSSION

A specific feature of the ion-beam synthesis of silicon quantum dots using intermediate heat treatments consists in the fact the preceding stage gives rise to potential sinks for the Si atoms introduced in the subsequent stage. These atoms can either form new stable nanoprecipitates (sinks) or diffuse to the previously formed nanoprecipitates and ensure an increase in their sizes. An increase in the size of the nanocrystals should give rise to a shift of the peak of the Raman scattering to 520 cm^{-1}, i.e., to the wavelength characteristic of scattering in bulk silicon. As the size of the nanocrystals decreases, the peak shifts to the longer wavelengths characteristic of scattering by the Si–Si bonds in amorphous Si (~480 cm^{-1}). As the nanocrystals become larger, the PL band caused by quantum-confinement effects should shift to longer wavelengths. Our measurements of the optical characteristics indicate that the

nanocrystals become smaller rather than larger if intermediate heat treatments are used. The data obtained by electron microscopy also directly indicate that the nanocrystals' sizes decrease (Fig. 2). It is apparent that the Si atoms are preferentially deposited on the newly formed sinks (primary silicon clusters) in the course of the intermediate heat treatments. In this context, it was of interest to estimate the probability of binding the Si atoms into the aforementioned clusters and the number and sizes of these clusters in relation to the concentration of implanted excess Si. A numerical simulation was used in the estimations. The scheme of Monte Carlo calculations employed was similar to that described in [17]; however, in contrast to [17], where two-dimensional space was considered, we solved the problem using a three-dimensional tetrahedral network that contained 10^6 nodes (this corresponds to the volume of $\sim 2 \times 10^{-17}$ cm^3). We used cyclic boundary conditions. The results of the simulation are shown in Fig. 4. It can be seen that, in the range of excess Si concentrations 0–20 at %, the probability of silicon binding increases rapidly as the dose increases; however, about half of the Si atoms remain free even if the supersaturation amounts to 10 at %. The prevalent type of precipitate is represented by small clusters that include no more than ten atoms. In the case of supersaturation amounting to 4 at %, the number of Si clusters incorporating 25–30 Si atoms is ~100 (the corresponding concentration is $\sim 5 \times 10^{18}$ cm^{-3}) and the number of clusters incorporating 95–100 Si atoms is ~10 (the concentration is $\sim 5 \times 10^{17}$ cm^{-3}). The observed decrease in the number of clusters formed at higher doses is caused by an increase in the size of these clusters, by their coagulation, or by exceeding the space involved in the calculations. If we compare the calculated concentrations of clusters with the nanocrystal concentrations experimentally observed after annealing ($\sim(10^{16}$–$10^{17})$ cm^{-3}), it seems likely that, for the introduced Si atoms, the nearest sinks are the newly formed clusters rather than the previously formed nanocrystals. As a result, the use of intermediate heat treatments leads to a decrease in the average sizes of the nanocrystals and corresponding variations in their optical characteristics.

The decrease in the nanocrystals' sizes as the intermediate heat treatments are introduced gives rise to different responses of the measurement methods to changes in the conditions of the ion-beam synthesis. The rapid decrease in the intensity of the Raman scattering with the retention of fairly intense PL when the first mode of implantation and annealing is replaced by the second is apparently caused by the fact that, for these two methods, the major contributions to the signals are made by nanocrystals of different sizes. Relatively large nanocrystals are needed for the observation of the Raman scattering. Evidence supporting this conclusion can be found in a number of publications [1, 3, 18]. In contrast, smaller Si nanocrystals can still contribute to the luminescence. Although it is not possible to reveal

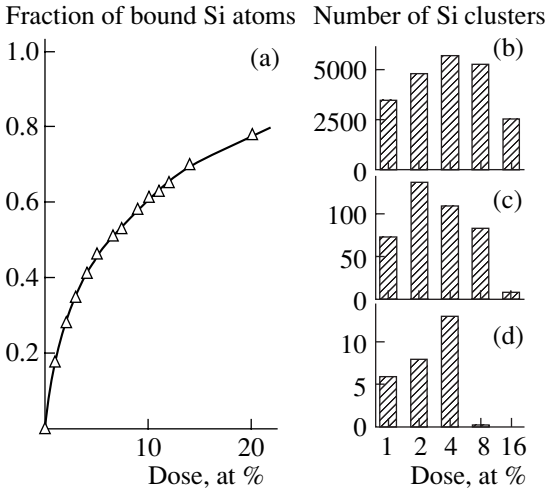

Fig. 4. (a) The fraction of bound Si atoms in relation to the Si ion dose. The number of Si clusters, with their sizes corresponding to (b) no more than 10 atoms, (c) 25–30 atoms, and (d) 95–100 atoms, in relation to the Si ion dose according to the results of the numerical simulation.

the characteristic features of crystallinity if the third mode of implantation and annealing is used, we believe that it is the nanocrystals (rather than defects or Si clusters) that are responsible for the photoluminescence in this case. The main argument in favor of this conclusion is the retention of the clearly pronounced PL band with a peak in the vicinity of 785 nm. In experiments where the conditions required for the synthesis of Si nanocrystals were satisfied, such bands were always observed at the wavelengths $\lambda > 700$ nm [1–9, 19]. Otherwise, only a broad PL band at $\lambda < 700$ nm with a very low intensity can be detected [2]. We believe that such changes in PL are related to deterioration of the crystallinity of Si in ultrasmall volumes. According to Veprek *et al.* [20], as a result of the effect of surface-layer strain on the lattice, the smallest possible size that Si nanocrystals can reach should be equal to 2–3 nm. The presence of a transitional surface layer with a thickness of ~1 nm in nanocrystals has also been reported [18, 21–23]. According to calculations [22], the surface layer exerts compression, and, in order for the diamond-like lattice to be preserved, the diameter of a silicon cluster should be no smaller than 2.3–2.8 nm (this corresponds to 300–500 atoms in a cluster). It is clear that the lattice can also be perturbed in clusters with larger sizes. For example, it was found experimentally [21] that the bond lengths and angles in implantation-synthesized Ge nanocrystals with sizes of no less than 14 nm differ somewhat from those in an ideal tetrahedron of bulk Ge. All these factors make the identification of small nanocrystals difficult when using the methods of Raman scattering and electron microscopy.

5. CONCLUSIONS

Experiments with the introduction of intermediate heat treatments and a constant total implantation dose of 10^{17} cm^{-2} used for the formation of silicon nanocrystals showed the following. Intermediate heat treatments do not lead to an increase in the sizes of nanocrystals, as would be expected if there was a diffusive drain of newly introduced excess Si atoms to these nanocrystals. In contrast, such heat treatments reduce the average size of silicon nanocrystals; as a result, the peak in the Raman spectrum shifts to longer wavelengths and the peak in the photoluminescence (PL) spectrum shifts to shorter wavelengths. According to the data of electron microscopy, the average size of the precipitates decreases from ~(4–5) nm to ~(3–4) nm. This decrease is caused by the high probability of nucleation in all the modes of implantation and annealing used in this study. This circumstance predetermines the preferential drain of newly introduced silicon to the forming centers and, correspondingly, the decrease in the average sizes of the precipitates. The high probability of the clusterization of Si atoms is confirmed by the results of a numerical simulation. The changes in the PL spectra as the nanocrystals' sizes decrease indicate that the PL sources are still represented by small silicon nanocrystals rather than, for example, silicon clusters. At the same time, as the average size of the precipitates decreases, it becomes nearly impossible to reveal the attributes of crystallinity using the Raman scattering and electron microscopy. The possible causes of this effect are (i) the increasing role of transitional surface layers and (ii) disruption of the lattice ideality in the nanocrystals as their sizes decreases. Due to differing sensitivity to the strains of the methods used, the PL data on the one hand and the data of the Raman scattering and electron microscopy on the other hand can be related to Si nanocrystals of different sizes. This circumstance should be taken into account when comparing and analyzing the results obtained by the above methods.

ACKNOWLEDGMENTS

We thank O.S. Stremyakova for her help in carrying out the experiments.

This study was supported in part by the Russian Foundation for Basic Research (project nos. 00-02-17963 and 04-02-16286) and INTAS (grant no. 00-0064).

REFERENCES

1. T. Shimizu-Iwaima, K. Fujita, S. Nakao, *et al.*, J. Appl. Phys. **75**, 7779 (1994).
2. P. Mutti, G. Ghislotti, S. Bertoni, *et al.*, Appl. Phys. Lett. **66**, 851 (1995).
3. E. Wendler, U. Herrmann, W. Wesh, and H. H. Dunken, Nucl. Instrum. Methods Phys. Res. B **116**, 332 (1996).
4. G. A. Kachurin, K. S. Zhuravlev, N. A. Pazdnikov, *et al.*, Nucl. Instrum. Methods Phys. Res. B **127–128**, 583 (1997).
5. G. A. Kachurin, A. F. Leĭer, K. S. Zhuravlev, *et al.*, Fiz. Tekh. Poluprovodn. (St. Petersburg) **32**, 1371 (1998) [Semiconductors **32**, 1222 (1998)].
6. A. Mimura, M. Fujii, S. Hayashi, *et al.*, Phys. Rev. B **62**, 12625 (2000).
7. G. A. Kachurin, S. G. Yanovskaya, D. I. Tetel'baum, and A. N. Mikhaĭlov, Fiz. Tekh. Poluprovodn. (St. Petersburg) **37**, 738 (2003) [Semiconductors **37**, 713 (2003)].
8. J. Zhao, D. S. Mao, Z. X. Lin, *et al.*, Appl. Phys. Lett. **74**, 1403 (1999).
9. G. A. Kachurin, S. G. Yanovskaya, K. S. Zhuravlev, and M.-O. Ruault, Fiz. Tekh. Poluprovodn. (St. Petersburg) **35**, 1235 (2001) [Semiconductors **35**, 1182 (2001)].
10. V. G. Kesler, S. G. Yanovskaya, G. A. Kachurin, *et al.*, Surf. Interface Anal. **33**, 914 (2002).
11. I. E. Tyschenko, L. Rebohle, R. A. Yankov, *et al.*, J. Lumin. **80**, 229 (1999).
12. B. G. Potters and J. H. Simmons, Phys. Rev. B **37**, 10838 (1988).
13. Y. Maeda, Phys. Rev. B **51**, 1658 (1995).
14. S. P. Withrow, C. W. White, A. Meldrum, *et al.*, J. Appl. Phys. **86**, 396 (1999).
15. L. You, C. L. Heng, S. Y. Ma, *et al.*, J. Cryst. Growth **212**, 109 (2000).
16. X. Du, M. Takeguchi, M. Tanaka, and K. Furuya, Appl. Phys. Lett. **82**, 1108 (2003).
17. A. F. Leĭer, L. N. Safronov, and G. A. Kachurin, Fiz. Tekh. Poluprovodn. (St. Petersburg) **33**, 389 (1999) [Semiconductors **33**, 380 (1999)].
18. G. A. Kachurin, S. G. Yanovskaya, V. A. Volodin, *et al.*, Fiz. Tekh. Poluprovodn. (St. Petersburg) **36**, 685 (2002) [Semiconductors **36**, 647 (2002)].
19. B. Fernandez, M. Lopez, C. Garcia, *et al.*, J. Appl. Phys. **91**, 798 (2002).
20. S. Veprek, Z. Iqbal, and F.-A. Sarott, Philos. Mag. B **45**, 137 (1982).
21. A. Cheung, G. de M. Azevedo, C. J. Glover, *et al.*, Appl. Phys. Lett. **84**, 278 (2004).
22. D. K. Yu, R. Q. Zhang, and S. T. Lee, Phys. Rev. B **65**, 245417 (2002).
23. F. Iacona, C. Bongiorno, C. Spinella, *et al.*, J. Appl. Phys. **95**, 3723 (2004).

Translated by A. Spitsyn

Semiconductors, Vol. 39, No. 5, 2005, pp. 557–564. Translated from Fizika i Tekhnika Poluprovodnikov, Vol. 39, No. 5, 2005, pp. 587–594.

LOW-DIMENSIONAL SYSTEMS

The Diffusion Mechanism in the Formation of GaAs and AlGaAs Nanowhiskers during the Process of Molecular-Beam Epitaxy

G. E. Cirlin[1, 2]^, V. G. Dubrovskiĭ[2], N. V. Sibirev[1], I. P. Soshnikov[2], Yu. B. Samsonenko[1, 2], A. A. Tonkikh[1, 2], and V. M. Ustinov[2]

[1]*Institute for Analytical Instrumentation, Russian Academy of Sciences, Rizhskiĭ pr. 26, St. Petersburg, 190103 Russia*
[2]*Ioffe Physicotechnical Institute, Russian Academy of Sciences, ul. Politekhnicheskaya 26, St. Petersburg, 194021 Russia*
^e-mail: cirlin@beam.ioffe.ru

Submitted September 27, 2004; accepted for publication October 12, 2004

Abstract—The formation of GaAs and AlGaAs nanowhiskers using molecular-beam epitaxy on GaAs (111)B surfaces activated with Au is theoretically and experimentally studied. It is experimentally shown that nanowhiskers whose length exceeds the effective thickness of the deposited GaAs by an order of magnitude can be grown. It is found that the experimental dependences of the nanowhisker length L on its diameter D can differ radically from those observed in the case of a vapor–liquid–solid growth mechanism. The $L(D)$ dependences obtained in this study are decreasing functions of D. The above effects are related to the existence of the diffusion transport of atoms from the surface towards the tips of the whiskers, which leads to a considerable increase in the growth rate of thin whiskers. A theoretical model of the formation of nanowhiskers in the process of molecular-beam epitaxy is developed. The model provides a unified description of the vapor–liquid–solid and diffusion growth mechanisms and qualitatively explains the experimental results obtained. © *2005 Pleiades Publishing, Inc.*

1. INTRODUCTION

Nanowhiskers (NWs) are crystals whose cross-sectional dimension D is of the order of 10–100 nm and whose length L exceeds D by an order of magnitude or more. The unique properties of NWs are first and foremost related to the high values of the L/D ratio in the nanometer size range [1]. NWs made of various semiconductor materials (such as Si, GaAs, and InP) are promising in relation to their application in microelectronics and optoelectronics [2–5] as well as in many other fields (where they find uses in multiple-tip cathodes, tips for tunneling microscopes, gas analyzers, etc.). The structural properties of NWs (their length, size, and areal density) are determined, to a large extent, by the preparation of the surface used and by the growth process itself. The fabrication of NW ensembles with controlled structural properties requires detailed studies of the processes used in NW formation. At present, NWs are usually grown by vapor-phase epitaxy (VPE) [2–4, 6–8] and, less frequently, by molecular-beam epitaxy (MBE) [5, 9–11] on surfaces activated with a catalyst substance. However, MBE has certain advantages over VPE as a result of its larger deviation from equilibrium growth conditions [12], which facilitates the attainment of considerably higher L/D ratios and smaller cross-sectional sizes.

Intensive investigations of the formation and structural properties of whiskers grown on activated surfaces was initiated by a publication of Wagner and Ellis [13], who studied Si whisker growth on Au-activated Si (111) surfaces. In Russia, progress in this field is predominantly related to the studies of Givargizov [14]. By the mid-1970s, the basic ideas about the vapor–liquid–solid (VLS) mechanism of whisker growth had already been formulated [14]. These ideas were subsequently extended to nanometer-sized whiskers and have remained in use until now [1, 15]. The growth of semiconductor whiskers is usually carried out in three stages [1]: (i) deposition of a thin catalyst film (in our case, Au) on the surface of a semiconductor (GaAs); (ii) heating of the surface, resulting in the formation of liquid-alloy (Au–GaAs) droplets; and (iii) epitaxial growth of a semiconductor material (e.g., GaAs or AlGaAs). The classical VLS growth mechanism is as follows. When the activated surface is heated, droplets of Au–GaAs liquid alloy form on this surface. During epitaxial growth, the solution becomes supersaturated due to adsorption of the semiconductor material from the gas phase at the surfaces of the droplets. Finally, crystallization takes place on the surface beneath the droplets. This process results in the growth of a whisker crystal whose diameter is approximately equal to that of a droplet; the droplet itself moves upwards on top of the whisker. The higher rate of crystal growth obtained from the liquid alloy as compared to the process at the nonactivated part of the surface can be explained by two circumstances [1, 13–15]: (i) better material adsorption at the surfaces of the droplets and (ii) a higher rate of formation of two-dimensional nuclei at the liquid–solid interface as compared to the vapor–solid interface. Obviously, in this classical VLS mechanism, the highest possible rate of whisker growth is determined by the flux of the constituents onto the surface. Thus, in general, the length of a whis-

ker growing in accordance with the VLS mechanism cannot exceed the effective thickness of the deposited material, i.e., the total amount of the material delivered to the surface during the growth process.

Since the cross-sectional dimensions of a crystal are determined by the diameter of a liquid-alloy droplet, which depends on the thickness of the Au film and the conditions under which the surface is heated (the character of the formation and coalescence of the droplets), the dependences of the whisker growth rate on the droplet diameter D have been the focus of previous studies [10, 14, 15]. Most of the experimental studies resulted in the conclusion that, both in the case of VPE [14, 15] and MBE [10], the growth rate increases as D increases. In order to explain the obtained dependences, Givargizov and Chernov suggested a phenomenological model that describes whisker formation by the VLS mechanism. This model (referred to below as the GCh theory) predicts that the vertical growth rate $V_L = dL/dt$ depends quadratically on $1/D$: $V_L \propto (A - B/D)^2$ [14]. Constants A and B are determined by the parameters of the epitaxial growth and the surface energy at the vapor–solid phase boundary. This dependence in the GCh theory is a consequence of the dimensional Gibbs–Thomson effect related to the finite curvature of the whisker surface [16]. The GCh theory explains, among other things, the existence of a certain minimum droplet diameter, below which whiskers cannot grow under the parameters present in the epitaxial process. This effect has been experimentally observed many times [14, 15]. In [17–19], we developed a more detailed kinetic model of NW growth by the VLS mechanism that generalizes the GCh theory. In particular, it was shown that the growth rate depends on D in a more complicated way; however, this dependence can be approximated by the GCh formula in a certain range of droplet diameters. As a result, the kinetic coefficient of crystallization from the liquid alloy was determined. It was shown that the ratio of the growth rates on activated and nonactivated surfaces approximately equals $(1/3)(\alpha_{vs}/\alpha_{ls})^2$ for the case of "narrow" NWs and $(\alpha_{vs}/\alpha_{ls})^2$ for "wide" NWs (here, α_{vs} and α_{ls} are the surface energies at the vapor/solid and liquid/solid phase boundaries, respectively). The model developed in [17–19] accounts for the higher rate of NW growth on an activated surface in comparison to that on nonactivated regions of the surface. However, this model still predicts that the NW growth rate increases with the diameter of the droplet and that the maximum growth rate equals the rate of the material deposition. Thus, the main features of NW formation by the VLS mechanism can be formulated as follows: (i) wide whiskers grow faster than narrow ones and (ii) the NW growth rate vanishes for $D = D_{\min}$, while for large D it approaches a limit value determined by the material deposition rate.

At the same time, large diffusion lengths for adatoms at the crystal surface (on the order of 1–10 μm for GaAs) are typical of MBE growth. Apparently, under certain conditions, the diffusion motion of adatoms from the substrate surface over the side facets of an NW into the droplet can lead to a considerable increase in the supersaturation in that droplet, and, consequently, in the vertical growth rate of the crystal. For this to occur, the supersaturation in the droplet must be lower than the supersaturation of the adatoms at the substrate surface. The mechanism of whisker crystal growth in which, for certain reasons, the tip of a whisker activates the diffusion of the adatoms and acts as a sink for them is called the diffusion mechanism [14]. A theoretical and experimental analysis of the diffusion growth of whisker crystals was carried out by Dittmar and Neumann even before the discovery of the VLS mechanism and was reported, e.g., in [20, 21]. Under certain approximations, the diffusion mechanism theory predicts that the growth rate depends on the diameter in the form $V_L \propto A + B/D$, where constants A and B are determined by the growth conditions, the whisker length, and the diffusion coefficient of the atoms on the whisker surface (the DN model). Consequently, in the case of the diffusion mechanism, the growth rate decreases as the diameter increases; i.e., narrow whiskers grow faster, as experimentally observed in [14, 20, 21]. Thus, the dependences of the vertical growth rate on the diameter are qualitatively different for the VLS and the diffusion mechanisms. In addition, in the latter case, the whisker growth rate is not limited by the rate of material deposition from the vapor phase. The results of a study reported in [9], which was devoted to the MBE growth of Si NWs on a Si (111) surface activated with Au, showed that the diffusion mechanism may be dominant in the formation of NWs by MBE. The experimental $L(D)$ dependence obtained in [9] corresponds to a purely diffusion-related mechanism of growth and was connected by the authors to the diffusion of adatoms over the surface of the whiskers towards their tips. However, no theoretical description of this effect was proposed. There are no similar data for the AlGaAs/{GaAs(111)B–Au} system.

In this paper, we report the results of theoretical and experimental study of the formation of GaAs and AlGaAs NWs grown by MBE on a GaAs (111)B surface activated with Au. This is a continuation of our previous experimental [10, 11] and theoretical [18, 19] studies of the formation and structural properties of NWs grown by MBE. Our primary objective is to study the dependence of the growth rate of GaAs and AlGaAs NWs on their diameters and on the parameters of the MBE process for fairly large effective thicknesses of the deposited material (500 nm and thicker), as well as to determine the mechanism of NW formation in the MBE technique. Particular attention is given to the diffusion motion of adatoms from the substrate surface over the side facets of an NW towards the droplet and to the contribution of this process to the net growth rate.

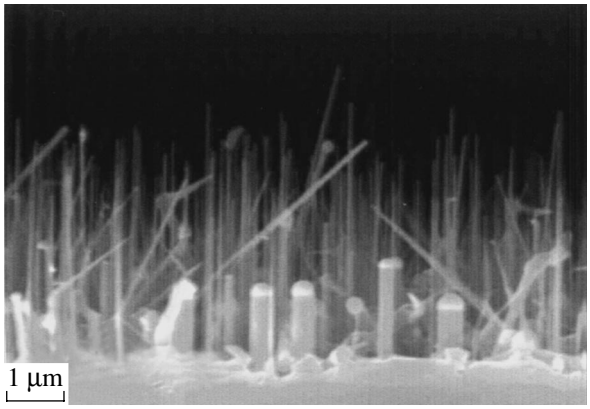

Fig. 1. A cross-sectional SEM image of a sample with GaAs NWs grown on a GaAs (111)B surface.

2. EXPERIMENTAL

GaAs and AlGaAs NWs were grown in an ÉP1203 MBE system on GaAs (111)B substrates covered by a Au layer, which was deposited beforehand in a VUP-5 sputtering unit. The three-stage technique used for the formation of the whiskers is described in detail elsewhere [10]; however, we modified one of the operations. At the stage immediately preceding the growth of the NWs, an oxide layer is removed from the Au-activated substrate surface. For this purpose, in the version of the technique described in [10], the substrate was heated in a growth chamber to 630°C and kept at this temperature for 5 min. In order to reduce the spread in the sizes of the eutectic droplets (for a given thickness of the deposited Au layer) formed during the heating of the surface, we abandoned the 5-min delay and raised the sample temperature to 630°C for a short period of time (the total duration of the heating cycle was no longer than 5 min). The thickness of the deposited Au layer was 2.5 nm and 1.25 nm for samples 1 and 2, respectively. In sample 1, the effective thickness of the deposited GaAs material was 1000 nm and the deposition rate was 1 monolayer (ML) per 1 s. In sample 2, a layer of $Al_{0.3}Ga_{0.7}As$ with the effective thickness of 725 nm was deposited at a rate of 1.4 ML/s. For both samples, the deposition of GaAs was carried out at a substrate temperature equal to 585°C. After growing the NWs, the temperature was rapidly lowered to room temperature, the samples were taken out of the growth chamber, and their structural parameters were investigated using a field-emission CamScan S4-90FE scanning electron microscope (SEM) operating in a secondary-electron mode. The electron energy in the probe beam was 20 keV. Typical SEM images of samples 1 and 2 with NWs are shown in Figs. 1 and 2, respectively. In the planar-geometry images, it can be seen that the NWs with smaller dimensions are, as a rule, grouped into an irregular mesh pattern, while the NWs with larger dimensions are located at the centers of the "cells" of this mesh. Furthermore, the mesh coincides with the boundaries of microcrystalline blocks. Apparently, this arrangement of NWs is related to specific features of the processes of Au coalescence on the surface of the samples.

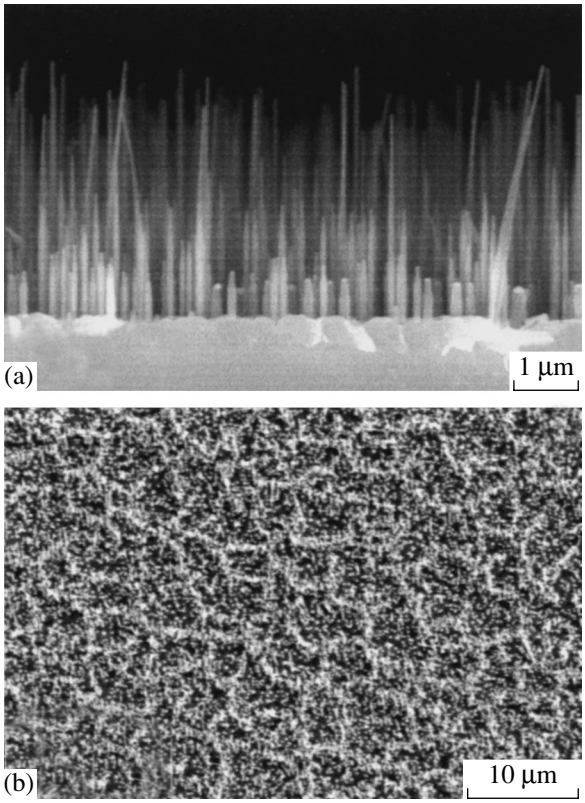

Fig. 2. SEM images of a sample with AlGaAs NWs grown on a GaAs (111)B surface: (a) cross-sectional and (b) planar geometry.

By analyzing the SEM images of samples 1 and 2, we can obtain experimental dependences of the NW height L on the NW cross-sectional size D. The resulting $L(D)$ dependence for sample 1 is shown in Fig. 3. We can see that the GaAs NWs can be as high as ~4500 nm, which exceeds the effective thickness of the deposited material by a factor of 4.5. In addition, it is seen that the maximum height is attained for the narrowest NWs ($D \approx 55$ nm). As D increases, the NW height decreases rapidly and, for $D \approx 150$ nm, falls to ~1600 nm. The L/D ratio in this sample varies from 100 for the narrowest whiskers to 2.5 for the widest ones. Figure 4 shows the experimental $L(D)$ dependence for sample 2. Here, the cross-sectional dimensions of the NWs are smaller than those in sample 1 due to the smaller thickness of the Au layer. The largest height of AlGaAs NWs is ~5300 nm, which exceeds more than seven-fold the effective thickness of deposited AlGaAs. Similarly to sample 1, the experimental $L(D)$ dependence is a rapidly decreasing function of the diameter. The growth rate is at its highest for the narrowest NWs with $D \approx 40$ nm, while, by $D \approx 100$ nm, the growth rate has already fallen by a factor of 5. The L/D ratio in sam-

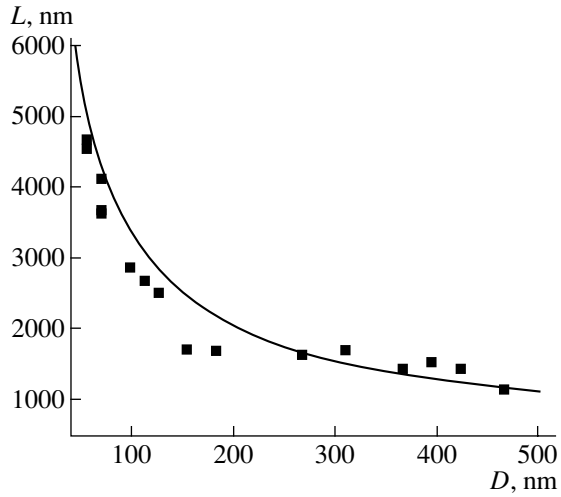

Fig. 3. The dots indicate the experimental dependence of the length of the GaAs NWs on their diameter for sample 1. The solid line indicates the $L(D)$ dependence calculated on the basis of the model described in the theoretical part of this paper.

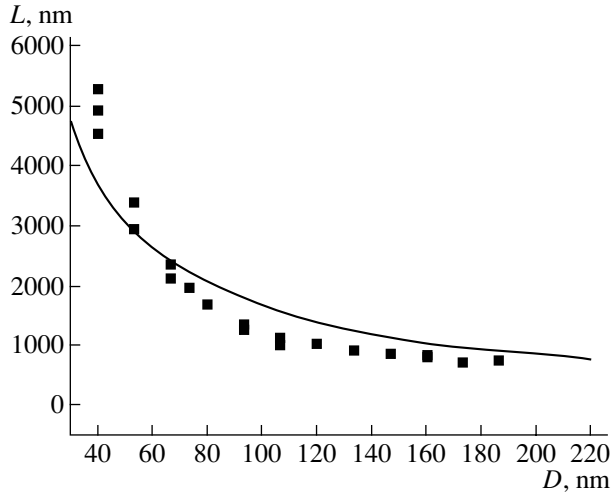

Fig. 4. The dots indicated the experimental dependence of the length of the AlGaAs NWs on their diameter for sample 2. The solid line shows the theoretical curve.

ple 2 varies from 130 to 3 as the diameter D increases. It should also be noted that, although the conditions of surface heating were the same for both samples, the NW diameter in sample 2 is smaller than in sample 1. This observation is related to the smaller amount of the deposited Au in sample 2 and, consequently, smaller size of the droplets.

The experimentally determined $L(D)$ curves shown in Figs. 3 and 4 differ radically from the corresponding dependences typical of the VLS growth mechanism. Recalling the discussion in the Section 1, we can conclude that, for the NWs under study, the diffusion growth mechanism is dominant. First, the maximum height of the GaAs and AlGaAs NWs severalfold exceeds the effective thickness of the deposited material. Second, in both samples, narrow NWs grow much faster than wide NWs. Third, no decrease of the NW height was observed in our experiments as the diameter decreased; in other words, there is no evidence of the existence of a minimum droplet diameter for which the growth rate becomes zero. All of these data suggest that there is a diffusion motion of atoms from the substrate surface over the NW side facets towards the tips. It should be noted that the height of the NWs grown from pure AlAs did not exceed the effective thickness of the deposited material and, consequently, the diffusion contribution to the growth process was not central in this case. This fact is related to the much smaller (by almost a factor of 50) diffusion length of Al atoms in comparison to that of Ga atoms. This effect leads to an order of magnitude increase in the growth rate of the narrow NWs and a radical change of the $L(D)$ dependence. The observed effect cannot be explained in the context of the VLS growth theory [14, 18, 19], and processes related to the diffusion motion of atoms over the surface must be taken into account. It should also be noted that our earlier experimental results [10, 18] for short NWs (with the effective thickness of the deposited GaAs <400 nm) prepared using the conventional mode of surface heating (with a 5-min storage at 630°C) indicated that L increased as D increased and that the NWs were consistent with a modified VLS growth model [18, 19]. Thus, as the NW length increases and the diameter decreases, a transition from the VLS to the diffusion mechanism of whisker formation takes place. To explain the observed effect, a theory is developed that takes into account the contributions of both mechanisms and the competition between them under different conditions of MBE growth.

3. THEORY

In order to take into account the diffusion contribution to the rate of NW growth, let us consider a model of NW formation in the MBE process, which is illustrated in Fig. 5. This model includes both the classical VLS mechanism of NW growth, in which growth occurs due to the adsorption of atoms at the surface of the droplets [14, 18, 19], and the diffusion-driven growth, due to the entry of atoms into the droplets through the NW side facets. At this stage, we do not take into account the formation of two-dimensional nuclei from adatoms diffusing along the side facets. Let us separately consider the processes that occur at the substrate, the NW side facets, and in the droplet at a whisker tip. Correspondingly, let us introduce the supersaturation of the adatoms at the substrate surface $\sigma = N/N_{eq} - 1$ (where N and N_{eq} are the actual and equilibrium areal densities of the adatoms at the substrate surface), the supersaturation of the adatoms at the NW side facets $\eta = n/n_{eq} - 1$ (where n and n_{eq} are the actual and equilibrium areal densities of the adatoms at the side facets), and the supersaturation of the liquid alloy $\zeta = C/C_{eq} - 1$ (where C and C_{eq} are the actual and equilibrium volume concentrations of the alloy). We

assume that the supersaturation of the alloy does not depend on its position within the droplet.

The substrate surface. We take into account (a) the supply of the material from the molecular beam $k_{vs}J$, where J is the flux density of the material onto the surface and k_{vs} is the coefficient of adsorption from the vapor phase at the substrate surface; (b) the desorption $-(\sigma + 1)N_{eq}/\tau_s$, where τ_s is the mean lifetime of the adatoms at the substrate surface; (c) the diffusion over the substrate surface $N_{eq}D_s\Delta\sigma$, where D_s is the diffusion coefficient of the adatoms at the substrate surface and Δ is the Laplace operator; and (d) the material flux from the substrate to the NW side facets j_{sf}. In a steady state, the kinetic equation for the supersaturation of adatoms at the substrate surface can be written as

$$\frac{k_{vs}}{N_{eq}} - \frac{(\sigma + 1)}{\tau_s} + D_s\Delta\sigma = 0. \quad (1)$$

Assuming that the diffusion vanishes at sufficiently large distances r from the center of a whisker, we obtain the boundary condition at infinity:

$$\sigma(r \longrightarrow \infty) = \frac{k_{vs}J\tau_s}{N_{eq}} - 1. \quad (2)$$

The second condition follows from the balance of matter at a whisker boundary:

$$\left.\frac{\partial\sigma}{\partial r}\right|_{r = R} D_s N_{eq} 2\pi R = j_{sf}, \quad (3)$$

where R is the radius of the whisker. It is reasonable to assume that the flux j_{sf} is proportional to the difference between the supersaturations at the substrate and at the NW side facets [22]:

$$j_{sf} = \frac{2\pi R}{l_s t_{sf}}[\sigma(R) - \eta(0)], \quad (4)$$

where l_s is the mean distance between the atoms at the surface and t_{sf} is the hopping time of an adatom from the substrate surface to an NW side facet.

Nanowhisker side facets. We take into account (a) the desorption $-(\eta + 1)n_{eq}/\tau_f$, where τ_f is the mean lifetime of the adatoms at the NW side facets; (b) the diffusion over the NW side facets $n_{eq}D_f\Delta\eta$, where D_f is the diffusion coefficient of the adatoms at the side facets; (c) the material flux from the substrate to the NW side facets j_{sf}; and (d) the material flux from the NW side facets into the droplet j_{fd}. It should be noted that the adsorption at the side facets of vertical NWs is virtually absent in the MBE process, which differentiates it from VPE [14] and the DN model [20, 21]. Similarly to (1), we obtain an equation for the supersaturation of adatoms at the NW side facets:

$$-\frac{(\eta + 1)}{\tau_f} + D_f\frac{\partial^2}{\partial z^2}\eta = 0. \quad (5)$$

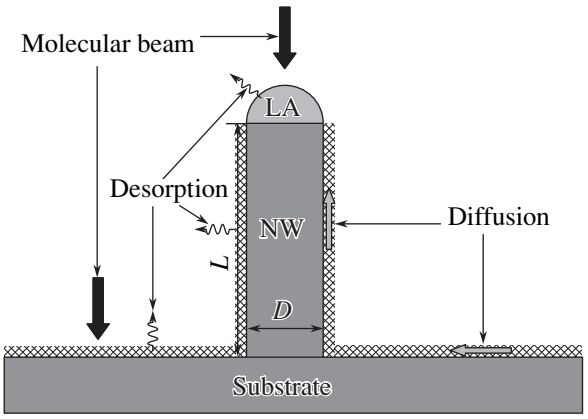

Fig. 5. A schematic representation of the processes taking place at the surface during the NW growth using the MBE method. LA denotes the liquid-alloy droplet and NW is a cylindrical whisker of length L and diameter D. The processes of adsorption from the molecular beam at the surface of the droplet and the substrate, diffusion of the adatoms over the surface of the substrate and the NW side facets, and desorption from the surface of the substrate and the side facets are illustrated.

The boundary conditions follow from the requirement of matter balance at the whisker–substrate and whisker–droplet boundaries:

$$-\left.\frac{\partial\eta}{\partial z}\right|_{z = 0} D_f n_{eq} 2\pi R = j_{sf}, \quad (6)$$

$$-\left.\frac{\partial\eta}{\partial z}\right|_{z = L} D_f n_{eq} 2\pi R = j_{fd}. \quad (7)$$

The material flux j_{fd} from the NW side facets into the droplet is proportional to the difference in the supersaturations:

$$j_{fd} = \frac{2\pi R}{l_f t_{fd}}[\eta(L) - \zeta]. \quad (8)$$

Here, l_f is the mean distance between the atoms at the whisker side facets, t_{fd} is the hopping time from the side facets to the droplet, and L is the whisker length.

The droplet. For simplicity, we assume that the contact angle of the droplet equals 90°. We take into account (a) the supply of the material from the molecular beam $k_{vl}J\pi R^2$, where k_{vl} is the coefficient of the adsorption from the vapor phase at the surface of the liquid droplet; (b) the desorption of the material from the droplet $-(\zeta + 1)r_l 2\pi R^2 C_{eq}/\tau_l$, where τ_l is the mean lifetime of a molecule in the surface layer of the liquid and r_l is the mean distance between the atoms in the liquid phase; (c) the removal of molecules from the droplet due to the NW crystallization $\pi R^2 V_L/\Omega_s$, where Ω_s is the volume per atom in the solid phase; and (d) the material flux from the NW side facets into the droplet j_{fd}.

Next, an expression for the NW growth rate V_L is required. We use the result obtained in [18], which is

valid for the case of monocentric nucleation, in other words, for sufficiently narrow NWs where a two-dimensional nucleus appearing at the surface of each whisker initiates crystallization over an entire facet before another nucleus has time to emerge. This assumption is justified when calculating the diffusion contributions to the growth rate, since these contributions are significant only for narrow whiskers. The correctness of the last assertion is supported both by the experimental data presented above and by theoretical considerations. Indeed, as the diameter increases, all the diffusion-related contributions should decay proportionally to $1/D$: the supply of atoms into the droplet from the NW side facets increases proportionally to D, while their contribution to the growth rate is proportional to D^2. In the case of monocentric nucleation, V_L is determined by the whisker radius R and the rate I of formation of the two-dimensional nuclei at the whisker surface from the liquid phase [18]:

$$V_L = \pi R^2 h I, \tag{9}$$

$$I(\zeta) = \sqrt{\frac{1}{\pi}}\frac{\Omega_l C_{\text{eq}}}{l_s^2 t_l}(\zeta+1)\sqrt{\Delta\mu}\exp[-F(\Delta\mu)], \tag{10}$$

$$\Delta\mu = \ln(\zeta+1) - \frac{R_0}{R}. \tag{11}$$

Here, Ω_l is the volume per atom in the liquid phase; h is the monolayer height; $a = \pi l_s^2(\alpha_{ls}/k_BT)^2$; t_l is the time between the two consecutive acts of incorporation of a molecule from the liquid phase into a single-atomic crystal step; $\Delta\mu$ is the effective supersaturation of the alloy, taking into account the dimensional Gibbs–Thomson effect [14]; $R_0 = 2(\Omega_s\gamma_{sv} - \Omega_l\gamma_{lv})/k_BT$ is a parameter of the GCh theory that has the dimensionality of length and is determined by the difference of the specific surface energies γ_{sv} and γ_{lv} at the solid–vapor and liquid alloy–vapor boundaries, respectively; $F(\Delta\mu) = a/\Delta\mu$ is the activation barrier for the formation of two-dimensional nuclei from the liquid phase at an NW surface; α_{ls} is the surface energy per unit length of the liquid–solid boundary; and k_B is the Boltzmann constant. The typical value of the energy constant a is ~10.

Thus, the equation for the supersaturation in the droplet can be written as

$$\pi R^2 k_{vl} J - 2\pi R^2 \frac{r_l C_{\text{eq}}}{\tau_l}(\zeta+1) - (\pi R^2)^2 \frac{h}{\Omega_s} I(\zeta) + j_{fd} = 0, \tag{12}$$

where the nucleation rate $I(\zeta)$ is determined by Eqs. (10) and (11). Obviously, in order to close Eq. (12), it is necessary to determine the flux j_{fd}. This task is performed by solving Eqs. (1)–(8); in addition, we obtain the spatial dependence of the supersaturation of adatoms. Here, we cite only the final result; thus, we write a dimensionless self-consistent equation for ζ as

$$U - \zeta = \frac{bd^2}{(1 + g_1/d)}\varphi(\zeta), \tag{13}$$

where $d = R/R_0$ is the dimensionless radius of an NW expressed in the units of characteristic length used in the GCh theory. Parameter b is given by

$$b = \frac{\sqrt{\pi}}{2}\frac{R_0^2}{l_s^2}\frac{\Omega_l}{\Omega_s}\frac{h}{r_l}\frac{\tau_l}{t_D} \sim \left(\frac{R_0}{l_s}\right)^2\frac{\tau_l}{t_l}. \tag{14}$$

This parameter is equal in its order of magnitude to the product of the squared characteristic length from the GCh theory expressed in the units of a lattice constant and the ratio of the lifetime of an atom in the liquid phase to the diffusion time in the liquid phase; thus, at $T = 585$°C, $b \sim 10^5$–10^6. Function

$$\varphi(\zeta) = (\zeta+1)\sqrt{\ln(\zeta+1) - 1/d} \times \exp\left[-\frac{a}{\ln(\zeta+1) - 1/d}\right] \tag{15}$$

is the dimensionless rate of formation of two-dimensional nuclei at an NW tip. The physical meaning of the quantity U on the left-hand side of (13) is the effective supersaturation in the vapor phase if the diffusion of atoms from the surface into the droplet is taken into account:

$$U = (\Phi+1)\frac{1 + g_0/d}{1 + g_1/d} - 1. \tag{16}$$

Here, $\Phi = k_{vl}J\tau_l/2r_lC_{\text{eq}} - 1$ is the actual supersaturation in the vapor phase, determined by the balance of the adsorption–desorption processes at the flat boundary of the liquid alloy. Its value increases as flux of the material to the surface increases and the temperature decreases. The quantities g_0 and g_1, which appear in (13) and (16), are found by solving the diffusion problems at the substrate surface and the NW side facets. These quantities depend on the ratio $\lambda = L/\sqrt{D_f\tau_f}$ of the NW length to the adatom diffusion length on the NW side facets and on the ratio $\rho = R/\sqrt{D_s\tau_s}$ of the NW diameter to the adatom diffusion length on the substrate surface. From (1)–(8), we obtain the following expressions for g_0 and g_1:

$$g_0(\rho,\lambda) = \frac{cc_0 f(\rho)}{f(\rho)\sinh\lambda + \alpha\cosh\lambda + \beta f(\rho)\cosh\lambda + \alpha\beta\sin\eta\lambda}, \tag{17}$$

$$g_1(\rho,\lambda) = \frac{c[f(\rho)\cosh\lambda + \alpha\sinh\lambda]}{f(\rho)\sinh\lambda + \alpha\cosh\lambda + \beta f(\rho)\cosh\lambda + \alpha\beta\sinh\lambda}.$$

Function $f(\rho)$ is given by

$$f(\rho) = \frac{Y(1,\rho)N_{eq}\sqrt{D_s/\tau_s}}{Y(1,\rho)N_{eq}\sqrt{D_s/\tau_s} + Y(0,\rho)/l_s t_{sf}}, \quad (18)$$

where $Y(\nu, \rho)$ is a Bessel function of the second kind. The constants α, β, c_0, and c, which appear in (17) and (18), are determined by the expressions

$$\alpha = l_s t_{sf} n_{eq}\sqrt{\frac{D_f}{\tau_f}}; \quad \beta = l_f t_{fd} n_{eq}\sqrt{\frac{D_f}{\tau_f}};$$
$$c_0 = 2\frac{\tau_s}{\tau_l}\frac{r_l C_{eq}}{N_{eq}}; \quad c = \frac{n_{eq}}{r_l C_{eq}}\frac{\tau_l}{\tau_f}\frac{\sqrt{D_f\tau_f}}{R_0}. \quad (19)$$

The NW growth rate is proportional to the difference between the effective supersaturation in the vapor phase and the supersaturation in the liquid alloy:

$$V_L = V_0(1 + g_1/d)(U - \zeta), \quad (20)$$

where $V_0 = 2r_l\Omega_s C_{eq}/\tau_l$. We note that the dependence of the growth rate on the NW diameter appears in the functions g_0 and g_1 in terms of the function $f(\rho)$, which equals unity for small ρ and tends to a constant value for large ρ. Thus, for large d, the diffusion contribution disappears and Eqs. (13) and (20) for $d \longrightarrow \infty$ and $U \longrightarrow \Phi$ reduce exactly to those obtained in [18]. Generally, the NW growth rate depends on the four dimensionless constants d, Φ, a, and b; in addition, it also depends on the form of the dependences of g_0 and g_1 on λ and ρ. Furthermore, formula (20) for the growth rate contains the quantity $V_0 \propto x_{eq}h/\tau_l$, where x_{eq} is the equilibrium specific concentration of the liquid alloy. For $x_{eq} \sim 0.1$ and conventional MBE growth temperatures, the typical values of V_0 are $\sim 10^{-3}$ nm/s. Finally, in order to convert the dimensionless radius d to R, a value of R_0 that typically equals several nanometers is required [14, 18].

The analytical and numerical calculations performed in the context of the described model show that, depending on the physical parameters, the NW length, and the growth conditions, it is possible to obtain NW growth modes approximating the classical VLS and diffusion mechanisms, as well as intermediate modes in which the NW growth rate attains a maximum for a certain diameter of the droplet. Other, more subtle, effects are possible. A detailed discussion of the theoretical results obtained for all the NW growth regimes is beyond the scope of this paper and will be reported separately. Here, we only describe the diffusion-controlled mode of NW growth, which appears in the model under consideration as one of the limiting cases and was observed in the experimental studies mentioned above. At the temperatures typical of the MBE process, the diffusion length of the adatoms on the surface is fairly large. According to the data reported in [23, 24], the diffusion length of Ga atoms on a GaAs (111)B surface at 585°C is several micrometers, and, on a side GaAs (110) surface, it is on the order of 10 μm. For AlGaAs with a 30% AlAs content, the adatom diffusion length amounts, on average, to ~30% of that for pure GaAs [23]. Thus, for the NW diameter range of interest, we can always assume that $\rho < 0.05$ and $f(\rho) \approx 1$. Considering the dependence on the NW length, we see that $\lambda \ll 1$ for low NWs and $\lambda \sim 1$ for the highest NWs (several micrometers in height). Next, let us take into account that, in contrast to the case of VPE, the supersaturation in the vapor phase in the MBE process is usually rather large (on the order of several tens). When estimating c_0, we assume that, in Eq. (19), $\tau_s \sim \tau_l$; then, $c_0 \sim x_{eq}/\theta_{eq}$, where θ_{eq} is the equilibrium coverage of the solid surface with adatoms. If we assume, for the purposes of the estimation, that $x_{eq} \sim 0.1$ and $\theta_{eq} \sim 10^{-4}$–10^{-5}, we obtain $c_0 \sim 10^3$–10^4. In addition, if we assume that $\sqrt{D_f\tau_f} \sim 10$ μm and $R_0 \sim 5$ nm, we find from (19) that $c \sim 0.1$–1. It follows from (17) that, for NW lengths less than or comparable to the adatom diffusion length ($\lambda \ll 1$ or $\lambda \sim 1$), $g_0 > g_1$ or even $g_0 = c_0 g_1 \gg g_1$. Then, we can conclude from (16) that, for all diameters, $U > \Phi \gg 1$. It is clear from (17) that, for $d \longrightarrow \infty$, $U \longrightarrow \Phi$ for any λ and, for $d \longrightarrow 0$ and $\lambda \longrightarrow 0$, $U \longrightarrow c_0(\Phi + 1) \gg \Phi$. It can be stated that, for all D that exceed the minimum value d_{min} considerably (for which the growth rate vanishes [18]), solution (13) satisfies the condition $\zeta \ll \Phi$. The minimum diameter of the droplet is found from the equation $d_{min} = \ln[U(d_{min}) + 1]$, which, for $\Phi \gg 1$, has the solution $d_{min} = 1/\ln[(g_0/g_1)(\Phi + 1)] \ll 1$. Consequently, in the case of MBE, the minimum diameter can be very small, in fact, considerably smaller than the size of the droplets actually present on the surface, and its existence does not manifest itself in the experiment.

For $U > \Phi \gg \zeta$ and $\rho \ll 1$, the following approximate solution for the NW growth rate can be obtained from (13), (16)–(18), and the definitions of Φ and V_0:

$$V_L = k_{vl}hV\left[1 + \frac{g_0(\lambda)}{d}\right], \quad (21)$$

where V is the material deposition rate in ML/s. Under the assumptions made, $g_0(\lambda)$ is a function of the NW length and can be written as

$$g_0(\lambda) = \frac{cc_0}{(\alpha + \beta)\cosh\lambda + (1 + \alpha\beta)\sinh\lambda}. \quad (22)$$

Expression (21) corresponds to a purely diffusive mechanism of NW growth and is similar to the formula obtained in the DN model; however, the dependence $g_0(\lambda)$ is of another type. The dependences $V_L(d)$ of different values of λ are shown in Fig. 6. Clearly, for $\lambda \ll (\alpha + \beta)$, $g_0 \approx cc_0/(\alpha + \beta)$ and the growth rate of an NW is independent of its length. It can also be seen from Eqs. (21) and (22) that, for $c_0 \gg 1$, the growth rate of thin whiskers can considerably exceed the rate of material deposition.

Numerical calculations of the $V(D)$ dependences were carried out on the basis of model equations (13) and (15)–(18). The whisker length was calculated as an integral of the growth rate with respect to time. The theoretical values of L for different D were compared with the experimental results for samples 1 and 2. The fol-

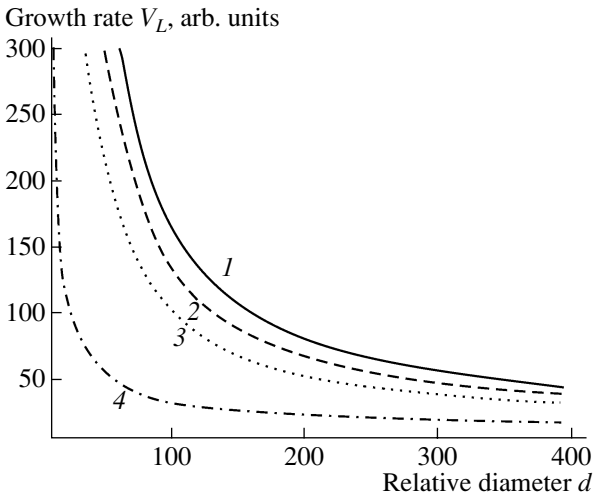

Fig. 6. Pure diffusion-type dependences of the growth rate of a NW on its diameter for λ = (*1*) 0, (*2*) 0.2, (*3*) 0.5, and (*4*) 2.

lowing values of the model parameters were used in the calculations: for sample 1, $\Phi = 25$, $a = 10$, $b = 10^5$, $c = 0.1$, $c_0 = 10^3$, $R_0 = 3$ nm, $\sqrt{D_f\tau_f} = 6$ μm, $V_0 = 0.007$ nm/s, and $\alpha = \beta = 0.4$; for sample 2, most of the parameters were the same except $\Phi = 35$, $c = 0.08$, and $\sqrt{D_f\tau_f} = 1.8$ μm. The growth duration was 2800 s for sample 1 and 1700 s for sample 2. The calculated $L(D)$ curves, shown by the solid lines in Figs. 3 and 4, are in satisfactory agreement with the experiment.

4. CONCLUSIONS

Thus, it is shown that, under the given conditions in the experiments described, GaAs and AlGaAs NWs formed by the MBE method on Au-activated GaAs (111)B substrates grow via the diffusion mechanism. The experimental dependence of the NW growth rate on the NW diameter is a decreasing function, qualitatively different from that expected for the VLS mechanism. We note that the results obtained in our previous studies [10, 11, 17, 18], along with those presented above, show that, during the MBE process, either the VLS or diffusion growth mechanism can be dominant, depending on the experimental conditions; in addition, intermediate growth modes can exist. We suggested a theoretical model providing a unified consideration of the VLS and diffusion mechanisms in NW growth. In the context of this model, the $L(D)$ dependence typical of the pure diffusion mechanism is derived as a limiting case, and the experimental results obtained in this study are described satisfactorily.

ACKNOWLEDGMENTS

We are grateful to V.M. Busov and S.I. Troshkov for carrying out the SEM measurements and V.P. Ulin for his help in preparing the GaAs (111)B substrates.

This study was supported in part by scientific programs of the Ministry of Industry, Science, and Technology of Russia and by the Russian Foundation for Basic Research (project no. 05-02-16495). G.E. Cirlin acknowledges the support of the Humboldt Foundation (Germany), and A.A. Tonkikh acknowledges the support of the Deutsche Forschungsgemeinschaft.

REFERENCES

1. K. Hiruma, M. Yazawa, T. Katsuyama, *et al.*, J. Appl. Phys. **77** (2), 447 (1995).
2. X. Duan, J. Wang, and C. M. Lieber, Appl. Phys. Lett. **76**, 1116 (2000).
3. Y. Cui and C. M. Lieber, Science **91**, 851 (2000).
4. K. Haraguchi, T. Katsuyama, K. Hiruma, and K. Ogawa, Appl. Phys. Lett. **60**, 745 (1992).
5. B. J. Ohlsson, M. T. Björk, M. H. Magnusson, *et al.*, Appl. Phys. Lett. **79**, 3335 (2001).
6. T. I. Kamins, X. Li, and R. Stanley Williams, Appl. Phys. Lett. **82**, 263 (2003).
7. J. Westwater, D. P. Gosain, S. Tomiya, *et al.*, J. Vac. Sci. Technol. B **15**, 554 (1997).
8. Y. Huang, X. Duan, Y. Cui, *et al.*, Science **294**, 1313 (2001).
9. L. Schubert, P. Werner, N. D. Zakharov, *et al.*, Appl. Phys. Lett. **84**, 4968 (2004).
10. A. A. Tonkikh, G. E. Cirlin, Yu. B. Samsonenko, *et al.*, Fiz. Tekh. Poluprovodn. (St. Petersburg) **38**, 1256 (2004) [Semiconductors **38**, 1217 (2004)].
11. V. G. Dubrovskii, I. P. Soshnikov, G. E. Cirlin, *et al.*, Phys. Status Solidi B **241** (7), R30 (2004).
12. A. Y. Cho and J. R. Arthur, Prog. Solid State Chem. **10**, 157 (1975).
13. R. S. Wagner and W. C. Ellis, Appl. Phys. Lett. **4** (5), 89 (1964).
14. E. I. Givargizov, *Growth of Whisker and Scaly Crystals from Vapors* (Nauka, Moscow, 1977) [in Russian].
15. D. N. Mcllroy, A. Alkhateeb, D. Zhang, *et al.*, J. Phys.: Condens. Matter **16**, R415 (2004).
16. E. I. Givargizov and A. A. Chernov, Kristallografiya **18**, 147 (1973) [Sov. Phys. Crystallogr. **18**, 89 (1973)].
17. N. V. Sibirev and V. G. Dubrovskiĭ, Pis'ma Zh. Tekh. Fiz. **30** (18), 79 (2004) [Tech. Phys. Lett. **30**, 791 (2004)].
18. V. G. Dubrovskiĭ, N. V. Sibirev, and G. E. Cirlin, Pis'ma Zh. Tekh. Fiz. **30** (16), 41 (2004) [Tech. Phys. Lett. **30**, 682 (2004)].
19. V. G. Dubrovskii and N. V. Cibirev, Phys. Rev. E **70**, 031604 (2004).
20. W. Dittmar and K. Neumann, in *Growth and Perfection of Crystals*, Ed. by R. H. Doremus, B. W. Roberts, and D. Turnball (Wiley, New York, 1958), p. 121.
21. W. Dittmar and K. Neumann, Z. Elektrochem. **64**, 297 (1960).
22. A. A. Chernov, E. I. Givargizov, Kh. S. Bagdasarov, *et al.*, in *Modern Crystallography*, Vol. 3: *Crystal Growth*, Ed. by B. K. Vaĭnshteĭn, A. A. Chernov, and L. A. Shuvalov (Nauka, Moscow, 1980; Springer, Berlin, 1984).
23. S. Koshiba, Y. Nakamura, M. Tsuchiya, *et al.*, J. Appl. Phys. **76**, 4138 (1994).
24. T. Takebe, M. Fujii, T. Yamamoto, *et al.*, J. Appl. Phys. **81**, 7273 (1997).

Translated by M. Skorikov

Semiconductors, Vol. 39, No. 5, 2005, pp. 565–571. Translated from Fizika i Tekhnika Poluprovodnikov, Vol. 39, No. 5, 2005, pp. 595–601.

AMORPHOUS, VITREOUS, AND POROUS SEMICONDUCTORS

The Electronic and Emissive Properties of Au-Doped Porous Silicon

V. E. Primachenko^, Ja. F. Kononets, B. M. Bulakh, E. F. Venger, É. B. Kaganovich, I. M. Kizyak, S. I. Kirillova, É. G. Manoĭlov, and Yu. A. Tsyrkunov

Lashkarev Institute of Semiconductor Physics, National Academy of Sciences of Ukraine, Kiev, 03028 Ukraine
^e-mail: pve18@isp.kiev.ua

Submitted June 15, 2004; accepted for publication August 9, 2004

Abstract—The temperature dependences of photovoltage induced by intense pulses of red and white light, along with the time-resolved spectral dependences of photoluminescence, are studied for porous silicon structures (*por*-Si/*p*-Si). These structures have been obtained by anode etching of *p*-Si with subsequent Au doping from an aqueous solution with Au ion concentrations of 10^{-4} and 10^{-3} M. The current–voltage characteristics and electroluminescence of the resulting *por*-Si/*p*-Si and *por*-Si:Au/*p*-Si structures are also studied after a deposition of semitransparent Au electrodes on *por*-Si. It is shown that the Au doping changes the sign of the boundary potential of *p*-Si from positive to negative, alters the magnitude and sign of the photovoltage in the *por*-Si films, and eliminates photomemory phenomena, which are associated with the capture of nonequilibrium electrons at grain-boundary traps and *por*-Si traps. The formation of Au nanocrystals in *por*-Si substantially affects the current–voltage and photoluminescence characteristics. Electroluminescence is observed for the Au/*por*-Si:(Au,10^{-3} M)/*p*-Si/Al structures and is attributed to emission from the nanocrystals.

1. INTRODUCTION

Silicon nanocrystals possess unique properties relating to the quantum-dimensional confinement of electron, hole, and exciton motion [1, 2]. In particular, Si nanocrystals give rise to photoluminescence (PL) and electroluminescence (EL) in the visible region of the spectrum of nanocomposite systems, which includes these nanocrystals. This effect is associated with an increase both in the band gap and the luminescence quantum yield in these nanocrystals in comparison with an indirect-gap single-crystal Si.

One type of nanocomposite system is porous silicon (*por*-Si), in which Si nanocrystals are distributed randomly or in the form of chains (threads) with the possible existence of air (vacuum) spacings (pores) between them. Depending on the fabrication and storage conditions, the *por*-Si films are mainly coated with hydrogen and/or oxide (SiO_x, $0 < x < 2$) films. The *por*-Si layers are usually formed on a single-crystal Si substrate by electrochemical (anodic) or chemical (stain) etching.

It is of certain scientific and practical interest to modify the *por*-Si layers by introducing various impurities, specifically, metal impurities. The simplest technique for doping *por*-Si layers with metals is the treatment of these layers in solutions containing doping metal ions. It is known that metal ions with a higher electrochemical (standard) potential than Si, when deposited on the surface of single-crystal or nanocrystalline silicon, are neutralized due to the trapping of electrons from the surface Si atoms. These ions become the nuclei of metal islands (nanocrystals) [3, 4]. Due to the oxidation–reduction process, the *por*-Si film, after doping with a metal possessing a positive standard potential, contains Si nanocrystals (with a higher degree of oxidation) as well as metal nanocrystals.

A metal-modified *por*-Si film can be of interest for various practical applications. First, it can be used for the development of effective electroluminescent and electron-emitting devices, since the introduction of metal nanocrystals improves the current flow through the film. In addition, light is not only emitted by the silicon nanocrystals but also by the metal nanocrystals. The luminescence and electron emission from two-dimensional metal island films vacuum-deposited onto insulating substrates have been observed on applying electric power to these films using various methods [5]. When *por*-Si films are doped with metals, their nanocrystals are located in three-dimensional space. Therefore, we can expect more efficient electron emission and luminescence from the surface unit area of a *por*-Si film that includes Si and metal nanocrystals. Second, *por*-Si films have a large total area of Si and metal nanocrystals, which have specific catalytic properties. As a result of this circumstance, a *por*-Si film can be effectively used for heterogeneous catalysis and for the development of various sensors, depending on the choice of metal and the specific conditions of doping with this metal.

In this study, we examined the electronic and emissive properties of *por*-Si films, which were obtained by anodic etching, after their doping with Au from solu-

tions containing the Au ion concentrations 10^{-4} and 10^{-3} M. It is noteworthy that we have previously studied the properties of *por*-Si films, which were obtained by stain etching, after their doping with Au from $(1–2) \times 10^{-5}$ M solutions both during and after their fabrication [6, 7]. The results obtained in this study and in [6, 7] differ substantially. This difference is associated both with the differing properties of the *por*-Si films when obtained by the two different methods [8, 9] and with the higher concentration of Au dopant used in this study.

2. EXPERIMENTAL

por-Si layers 1–5 μm thick were formed on the mechanochemically polished (100) surface of *p*-Si:B with $\rho = 10\ \Omega$ cm by anodization of the samples in a $HF : H_2O : C_2H_5OH = 1 : 1 : 2$ solution at a current density of 8–20 mA/cm^2 for 10–20 min. An Al contact was preliminarily deposited onto the rear surface of the sample and fired at 400°C. Prior to the anodization, this contact was covered with lacquer, and the samples were rapidly treated in HF and rinsed in distilled water.

We studied the undoped Si reference samples with the *por*-Si layer as well as samples doped for 1 h with Au from aqueous 10^{-4} and 10^{-3} M $AuCl_3$ solutions. Immediately prior to the doping, the samples were treated in 0.5% aqueous HF for 1 min to remove oxide from the *por*-Si layer.

We studied, for both the undoped and Au-doped samples, the time-resolved PL spectra at room temperature [10] and the temperature dependences of the capacitive photovoltage that emerged when the *por*-Si side of the sample was exposed to the pulses of white and red light [9]. Semitransparent Au layers were also vacuum-deposited on the *por*-Si layer, and we studied the current–voltage (*I–V*) characteristics of the Au/*por*-Si/*p*-Si/Al and Au/*por*-Si:Au/*p*-Si/Al structures and their EL under a pulsed voltage.

The PL was excited by radiation from a nitrogen laser ($\lambda = 337$ nm, $\tau = 8$ ns, and $P_{imp} \approx 2$ kW). Stroboscopic detection of the PL signal was carried out in a photon-counting mode. The duration of the measurement strobe pulse, in which the photons were accumulated, was 250 ns. In this study, we report the spectral dependences of PL, which were measured in the first strobe pulse ($t \le 250$ ns) after the PL excitation, and the integrated spectral dependences of PL, which were obtained during the PL relaxation from $t \ge 250$ ns to its complete decay. The PL relaxation times were also determined.

In order to measure the photovoltage for the *por*-Si/*p*-Si and *por*-Si:Au/*p*-Si samples, a sample–mica measuring capacitor was formed. The rear surface of the capacitor was covered with a semitransparent SnO_2:Sb layer. The photovoltage, which emerged in the SnO_2/*por*-Si/*p*-Si/Al capacitor under its irradiation with pulsed light, was detected using a storage oscilloscope. The pulsed light was generated by an ISSh-100 flash lamp with a pulse intensity of 10^{21} photon/(cm^2 s) and duration of 10 μs in the form of separate pulses or a train of pulses or with a frequency of 1 Hz. The temperature dependences of the photovoltage were measured as the temperature was decreased from 300 to 100 K in a cryostat evacuated to 10^{-4} Pa. In order to increase the capacitor temperature, an electrical heater was mounted in the cryostat.

The photovoltage was measured for pulses of both white and red light. In the latter case, we used a KS-19 optical filter, which transmitted light in the wavelength range 700–2700 nm. In the case of exposure to pulses of red light, which is mainly absorbed in *p*-Si [11], we measured the photovoltage, which emerges only in the Si substrate and equals the boundary potential in *p*-Si with the opposite sign in terms of the calibration coefficient of the photovoltage measurement circuit [9]. Note that the intensity of the light in the pulse is sufficient to flatten the energy bands of *p*-Si and allows us to disregard the Dember photovoltage, as the mobilities of nonequilibrium electrons and holes equalize due to their mutual scattering at high concentrations [12]. On irradiation with the pulses of white light, we measured the total photovoltage, which emerges both in *p*-Si and in *por*-Si, in which the light with a shorter wavelength is absorbed. The measurements showed that the photovoltage signal obtained using the first pulse of light could differ from the signal obtained using the second or any subsequent pulse in the train. This behavior is associated with the capture of nonequilibrium charge carriers at traps in the *por*-Si/*p*-Si interface or in *por*-Si. When the red light was used, the nonequilibrium electrons were captured at the *por*-Si/*p*-Si interface. In this case, after each measurement, the sample was heated to a temperature at which the traps were emptied of the captured electrons. Then, the sample was cooled again to the temperature of the photovoltage measurement using the first and second pulses. Note that the photovoltage signals obtained using the second and subsequent pulses of light were indistinguishable, which indicates that the traps were saturated with nonequilibrium carriers even under the effect of the first pulse of light.

To observe the EL of *por*-Si and *por*-Si:Au and to measure the *I–V* characteristics, we deposited semitransparent (d = 20–40 nm) Au electrodes onto *por*-Si in vacuum. The area of the electrodes varied within the range 1–10 mm^2. The *I–V* characteristics and the EL were measured during an alternate application of positive and negative voltage pulses 15-μs wide with a repetition frequency of 1 kHz and the varying of their amplitude within the range 0–150 V. The magnitudes of the pulse voltages at the *por*-Si and *por*-Si:Au structures, the current through the structures, and the EL intensity were simultaneously measured using an S1-103 four-trace oscilloscope. During this procedure, the light from the structures for the EL measurement was guided using an optical fiber from a dark chamber to an FÉU-79 photoelectron multiplier, whose signal was then recorded using the oscilloscope.

3. RESULTS AND DISCUSSION

Study of the PL decay after its excitation showed that the decay can be described, in its a first approximation, by three time intervals, which is similar to the case of the chemically prepared *por*-Si lightly Au-doped from the 2×10^{-5} M solution [7]. The PL intensity I_{pl} for the initial and doped samples preferentially decays even during the first strobe pulse ($t < 250$ ns). Then, I_{pl} decreases by an order of magnitude over the time τ_1. This PL decay makes the main contribution to the integrated PL magnitude that we determined. Finally, the tail of the PL decay is observed over the time τ_2. This tail amounts to approximately 10% of the integrated PL magnitude. It was found that the values of τ_1 and τ_2 virtually coincided for the undoped sample and the sample doped with Au from the 10^{-4} M solution. These values are equal to 100 and 300 μs. After the doping with Au from the 10^{-3} M solution, they decrease to $\tau_1 \approx 35$ μs and $\tau_2 = 230$ μs.

Figures 1a and 1b show the spectral dependences $I_{pl}(h\nu)$ obtained (a) within the first strobe (rapid PL and $t < 250$ ns) and (b) within the integrated time interval from 250 ns to the complete PL decay. It should be noted here that the undoped samples were treated in an 0.5% aqueous HF solution prior to the measurement to etch the oxide film from *por*-Si. This treatment was also used in the case of the samples subsequently doped with Au to ensure identical conditions and, thus, allow the effect of the doping metal to be revealed. Figures 1a and 1b show that the doping with Au from the 10^{-4} M solution somewhat increases both the PL within the first strobe pulse and the integrated PL, which can be associated with the oxidation of Si nanocrystals due to the oxidation–reduction processes in the course of the doping with metal. The maxima of the dependences $I_{pl}(h\nu)$ within the first strobe pulse are in the region 2–2.05 eV, and those of the integrated dependences $I_{pl}(h\nu)$ are in the region 1.85–1.90 eV. The dependences $I_{pl}(h\nu)$ for the undoped sample and the sample doped with Au from the 10^{-4} M solution are mainly associated with a radiative recombination of free and bound (into excitons) electron–hole pairs excited by the laser radiation in Si nanocrystals of various sizes. In contrast, the integrated dependences $I_{pl}(h\nu)$, which mainly decay over the time τ_1, can be associated with a radiative recombination of excitons bound to the Si=0 centers on the surface of the Si nanocrystals. The reasons for this PL subclassification were analyzed in detail in [7]. Regarding the relaxation of the PL tail over the time τ_2, we believe that this prolonged time, as in [7], is associated with the behavior of nonequilibrium carriers. In the case of *por*-Si obtained by anodization, the electrons are captured by the traps in the shells of the Si nanocrystals. These electrons are then reversely transported into the nanocrystals for the subsequent radiative recombination of the electron–hole pairs.

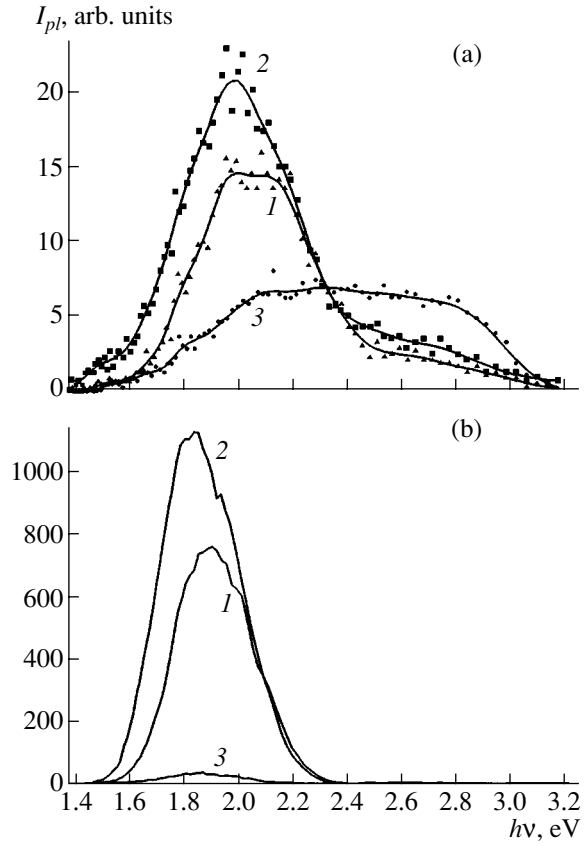

Fig. 1. (a) Spectral dependences of the PL obtained within the first strobe pulse ($t < 250$ ns) and (b) the integrated spectra obtained during the PL relaxation with $t > 250$ ns to its complete decay. Curves *1* correspond to the undoped *por*-Si/*p*-Si structure, and curves (*2*) and (*3*) correspond to the structures doped with Au using the 10^{-4} M and 10^{-3} M solutions, respectively.

Quite another situation is realized for the samples doped with Au from the 10^{-3} M $AuCl_3$ solutions. The PL intensity, especially its integrated part, substantially decreases (Fig. 1, curve *3*). In addition, after doping, the PL peak in the dependences $I_{pl}(h\nu)$ within the first strobe pulse is broad. This peak is located in the region 2.2–2.6 eV, while the location of the peak of the integrated dependence $I_{pl}(h\nu)$ does not change (1.85 eV). These facts suggest that it is the emission of light by the laser-excited hot electrons in the Au nanocrystals rather than the recombination of free or bound (in excitons) electron–hole pairs in the Si nanocrystals that mainly contributes to the PL in this case [5]. The pulses of a nitrogen laser, as applied in this experiment, are sufficiently powerful for this purpose (2×10^4 W/cm^2). In addition, at these levels of power, the luminescence and electron emission have also been observed for an island Au film in the case of the use of a CO_2 laser [5]. We believe that the Au nanocrystals also contribute to PL in the case of Au doping from the 10^{-4} M solution. This inference is supported by higher intensity of the PL in the region $h\nu > 2.3$ eV compared with the undoped

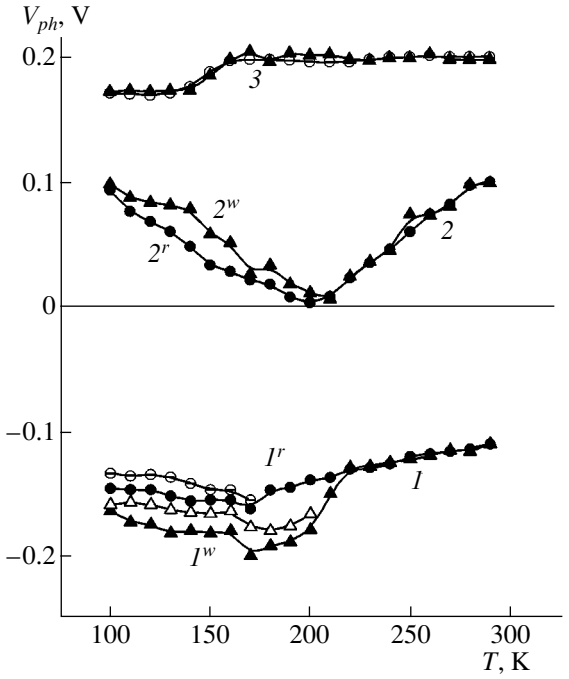

Fig. 2. Temperature dependences of the photovoltage V_{ph} of the (*1*) *por*-Si/*p*-Si, (*2*) *por*-Si:Au [10^{-4} M]/*p*-Si, and (*3*) *por*-Si:Au [10^{-3} M]/*p*-Si structures. The filled circles and triangles correspond to the values of V_{ph} obtained for the first pulses of red (*r*) and white (*w*) light, respectively. The open circles and triangles correspond to the values of V_{ph} obtained for the second pulses of light.

sample (Fig. 1, curves *1*, *2*). However, the preferential luminescence of the Au nanocrystals manifests itself only in the case of doping from the 10^{-3} M solution, as the Au nanocrystals are formed in a sufficiently large amount. Moreover, the Au nanocrystals, when absorbing or reflecting the laser radiation, ensure the necessary conditions for its weaker absorption by the Si nanocrystals.

Figure 2 shows the temperature dependences of the photovoltage V_{ph} of the undoped (curves *1*) and Au-doped (the 10^{-4} M solution, curves *2*, and the 10^{-3} M solution, curve *3*) structures. The filled circles and triangles denote the points obtained for the first pulses of red and white light, respectively, and the open circles and triangles denote the points obtained for the second pulses. We can see from Fig. 2 that, prior to doping, all the values of V_{ph} were negative with the minus at the SnO_2:Sb electrode, whereas, after doping, the values of V_{ph} are always positive. It is noteworthy that the values of V_{ph} obtained for the red light are equal to the boundary potential φ_s of the Si substrate with the opposite sign. Thus, close to room temperature, the outward bending of energy bands for the *p*-Si substrate amounts to 0.11 eV for the undoped structure, while the inward bending for the substrates doped from the 10^{-4} M and 10^{-3} M solutions is 0.10 and 0.20 eV, respectively. Thus, Au doping of the *por*-Si/*p*-Si structures changes the depletion boundary layers to ones enriched with holes. Calculations carried out using a similar approach to that in [13] show that the Fermi level at $T \approx 300$ K is located 0.295 eV below the Si midgap E_i in the *p*-Si bulk. At the interface with *por*-Si, this level is located 0.185, 0.295, and 0.495 eV below E_i for the undoped structures and the structures doped from the 10^{-4} M and 10^{-3} M solutions, respectively.

Since the Fermi level shifts towards the valence band as the temperature decreases, the boundary electron states of the *p*-Si substrate are positively charged, which leads to an increase in $\varphi_s = -V_{ph}$. These portions of increase in φ_s in the dependences $V_{ph}(T)$ are observed for curve *1* at $T > 170$ K and for curve *2* at $T > 200$ K. The decrease in φ_s for curve *1* at $T < 170$ K and for curve *2* at $T < 200$ K are indicative of a reconstruction of the system of boundary electron states at the *por*-Si/*p*-Si interface when these temperatures are reached. This phenomenon is caused by the reversible structural changes at the interface [8, 9]. The density of boundary electron states can be estimated for the portions where φ_s increases as the temperature decreases, i.e., when the reconstruction of the system of boundary electron states has not yet occurred [13]. It was found that, for the undoped structure, the density of boundary electron states in the energy interval from 0.19 to 0.29 eV below E_i increases from 1×10^{11} to 6×10^{11} cm^{-2} eV^{-1}. For the structure doped from the 10^{-4} M solution, this quantity equals 2.5×10^{13} cm^{-2} eV^{-1} in the region of 0.4 eV below E_i, and, for the structure doped from the 10^{-3} M solution, the concentration at the valence-band top is 2×10^{15} cm^{-2} eV^{-1}.

For curve *3* (Fig. 2) and curves *1* at $T > 220$ K and curves *2* at $T > 210$ K, the values of V_{ph} coincide for the pulses of red (V_{ph}^r) and white (V_{ph}^w) light. This means that the photovoltage signals are formed only due to the flattening of the energy bands of *p*-Si. However, at $T <$ 220 K for curve *1* and $T < 210$ K for curve *2*, the values of V_{ph} for the pulses of white and red light differed. This observation is associated with the emergence of photovoltage signals in the layers of *por*-Si and *por*-Si:Au, which are equal to $V_{ph}^{por\text{-}Si} = V_{ph}^w - V_{ph}^r$, as the white light is absorbed into them. The photovoltage $V_{ph}^{por\text{-}Si}$ is observed only for a definite temperature region. This photovoltage is caused by stresses that emerge in the *por*-Si layers as the temperature varies. Theses stresses lead to the formation of built-in charge, which gives rise to $V_{ph}^{por\text{-}Si}$. Figure 3 shows the temperature dependences of $V_{ph}^{por\text{-}Si}$, which also indicate that the signs of the photovoltage in the *por*-Si layers (curve *1*) and *por*-Si:Au layers (curve *2*) are opposite. In turn, the signs of the built-in charge that emerges in these layers are also different. The absolute values of $V_{ph}^{por\text{-}Si}$, in both cases,

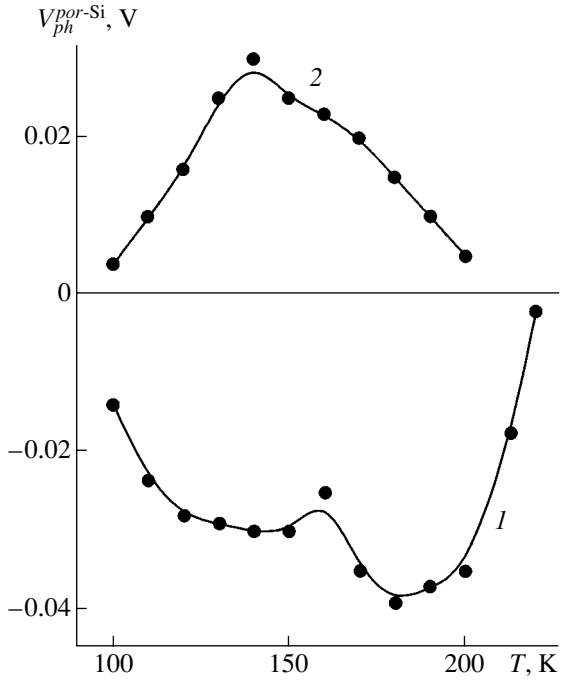

Fig. 3. Temperature dependences of the photovoltage $V_{ph}^{por\text{-Si}}$ for the layers of (*1*) *por*-Si and (*2*) *por*-Si:Au [10^{-4} M].

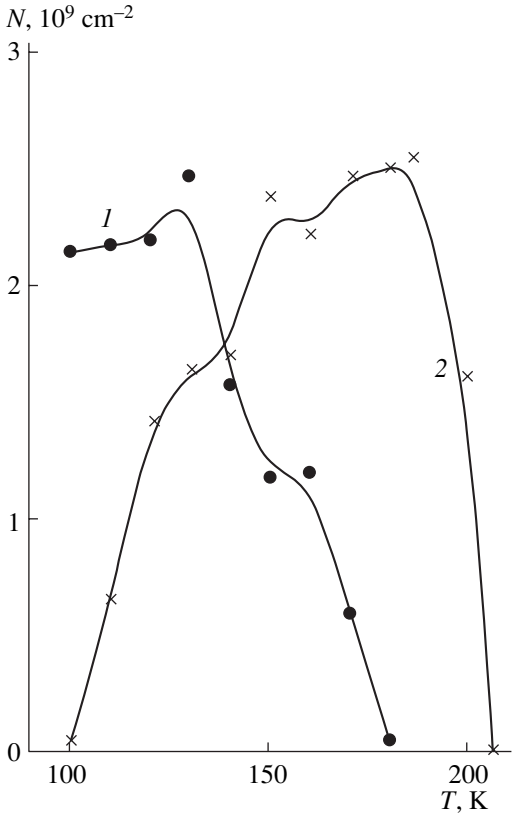

Fig. 4. Temperature dependences of the concentrations of nonequilibrium electrons captured (*1*) by the traps at the *p*-Si boundary and (*2*) by the traps in the *por*-Si layer for the *por*-Si/*p*-Si structure.

initially increase as the temperature increases and then decrease, which reflects the complexity of the processes occurring in the films as the temperature is varied. In the case of doping with Au from the 10^{-3} M solution (Fig. 2, curve *3*), photovoltage is not observed at all in the *por*-Si:Au.

Doping of the *por*-Si/*p*-Si structures with Au for both the used concentrations leads to the disappearance of the effects of photomemory V_{ph} [3], which are observed for the undoped structure (Fig. 2, curves *1*) under exposure to the pulses of the red and white light at $T < 180$ K and $T < 210$ K. The absolute values of V_{ph} obtained for the second and each subsequent pulse of light in the train are smaller. This observation indicates that nonequilibrium electrons are captured by the boundary traps of *p*-Si under exposure to the first pulse of red light or that the electrons are captured both by the boundary traps and by the traps in the *por*-Si layers under exposure to the first pulse of white light. The temperature dependences of the number of electrons captured both by the boundary traps and by the traps in the *por*-Si film can be calculated from the difference between the dependences $V_{ph}^{r}(T)$ and $V_{ph}^{w}(T)$ obtained for the first and second pulses (Fig. 2). These dependences are shown in Fig. 4. We can see that the number of electrons captured by the boundary traps increases as the temperature decreases, while the number of electrons captured by the *por*-Si traps rapidly increases at $T \approx 210$–190 K and then decreases as the temperature decreases further. Since the traps were saturated with electrons under the first pulse of light, the dependences $N(T)$ (Fig. 4) are, simultaneously, the temperature dependences of the concentration of the traps that capture the electrons at the boundary and in the *por*-Si layer. The nonmonotonic dependence $N(T)$ for the traps in the *por*-Si layer (curve *2*) is probably associated with the reversible structural changes in the *por*-Si layers as temperature is varied, which follows from the similarity of this dependence to the dependence $V_{ph}^{por\text{-Si}}(T)$ (Fig. 3, curve *1*).

Figure 5 shows the *I*–*V* characteristics of the Au/*por*-Si/*p*-Si/Al and Au/*por*-Si:Au/*p*-Si/Al structures. These *I*–*V* characteristics are obtained by applying voltage pulses with a width of 15 μs to the structures. The *por*-Si layer was 5 μm thick. We can see that the *I*–*V* characteristics for the undoped structure, as well as for the structure that was lightly doped with Au from the 10^{-4} M solution, are of a diode-type and have rectification factors of about 10^3 and 30, respectively, for a bias of ~4 V. The forward (conducting) current direction corresponds to the positive voltage applied to *p*-Si. The forward currents for the structure lightly doped with Au from the 10^{-4} M solution are lower than those the undoped structure. We believe that this effect is caused by the oxidation of the Si nanocrystals, which

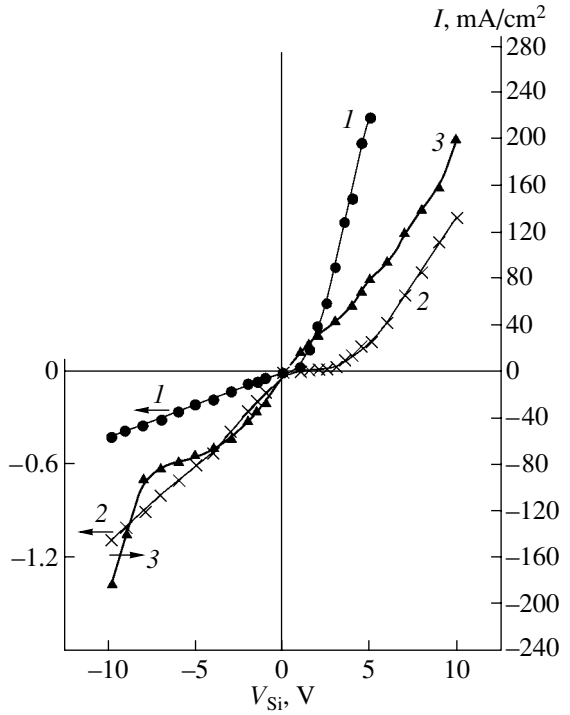

Fig. 5. Current–voltage characteristics of the (*1*) Au/*por*-Si/*p*-Si/Al, (*2*) Au/*por*-Si:Au [10^{-4} M]/*p*-Si/Al, and (*3*) Au/*por*-Si:Au [10^{-3} M]/*p*-Si/Al structures.

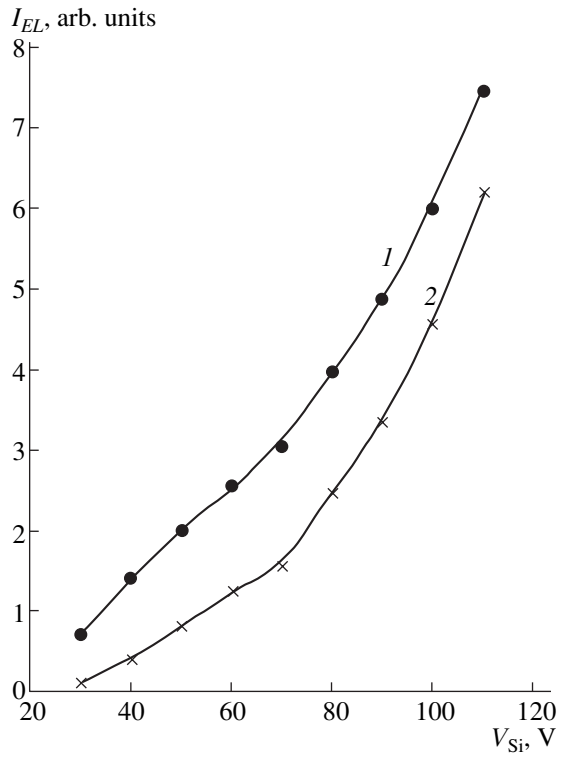

Fig. 6. Voltage dependence of the electroluminescence intensity for the Au/*por*-Si:Au [10^{-3} M]/*p*-Si/Al structure. Curve *1* corresponds to a positive voltage applied to *p*-Si and curve *2* corresponds to a negative voltage applied to *p*-Si.

hampers the current flow through the *por*-Si layer because the number of the Au nanocrystals is still not large enough. The current of the reverse *I–V* characteristic of the structure doped with Au from the 10^{-4} M solution is higher than the reverse current of the undoped structure over the entire voltage range (0–10 V) by a factor of approximately 3. The structure doped heavily with Au from the 10^{-3} M solution is nonrectifying. In the range from +4 to –4 V, the *I–V* characteristics are nonrectifying at a resistance of 65 Ω for a structure with an area of 1 cm^2. Thus, Au doping lowers or eliminates the barrier blocking the current flow through the *por*-Si/*p*-Si junction. Note that this inference is consistent with the photovoltage measurements, which showed that doping changes the surface depletion layer of *p*-Si to a layer that has pronounced hole enrichment.

For the structure doped with Au from the 10^{-3} M solution, at high positive and negative voltages (higher than 8 V), the current increases more rapidly than according to the linear law, which is characteristic of the conductivity of island films composed of various metals [5]. In our case, this conductivity, in principle, can be conductivity through the mixture of the Au and Si islands. Only for this structure did we succeed in observing the EL, which emerged at a voltage of ~40 V independently of the voltage polarity. The EL intensity I_{el} was higher when a positive voltage V was applied to *p*-Si. As the amplitude of the voltage pulses increases, the ratio between the intensities I_{el} of the EL for the two polarities of pulses tended to unity (Fig. 6). Figure 6 shows that the dependences $I_{el}(V)$ that originate in the region of superlinearity of the *I–V* characteristics are themselves superlinear. This circumstance is characteristic of the luminescence of the island metal films, in which, as was satisfactorily demonstrated in our experiments, the luminescence intensity is proportional to the power introduced into the film [5]. We believe that, in our case, it is the Au islands that emit, since it was more difficult to obtain the luminescence of a Si island film than a Au island film [5]. In addition, for the undoped *por*-Si/*p*-Si structures, which have only Si islands (nanocrystals), the EL was unobservable for voltage applied as high as ±150 V, while the forward current of the *I–V* characteristic was as high as 7.5 A/cm^2. In contrast, the EL emergence for the *por*-Si:Au/*p*-Si structure doped with Au from the 10^{-3} M solution was observed for a current of 0.8 A/cm^2.

To obtain more efficient EL, we intend, in future, to carry out doping of thinner *por*-Si layers grown on *n*-Si, where EL has considerably better parameters [14–16].

4. CONCLUSIONS

(i) Based on the study of the temperature dependences of photovoltage, it is shown that Au doping of *por*-Si/*p*-Si structures via their treatment in 10^{-4} M and 10^{-3} M aqueous $AuCl_3$ solutions causes the following phenomena. It transforms the depleted Si boundary layer into a highly hole-enriched layer, affects the mag-

nitude and sign of the photovoltage in the *por*-Si layer, and eliminates the photomemory effects that are associated with the capture of nonequilibrium electrons by traps at the *p*-Si boundary and in the *por*-Si layer; in addition, it also substantially increases the density of boundary electron states to 2×10^{15} cm^{-2} eV^{-1}.

(ii) Au doping of the *por*-Si/*p*-Si structure using the 10^{-4} M solution leads to a certain increase in the rapid and time-integrated relaxation of the photoluminescence (PL), which is associated with oxidation of the Si nanocrystals. Doping using the 10^{-3} M solution substantially decreases the PL intensity, especially the integrated PL intensity, and affects the spectral distribution of the rapid PL component. This phenomenon is caused by a redistribution of the contribution to the PL of emission from the Si nanocrystals and Au nanocrystals that are formed in the *por*-Si film as a result of the doping.

(iii) Doping with Au appreciably affects the current–voltage characteristics of the Au/*por*-Si/*p*-Si/Al structures. This circumstance is associated with the elimination of the depletion layer in the *p*-Si substrate, the oxidation of the Si nanocrystals in the *por*-Si layer, and the nucleation of the Au nanocrystals in the *por*-Si layer. The electroluminescence associated with Au nanocrystals was observed for the Au/*por*-Si:Au [10^{-3} M]/*p*-Si/Al structure.

REFERENCES

1. A. G. Gullis, L. T. Canham, and P. D. J. Calcott, J. Appl. Phys. **82**, 909 (1997).
2. D. Kovalev, H. Heckler, G. Polisski, and F. Koch, Phys. Status Solidi B **215**, 871 (1999).
3. V. E. Primachenko and O. V. Snitko, *Physics of Semiconductor Surfaces Doped with Metals* (Naukova Dumka, Kiev, 1988) [in Russian].
4. I. Coulthard, R. Sammyniaken, S. J. Naftel, *et al.*, Phys. Status Solidi A **182**, 157 (2000).
5. R. D. Fedorovich, A. G. Naumovets, and P. M. Tomchuk, Phys. Rep. **328** (2–3), 74 (2000).
6. É. B. Kaganovich, I. M. Kizyak, S. I. Kirillova, *et al.*, Optoélektron. Poluprovodn. Tekh., No. 37, 136 (2002).
7. E. F. Venger, S. I. Kirillova, I. M. Kizyak, *et al.*, Fiz. Tekh. Poluprovodn. (St. Petersburg) **38**, 117 (2004) [Semiconductors **38**, 113 (2004)].
8. E. F. Venger, T. Ya. Gorbach, S. I. Kirillova, *et al.*, Fiz. Tekh. Poluprovodn. (St. Petersburg) **36**, 349 (2002) [Semiconductors **36**, 330 (2002)].
9. E. F. Venger, É. B. Kaganovich, S. I. Kirillova, *et al.*, Fiz. Tekh. Poluprovodn. (St. Petersburg) **33**, 1330 (1999) [Semiconductors **33**, 1202 (1999)].
10. É. B. Kaganovich, É. G. Manoĭlov, and S. V. Svechnikov, Ukr. Fiz. Zh. **46**, 1196 (2001).
11. L. Burstein, Y. Shapira, J. Partee, *et al.*, Phys. Rev. B **55**, R1930 (1997).
12. Z. S. Gribnikov and V. I. Mel'nikov, Fiz. Tekh. Poluprovodn. (Leningrad) **2**, 1352 (1968) [Sov. Phys. Semicond. **2**, 1133 (1968)].
13. S. I. Kirillova, V. E. Primachenko, E. E. Venger, and V. A. Chernobai, Semicond. Phys. Quantum Electron. Optoelectron. **4**, 12 (2001).
14. W. Long, P. Steiner, and F. Kozlowski, J. Lumin. **57**, 341 (1993).
15. N. Labic and J. Linnros, J. Appl. Phys. **80**, 5971 (1996).
16. S. K. Lazaruk, P. V. Zhagiro, A. A. Leshok, and V. E. Borisenko, Izv. Akad. Nauk, Ser. Fiz. **66**, 179 (2002).

Translated by N. Korovin

Semiconductors, Vol. 39, No. 5, 2005, pp. 572–576. Translated from Fizika i Tekhnika Poluprovodnikov, Vol. 39, No. 5, 2005, pp. 602–607.

AMORPHOUS, VITREOUS, AND POROUS SEMICONDUCTORS

The Influence of Vacuum Annealing Temperature on the Fundamental Absorption Edge and Structural Relaxation of *a*-SiC:H Films

A. V. Vasin*^, A. V. Rusavsky*, V. S. Lysenko*, A. N. Nazarov*, V. I. Kushnirenko*, S. P. Starik, and V. G. Stepanov***

**Institute of Semiconductor Physics, National Academy of Sciences of Ukraine, Kiev, 03026 Ukraine*

^e-mail: vasin@labl5.kiev.ua

***Institute of Superhard Materials, 04074 Kiev, Ukraine*

Submitted August 23, 2004; accepted for publication October 6, 2004

Abstract—The effect of vacuum annealing temperature on the characteristics of the fundamental absorption edge and short-range order reconstruction in amorphous hydrogenated silicon carbide (*a*-SiC:H) films obtained by magnetron sputtering of silicon in an Ar/CH_4 mixture is experimentally investigated. It is shown that redistribution of chemically bound hydrogen occurs at low annealing temperatures (450°C). This redistribution is determined by (i) breakage of silicon–hydrogen bonds and (ii) trapping of atomic hydrogen by carbon dangling bonds. These processes lead to an enhancement of visible photoluminescence. Breakage of carbon–hydrogen bonds and clusterization of amorphous carbon occur at higher annealing temperatures. The proposition that the main nonradiative recombination centers in *a*-SiC:H films are electronic states related to the carbon dangling bonds is justified. © *2005 Pleiades Publishing, Inc.*

1. INTRODUCTION

Hydrogenated amorphous silicon carbide *a*-SiC:H, along with *a*-Si:H, *a*-Ge:H, *a*-C:H, *a*-SiGe:H, and a number of other compounds, belongs to the class of hydrogenated amorphous semiconductors. Its large band gap, high thermal conductivity, high resistance to electrical breakdown, photosensitivity, and the possibility of the low-temperature synthesis of layers with large areas make amorphous and nanocrystalline silicon carbide a promising material for thin-film microelectronics and optoelectronics. However, the structure of amorphous silicon carbide leads to a high concentration of various structural defects, for example, micropores, density and composition fluctuations, dangling bonds, and variations in the lengths and angles of interatomic bonds. Materials with very high defect concentrations have no practical uses. The specific features of the electronic properties of hydrogenated amorphous semiconductors are determined by the strong interaction of the hydrogen incorporated into the film structure with many of the above-mentioned defects. For example, it is well known that *a*-SiC:H films, in contrast to *a*-SiC, can show intense photoluminescence and electroluminescence at room temperature in the visible spectral range, due to the fact that atomic hydrogen can passivate defect states (centers of nonradiative recombination). At higher temperatures (400–600°C), intense redistribution of the bound hydrogen in the bulk of the *a*-SiC:H films occurs and hydrogen effuses from the films, which leads to significant changes in their electronic properties [1–3]. A detailed investigation of the changes in the structural and optical properties occurring at high temperatures is necessary to gain a deeper insight into specific features of the electronic properties of *a*-SiC:H films and to optimize the synthesis technology.

2. EXPERIMENTAL

Films of amorphous hydrogenated silicon carbide were deposited by the dc magnetron sputtering of a single-crystal silicon target (4 cm in diameter) in a gas mixture $Ar(60\%)/CH_4(40\%)$. This technology makes it possible to deposit films at relatively low substrate temperatures without using chemically active silicon-containing gases. The working volume was first evacuated to reduce the pressure of the residual gases to $\sim 10^{-5}$ Pa and, then, a working gas mixture with a pressure of 5 Pa was introduced. The substrates (quartz and silicon wafers) were heated by halogen lamps to 200°C. The magnetron discharge current and voltage were 200 mA and 250 V, respectively. The distance from the target to the substrate was 6 cm. The film homogeneity was increased using translational–rotational motion of the substrate holder above the target. Before the deposition, the target was kept under the operating discharge conditions for 5 min with the shutter closed to degas the target surface and carbonize it to the necessary degree. Under the noted operating conditions, the deposition rate was ~4 nm/min. After the deposition, the substrates with 300-nm *a*-SiC:H films were cut into several parts, which were then subjected to isochronous annealing in

vacuum for 15 min at various temperatures up to T_a = 850°C at a pressure of 10^{-4} Pa.

The films were analyzed by Auger electron spectroscopy (AES) on a JUMP-10S spectrometer and by absorption spectroscopy in the visible (SPECORD M40) and infrared (Infralum FT-801 Fourier Spectrometer) spectral ranges. Raman scattering measurements were performed on a DFS-24 double monochromator with a cooled photomultiplier operating in a photon-counting mode. The raman spectra were excited by an argon laser (with the wavelength λ = 514 nm). The photoluminescence (PL) was excited by an ILGI-503 nitrogen laser with a wavelength of 337.1 nm and was measured using an MDR-23 monochromator and an FÉU-100 photomultiplier.

3. RESULTS

3.1. Film Composition

The films' composition was analyzed by AES. The relative sensitivities of silicon and carbon were determined using the spectra of a single-crystal sample of 6*H*-SiC. Quantitative analysis of the Auger spectra of *a*-SiC:H showed that the films under study had the following composition: 40, 55, 3 and 2 at % of Si, C, O, and N, respectively. High-vacuum annealing at temperatures of up to 850°C did not lead to significant changes in the film composition.

3.2. The Raman Spectra

The initial films and the films annealed at temperatures below 750°C showed no Raman peaks in the range 400–1600 cm^{-1}. This fact indicates that these films contain no microclusters of free silicon and carbon, which are characterized by Raman bands in the ranges 460–520 cm^{-1} (Si–Si) and 1000–1600 cm^{-1} (C–C) [4]. The absence of Raman bands in the range 700–800 cm^{-1} (characteristic of Si–C vibrations) can be explained by the very low Raman cross section for the amorphous film structure.

At an annealing temperature of 750°C, a weak wide band peaked near 1400 cm^{-1} is observed in the Raman spectra of the films (Fig. 1). Increasing the temperature to T_a = 850°C results in a blue shift of the band to 1440 cm^{-1}. No signals in the range 460–520 cm^{-1} and at 800 cm^{-1} were detected. The band near 1400 cm^{-1} can be unambiguously assigned to amorphous carbon clusters. The Raman spectra of amorphous carbon are generally a superposition of two bands, which are denoted as *G* (graphitic, 1500–1600 cm^{-1}) and *D* (disordered, 1300–1400 cm^{-1}). These bands indicate the presence of structural units in the form of graphite hexagons (although strongly distorted). The absence of individual *D* and *G* bands indicates strong disorder in the carbon clusters. The blue shift of the observed band after annealing at 850°C can be explained by an increase in the size of the clusters and a partial relaxation of the stresses contained in them.

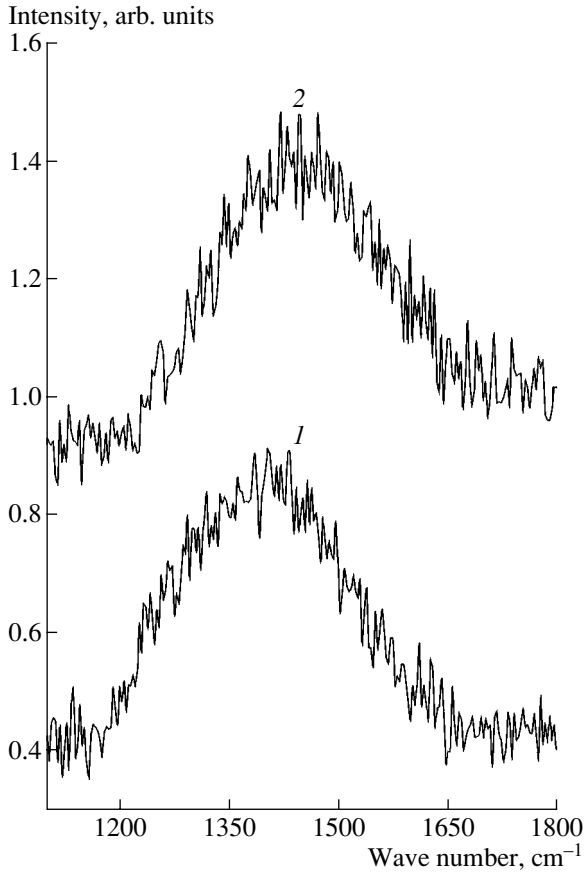

Fig. 1. Raman spectra of the *a*-SiC:H films after vacuum annealing at (*1*) 750 and (*2*) 850°C.

3.3. Absorption Edge

One of the main characteristics of semiconductors is their band gap. The band gap concept is retained for amorphous semiconductors despite the fact that this parameter has no clear formal definition, as it does in the case of the band structure of crystalline semiconductors. The electronic properties of amorphous semiconductors are generally considered in terms of the energy distribution of the electronic density of states. Usually, the optical band gap E_g of amorphous semiconductor films is experimentally determined by a linear extrapolation of the absorption spectrum to zero according to the Tauc relation [5], which describes the dispersion of the absorption coefficient of a material near the fundamental absorption edge:

$$\alpha h\nu = B(h\nu - E_g)^2. \quad (1)$$

Here, α is the absorption coefficient, $h\nu$ is the photon energy, E_g is the band gap, and *B* is a coefficient whose physical meaning is still under debate. In fact, as long-term experience has shown, the behavior of the absorption coefficient of many amorphous semiconductors near the absorption edge can be described by a simple power law, which makes it possible to determine the

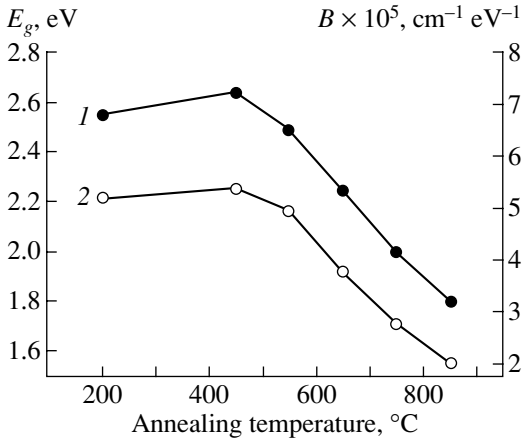

Fig. 2. Dependences of the (*1*) optical band gap E_g and (*2*) coefficient B on the vacuum annealing temperature.

optical band gap E_g. However, while the dependences of the density of states and transition matrix elements on energy remain unknown, we cannot unambiguously determine whether the value of E_g is indeed the band gap in the density of states or if this is some other characteristic energy related to the mobility gap [6].

Attempts have been made to interpret the coefficient B, i.e., the slope of the linear portion of the Tauc dependence, in terms of structural disorder. Regarding the application of this interpretation to *a*-SiC:H, many researchers believe that the coefficient B is directly related to structural and chemical disorder; however, the existing experimental data are very contradictory. Thus, in our opinion, the current understanding of the character of optical transitions in disordered systems is insufficient and the experimental and theoretical investigation of *a*-SiC:H should be continued.

The fundamental absorption edge of the *a*-SiC:H films was analyzed by studying the absorption spectra of the films on quartz substrates in the wavelength range 200–800 nm. Analysis of the edge of the fundamental absorption using the Tauc relation showed that the optical band gap of the as-deposited *a*-SiC:H films is ~2.6 eV. Figure 2 shows the dependence of the optical band gap E_g and the coefficient B on the vacuum annealing temperature. After annealing at T_a = 450°C, a slight increase in E_g is observed. At higher annealing temperatures, E_g gradually decreases. The coefficient B changes in a similar way.

3.4. Infrared Spectroscopy

Clearly, the temperature dependence of the parameters of the fundamental absorption edge should be determined by changes in the character of the short-range order. The behavior of chemically bound hydrogen and the structural changes after annealing were studied by infrared (IR) absorption spectroscopy. Figure 3 shows the transmission spectra of the films before (spectrum *1*) and after annealing at various temperatures (spectra *2–6*). In the spectrum of the initial film, an absorption band at about 800 cm^{-1} is dominant. This band can be assigned to Si–C stretching vibrations. Along with this main band, two additional bands at about 1000 and 2100 cm^{-1} are also observed. The absorption near 2100 cm^{-1} is due to the stretching vibrations of hydrogen bonds of the Si–Si–H_n and C–Si–H_n types (n = 1–3). The absorption near 1000 cm^{-1} is due to vibrations of the carbon–hydrogen bonds in CH_n radicals, i.e., in structural chains of the Si–C–H_n type, which are chemically bound to the Si atoms [7, 8].

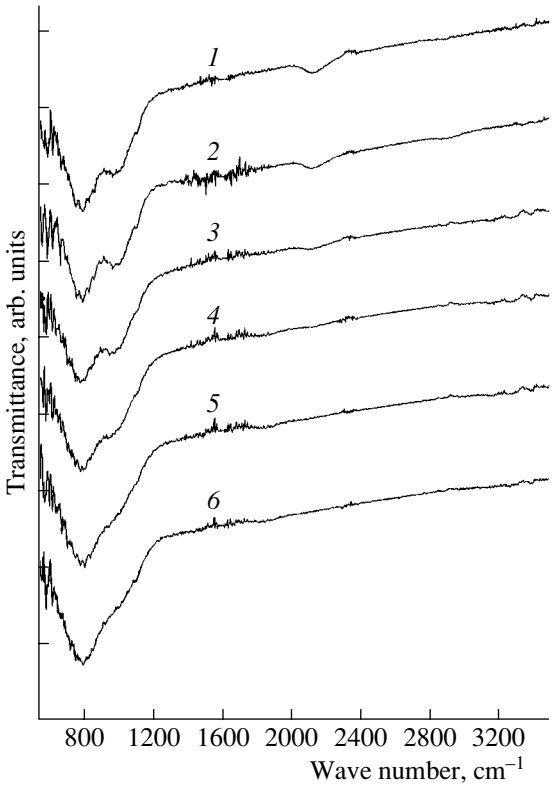

Fig. 3. Infrared transmission spectra of the *a*-SiC:H films (*1*) before and (*2–6*) after vacuum annealing at (*2*) 450, (*3*) 550, (*4*) 650, (*5*) 750, and (*6*) 850°C.

A quantitative analysis of the intensities of the absorption bands was performed using a computer simulation of the spectra as the superpositions of three Gaussian profiles peaked at about 800, 1000, and 2100 cm^{-1}. Figure 4a shows the temperature dependence of the intensity of the Si–H_n (I_{2100}) band normalized to the intensity of the absorption of the as-deposited film. It can be seen that the intensity of the band at 2100 cm^{-1} rapidly decreases as the annealing temperature increases before vanishing at T_a > 650°C. The amplitude of the absorption band near 800 cm^{-1} underwent only insignificant changes after annealing. In order to describe the changes in the relative intensity of the absorption near 1000 cm^{-1}, we used the ratio of the intensities of the Si–C–H and Si–C bonds (I_{1000} and I_{800}, respectively). The dependence of the ratio I_{1000}/I_{800} on the annealing temperature is shown in Fig. 4b. After

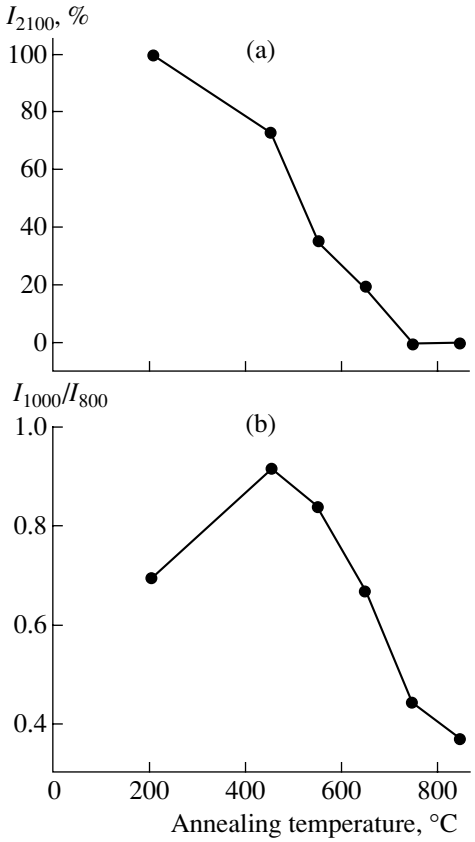

Fig. 4. Dependences of the absorption band intensities on the annealing temperature: (a) the reduced intensity of the absorption band near 2100 cm^{-1} (the band intensity of the initial sample is assumed to be 100%) and (b) the ratio of the intensities of the absorption bands near 1000 cm^{-1} (I_{1000}) and 800 cm^{-1} (I_{800}).

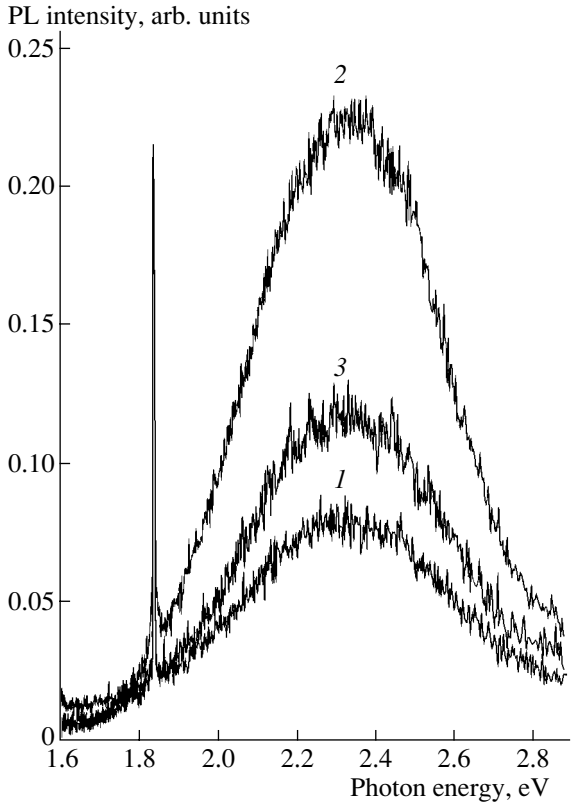

Fig. 5. Photoluminescence spectra of the *a*-SiC:H films (*1*) as-deposited and (*2*, *3*) after vacuum annealing for 15 min at (*2*) 450 and (*3*) 550°C.

low-temperature annealing (T_a = 450°C), a significant increase in the relative intensity of I_{1000} is observed, which is indicative of an increase in the concentration of carbon–hydrogen bonds. At T_a > 550°C, the ratio of the intensities gradually decreases.

It is noteworthy that even annealing at the maximum temperature used (850°C) does not lead to a decrease in the width of the main Si–C absorption band (800 cm^{-1}). In contrast, after annealing at 650°C and higher, this band somewhat broadened. This fact indicates that no significant ordering of the angles and lengths of the Si–C bonds occurs in this temperature range.

3.5. Photoluminescence

Photoluminescence was measured at room temperature. The as-deposited *a*-SiC:H films showed very weak luminescence in the visible range, with the maximum intensity at 2.3 eV (Fig. 5, spectrum *1*). However, after vacuum annealing at a temperature of 450°C, the PL intensity increases several times (Fig. 5, spectrum *2*). At the annealing temperature T_a = 550°C (Fig. 5, spectrum *3*) and above, the PL intensity gradually decreases. The narrow line at about 1.85 eV is one of the laser harmonics, which can serve as a reference in the estimation of the energy position of the PL band. It should be noted that the energy position and width of the PL band did not change with an increase in the annealing temperature.

4. RESULTS AND DISCUSSION

As was noted above, according to the results of the Auger electron analysis, the content of carbon and silicon in the films under study corresponds to the stoichiometric composition of crystalline silicon carbide, with a small excess of carbon, and residual oxygen and nitrogen impurities. The absence of peaks due to amorphous silicon and amorphous carbon in the Raman spectra of the as-deposited films indicates that the structure of these films is homogeneous at the macro- and microscopic levels. Clusterization of the amorphous carbon is observed only at high annealing temperatures. However, it is clear that, under such synthesis conditions, composition fluctuations are possible at the nanoscopic level. The elemental composition of the films barely changed after annealing (except in relation to hydrogen). Therefore, we can reasonably conclude that the change in the optical band gap as a result of annealing is not related to changes in the composition. We suggest that one of the factors controlling the change in E_g upon annealing is the change in the num-

ber and type of hydrogen bonds. Chemically bound hydrogen can affect the optical band gap because the energy of the electronic transitions between the bonding and antibonding states associated with C–H and Si–H bonds is much higher than the energy of the transitions related to Si–C bonds. It is also known that the energy of a C–H bond (4.2 eV) is higher than the energy of a Si–H bond (3.4 eV) [7]. Therefore, it might be expected that the contribution of C–H bonds to the increase in the optical band gap is larger than the corresponding contribution of Si–H bonds. This is confirmed by an insignificant increase in E_g after vacuum annealing at 450°C. At this temperature, Si–H bonds break, whereas C–H bonds are still stable [9]. The released, weakly bound, atomic hydrogen migrates throughout the film and can be captured by the dangling carbon bonds. This leads to an increase in the number of C–H bonds and the relative intensity of the absorption near 1000 cm^{-1}. In this case, the increase in E_g due to the increase in the number of C–H bonds dominates over the competing effect of a reduction in E_g due to the decrease in the number of Si–H bonds. At higher temperatures (≥550°C), both the Si–H and C–H bonds break.

The above data are in good agreement with the results of [1]. It was found in [1] that the concentration N_s of paramagnetic centers in stoichiometric *a*-$Si_{0.5}C_{0.5}$:H films obtained by decomposition of a methane/silane mixture in a high-frequency glow discharge plasma increases by 1–1.5 orders of magnitude after vacuum annealing at 300–500°C. It was suggested in [1] that, at relatively low temperatures, weakly bound hydrogen is released and diffuses from the nanopores into the film bulk. This process is accompanied by an additional passivation of dangling bonds. With an increase in the annealing temperature to above 500°C, a gradual increase in N_s was observed. The results we obtained from measurements of the electron spin resonance in the *a*-SiC:H films are in complete agreement with the data of [1]. In addition, as was shown above, we observed a sharp increase in the visible PL intensity after low-temperature annealing. This circumstance provides a basis for the belief that the nonradiative recombination centers in amorphous silicon carbide films are electronic states related to dangling carbon bonds.

The decrease in E_g at high annealing temperatures (above 650°C) can be explained by the clusterization of free unhydrogenated carbon (C–C bonds). This clusterization of free carbon indicates that the structural inhomogeneity of the film increases. This conclusion is confirmed by the broadening of the absorption band near 800 cm^{-1}. The reason for the increase in the chemical and structural inhomogeneity is the instability of the chemically disordered system. However, the fact that the parameters of the PL band (except for its amplitude) do not change during annealing indicates the presence of structural regions with electronic properties that change little during this process. We believe that these regions are amorphous clusters of stoichiometric unhydrogenated silicon carbide, in which the atomic coordination corresponds to that in bulk silicon carbide. It would seem that the radiative recombination occurs specifically in these regions. These chemically ordered clusters are thermally stable, and the energy of the radiative transitions, as well as the local optical band gap of these clusters, does not change as the annealing temperature is increased up to 850°C. The change in the short-range order structure, the clusterization of free carbon, and the corresponding change in the absorption near the fundamental above edge occur in inhomogeneous chemically disordered regions. From this point of view, we have to admit that the value of the optical band gap obtained from the Tauc relation is not quite adequate for multicomponent amorphous semiconductors, which are characterized by structural and chemical inhomogeneity.

5. CONCLUSIONS

The effect of the temperature of vacuum annealing on the fundamental absorption edge and the short-range order structure in *a*-SiC:H films was investigated. It was ascertained that, at relatively low vacuum annealing temperatures (450°C), a redistribution of chemically bound hydrogen occurs: the breakage of Si–H bonds, trapping of atomic hydrogen by dangling carbon bonds, and, as a result, PL enhancement. At high annealing temperatures (above 650°C), clusterization of free carbon occurs. It is shown that the change in the optical band gap due to vacuum annealing is controlled by changes in the number and type of hydrogen bonds and the clusterization of free carbon. Based on an analysis of the effect of the annealing temperature on the fundamental absorption edge and PL parameters, a structural model of *a*-SiC:H films is proposed, according to which an *a*-SiC:H film consists of homogeneous clusters of amorphous silicon carbide incorporated into a matrix of chemically disordered *a*-$Si_{1-x}C_x$:H solid solution.

REFERENCES

1. I. N. Trapeznikova, O. I. Kon'kov, V. E. Chelnokov, *et al.*, in *Proceedings of 5th International Conference on SiC and Related Materials* (Washington, DC, 1993), p. 125.
2. I. Magafas, J. Non-Cryst. Solids **318**, 158 (1998).
3. A. L. Baia Neto, S. S. Camargo, Jr., and R. Carius, Surf. Coat. Technol. **120–121**, 395 (1999).
4. R. Messier, A. P. Giri, and R. A. Roy, J. Vac. Sci. Technol. A **2**, 500 (1984).
5. J. Tauc, R. Grigorovici, and A. Vancu, Phys. Status Solidi **15**, 627 (1966).
6. N. F. Mott and E. A. Davis, *Electronic Processes in Non-Crystalline Materials*, 2nd ed. (Clarendon, Oxford, 1979; Mir, Moscow, 1982).
7. J. Cui, Rusli, and S. F. Yoon, J. Appl. Phys. **89**, 2699 (2001).
8. A. L. Baia Nato, S. S. Camargo, R. Carius, *et al.*, Surf. Coat. Technol. **120–121**, 395 (1999).
9. L. Magafas, J. Non-Cryst. Solids **238**, 158 (1998).

Translated by Yu. Sin'kov

Semiconductors, Vol. 39, No. 5, 2005, pp. 577–584. Translated from Fizika i Tekhnika Poluprovodnikov, Vol. 39, No. 5, 2005, pp. 608–615.

AMORPHOUS, VITREOUS, AND POROUS SEMICONDUCTORS

Simulation of the Electrical Properties of Polycrystalline Ceramic Semiconductors with Submicrometer Grain Sizes

I. V. Rozhanskiĭ^ and D. A. Zakheim

Ioffe Physicotechnical Institute, Russian Academy of Sciences, Politekhnicheskaya ul. 26, St. Petersburg, 194021 Russia

^e-mail: igor@quantum.ioffe.ru

Submitted October 5, 2004; accepted for publication October 12, 2004

Abstract—A numerical model for the calculation of the electrical characteristics of polycrystalline ceramic semiconductors is suggested. The model is applicable in a situation where the average grain size is comparable with the depletion region width near a grain boundary and the double Schottky barriers of neighboring boundaries overlap. The two-dimensional calculation is carried out in the diffusion–drift approximation using the Voronoi grid method. The effect of crystalline grain size on the current–voltage characteristic and specific capacitance of the material is analyzed using *p*-$SrTiO_3$ as an example. © *2005 Pleiades Publishing, Inc.*

1. INTRODUCTION

Polycrystalline ceramic semiconductors based on $BaTiO_3$, $SrTiO_3$, ZnO, etc. have been widely used in various fields of microelectronics for many years [1–4]. These materials have a complex grain structure, and the grain boundaries profoundly affect the corresponding electrical characteristics. The segregation of charged defects at the grain boundaries and diffusion of the compensating impurity over the boundaries in a uniformly doped polycrystalline semiconductor lead to the emergence of uncompensated electrical charge at these boundaries, which forms a double Schottky barrier (see, for example, [4–6]).

It is known that, for a specified level of bulk doping, barrier width and height depend on the concentration of compensating impurity at the boundaries. Small variations in this concentration can change the electrical conductivity of a boundary by several orders of magnitude. Thus, the same material can be used to fabricate resistors, capacitors, or nonlinear varistors [7], which opens up the possibility of developing integrated circuits for passive components based on ceramic semiconductors [2]. Another important and promising application is the use of transparent thin-film transistors based on polycrystalline ZnO in liquid-crystal displays with an active matrix [8]. In addition, due to the large magnitude of their permittivity, polycrystalline ceramic materials are used to fabricate compact capacitors. They are also considered as the most suitable materials for application in the next generation of random-access memory devices [2, 9]. Due to polycrystallinity, the effective relative permittivity in such materials can equal several thousand. According to modern requirements for the miniaturization of electronic components, thin polycrystalline films with a characteristic grain size of ~100 nm or smaller are of particular interest. A decrease in grain size to values comparable with the width of the depletion region near a grain boundary leads to a substantial overlap of double Schottky barriers and substantially changes the electrical properties of the material. In this context, the problem regarding the calculation of the characteristics of such systems emerges.

At present, there are analytical [4–6] and numerical [10, 11] models that describe the electrical properties of a single grain boundary. However, a transition from the properties of a single boundary to a macroscopic sample with numerous grains calls for a description of the grain structure of a ceramic material. This description is usually based on a quasi-3D regular model (brick-wall model) where all grains are cubes of the same size [3, 12], which does not fully reflect the structure of an actual polycrystalline ceramic material. A more adequate approach to the simulation of the structure based on the Voronoi grid has also been suggested [13, 14]. However, both in regular models and in the Voronoi grid models, the grain boundaries are considered as independent elements and their electrical characteristics are calculated using one-dimensional models of a single boundary. Such an approach is quite adequate if the characteristic grain size substantially exceeds the thickness of the depletion layer at a grain boundary. To give a specific example, the typical grain size in $Ba(Sr)TiO_3$-based ceramics, which were described in [15, 16], and in ZnO-based ceramics, which were obtained by sintering in [17], is 1–10 μm, while the width of the boundary depletion layer is tens of nanometers. As the grain size decreases to values comparable with the thickness of the depletion region, the potential barriers of neighboring boundaries overlap. This situation is, for example, characteristic of polycrystalline ceramic films obtained using the deposition method [8, 9], where the characteristic grain size is 100–10 nm. To describe such a structure correctly with regard to the

overlap of the double Schottky barriers, a complete simulation of charge transport is needed in a multigrain system.

Thus, there exist numerous studies that are devoted to the analytical description and simulation of charge transport in polycrystalline ceramic semiconductors using the diffusion–drift approach and assuming independent double Schottky barriers.

In contrast to these studies, we suggest, in this paper, a two-dimensional (2D) diffusion–drift model of polycrystalline semiconductors that makes it possible to describe the transition from a case of large grains to the case where the grain size is comparable with the width of the depletion boundary layer. This model allowed us to calculate variations in the current–voltage (*I–V*) characteristic and a decrease in specific capacitance as the average grain size decreased. Using *p*-$SrTiO_3$ as our example, we show that, at the average grain size $D \lesssim 150$ nm, the shape of the *I–V* characteristic and the form of the dependence of the specific capacitance on the number of grain boundaries change radically and that the threshold voltage increases. As the grain size decreases further, the effect of polycrystallinity disappears, and the sample behaves like a capacitor uniformly filled with insulator. In this case, the specific capacitance becomes independent of the grain size and depends only on the sample thickness. Based on the results of the calculations, we suggest ways to optimize the capacitance of the sample as its size decreases.

2. MODEL

2.1. The Two-Dimensional Voronoi Construction

The grain structure of the material was simulated using a 2D Voronoi grid [18]. The point nodes, i.e., nuclei, were randomly distributed in a rectangular region corresponding to a macroscopic sample. Then, a set of space points, which lie nearer to a given node than to its neighboring nodes, was associated with each node (the Voronoi cell). The grid cells were identified with semiconductor grains. Such a construction is similar to the actual formation of the grain structure [13]. The entire sample bulk was considered to be uniformly donor- or acceptor-doped. In contrast, the concentration of another type of impurity had sharp maxima near the grain boundaries and was equal to zero in the grain bulk. As a rule, the depth of the penetration of the impurity, which diffuses along the grain boundaries, into the semiconductor bulk did not exceed several monolayers. In our model, the concentration profile of the compensating impurity along the normal to the boundary is described by a Gaussian distribution. This distribution is of course narrower than the width of the boundary depletion layer. To simulate nonrectifying contacts, the impurity concentration was intentionally assumed to be zero in the near-contact regions, i.e., at a certain specified distance from two opposite sample boundaries.

2.2. Calculation of the Equilibrium State

The equilibrium distributions of the electrical potential and carrier concentrations are found by numerically solving the Poisson equation

$$\Delta\phi(x, y) = -\frac{e}{\varepsilon\varepsilon_0}[-n(\phi) + p(\phi) - N_A^-(\phi) + N_D^+(\phi)], \quad (1)$$

where the concentrations of free electrons and holes (n and p) and of ionized acceptors and donors (N_A^- and N_D^+) at a point with a specified potential are described by the Fermi statistics [19]:

$$\begin{aligned} n &= N_c\Phi_{1/2}[(E_F - E_c + e\phi)/kT], \\ p &= N_v\Phi_{1/2}[(-E_F - e\phi)/kT], \\ N_D^+ &= N_D(x, y)F[(E_F - E_D + e\phi)/kT], \\ N_A^- &= N_A(x, y)F[(-E_F + E_A - e\phi)/kT]. \end{aligned} \quad (2)$$

Here, N_c and N_v are the effective densities of states of electrons and holes; $N_A(x, y)$ and $N_D(x, y)$ are the acceptor and donor distribution profiles; E_F is the Fermi level; E_c is the conduction-band bottom; E_D and E_A are the energies of the donor and acceptor levels, respectively; the valence band top is assumed to be zero in the energy scale; F and $\Phi_{1/2}$ are the Fermi function and the Fermi integral, respectively; T is the temperature; k is the Boltzmann constant; ε is the relative permittivity; ε_0 is the permittivity of free space; and e is the elementary charge.

The Fermi level E_F can be found from the electrical neutrality condition for the total volume (V) of the sample:

$$\int_V [p(x, y) - n(x, y) + N_D^+(x, y) - N_A^-(x, y)]dxdy = 0. \quad (3)$$

Substituting expressions (2) into Eqs. (1) and (3), we obtain a set of two equations, in which the unknown quantities are the potential $\phi(x, y)$ and the Fermi level E_F.

We imposed zero boundary conditions on the potential at two opposite boundaries of the sample and on the normal component of the electric field at the other two opposite boundaries. In order to solve Eqs. (1) and (3) numerically, we wrote them in the form of finite differences on a rectangular grid using a second-order difference scheme. The obtained set of nonlinear algebraic equations with respect to the values of the potential at the grid nodes $\phi_{i,j}$ and the Fermi level E_F was solved using Newton's method. At each step of this iteration, we used a method involving a multifrontal LU expansion of sets of linear equations that featured a sparce asymmetric matrix [20]. This circumstance allowed us to use grids including as many as 10^5 nodes.

2.3. Simulation of Time-Dependent Effects

In the diffusion–drift approximation, the expressions for the densities of the electron and hole current components take the form

$$\begin{aligned} \mathbf{J}_n &= en\mu_n\nabla\phi + eD_n\nabla n, \\ \mathbf{J}_p &= ep\mu_p\nabla\phi - eD_p\nabla p, \end{aligned} \tag{4}$$

where the electron and hole mobilities (μ_n and μ_p) are related to diffusion coefficients (D_n and D_p) by the Einstein relations

$$\begin{aligned} \frac{\mu_n}{D_n} &= \frac{1}{n_0}\frac{dn_0}{dE_F}, \\ \frac{\mu_p}{D_p} &= \frac{1}{p_0}\frac{dp_0}{dE_F}, \end{aligned} \tag{5}$$

where n_0 and p_0 are the equilibrium electron and hole concentrations.

The continuity equations for electrons and holes are written as

$$\begin{aligned} \frac{dn}{dt} &= \frac{1}{e}\mathrm{div}\mathbf{J}_n - R_{e\to h} - R_{e\to D}, \\ \frac{dp}{dt} &= \frac{1}{e}\mathrm{div}\mathbf{J}_p - R_{e\to h} - R_{h\to A}, \end{aligned} \tag{6}$$

where $R_{e\to h}$ is the total recombination rate of the electron–hole pairs, i.e., the difference between the generation and recombination rates, while $R_{e\to D}$ and $R_{h\to A}$ are the total rates of electron and hole capture by ionized donors and acceptors, respectively.

The concentrations of localized charges (ionized donors and acceptors) can vary only due to the capture and emission of electrons and holes:

$$\begin{aligned} \frac{dN_D^+}{dt} &= -R_{e\to D}, \\ \frac{dN_A^-}{dt} &= -R_{h\to A}. \end{aligned} \tag{7}$$

The expressions for the recombination rates are given by the formulas [19]

$$\begin{aligned} R_{e\to h} &= \alpha_{eh}[np - n_0p_0], \\ R_{e\to D} &= \alpha_{eD}\left[nN_D^+ - n_0N_{A0}^+\frac{N_D - N_D^+}{N_D - N_{D0}^+}\right], \\ R_{h\to A} &= \alpha_{hA}\left[pN_A^- - p_0N_{A0}^-\frac{N_A - N_A^-}{N_A - N_{A0}^-}\right], \end{aligned} \tag{8}$$

where N_A and N_D are the total concentrations of acceptors and donors, N_A^- and N_D^+ are the concentrations of ionized acceptors and donors, and index 0 denotes the corresponding equilibrium concentrations. The quantities α_{eh}, α_{eD}, and α_{hA} are the constants for the electron–hole, electron–donor, and hole–acceptor recombination processes.

When Eqs. (6) and (7) are combined with Poisson equation (1), they form a complete set of equations for the unknown functions $n(x, y)$, $p(x, y)$, $N_A^-(x, y)$, $N_D^+(x, y)$, and $\phi(x, y)$.

An external electric field is then applied along the x axis of the rectangular calculation region $x \in [x_0, x_L]$, $y \in [y_0, y_L]$. The contacts are located at the left-hand ($x = x_0$) and right-hand ($x = x_L$) boundaries of the region. The Dirichlet boundary conditions are imposed on these boundaries:

$$\begin{aligned} \phi(x_0, y) &= U, \\ \phi(x_L, y) &= 0, \\ N_\alpha(x_0, y) &= N_{\alpha 0}(x_0, y), \\ N_\alpha(x_L, y) &= N_{\alpha 0}(x_L, y), \end{aligned} \tag{9}$$

where $N_\alpha = \{n, p, N_A^-, N_D^+\}$, i.e., all the concentrations n, p, N_A^-, and N_D^+ are equated to their equilibrium values. The Neumann conditions are imposed at the above boundaries in the direction of the external electric field,

$$\left.\frac{\partial\phi(x, y)}{\partial y}\right|_{y = y_0} = \left.\frac{\partial\phi(x, y)}{\partial y}\right|_{y = y_L} = 0,$$

$$\left.\frac{\partial N_\alpha(x, y)}{\partial y}\right|_{y = y_0} = \left.\frac{\partial N_\alpha(x, y)}{\partial y}\right|_{y = y_L} = 0.$$

In order to calculate the direct current when applying the potential U, the derivatives in the first terms of continuity equations (6) and (7) are assumed to be equal to zero. After writing the set of Eqs. (6), (7), and (1) on the rectangular grid, we obtain a set of algebraic equations with respect to the vector of the unknown quantities

$$\mathbf{X} = \{n_0..n_L, p_0..p_L, N_{A0}^-..N_{AL}^-, N_{D0}^+..N_{DL}^+, \phi_0..\phi_L\}.$$

As in the calculation of the equilibrium state, the numerical solution of the set is carried out by Newton's method in combination with the multifrontal LU expansion [20].

The resulting algorithm allows us to simulate both the steady state and time evolution of the system when imposing time-dependent boundary conditions. In the latter case, the derivatives in the first terms in Eqs. (6) and (7) are nonzero and the entire set of Eqs. (6), (7), and (1) is solved by the implicit Euler method. Then, the corresponding set of nonlinear algebraic equations for every time iteration can be solved by Newton's method.

In order to simulate the capacitance of the system, we analyzed the time variation in the electric-current response to a step variation in the voltage. First, we simulated the steady state for a constant voltage U. In

Parameters of $SrTiO_3$ used in the calculation

Parameter	Value
E_g	3 eV
E_A	0.15 eV
E_D	2.85 eV
N_A	2×10^{19} cm^{-3}
N_D	$(0.8–2) \times 10^{14}$ cm^{-2}
μ_p	0.5 cm^2 V^{-1} s^{-1}
α_{hA}	10^{-8} cm^3 s^{-1}
ε	300

Note: E_g is the band gap. The parameters are given for $T = 300$ K. The effective hole and electron masses were assumed to be equal, $m_p = m_n = m_0$, where m_0 is the free-electron mass.

this case, the boundary condition for the potential at the left-hand contact was assumed to be $\phi(x_0, y) = U$. Then, at an instant chosen as the origin ($t = 0$), the boundary condition at the left-hand contact was used in the form $\phi(x_0, y) = U + dU$, and the time dependence $I(t)$ for the current through the contacts was calculated until the steady-state value $I(\infty)$ was attained. In the absence of leakage current ($I(\infty) = 0$), the differential capacitance of the system can be calculated by integrating the response $I(t)$:

$$c(U) = \frac{dQ}{dU} = \frac{1}{dU}\int_0^\infty I(t)dt. \quad (10)$$

In the presence of leakage current, the definition of the system capacitance generally becomes ambiguous. In what follows, the capacitance for this case is calculated assuming the presence of an active leakage resistance in the system, which shunts the capacitance:

$$c(U) = \frac{1}{dU}\int_0^\infty [I(t) - I(\infty)]dt. \quad (11)$$

3. RESULTS OF NUMERICAL CALCULATIONS

The simulation was carried out for a standard example of a uniformly Ni-doped polycrystalline *p*-$SrTiO_3$ semiconductor. The physical parameters of this material, which were taken from [11, 15], are given in the table.

In the calculations, since the electron concentration in a *p*-type semiconductor is vanishingly small, we disregarded the electron–hole recombination and electron capture by donors ($\alpha_{eh} = \alpha_{eD} = 0$). In order to estimate the constant for the hole capture by acceptor levels α_{hA}, we used the expression $\alpha_{hA} = SV_{kT}$, where V_{kT} is the average hole thermal velocity and S is the effective capture cross section [19]. For S, we can use the estimate $S \sim a^2$, where $a \approx 0.4$ nm is the lattice constant for $SrTiO_3$. The average hole thermal velocity is $V_{kT} \sim \sqrt{kT/m_p} \approx 7 \times 10^6$ cm/s; consequently, it follows that $\alpha_{hA} \sim 10^{-8}$ cm^3/s. This estimate is sufficient for the simulation, since the shape of the time response, i.e., the characteristic current-relaxation time, depends on α_{hA}, whereas dc conductivity and capacitance are independent of α_{hA}.

It is known that, just like holes, positively charged oxygen vacancies operate as mobile charge carriers in $SrTiO_3$. The number of vacancies in the sample is constant at room temperature and depends on the conditions and technology applied in the ceramics fabrication [11]. In order to carry out a quantitative comparison with the experiment, it is important to take into account all the types of charged defects that are present in the specific material under study; this can be achieved by analogy with charge carriers of various types, which are taken into account in the model. Furthermore, we do not consider the charge transport associated with the oxygen vacancies. First, this transport mechanism is characteristic only of a specific type of ceramics, and, second, the inclusion of this mechanism does not affect the qualitative conclusions of the theory.

3.1. An Isolated Grain Boundary

Let us first consider the electrical characteristics of an isolated plane grain boundary between two semiinfinite grains.

The calculation performed using the algorithm described in Subsection 2.2 allows us to determine the potential barrier profile at the grain boundary in the absence of an external electric field. The height of this barrier and the width of the depletion region when without mobile carriers can be estimated in the Schottky approximation [6]:

$$\Phi_b = \frac{eN_S^2}{8\varepsilon\varepsilon_0 N_V}, \quad (12)$$
$$d = N_S/N_V,$$

where N_V is the concentration of acceptors in the bulk, N_S is the concentration of donors at the surface, and d is the width of the region depleted of mobile carriers at one side of the boundary.

Figure 1 shows the potential-barrier profiles calculated using the simulation (the solid line) and the Schottky approximation (dashed line). The surface concentration of the donor impurity at the grain boundary varied from 8×10^{13} to 2×10^{14} cm^{-2}. The barriers calculated in the Schottky approximation were somewhat narrower, since the thermal spread of the carrier concentration profiles was not taken into account in this approximation. Figure 1 shows that the potential barrier at the boundary is very sensitive to a variation in the compensating-impurity concentration, which makes it possible to affect the electrical properties of the material as a whole by slightly varying this concentration.

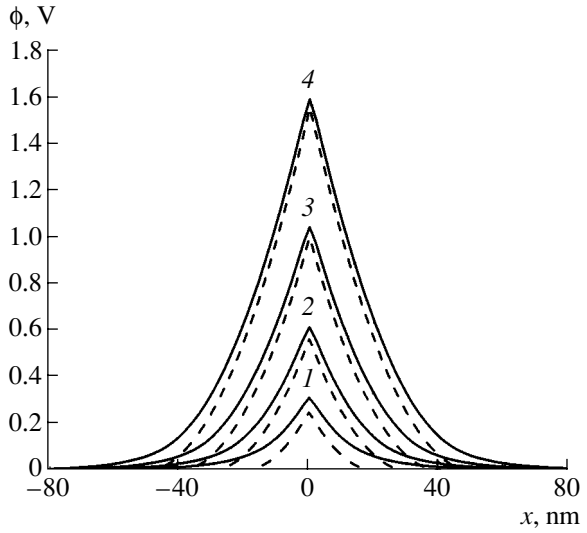

Fig. 1. The steady-state potential profile near the grain boundary. The result of our simulation is shown by the solid line, and the calculation in the Schottky approximation is shown by the dashed line. The surface donor concentrations at the grain boundary N_S are (*1*) 8×10^{13}, (*2*) 1.2×10^{14}, (*3*) 1.6×10^{14}, and (*4*) 2×10^{14} cm^{-2}.

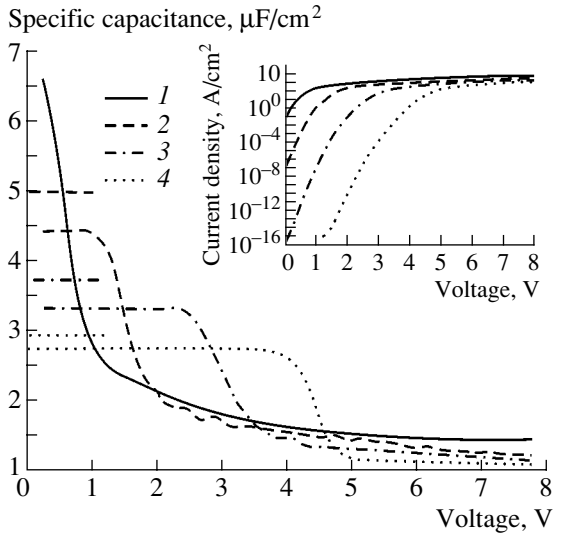

Fig. 2. Capacitance–voltage characteristics of the grain boundary. The surface donor concentrations at the grain boundary are (*1*) 8×10^{13}, (*2*) 1.2×10^{14}, (*3*) 1.6×10^{14}, and (*4*) 2×10^{14} cm^{-2}. The current–voltage characteristics for the same values of N_S are shown in the inset.

Low barriers correspond to a conducting state, whereas the presence of high barriers at the boundaries blocks conductivity and the material behaves as an electrical capacitor. In the case of medium-height barriers, the conductivity increases drastically if a threshold voltage V_c is applied to them, giving rise to varistor-type characteristics. In the Schottky approximation, the threshold voltage is given by [6]

$$V_c = \frac{eN_S^2}{2\varepsilon\varepsilon_0 N_V}. \quad (13)$$

Figure 2 shows the current–voltage (*I–V*) and capacitance–voltage (*C–V*) characteristics calculated for the same set of concentrations of the near-boundary impurity as in Fig. 1. The higher the impurity concentration, the higher the barrier and, consequently, the threshold voltage. The capacitance remains constant up to the threshold voltage, which corresponds to the onset of boundary-related leakage in the corresponding *I–V* characteristic. The capacitance of the boundary region in the absence of leakage in the Schottky approximation is $c = \varepsilon\varepsilon_0/d$. The simulation shows that the Schottky approximation, which is shown by the short line segments in Fig. 2, overestimates the capacitance due to the incorrect estimation of the width of the depletion region.

3.2. The Effect of Grain Size on Current–Voltage Characteristics

According to expression (12), for a grain size comparable with the width of the depletion region *d*, the representation of a polycrystalline semiconductor as a system of separate double Schottky barriers becomes inaccurate. Figure 3 shows the calculated electric-current densities in relation to the voltage applied to the system. The calculations were performed for polycrystalline samples of a fixed size ($L_x \times L_y$, $L_x = L_y = 600$ nm) but with a varying number of grains. The average grain size *D* varied from 85 to 300 nm. The threshold voltage V_c is shown in the inset in Fig. 3 as a function of the average grain size. The calculation was carried out using the

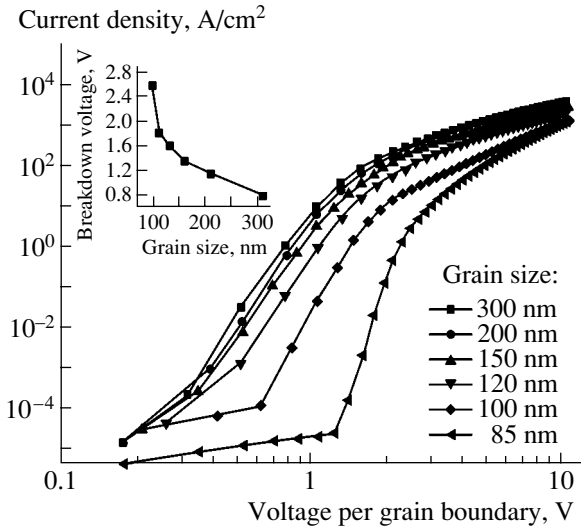

Fig. 3. Current–voltage characteristics for different average grain sizes. $N_S = 1.2 \times 10^{14}$ cm^{-2}. The threshold voltage V_c as a function of the average grain size is shown in the inset.

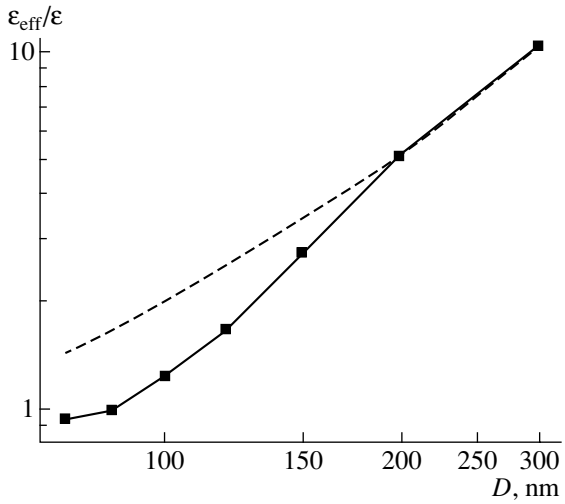

Fig. 4. Effective permittivity as a function of the average grain size. The results of the exact numerical calculation are shown by the solid line, and results of the calculation using expression (15) are shown by the dashed line.

parameters listed in the table and the surface concentration of the donor impurity $N_S = 1.2 \times 10^{14}$ cm^{-2} (see Fig. 1). For this impurity concentration, the characteristic size of the grain region, which is depleted of mobile carriers, in Schottky approximation (12) is $2d$ = 60 nm. The ratio of this quantity to the average grain size, $\xi = 2d/D$, is varied from 0.2 to 0.7. The voltage applied to the system (in the x direction) divided by the average size of grain boundaries in this direction is plotted on the abscissa axis in Fig. 3. It can be seen that, in the case of large grains (small ξ), the dependences of the current density on the reduced voltage coincide; i.e., a polycrystalline material is actually a system of separate double Schottky barriers with corresponding I–V characteristics. The conductivity of the material is proportional to the number of grain boundaries in the direction of the applied voltage. However, as the size of the grains decreases, starting from D = 150 nm ($\xi = 0.4$), the neighboring double Schottky barriers overlap. In this case, the I–V characteristics shift to higher voltages, whereas the threshold voltage V_c increases abruptly.

3.3. The Grain-Size Dependence of the Capacitance

From the viewpoint of developing small-size capacitors, e.g., for random-access memory devices, the value $N_S = 1.2 \times 10^{14}$ cm^{-2} is optimal among the above set of donor concentrations at the boundary (Figs. 1, 2). This value allows the attainment of the highest capacitance possible without leakage for voltages up to $V_0 = 1$ V. The external voltage applied to the system was selected so that the voltage drop across each boundary did not exceed this value, $V < V_0 m$ (where m is the average number of intersections between the boundaries and the x axis in the calculation region). The capacitance of a polycrystalline sample was calculated by simulating the carrier transport and integrating the time dependence of the current response to a step voltage with the amplitude V using Eq. (10). The results of the calculation were averaged over several random representations of the structure. We calculated the capacitance for the above-mentioned samples of fixed size, $L_x = L_y$ = 600 nm, containing varying numbers of grains. In this case, the obtained capacitance was divided by the width of the calculation region L_y; i.e., we calculated the specific capacitance of the system. The effective permittivity is related to the specific capacitance by $\varepsilon_{eff} = cL_x/\varepsilon_0$. Figure 4 shows the obtained dependence of ε_{eff}, normalized by permittivity of the material (for the case of $\varepsilon = 300$) on the average grain size.

For a fixed width of the depletion region d and size of the calculation region L_x, the ratio $m = L_x/D - 1$ yields the average number of grain boundaries, which intersect the x axis. Since the boundary capacitors along the x axis are electrically connected in series, the total capacitance of the system, in the first approximation, should decrease proportionally to $1/m$ as the number of grain boundaries between the contacts increases,

$$c(n) = \frac{\varepsilon\varepsilon_0}{md}. \tag{14}$$

For the effective permittivity, we have

$$\varepsilon_{eff}(D) = \frac{\varepsilon L_x D}{d(L_x - D)}. \tag{15}$$

Figure 4 shows a comparison between dependence (15), indicated by the dashed line, and the exact numerical calculation. We can see that, as the grain size decreases, the capacitance of the system, from D = 150 nm, decreases much more rapidly. For $D < 100$ nm, this quantity virtually coincides with the capacitance of a homogeneous plane capacitor. This result suggests that, for these and smaller grain sizes, the entire ceramics bulk appears to be depleted of charge carriers, and the effect of the increase in capacitance due to polycrystallinity disappears. This transition is illustrated by Fig. 5, which shows the potential profiles calculated for two model structures of the same size containing (a) 4×4 grains and (b) 8×8 grains. For the former case (Fig. 5a), the average grain size is D = 150 nm, which corresponds to the onset of the overlap of the neighboring potential barriers. For the latter number of grains (Fig. 5b), where the average grain size is 75 nm, the barriers overlap appreciably; therefore, in this case, the region depleted of free carriers is extended over the entire system.

The effect of the polycrystallinity of semiconductor ceramics manifests itself in the fact that the characteristic thickness, which determines the sample capacitance, is the width d of the depletion region at a bound-

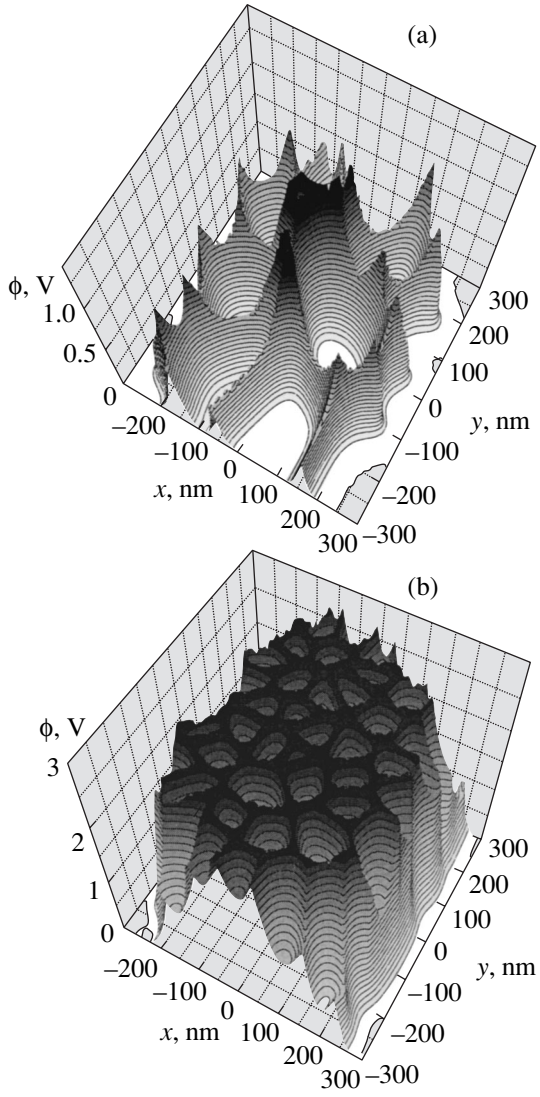

Fig. 5. The potential profile for structures of the same size that contain (a) 4×4 and (b) 8×8 grains.

ary. For samples with the thickness $L \gg d$, this effect produces a considerable increase in the capacitance in comparison with the capacitance of a capacitor filled with homogeneous insulator and possessing the thickness L and the same permittivity. We can see from expression (14) that, in this case, the smaller the number of grains in a polycrystalline sample, i.e., the larger the average grain size for a specified sample thickness, the greater its capacitance is. Therefore, to attain the greatest possible capacitance, the size of a polycrystalline sample must be comparable with the grain size. Thus, with regard to the requirement of miniaturization, it is desirable to optimize the design and fabrication technology of devices based on polycrystalline ceramic semiconductors so as to decrease the grain size and simultaneously decrease the size of the operation region. However, on attaining an average grain size of 150 nm, at which the depletion regions of neighboring grain boundaries begin to overlap, the effect of polycrystallinity disappears. In this case, a ceramic semiconductor of thickness L behaves like a capacitor uniformly filled with insulator, i.e., whose capacitance is $c = \varepsilon\varepsilon_0/L$. A further possible way of increasing the capacitance is related to a decrease in the thickness of the entire sample. In such a situation, a further decrease in grain size has no additional effect on the capacitance.

4. CONCLUSIONS

In this study, we suggested and implemented a simulation model that allowed us to calculate the electrical characteristics of polycrystalline ceramic semiconductors. The model is valid in a situation where the average grain size is comparable with the width of the depletion region near a grain boundary and the double Schottky barriers of neighboring boundaries overlap. Using p-$SrTiO_3$ as an example, we evaluated the effects of a variation in the current–voltage characteristic and a decrease in the specific capacitance as a result of a decrease in the average grain size. It is shown that, at $\xi = 0.4$ (ξ is the ratio of the width of the depletion region to the grain size), the shape of the I–V characteristic and the form of the dependence of the capacitance on the number of grain boundaries change abruptly, and the threshold voltage increases. The calculation of the dependence of the specific capacitance on the average grain size shows that the effect of the overlap of barriers of neighboring grain boundaries becomes significant at the average grain size $D \lesssim 150$ nm. As the grain size further decreases, the effect of polycrystallinity disappears and the sample behaves like a capacitor uniformly filled with insulator. Thus, we solved the problem of finding the minimum grain size at which ceramics still retains the important property of high capacitance.

ACKNOWLEDGMENTS

We thank S.A. Gurevich for supervising this study and S.P. Voskoboĭnikov and G.D. Fleishman for their helpful advice on the numerical methods used in the simulation.

REFERENCES

1. N. Setter and R. Waser, Acta Mater. **48**, 151 (2000).
2. N. Setter, J. Eur. Ceram. Soc. **21**, 1279 (2001).
3. R. Waser and R. Hagenbeck, Acta Mater. **48**, 797 (2000).
4. K. M. Doshchanov, Fiz. Tekh. Poluprovodn. (St. Petersburg) **32**, 690 (1998) [Semiconductors **32**, 619 (1998)].
5. G. E. Pike, Phys. Rev. B **30**, 795 (1984).
6. G. Blatter and F. Greuter, Phys. Rev. B **34**, 8555 (1986).
7. L. M. Levinson and H. R. Philipp, Am. Ceram. Soc. Bull. **65**, 639 (1986).

8. F. M. Hossain, J. Nishii, and S. Takagi, J. Appl. Phys. **94**, 7768 (2003).
9. D. E. Kotecki, D. Baniecki, H. Shen, *et al.*, IBM J. Res. Dev. **43** (3), 367 (1999).
10. R. Hagenbeck, L. Schneider-Stormann, M. Vollmann, and R. Waser, Mater. Sci. Eng. B **39**, 179 (1996).
11. T. Holbing and R. Waser, J. Appl. Phys. **91**, 3037 (2002).
12. J. Fleig, S. Rodewald, and J. Maier, J. Appl. Phys. **87**, 2372 (2000).
13. M. Bartkowiak and G. D. Mahan, Phys. Rev. B **51**, 10825 (1995).
14. T. Nagaya and Y. Ishibashi, Jpn. J. Appl. Phys. **36**, 6136 (1997).
15. M. Volmann and R. Waser, J. Electroceram. **1**, 51 (1997).
16. T. Shimizu, N. Gotoh, N. Shinozaki, and H. Okushi, Appl. Surf. Sci. **117–118**, 400 (1997).
17. M. Kuwabara, H. Matsuda, and Y. Ohba, J. Mater. Sci. **34**, 2635 (1999).
18. N. N. Medvedev, *The Voronoi–Delone Method in Studies of Noncrystalline Systems' Structure* (Novosibirsk, 2000) [in Russian].
19. V. L. Bonch-Bruevich and S. G. Kalashnikov, *Physics of Semiconductors*, 2nd ed. (Nauka, Moscow, 1990) [in Russian].
20. T. A. Davis, *UMFPACK Version 4.1 User Guide*, http://www.cise.ufl.edu/research/sparse/umfpack/(2003).

Translated by N. Korovin

Semiconductors, Vol. 39, No. 5, 2005, pp. 585–590. Translated from Fizika i Tekhnika Poluprovodnikov, Vol. 39, No. 5, 2005, pp. 616–622.

AMORPHOUS, VITREOUS, AND POROUS SEMICONDUCTORS

Features of the Vibrational Spectra of Diamond-like and Polymer-like *a*-C:H Films

E. A. Konshina^ and A. I. Vangonen

Vavilov State Optical Institute, All-Russia Research Center, Birzhevaya liniya 12, St. Petersburg, 199034 Russia

^e-mail: eakonshina@mail.ru; konshina@soi.spb.ru

Submitted February 16, 2004; accepted for publication October 15, 2004

Abstract—Comparative analysis of the IR spectra of multiple frustrated total internal reflection (MFTIR) in the range 4000–1000 cm^{-1} is performed for diamond-like and polymer-like *a*-C:H films with the refractive indices $n \geq 2.0$ and $n \leq 1.7$, respectively. The films are obtained by chemical-vapor deposition from octane, cyclohexane, toluene, and acetylene under various conditions using a dc glow discharge plasma. Characteristic features are found in the vibrational spectra of *a*-C:H films with different refractive indices. A peak at 1250 cm^{-1}, which is independent of the initial hydrocarbon, is observed in the spectra of the diamond-like films. Additional peaks at 3400 and 1700 cm^{-1}, due to O–H and C=H vibrations, are present in the spectra of the polymer-like films. It is shown that the integrated intensity of the band of CH vibrations peaked at ~2900 cm^{-1} decreases exponentially by an order of magnitude with an increase in *n* from 1.55 to 2.4. © *2005 Pleiades Publishing, Inc.*

1. INTRODUCTION

The refractive index *n* of films based on amorphous hydrogenated carbon (*a*-C:H) and prepared by chemical-vapor deposition (CVD) in a dc glow discharge plasma [1] can be changed from 1.5 to 2.4 at a wavelength of 0.63 μm [2]. Simultaneously with this increase in the refractive index, a decrease in the photonic band gap from 2.3 to 0.8 eV [3], a decrease in the resistivity from ~10^{13} to ~10^{7} Ω cm, and an increase in the film absorption in the visible spectral range [4] have been observed.

a-C:H films with a refractive index exceeding 2.0 can be arbitrarily assigned to diamond-like films. Due to their combination of chemical and mechanical durability, radiation resistance, and transparency in the IR region, diamond-like films can be used as protective coatings for infrared (IR) optics, in particular, for copper mirrors [5]. *a*-C:H films that are transparent in the visible spectral range, with $n < 1.7$ and high resistivity (~10^{13} Ω cm), can arbitrarily be referred to as polymer-like. In an earlier study, we used polymer-like films as orienting layers for liquid crystals (LCs) [6]. Black *a*-C:H films, which absorb light in the visible range and have $n \approx 2.2$, can be used as light-blocking layers in reflective light modulators based on LCs [7]. *a*-C:H films with $n \approx 2$ are ideal antireflection coatings for germanium with $n = 4$ [8–12]. These films differ from well-known multilayer antireflection coatings in their high chemical durability and mechanical strength. We have also used *a*-C:H films to increase the transparency of Ge output windows in LC modulators operating in the mid-IR region [13].

The spectral dependences of absorption in the frequency range 25000–4000 cm^{-1} and their correlation with the other properties exhibited by *a*-C:H films were investigated in [14]. The purpose of this study is to analyze the IR spectra of the multiple frustrated total internal reflection (MFTIR) of *a*-C:H films in the range from 4000 to 1000 cm^{-1}. Specific features of the IR absorption spectra of the diamond- and polymer-like films and the correlation of their refractive index with the film absorption are discussed, as well as the effect of the type of initial hydrocarbon used for deposition in a glow discharge plasma on the IR spectra.

2. EXPERIMENTAL TECHNIQUE AND RESULTS

2.1. Preparation of a-C:H Films in a dc Glow Discharge Plasma

The *a*-C:H films were obtained by CVD in a dc glow discharge plasma using a special multielectrode system that had a region of magnetron plasma localized near the anode [1]. This system made it possible to widely vary the pressure in the vacuum chamber, specifically, from 0.3 to 0.01 Pa. The films were deposited at substrate temperatures ranging from 20 to 50°C from vapors discharged by liquid and gaseous hydrocarbons: toluene, cyclohexane, octane, acetylene, and a mixture of acetylene and argon. The substrate was heated via the bombardment of its surface with ions at relatively high energies.

2.2. Measurement of the IR MFTIR Spectra of a-C:H Films

Infrared spectroscopy is widely used to study the optical absorption and structural features of *a*-C:H films [8–12, 15–17]. However, this method is not sufficiently sensitive for systems composed of *a*-C:H films

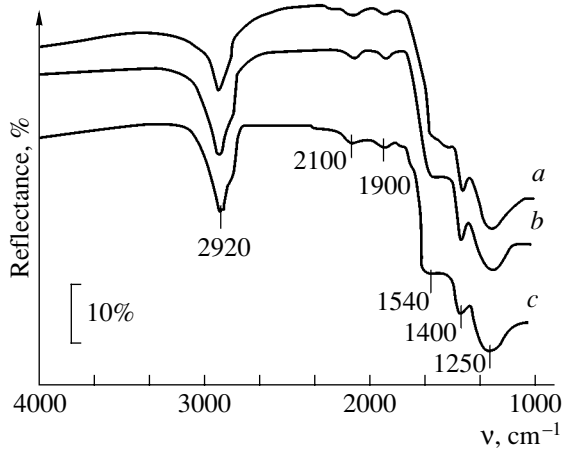

Fig. 1. Infrared MFTIR spectra of the *a*-C:H films with the refractive index $n = 2.3–2.4$ prepared from vapors of (*a*) toluene, (*b*) octane, and (*c*) cyclohexane at a pressure of 0.01–0.03 Pa and a discharge power of 10–13 W.

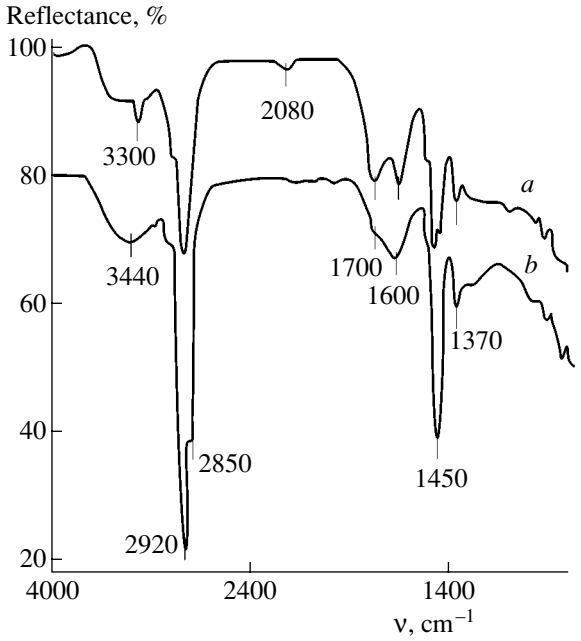

Fig. 2. Infrared MFTIR spectra of the *a*-C:H films with the refractive indices $n = 1.64$ and 1.55 prepared from vapors of (*a*) toluene and (*b*) octane, respectively, at a pressure of 0.3 Pa and a discharge power of 2 W.

and semiconductors with high refractive indices (Si and Ge) due to the significant interference effect. The use of the MFTIR method excludes the influence of the interference effect and makes it possible to record the vibrational spectra of thin *a*-C:H films [18–20]. The IR MFTIR spectra were measured on a PE spectrophotometer with an MFTIR attachment in the frequency range $\nu = 4000–1000$ cm^{-1}. A single-crystal germanium prism, which provided 12 reflections of IR radiation from a plane surface at an angle of 45°, served as the MFTIR element. Figure 1 shows the IR MFTIR spectra of *a*-C:H films with the refractive index $n = 2.3–2.4$. These films were obtained from (*a*) toluene, (*b*) octane, and (*c*) cyclohexane vapors at pressures of 0.01–0.03 Pa and discharge powers of 10–13 W. The refractive index was determined by multiangle ellipsometry at a wavelength of 0.63 μm [2]. Figure 2 shows the IR MFTIR spectra of *a*-C:H films with the refractive indices $n = 1.64$ and 1.55, which were prepared at a vacuum-chamber pressure of ~0.3 Pa and a discharge power of 2 W from (*a*) toluene and (*b*) octane vapors, respectively.

Table 1 contains the frequencies of the absorption bands in the IR MFTIR spectra of the diamond- and polymer-like *a*-C:H films, their identification [15, 18, 20], and the band intensities.

2.3. Calculation of the Absorption Coefficient of a-C:H Films

In MFTIR spectroscopy, the reflection can be described by the expression

$$R^N = (1 - \alpha d_e)^N, \quad (1)$$

where R is the reflection coefficient for one face of the MFTIR element, N is the number of reflections, α is the natural absorption coefficient, and d_e is the effective thickness [21]. In the case under consideration, $N = 12$.

If $\alpha d_e \ll 1$, the reflection loss increases by a factor of N:

$$R^N \approx 1 - N\alpha d_e. \quad (2)$$

Hence, the absorption coefficient can be calculated as

$$\alpha = 1 - R^N/Nd_e. \quad (3)$$

The penetration depth d_p of IR radiation at the angle of incidence $\theta = 45°$ is calculated by the formula

$$d_p = \lambda_1/2\pi(\sin^2\theta - n_{21}^2)^{1/2}, \quad (4)$$

where the wavelength $\lambda_1 = \lambda/n_1$, $n_{21} = n_2/n_1$, $n_1 = 4$ is the refractive index of Ge, and n_2 is the refractive index of the *a*-C:H film.

As was shown in [22], the refractive index n_2 of *a*-C:H films has a low dispersion in the IR region. Therefore, when calculating the absorption coefficient from formula (3), we used the values of n_2 obtained by ellipsometry for $\lambda = 0.63$ μm. The values of the refractive index n_2 and the thickness d for a number of *a*-C:H films, along with the chemical formulas of the initial hydrocarbons used for the film deposition and the calculated value of d_p for two frequencies: $\nu = 2920$ and 1250 cm^{-1}, are listed in Table 2. In the range 3300–2700 cm^{-1}, $d > d_p$; therefore, the effective thickness $d \approx d_p$. In the range 1800–1000 cm^{-1}, $d_e \ll d_p$; hence, we can assume that the electromagnetic field remains constant within the film thickness and $d_e \approx d$. In order to

calculate the absorption coefficient in the range 3300–2700 cm^{-1}, we used the values of d_p calculated from formula (4) for the corresponding frequency. The values of d obtained by ellipsometry were used to calculate the absorption coefficient in the range 1800–1000 cm^{-1}. The results of a computer-aided decomposition of these bands into individual vibrations—the frequency maxima ν, the widths at half-maximum $(\Delta\nu)_{1/2}$, and the integrated intensities I of the bands fitted by Gaussian curves—are listed in Table 3.

3. RESULTS AND DISCUSSION

3.1. Comparison of the Vibrational Spectra of Diamond- and Polymer-like a-C:H Films

In Figs. 1 and 2, two common absorption regions can be distinguished for the MFTIR spectra of the diamond- and polymer-like films: bands in the ranges 3300–2700 and 1800–1000 cm^{-1}. The former band is due to the stretching vibrations of C–H groups. In the latter band, peaks resulting from the stretching vibrations of carbonyl groups, single (C–C) and double (C=C) bonds, and bending vibrations of C–H groups can be distinguished. In addition, weak peaks at 2100 and 1900 cm^{-1} (Fig. 1) and 2080 cm^{-1} (Fig. 2) due to the stretching vibrations of the C≡C bonds were observed in the spectra.

It should be noted that the MFTIR spectra of the diamond-like *a*-C:H films (Fig. 1) prepared from different hydrocarbons (octane, toluene, and cyclohexane) do not demonstrate any significant differences. They are similar to the spectra of the *a*-C:H films with $n \geq 2.0$ prepared from acetylene [22]. Hence, we can conclude that, independent of the chemical nature of the initial hydrocarbon, the diamond-like *a*-C:H films produce typical IR MFTIR spectra. It can be seen from Table 1 that these spectra differ from the spectra of the polymer-like *a*-C:H films by the weak intensity of their stretching-vibration band in relation to the CH groups, the absence of the absorption band peak at 1700 cm^{-1} for the carbonyl C–O groups, and the presence of a band in the vicinity of 1250 cm^{-1} due to the vibrations of the C–C bonds at the branching points of the film structure.

At the same time, the IR MFTIR spectra of the polymer-like *a*-C:H films prepared from toluene and octane (Fig. 2) are similar to previously measured spectra of polymer-like films prepared from benzene, toluene [18], and acetylene [18, 19]. All the spectra of the polymer-like films show the presence of absorption bands due to the stretching vibrations of carbonyl and hydroxyl (~3400 cm^{-1}) groups. According to our investigations, the intensity of these bands may increase during the storage of the *a*-C:H films in air at room temperature [20]. This discovery indicates that the nature of these films is related to the chemisorption of water and oxygen from the atmosphere on the film surface after the extraction of the samples from the vacuum chamber. The adsorption is caused by the presence of micropores in the structure of the polymer-like films. In [2], an ellipsometric investigation of the *a*-C:H films showed that the porosity of films with a low refractive index can be as high as 7%.

The properties of *a*-C:H films depend on the discharge power on the substrate. As can be seen from Figs. 1 and 2, an increase in the power by a factor of 5 (from 2 to 10 W) leads to significant changes in the IR MFTIR spectra of the *a*-C:H films. Deposition of the *a*-C:H films from a hydrocarbon plasma occurs due to the interaction of positive ions with neutral molecules and their fragments, which are formed as a result of the destruction, on a substrate. The higher the discharge

Table 1. The frequencies, intensities, and nature of the vibrations in the IR spectra of *a*-C : H films with high and low refractive indices in the range 4000–1000 cm^{-1}

Frequency, cm^{-1}	Nature of vibration	Intensity	
		$n \geq 2$	$n \leq 1.7$
~3400	ν(–OH)		medium
3300	ν(≡CH)		low
3100	ν(=CH) aromatic sp^2	low	low
3050	ν^{as}(=CH) aromatic sp^2	low	low
3000	ν(=CH) olefine sp^2	low	low
2920	ν^{as}(–CH) sp^3	high	high
2850	ν^{s}(–CH_2) sp^3	medium	medium
1900–2100	ν(C≡C)	very low	very low
~1700	ν(C=O)		high
1600	ν(C–C) aromatic		medium
1540	ν^{as}(C=C) polyene	medium	
1450	δ^{as}(–CH_3)		medium
1440	δ(–CH)	medium	
1370–1375	δ^{s}(–CH_3)		medium
1250	ν(C–C) complex branching	medium	

Note: ν^{s} and ν^{as} are the symmetric and asymmetric stretching vibrations and δ^{s} and δ^{as} are the symmetric and asymmetric bending vibrations, respectively, in aromatic, olefine, and polyene compounds.

Table 2. Refractive indices and film thicknesses

Formula of the initial hydrocarbon	n_2	d, μm	d_p, μm	
			ν = 2920 cm^{-1}	ν = 1250 cm^{-1}
C_8H_{18}	1.55	0.259	0.234	0.549
C_8H_{18}	2.4	0.468	0.376	0.883
$C_6H_5CH_3$	1.64	0.262	0.238	0.559
$C_6H_5CH_3$	2.32	0.556	0.342	0.796
C_2H_2	2.05	0.72	0.278	0.648

Table 3. Decomposition of the spectral bands

Formula of the initial hydrocarbon	$C_6H_5CH_3$				C_8H_{18}			
n_2	2.31		1.65		2.4		1.55	
ν, cm^{-1}	$(\Delta\nu)_{1/2}$, cm^{-1}	*I*, arb. units	$(\Delta\nu)_{1/2}$, cm^{-1}	*I*, arb. units	$(\Delta\nu)_{1/2}$, cm^{-1}	*I*, arb. units	$(\Delta\nu)_{1/2}$, cm^{-1}	*I*, arb. units
3300	76	2655	–	–	76	1082		
3100	88	7283	88	11077	90	6820		
3000	80	43126	78	43096	80	11112		
2963	–	–	–	–	–	–	69	46097
2920	89	35939	87	74985	87	45156	89	243590
2850	78	11777	76	31527	79	14826	77	127912
1600	154	43250			196	68933		
1429	130	31387			77	26303		
1250–1273	167	52976			212	81515		

power, the higher the energy of the positive ions and the greater their effect on deposition. The interaction of ions with the surface of a growing film may lead to a breaking of chemical bonds, diffusion and desorption of individual atoms weakly bound to the film surface, and matching of the film structure as a result of the formation of four-coordinated carbon atoms. During the deposition of the polymer-like films, the fraction and the energy of the positive ions involved in the deposition process are generally much lower than in the case of the diamond-like films. This circumstance manifests itself in the structural features and macroscopic properties of the deposited films.

3.2. The Absorption Band Produced by the Stretching Vibrations of CH Groups

The broad absorption band produced by the stretching vibrations of CH groups is typical of all *a*-C:H films prepared by the CVD of hydrocarbons in a glow discharge plasma [9, 11, 17, 18, 23–25]. The intensity of this band in the IR spectra can change as a result of the value of the negative potential and the type of initial hydrocarbon [9, 10], the discharge power [16], the pressure in the chamber [11, 17], and the gas temperature and subsequent annealing of the *a*-C:H films [11, 24]. Analysis of this band yields qualitative and quantitative information on the hybridization states of the carbon atoms in the deposited films that is in agreement with the results obtained by other methods: nuclear magnetic resonance, mass spectroscopy, and electron energy-loss spectroscopy [16, 26–28].

The results of a computer-aided decomposition of this band (Table 3) show that the vibrations of the –CH and $–CH_2$ groups in the sp^2 hybridization state near 2920 and 2850 cm^{-1} are characteristic of the IR spectra of the diamond- and polymer-like films investigated here. The intensity of the bands resulting from the vibrations of the =CH groups in the sp^2 state was, for all the spectra obtained, lower than the intensity of the bands caused by the vibrations of the –CH and $–CH_2$ groups in the sp^2 hybridization state. The reason for these results is that the symmetric vibrations of the atoms in the sp^2 state weakly manifest themselves in IR spectra [29]. The bands arising as a result of the vibrations of the –CH groups in the sp^2 state were absent in the spectrum of the polymer-like film prepared from octane with n = 1.55, whereas the spectra of the diamond-like films obtained from the same hydrocarbon under other deposition conditions contained bands peaked near 3100 and 3000 cm^{-1}, which are characteristic of the vibrations of the =CH groups in the sp^2 state (Table 3). The spectra of the polymer- and diamond-like films (n = 1.65 and 2.31, respectively) deposited from the aromatic hydrocarbon toluene also contain these bands. Thus, we can conclude that the chemical nature of the initial hydrocarbon may affect the structure of the polymer-like *a*-C:H films to a larger extent than the structure of the diamond-like films.

The intensity of the absorption band in the range 3400–2600 cm^{-1} in the spectra of the polymer-like *a*-C:H films (Fig. 2) is much higher than the spectra of the diamond-like films (Fig. 1). This circumstance indicates that the content of bound hydrogen in the polymer-like films exceeds that in the diamond-like films. Figure 3 shows the correlation between the refractive index of the *a*-C:H films and the integrated intensity (in arbitrary units) of the band peaked at 2900 cm^{-1}. With a change in the refractive index from 1.55 to 2.4, the integrated intensity of the band attributed to the stretching vibrations of the CH groups exponentially decreases by an order of magnitude. Hence, a decrease in the content of bound hydrogen is accompanied by an increase in

the refractive index of the *a*-C:H films, which indirectly proves that the film structure becomes denser.

3.3. Interpretation of the Medium-Range Order Structure of the a-C:H Films Using the IR MFTIR Spectra

The information obtained on the short-range order structure from the analysis of the absorption band of the CH vibrations is insufficient for interpreting the macroscopic properties of *a*-C:H films, which are determined by either the medium-range order or the nanostructure. Study of the specific features of the band in the range 1800–1000 cm^{-1} in the IR spectra of the *a*-C:H films yields information on the medium-range order found in their structure. For example, the peaks near 1540 and 1600 cm^{-1} resulting from the vibrations of the C=C bonds in polyene chains and polycyclic aromatic rings are indicative of the existence of medium-range order elements in the film structure. In an earlier study, we obtained clear evidence, using resonance Raman spectroscopy, indicating the aggregation of polyene chains and polycyclic aromatic rings into π-conjugated clusters in the structure of *a*-C:H films prepared from acetylene [30].

In addition, polyene chains of the type –C≡C– are present in the structure of the *a*-C:H films, which is indicated by very weak bands in the IR spectrum near 1900 and 2100 cm^{-1}. These bands are characteristic of the spectra of all the films under study, irrespective of the refractive index.

The intensity of the band near 1250 cm^{-1}, produced by the stretching vibrations of C–C bonds, indicates that the structure of the *a*-C:H films contains four-coordinated carbon atoms. Since their presence is characteristic of the spectra of the diamond-like *a*-C:H films, we can suggest that these carbon atoms are four-functional branching points, which combine individual π-conjugated clusters composed of three- and two-coordinated atoms, that result in the structure being more compact and thus ensure its mechanical strength. In a previous study, we found that simultaneously with the decrease in the intensity of the band at 1250 cm^{-1}, an increase in the intensity of the band at 1700 cm^{-1} occurred in the IR MFTIR spectra of *a*-C:H films prepared from acetylene [19]. This correlation confirms the effect of the four-functional branching points on the packing density of the structure. A low refractive index (1.5) and high resistivity (up to 10^{13} Ω cm), which are characteristic of the polymer-like films, are related to the presence of both voids and CH groups between π-conjugated clusters in the sp^3 state. These voids and CH groups hinder the clusters' approach to each other, which results in a more loosely packed structure than in the diamond-like *a*-C:H films.

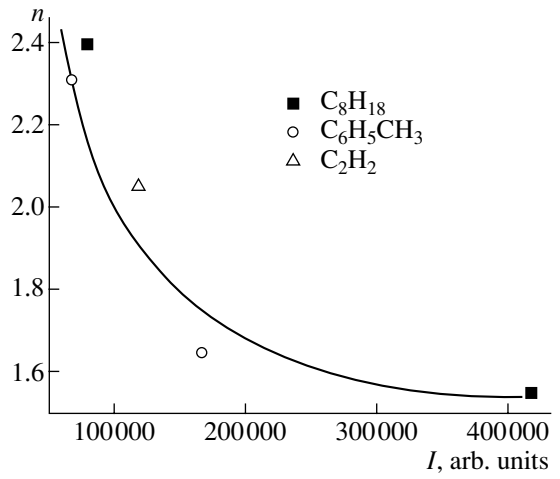

Fig. 3. Correlation between the refractive index of the *a*-C:H films and the integrated intensity of the band in the range 3400–2600 cm^{-1}.

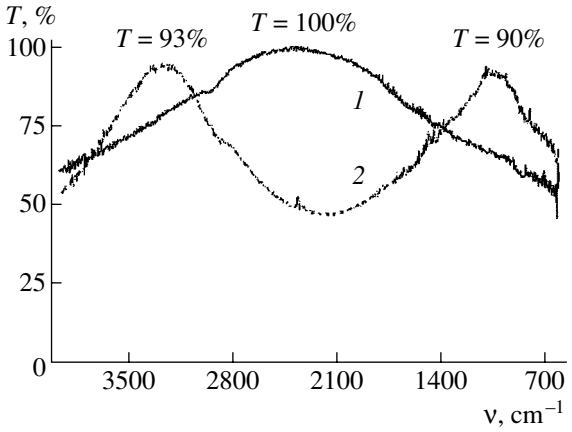

Fig. 4. Transmission spectra (*T*) of germanium coated with quarter-wave *a*-C:H layers for wavelengths of (*1*) 4 and (*2*) 10 μm.

3.4. The Use of a-C:H Films to Increase the Transmission of Germanium

When *a*-C:H films are used as antireflection coatings in the IR region, the absorption bands characteristic of their vibrational spectra must be taken into account. The spectra in Fig. 4 illustrate the effect of the absorption in *a*-C:H films with $n \approx 2$ on the transmission of germanium. Single-layer coatings based on *a*-C:H films with the optical thickness λ/4 equal to 0.5 and 1.25 μm for λ = 4 and 10 μm, respectively, were deposited from acetylene by the above-described method onto both sides of a Ge substrate. Due to the absence of absorption in *a*-C:H in the range 3.5–5 μm, an increase of up to 100% in the transmission of Ge was obtained in this spectral region (Fig. 4). For wavelengths above 5 μm, the effect of the absorption of IR radiation in the *a*-C:H films becomes more pronounced.

Therefore, as can be seen in Fig. 4, the transmission of a Ge sample that has both sides coated with *a*-C:H films does not exceed 90% at a wavelength of 10 μm due to the absorption loss in the *a*-C:H coatings.

4. CONCLUSIONS

The IR MFTIR spectra of diamond-like ($n \geq 2.0$) and polymer-like ($n \leq 1.7$) *a*-C:H films deposited from octane, cyclohexane, toluene, and acetylene in a dc glow discharge plasma were analyzed. A characteristic feature of the IR MFTIR spectra of the films with $n \geq 2.0$ is the presence of a band at ~1250 cm^{-1} due to the stretching vibrations of the C–C bonds in four-functional branching points of the structure. This band weakly manifests itself or is almost absent in the spectra of the *a*-C:H films with refractive indices below 1.7. The spectra of these films show strong absorption bands due to the stretching (~2920 cm^{-1}) and bending (~1450 cm^{-1}) vibrations of CH groups, as well as of carbonyl (~1700 cm^{-1}) and hydroxyl (~3400 cm^{-1}) groups. The latter are due to the chemisorption of water and oxygen from the environment, which is facilitated by the presence of micropores in the structure resulting from weak branching.

The correlation between the refractive index of the *a*-C:H films and the integrated intensity of the absorption band peaked at about 2900 cm^{-1} is ascertained. It is shown that, with an increase in n in the range from 1.55 to 2.4, the integrated intensity of this band decreases exponentially by an order of magnitude. It can concluded that polymer-like *a*-C:H films differ from diamond-like ones in that they possess a higher content of bound hydrogen.

It is shown that the chemical nature of the initial hydrocarbon used for the film deposition in a plasma may manifest itself in the IR spectra of the *a*-C:H films with $n \leq 1.7$. This reason for this circumstance is that fragments of the initial molecules formed during the hydrocarbon decomposition in a glow discharge plasma can serve as structural elements of the polymer-like films. This behavior is not typical of the diamond-like films, which are deposited under conditions in which there is a strong interaction between ions with relatively high energies and the substrate, which facilitates the destruction, branching, and matching of the condensate.

Thus, we can conclude that the IR MFTIR spectra of *a*-C:H films yield information about the specific features of the film structure and its packing density, which makes it possible to identify *a*-C:H films as being either of a diamond- or polymer-like nature. The results obtained can be used to design monolayer and multilayer optical coatings with different refractive indices for optical devices based on *a*-C:H films operating in the IR spectral region.

REFERENCES

1. E. A. Konshina, Zh. Tekh. Fiz. **72** (6), 35 (2002) [Tech. Phys. **47**, 690 (2002)].
2. V. A. Tolmachev and E. A. Konshina, Diamond Relat. Mater. **5**, 1397 (1996).
3. E. A. Konshina, Fiz. Tverd. Tela (St. Petersburg) **37**, 1120 (1995) [Phys. Solid State **37**, 610 (1995)].
4. E. A. Konshina, Zh. Tekh. Fiz. **70** (3), 87 (2000) [Tech. Phys. **45**, 374 (2000)].
5. E. A. Konshina, Zh. Tekh. Fiz. **68** (9), 59 (1998) [Tech. Phys. **43**, 1062 (1998)].
6. E. A. Konshina, Kristallografiya **40**, 1074 (1995) [Crystallogr. Rep. **40**, 999 (1995)].
7. E. A. Konshina and A. P. Onokhov, Zh. Tekh. Fiz. **69** (3), 80 (1999) [Tech. Phys. **44**, 340 (1999)].
8. J. Zelez, RCA Rev. **43**, 665 (1982).
9. A. Bubenser, B. Dischler, G. Brandt, and P. Koidl, J. Appl. Phys. **54**, 4590 (1983).
10. K. Enke, Appl. Opt. **24**, 508 (1985).
11. S. F. Pellicori, C. M. Peterson, and T. P. Henson, J. Vac. Sci. Technol. A **4**, 2350 (1986).
12. L. Klibanov, N. I. Croitoru, A. Seidman, *et al.*, Opt. Eng. **39**, 989 (2000).
13. M. V. Gryaznova, I. I. Danilov, S. G. Ivanov, *et al.*, in *Proceedings of V International Conference on Applied Optics* (St. Petersburg, 2002), Vol. 1, p. 163.
14. E. A. Konshina, Fiz. Tekh. Poluprovodn. (St. Petersburg) **33**, 469 (1999) [Semiconductors **33**, 451 (1999)].
15. B. Dischler, A. Bubenzer, and P. Koidl, Solid State Commun. **48**, 105 (1983).
16. Fangoing Zhang, Guanghua Chen, Yafei Zhang, and Gong Yu, Phys. Status Solidi A **109**, K39 (1988).
17. E. A. Konshina, Opt.–Mekh. Prom-st, No. 2, 15 (1987).
18. R. Memming, Thin Solid Films **143**, 279 (1986).
19. E. A. Konshina, A. V. Baranov, and V. B. Yakovlev, Zh. Prikl. Spektrosk. **48**, 957 (1988).
20. A. I. Vangonen, E. A. Konshina, and V. A. Tolmachev, Zh. Fiz. Khim. **71**, 1102 (1997).
21. N. J. Harrick, *Internal Reflection Spectroscopy* (Wiley, New York, 1967; Mir, Moscow, 1970).
22. V. B. Yakovlev, L. K. Vasil'eva, V. V. Veremeĭ, and E. A. Konshina, Zh. Prikl. Spektrosk. **53**, 863 (1990).
23. M. P. Nadler, T. M. Donovan, and A. K. Green, Thin Solid Films **116**, 241 (1984).
24. I. Watanabe, S. Hasegawa, and Y. Kurato, Jpn. J. Appl. Phys. **21**, 856 (1982).
25. D. R. McKenzie, R. C. McPhedran, N. Savvides, and D. J. H. Cockayne, Thin Solid Films **108**, 247 (1983).
26. K. Walters, P. Honeybone, D. W. Huxley, *et al.*, Phys. Rev. B **50**, 831 (1994).
27. M. Jäger, J. Gottwald, H. W. Spiess, and R. J. Newport, Phys. Rev. B **50**, 846 (1994).
28. J. R. Honeybone, R. J. Newport, J. K. Walters, *et al.*, Phys. Rev. B **50**, 839 (1994).
29. J. Robertson, Prog. Solid State Chem. **21**, 199 (1991).
30. A. V. Baranov and E. A. Konshina, Opt. Spektrosk. **65**, 856 (1988) [Opt. Spectrosc. **65**, 506 (1988)].

Translated by Yu. Sin'kov

Semiconductors, Vol. 39, No. 5, 2005, pp. 591–593. Translated from Fizika i Tekhnika Poluprovodnikov, Vol. 39, No. 5, 2005, pp. 623–626.

PHYSICS OF SEMICONDUCTOR DEVICES

Electric Fatigue in MOS Structures due to Lowering of the Potential Barrier during the Field Ionization of Insulator Atoms

I. S. Savinov

Moscow Power Engineering Institute, ul. Krasnokazarmennaya 17, Moscow, 111250 Russia
e-mail: voronkoven@mpei.ru

Submitted January 26, 2004; accepted for publication March 1, 2004

Abstract—The influence of the ionized charge in an insulator on the excess current in an MOS structure is calculated. A comparison of numerical simulation results and experimental data shows that this effect can be responsible for a time-dependent breakdown of an ultrathin gate oxide in MOS transistors. © *2005 Pleiades Publishing, Inc.*

1. INTRODUCTION

The reliability and long-term stability of parameters in a range of operational conditions is a major requirement for modern integrated circuits based on metal–oxide–semiconductor (MOS) transistors. The transition of modern technology to the submicrometer level and the use of ultrathin (thinner than 8 nm) gate oxides gives rise to new effects that are potential sources of device instability and degradation.

The objective of this study is a consideration of one of the possible causes of a temporal decrease in the dielectric strength of an ultrathin gate oxide after exposure of an MOS structure to voltages close to the permissible maximum [1–3]. In Russian publications, temporal degradation of device and material parameters arising under electrical overloads is referred to as electric stress or electric fatigue. In this paper, we adhere to the former term and attribute the effects of reversible parameter degradation to electric fatigue. The term "electric stress" includes both reversible and irreversible degradation effects arising under high energy loads.

2. MODEL

The motivation for this study came from the experimental fact that, after the exposure of an MOS structure to high electric fields, the positive charge in an insulator, as well as leakage current in the case of thin insulators, increases [1].

The simulation model used in this study is based on the assumption that ionized defects (positive ions) located near an interface give rise to a local lowering of the potential barrier between an electrode and insulator, which locally increases the electron injection into the insulator. The latter process results in an additional leakage current and a decrease in the breakdown voltage. The objective of this study, within the suggested model, was to analyze the conditions that need to be imposed on ion concentration and distribution to ensure the generation of excess currents identical, in relation to their order of magnitude, to those experimentally observed.

Let us consider the Si–SiO_2–*poly*-Si structure, which is used most frequently in transistors (*poly*-Si is polycrystalline silicon). An energy-level diagram of this structure is shown in Fig. 1. It is assumed that, under an applied external electric field, the charge transport through the interface is controlled by the Fowler–Nordheim mechanism. We restrict the analysis to a situation in which the applied voltage is relatively low and the potential barrier is constant. In the numerical calculations, we assume that the potential-barrier height at the Si–SiO_2 interface is $eU_b = 2.7$ eV.

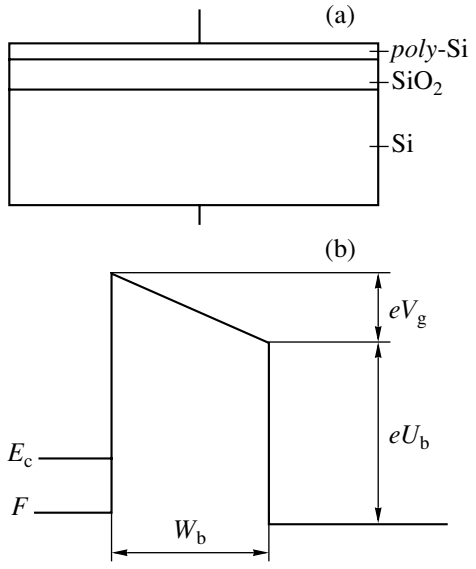

Fig. 1. Schematic representation of (a) the structure under consideration and (b) a portion of the corresponding energy-level diagram.

1063-7826/05/3905-0591$26.00 © 2005 Pleiades Publishing, Inc.

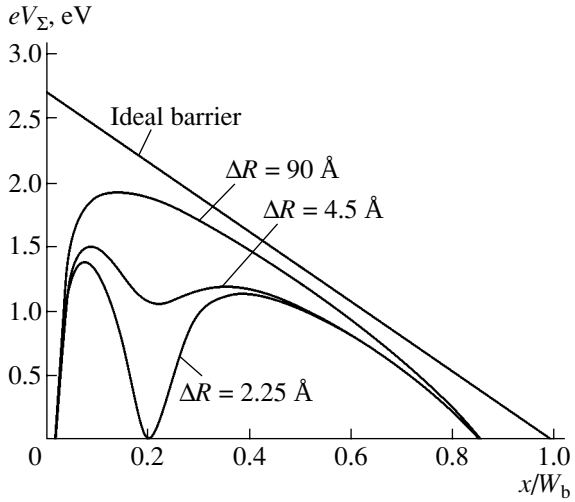

Fig. 2. Diagrams of the potential barrier in the insulator layer at various distances $\Delta r = \Delta R/W_b$ of the electron trajectory from the ion position.

Let the ion potential distribution at distances larger than the atomic size be described by the Coulomb law. We also assume that the Si layer is an electrostatic "mirror." In this case, the potential distribution can be determined using the mirror image method. In the case of cylindrical coordinates, the potential at the point (x, r) is given by (see [4])

$$V(x, r, a_1) = \frac{e}{4\pi\varepsilon\varepsilon_0 W_b}\Bigg([\Delta r^2 + (x - a_1)^2]^{-\frac{1}{2}} - [\Delta r^2 + (x + a_1)^2]^{-\frac{1}{2}} + \sum_{n=1}^{\infty}\Big\{[\Delta r^2 + (2n + x - a_1)^2]^{-\frac{1}{2}} - [\Delta r^2 + (2n - x - a_1)^2]^{-\frac{1}{2}} + [\Delta r^2 + (2n - x + a_1)^2]^{-\frac{1}{2}} - [\Delta r^2 + (2n + x + a_1)^2]^{-\frac{1}{2}}\Big\}\Bigg), \quad (1)$$

where $\Delta r = |r - r_1|$, a_1 and r_1 are the ion coordinates, the x axis is normal to the insulator layer, all the coordinates are given in units of the insulator film thickness W_b, and $\varepsilon\varepsilon_0$ is the Si permittivity.

The mirror image of an electron passing through the barrier gives rise to deformation of the electrostatic potential profile. Let us take into account these distortions as follows:

$$V_e(x, r) = \frac{e}{4\pi\varepsilon\varepsilon_0 W_b} \times \left[-\frac{1}{\sqrt{2x^2}} + \sum_{n=1}^{\infty}(2n - |2n + 2x|)\right]. \quad (2)$$

Using the notation of Fig. 1, the resulting potential distribution is written as

$$V_\Sigma(x, r, a_1) = V(x, r, a_1) + V_e(x, r) + U_b - xV_g, \quad (3)$$

where V_g is the external potential difference applied to the insulator. The potential at the left-hand insulator boundary ($x = 0$ in Fig. 2) is assumed to be zero.

The tunneling current increment caused by a single ion in the insulator is given by

$$\Delta I = \frac{4\pi e m^2 kT}{h^3}\exp\left(-\frac{E_c - F}{kT}\right) \times \int_0^{v_{x\max}} \exp\left(-\frac{m v_x^2}{2kT}\right) v_x dv_x, \quad (4)$$

where

$$v_{x\max} = \sqrt{\frac{2eU_b}{m}},$$

E_c and F are the conduction band top and the Fermi level of polycrystalline silicon, and v_x is the electron-velocity component.

The difference between the probability that an electron overcomes the potential barrier in the presence of an ion and the probability that the electron overcomes the initial potential barrier per unit area is given by

$$\Delta P = \int_0^1\int_{R_a/W_b}^{\infty} 2\pi r\left\{\exp\left[-\frac{2\sqrt{2m}}{\hbar}\int_0^1 (V_\Sigma - E)^{1/2}dx\right] - \exp\left[-\frac{2\sqrt{2m}}{\hbar}\int_0^1 (V_\Sigma - V - E)^{1/2}dx\right]\right\}dr\,da, \quad (5)$$

where R_a is the shortest distance at which an electron can leave the ionized atom center and avoid trapping. The probability that the electron overcomes the potential barrier is averaged with respect to all the possible ion positions in the insulator layer.

3. RESULTS AND DISCUSSION

It follows from the experimental data presented in [1] that a long-term electric stress initially causes an insignificant increase in the leakage current. However, at $\sim 2 \times 10^3$ s, the current becomes noisy and drastically increases; then, in the next $\sim 2 \times 10^3$ s, a thermal breakdown develops.

In [1], the phenomenon of an increase in the leakage current under low fields was referred to as a quasi-breakdown, and the dependence of this leakage current on the gate voltage was determined. It was also reported that the quasi-breakdown phenomenon develops in individual localized regions of a sample and can be observed only in thin (<8 nm) silicon oxide films. Thus, it follows from the results of [1] that the total area where the quasi-breakdown phenomenon develops amounts to ~0.001 of the total sample area.

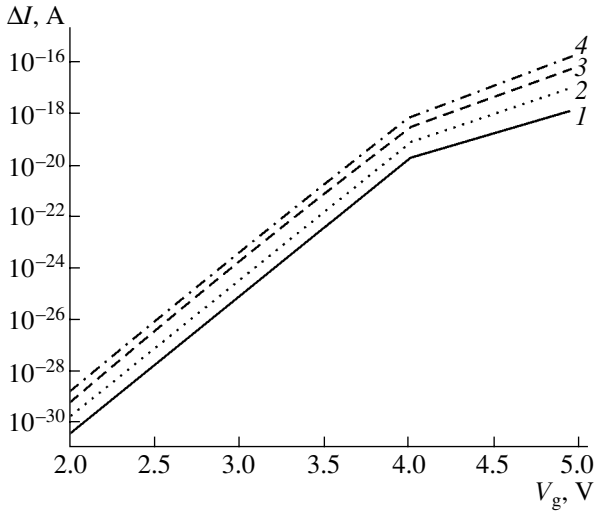

Fig. 3. Calculated dependences of the leakage current ΔI on the gate voltage V_g when the insulator contains from one to four longitudinally arranged positive ions (curves *1–4*, respectively).

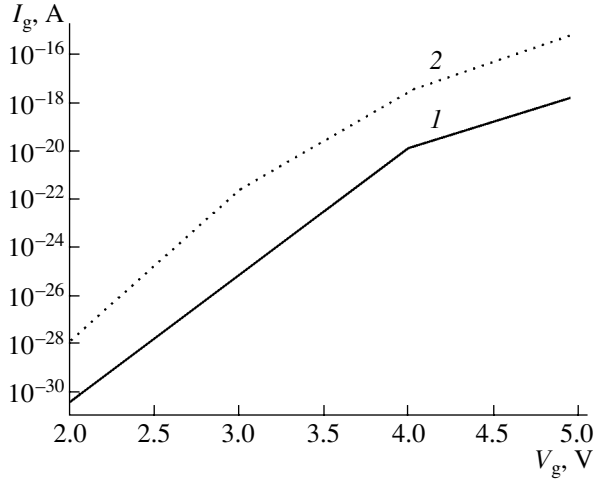

Fig. 4. The calculated dependence of the leakage current I_g on the gate voltage V_g at the potential-barrier heights U_b = (*1*) 2.7 and (*2*) 2.6 eV.

If we set R_a = 1 Å, which is approximately equal to the atomic radius, Eq. (4) can be used to find that the tunneling current increment caused by a single ion is 10^{-27} A.

By calculating the additional tunneling current caused by a single positive ion at various gate voltages, we obtain the dependence of the leakage current on the gate voltage. In this case, as before, we set the insulator thickness equal to 4.5 nm, which corresponds to the sample thickness used in [1]. The obtained dependence agrees well with the similar dependence reported in [1]. It is clear that several ions arranged one after another in the longitudinal direction lower the potential barrier more efficiently and lead to a larger increase in the tunneling current. In order to take these observations into account, we need to introduce several new terms into relation (3):

$$V_\Sigma(x, r, a_1) = V_1(x, r, a_1) + \ldots + V_4(x, r, a_1) + V_e(x, r) + U_b - xV_b. \quad (6)$$

Figure 3 shows the calculated dependences of the excess current ΔI on the gate voltage V_g for various numbers of ions located near the interface. In general, these dependences are similar to the experimental curves obtained in [1].

It follows from Fig. 3 that such spatial combinations of ions cause a significant increase in the leakage current; however, it should be remembered that these results represent only approximate estimates and are not quantitatively accurate. It can be shown that even a small inaccuracy in the potential-barrier height introduces an error of several orders of magnitude. Figure 4 shows the dependence of the tunneling current on the gate voltage for two barrier heights.

Let us estimate the highest possible leakage current under the assumption that, as in [1], the sample area is 10^{-4} cm^2. The total current is given by

$$I = \Delta J \gamma N_a, \quad (7)$$

where N_a is the number of atoms located at the sample surface, γ is the fraction of positively ionized surface atoms, and ΔJ is the additional tunneling current per conductivity channel.

Based on the results of [1], the order of magnitude of γ can be assumed to be equal to 0.001, which means that one in a thousand surface atoms is ionized. The value of γ can be estimated from the results of [5], where it was shown that the average distance between ionized defects in SiO_2 becomes equal to 3 nm at a voltage close to the breakdown value. As a result, relation (7) yields the current ~10^{-8} A, which is in good agreement with the data presented in [1].

4. CONCLUSION

Our analysis shows that the formation of positive ions in an insulator with a further decrease in the potential-barrier height can be one of possible mechanisms that initiate the leakage of current in the gate oxide of MOS transistors exposed to gate voltages close to the permissible maximum.

REFERENCES

1. O. Briere, A. Halimaoui, and G. Chibaudo, Solid-State Electron. **41**, 347 (1997).
2. T. Brozek, E. C. Szyper, and C. R. Viswanathan, Solid-State Electron. **41**, 995 (1997).
3. A. S. Dudnikov and N. A. Zaĭtsev, Élektron. Tekh., Ser. 3: Mikroélektron., No. 1, 33 (2001).
4. F. W. Shmidlin, J. Appl. Phys. **37**, 2823 (1966).

Translated by A. Kazantsev

Semiconductors, Vol. 39, No. 5, 2005, pp. 594–599. Translated from Fizika i Tekhnika Poluprovodnikov, Vol. 39, No. 5, 2005, pp. 627–632.

PHYSICS OF SEMICONDUCTOR DEVICES

Tunnel-Recombination Currents and Electroluminescence Efficiency in InGaN/GaN LEDs

N. I. Bochkareva*^, E. A. Zhirnov, A. A. Efremov***, Yu. T. Rebane*, R. I. Gorbunov*, and Yu. G. Shreter***

**Ioffe Physicotechnical Institute, Russian Academy of Sciences, St. Petersburg, 194021 Russia*
^e-mail: n.bochkareva@mail.ioffe.ru
***Department of Physics, Bath University, Bath, BA2 7AY, UK*
****St. Petersburg State Polytechnical University, St. Petersburg, 194251 Russia*
Submitted June 29, 2004; accepted for publication July 12, 2004

Abstract—The mechanism of injection loss in *p*-GaN/InGaN/*n*-GaN quantum-well LEDs is analyzed by studying the temperature and current dependences of external quantum efficiency in the temperature range 77–300 K and by measuring transient currents. The data obtained are interpreted in terms of a tunnel-recombination model of excess current, which involves electron tunneling through the potential barrier in *n*-GaN and the over-barrier thermal activation of holes in *p*-GaN. At a low forward bias, the dominant process is electron capture on the InGaN/*p*-GaN interface states. At a higher bias, the excess current sharply increases due to an increase in the density of holes on the InGaN/*p*-GaN interface and their recombination with the trapped electrons. The injection of carriers into the quantum well is limited by the tunnel-recombination current, which results in a decrease in efficiency at high current densities and low temperatures. The pinning of the Fermi level is attributed to the decoration of heterointerfaces, grain boundaries, and dislocations by impurity complexes. © *2005 Pleiades Publishing, Inc.*

1. INTRODUCTION

One of the principal problems in the design of GaN-based LEDs is the need to raise the quantum efficiency of electroluminescence (EL) at high injection levels. Usually, the maximum external quantum efficiency in LEDs is observed at small currents, 0.1–1 mA, and it decreases significantly as the working current is raised to 20 mA [1]. An anomalous decrease in the EL efficiency has also been observed at temperatures below 150 K for injection currents $J > 100$ μA [2–4], whereas the photoluminescence efficiency has been observed to increase upon cooling [3].

Different models considering the quantum efficiency limitation and nonradiative recombination loss in GaN LEDs can be found in a number of publications. The decrease in efficiency at higher injection levels is attributed, e.g., to the depression of electron capture into the InGaN quantum well (QW) and the injection of electrons into *p*-GaN "over" the QW [1]. As alternative causes of the decrease in GaN LED efficiency during cooling, electron capture into the tails of the density of states [2] or into localized states [3] have been discussed, as well as an increase of the drift velocity of electrons injected into *p*-GaN, which results from a freeze-out of holes and increase in the electric field in *p*-GaN [4].

In this study, the mechanism of injection loss in GaN LEDs is analyzed based on the measured temperature dependences of the current and EL efficiency in the temperature range 77–300 K and on transient current measurements. It is shown that the anomalous decrease in efficiency during cooling occurs only at high currents ($J \gtrsim 1$ mA). In contrast, in the low-current range $J \lesssim 50$ μA, the efficiency increases as the temperature decreases.

The data are interpreted in terms of the tunnel-recombination model of current flow across a heterostructure. The model involves the tunneling of electrons through the potential barrier in *n*-GaN, their capture by localized states at the InGaN/*p*-GaN heterointerface, and their recombination with holes thermally activated over the barrier into *p*-GaN. At a low bias, the electron capture process dominates. When, at higher biases, the density of holes on the heterointerface increases, the tunnel-recombination current increases sharply. The Fermi level pinning on the heterointerface with a high density of states suppresses the injection of carriers into the QW, which is the major cause of the decrease in efficiency at high currents and low temperatures. The most probable sources of the deep states responsible for the Fermi level pinning on the InGaN/GaN heterointerface are impurity complexes on the heterointerface and dislocations.

2. EXPERIMENT

We studied MOCVD-grown blue *p*-GaN/InGaN/*n*-GaN LEDs with the QW in the *p–i–n* structure possessing an active layer $In_xGa_{1-x}N$ of 30 Å in thickness. The details of the LED structure are presented in [5].

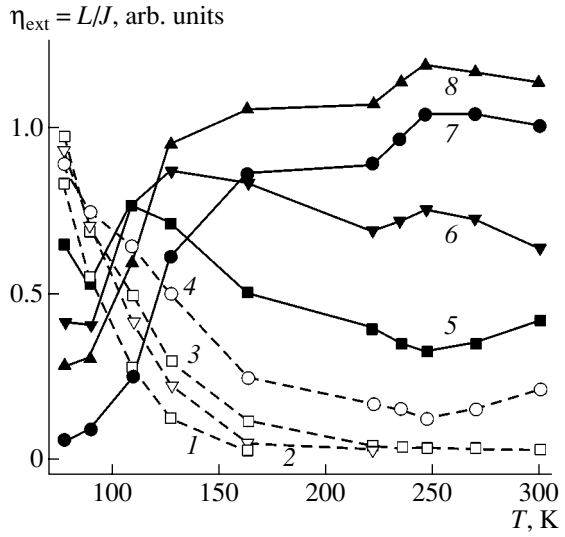

Fig. 1. Temperature dependences of the EL efficiency of a blue LED at dc forward currents J of (*1*) 4×10^{-4}, (*2*) 10^{-3}, (*3*) 2×10^{-3}, (*4*) 10^{-2}, (*5*) 3×10^{-2}, (*6*) 0.1, (*7*) 0.4, and (*8*) 20 mA.

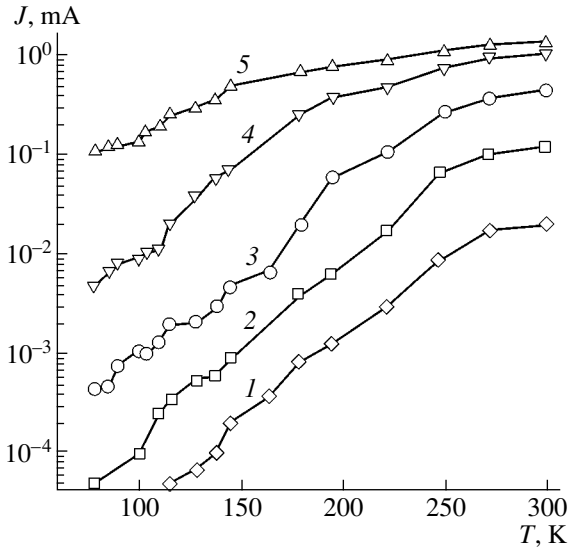

Fig. 2. Temperature dependences of the forward current in an LED under dc biases U of (*1*) 2.7, (*2*) 2.9, (*3*) 3.12, (*4*) 3.5, and (*5*) 4.05 V.

The current–voltage (*I–V*) and luminescence–voltage (*L–V*) characteristics were studied in the temperature range $T = 77$–300 K. The temperature dependences of the structure capacitance $C(T)$, current $J(T)$, and EL efficiency $\eta_{ext}(T)$ were also studied.

The transient currents in the LEDs were studied using square pulses of forward bias with an amplitude of 0.3–3.2 V, width of 1–100 μs, and repetition frequency of 1 kHz. The initial current was limited by series resistors: a ballast resistor $R_1 = 1$ kΩ and load resistor $R_2 = 100$ Ω. The voltage across the load resistor, which is proportional to the transient current, was analyzed using a BCI-280 boxcar integrator. The kinetics of the transient current in a time interval of 10 ns to 30 μs after the leading edge of a pulse, as well as the dependences of this current on the pulsed bias at a constant delay, was measured. In order to improve the signal-to-noise ratio, we employed voltage pulse gating across the load resistor at a gate width of 10–400 ns and accumulation of n pulses ($n = 8$–128).

Temperature dependences of the EL efficiency. Figure 1 shows temperature dependences of the efficiency of the LED emission $\eta_{ext} = L/J$ measured at different currents. At a current of 0.4–10 μA, the efficiency increases as the temperature decreases. The strongest increase in the efficiency is observed for cooling occurring below ~150 K. At a higher current, the opposite behavior is observed: the efficiency decreases as the sample is cooled, with the strongest decrease in the efficiency being observed at $T < 150$ K; in addition, some decrease is also evident at ~250 K. In the range of current $J \sim 100$ μA, $\eta_{ext}(T)$ exhibits peaks at about 150 and 250 K.

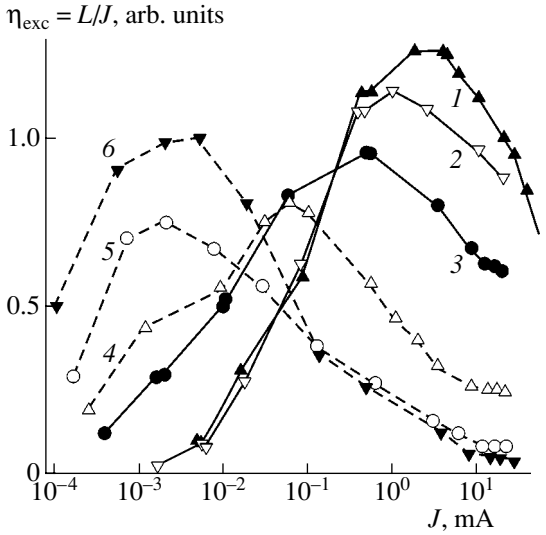

Fig. 3. The EL efficiency of a blue LED vs. the forward current at temperatures T of (*1*) 300, (*2*) 222, (*3*) 128, (*4*) 110, (*5*) 90, and (*6*) 78 K.

Temperature dependences of current. Figure 2 shows the temperature dependences of the forward current in the LED. $\log J(T)$ exhibits steps at the same temperatures as those observed in the $\eta_{ext}(T)$ dependences, i.e., at about 150 and 250 K. As the bias increases, the portion demonstrating weak temperature dependence of the current is extended to lower temperatures.

Dependences of the EL efficiency on current. Figure 3 shows the current dependences of the EL efficiency. At room temperature, the curve $\eta_{ext}(J)$ exhibits a peak at about 2–4 mA. As the temperature decreases,

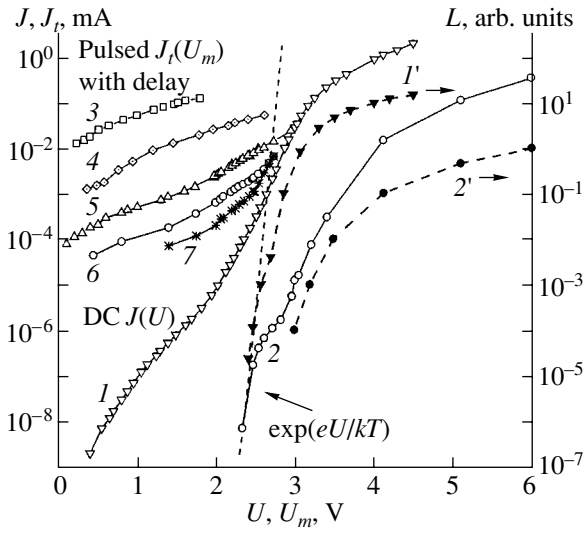

Fig. 4. *I–V* characteristics of a blue LED under (*1*, *2*) dc and (*3–7*) pulsed bias. Curves *1*' and *2*' illustrate the emission intensity *L* vs. dc bias. Temperatures: (*1*, *3–7*, *1*') 300 K; (*2*, *2*') 78 K. Delay time: (*3*) 0.05, (*4*) 0.25, (*5*) 1, (*6*) 2, and (*7*) 4 μs.

the $\eta_{ext}(J)$ peak is shifted to lower current values. Thus, a tendency is observed in which the efficiency at low temperatures and high current approaches that seen at room temperature and low current.

Current–voltage and luminescence–voltage characteristics at dc bias. Figure 4 shows the *I–V* and *L–V* characteristics. The forward *I–V* characteristics of the LEDs under study at a dc bias (curves *1*, *2*) are similar to those observed earlier for GaN-based LEDs [6–8]. The authors of [6–8] concluded that tunneling is the dominant current transport mechanism. The room-temperature forward *I–V* characteristic of the LED in the logarithmic scale, $\log J(U)$ (curve *1*), exhibits a characteristic shoulder in the range of bias ~(1–2.3) V and current 1 nA–1 μA, which is usually attributed to the effect of the large amount of dislocations and defects in GaN-based structures [8].

At 300 K, a sharp increase in the EL is observed at the "switch-on" voltage $U_{EL} \approx 2.4$ V (curve *1*'). The EL intensity in the initial portion of the $\log L(U)$ curve for currents $J \lesssim 1$ mA, i.e., below the current corresponding to the $\eta_{ext}(J)$ peak, can be approximated by the exponent $L \propto \exp(U/U_t)$, where U_t = 26–52 mV. At the bias $U < U_{EL}$, the current flowing through the LED does not contribute to the EL. At low voltages, this excess current (~2 μA at 2.4 V) depends linearly on the bias, while, at $U \gtrsim 2$ V, it can be approximated as $J \propto \exp(U/U_t)$, where $U_t > 140$ mV. In the range of currents ~(1–20) mA, the slope of the $\log J(U)$ and $\log L(U)$ curves gradually decreases; moreover, the slope of $\log L(U)$ becomes less steep than that of the $\log J(U)$ curves, which reflects the decrease in efficiency as the current increases. Therefore, the maximum quantum efficiency corresponds to the largest slope of the $\log J(U)$ curve. This trend is also observed at low temperatures (curves *2*, *2*').

Pulsed and high-frequency *I–V* characteristics. Figure 4 (curves *3–7*) shows the dependences of the transient current measured at a 50-ns to 4-μs delay after the leading edge of a square pulse of bias (with a width of 1–100 μs) on the pulse amplitude $J_t(U_m)$. The transient current at $U_m \lesssim 2.3$ V exceeds the dc current by several orders of magnitude, but it is close to the dc current found at working currents. The kinetics of the transient current is characterized by a stretched exponent [5]. The inflections in the $\log J(U)$ and $\log J_t(U_m)$ curves appear in the same range of bias. It is also noteworthy that similar behavior is observed in the dependences of the active component of the low-signal current of the LED at 1-MHz and 100-kHz frequencies as functions of the dc bias, which were obtained in the measurements of the conductance–voltage characteristics.

3. DISCUSSION

3.1. Tunneling and Injection in an LED

The excess tunnel-recombination current at low biases, $U < U_{EL}$. Tunneling is generally agreed to be the principal mechanism of current transport in diode structures with InGaN QWs [6–8].

For the case of a uniform energy distribution of states in the band gap and recombination in the neutral region, the tunnel-recombination current in a forward-biased *p–n* junction may be written as

$$J_{t-r} = J_0 \exp[(U - U_{bi})/U_t]. \quad (1)$$

Here, U_{bi} is the built-in voltage of the *p–n* junction and $U_t \propto [N_a N_d/(N_a + N_d)]^{1/2}$, where N_a and N_d are the concentrations of acceptors in the *p*-type region and donors in the *n*-type region, respectively [9].

The tunnel current observed at a low bias in the diodes under study sharply increases near the switch-on voltage $U_{EL} \approx 2.4$ V. The excess current at $U < U_{EL}$, which does not generate light, may be related to carriers that bypass the QW in the energy space by tunneling under the QW to the InGaN/*p*-GaN heterointerface with a high density of states (Fig. 5). The well-defined steps on the temperature dependence of the current at a dc forward bias (Fig. 2) imply a nonuniform distribution of the interface states in the band gap and indicate the presence of two groups of states. It should be noted that tunneling along the grain boundaries might also be a source of the excess current.

In the LEDs under study, *n*-GaN is more heavily doped than *p*-GaN ($N_d = 10^{18}$ cm^{-3} and $N_a = 2 \times 10^{17}$ cm^{-3}). Taking into account the large effective hole mass in GaN, $m_h = 2.2m_0$ (m_0 is the free electron mass) [10], we can suggest a tunnel-recombination model of the current transport across the heterostructure, which

involves electron tunneling through the potential barrier in *n*-GaN and the thermal activation of holes over the potential barrier in *p*-GaN (J_n and J_p, respectively, Fig. 5).

The pulsed and static *I–V* characteristics at $U < U_{EL}$. The proposed model is confirmed by the behavior of the *I–V* characteristics observed for dc and transient currents. As can be seen in Fig. 4, these curves demonstrate a similar nonlinearity, which is typical when the trapping of carriers plays a decisive role in current transport.

The decay of the current after the barrier reduction by the pulsed voltage at the leading edge of the pulse at $t = 0$ can be related to the electron capture by free localized states on the internal interfaces, i.e., the InGaN/GaN heterointerface, grain boundaries, and dislocations in *n*-GaN. At low forward biases, the increase in the negative charge on the interface states Q_i compensates the initial decrease in the barrier for the electrons.

The tunnel-recombination current at $U > U_{EL}$. Pinning of the Fermi level on the InGaN/GaN heterointerface and suppression of the injection into the InGaN QW. The rise in the forward bias results in a gradual saturation of the trap centers and increase in the injection current into the QW. A comparison of the $J(U)$ and $J_t(U_m)$ dependences leads to the conclusion that the interface traps are completely filled at the trap-filling-limit voltage $U_{TFL} \approx 3$ V. Indeed, as can be seen in Fig. 4, in the vicinity of this bias, the dc current gradually increases to the level of the pulsed current. In this range of bias, $U \approx U_{TFL}$, the maximum quantum efficiency of the EL is observed.

For radiative band-to-band recombination, the recombination current in the *p–i–n* structure equals $J \propto \exp(qU/kT)$ [11]. At room temperature, the luminescence–voltage dependence (Fig. 4, curve *1*') is close to a dependence of this kind only at low biases ($U \lesssim 2.7$ V). As the bias increases, the slope of both the $\log L(U)$ and $\log J(U)$ curves decreases. In this case, $\partial \log L/\partial U < \partial \log J/\partial U$, and the light intensity increases more slowly than the current.

At $U > U_{TFL}$, the EL efficiency decreases. This behavior can be attributed to the limitation of the carrier injection into the QW, related to the recombination of holes with the electrons captured on the localized states on the heterointerface. As the hole density on the heterointerface increases, the tunneling and recombination on the heterointerface again become the dominant processes; therefore, in the total current, the fraction of current injected into the QW decreases. Taking into account that

$$U_{bi} - U = U_n + U_p,$$

where U_n and U_p are the potential barrier height in the *n*- and *p*-type regions, respectively, and in accordance with the neutrality condition $Q_i = Q_n - Q_p$, where Q_i, $Q_n = (2q\varepsilon N_d N_n)^{1/2}$, and $Q_p = (2q\varepsilon N_a N_p)^{1/2}$ are the charges on the heterointerface states and ionized impurities in the depleted *n*- and *p*-type regions, respectively, the expressions for U_n and U_p at $N_d \gg N_a$ are easily obtained:

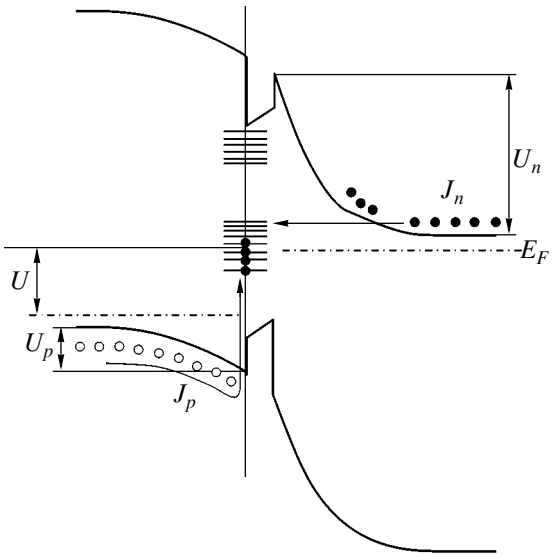

Fig. 5. The band structure of an LED. E_F indicates Fermi level; U_p and U_n, the potential barriers for holes in the *p*-type region and electrons in the *n*-type region; J_n, the tunnel current of electrons in the *n*-type region; J_p, the thermally activated current of holes in the *p*-type region; and U, the forward bias.

$$U_n \approx \frac{Q_i^2}{2q\varepsilon N_d}, \quad U_p \approx U_{bi} - \frac{Q_i^2}{2q\varepsilon N_d} - U.$$

When recombination on the heterointerface is dominant, the electron tunnel current J_n through the potential barrier in *n*-GaN equals the current J_p of the holes, which are thermally activated over the barrier in *p*-GaN. Taking into account relation (1), we obtain

$$J_{0t}\exp\left(-\frac{\alpha Q_i^2}{U_t}\right) = J_{0p}\exp\left[-\frac{q(U_{bi} - \alpha Q_i^2 - U)}{kT}\right], \quad (2)$$

where J_{0t} and J_{0p} are the saturation current densities for the barriers in the *n*- and *p*-type regions, respectively, and $\alpha = (2q\varepsilon N_d)^{-1}$. For $U_t \gg kT/q$, we obtain the height of the barrier for the electrons in the *n*-type region:

$$U_n \approx U_{bi} - \frac{kT}{q}\ln\frac{J_{0p}}{J_{0t}} - U. \quad (3)$$

As a result, at $U > U_{TFL}$ and $U_t \gg kT/q$, virtually all the excess bias falls on *n*-GaN. In this situation, the rise of the hole density on the interface becomes slower as the bias increases. It in necessary to note that, when there is a low density of states on the InGaN/GaN interface and the heterostructure current $J \propto \exp(qU/kT)$, the voltage should drop mainly across the *p*-type region, due to the lower doping level, until the hole density on the interface $p_i \propto \exp(qU/kT)$ becomes equal to the

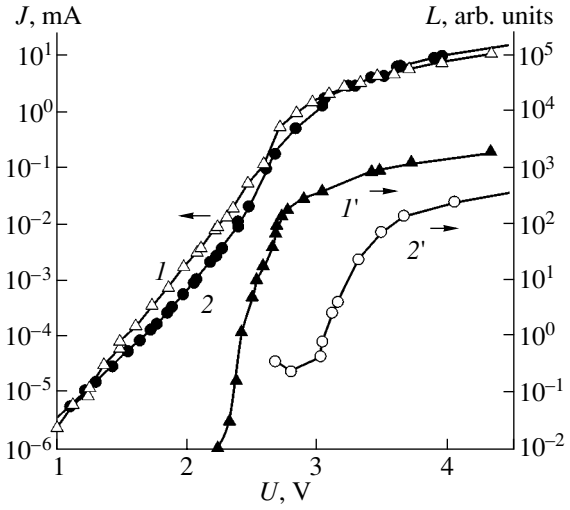

Fig. 6. (*1*, *2*) *I–V* and (*1*', *2*') *L–V* characteristics under a dc bias for (*1*, *1*') blue and (*2*, *2*') violet LEDs.

electron density on the interface n_i [11]. Then, a further increase in bias would be divided in equal parts between the *p*- and *n*-type regions, so that $J \propto p_i n_i \propto \exp(qU/kT)$ [11]. The increase in the tunnel-recombination current J_{t-r} is followed by a slower increase in the injection current, which generates light. Using (2) and (3), we obtain, for J_{t-r},

$$J_{t-r} = J_{0t}(J_{0p}/J_{0t})^{kT/U_t}\exp\left(\frac{U_{bi}-U}{U_t}\right). \qquad (4)$$

Due to the depression of the injection efficiency as the forward bias increases at $U > U_{TFL}$, the EL efficiency $\eta_{ext}(J)$ passes through a maximum at a relatively low current, ~(1–3) mA. It then significantly decreases at the working current ~20 mA.

The effect of the tunnel-recombination current on the EL intensity is confirmed by the following experimental data. In the blue diodes with large excess current ($J > 0.1$–0.2 mA at 2.6 V), the decrease in quantum efficiency begins at lower biases and is followed by the leveling-off of the EL intensity. This behavior is illustrated by Fig. 6, which shows the *I–V* and *L–V* characteristics of this diode.

The interconnection between the tunnel-recombination current and quantum efficiency at high voltages is especially distinct for violet diodes (which have an emission peak wavelength $\lambda_{max} \approx 400$ nm). Due to the larger band gap in $In_xGa_{1-x}N$, the voltage necessary for the generation of light in these diodes (under the domination of the tunneling mechanism of current transport $U_{EL} \approx h\nu - (\mu_n + \mu_p)$, where μ_n and μ_p are the Fermi energies E_F in *n*- and *p*-GaN, respectively) must exceed that in the blue LEDs ($\lambda_{max} = 465$ nm) by $\Delta h\nu/q \approx 0.44$ V (here, $\Delta h\nu$ is the difference between the photon energies). For the violet diodes, the $\log L(U)$ curves are shifted to higher voltages (see curve *2*', Fig. 6), but the *I–V* characteristics for both types of diodes are close (cf curves *1* and *2*). In these diodes, the excess current reaches 1–2 mA at $U = 3$–3.1 V (curve *2*), which results in a decrease in the light intensity even at currents <1 mA.

As the temperature decreases, the tunnel-recombination current at low biases decreases, as a result of the decrease in the hole density on the InGaN/*p*-GaN interface, whereas the efficiency increases, reaching its maximum at $U = U_{TFL}$. Since the traps are completely filled, at a further rise in the bias, virtually all the voltage rise drops across the *p*-type region, in accordance with the doping levels in *p*- and *n*-GaN, and the density of holes, both free and trapped, on the heterointerface sharply increases as the bias rises. However, the decrease in efficiency observed as the current rises actually begins at low currents, because, as follows from (3), the equality between the hole and electron currents is established after a small decrease in U_n; again, the entire voltage increase drops across the *n*-type region. As a result, the injection current is depressed as the bias increases in the $U > U_{TFL}$ range. As the temperature increases, the density of free and trapped holes on the InGaN/GaN heterointerface increases, and a stronger depression of the barrier for electrons U_n is necessary to balance the hole current with the current of the electrons in the heterointerface states. As a result, the decrease in efficiency at higher temperatures occurs at higher currents.

3.2. The Possible Sources of Injection Loss in LEDs

A possible source of the tunnel-recombination current on the heterointerface, which suppresses the injection, may be the segregation of the residual impurities. For example, the segregation of oxygen and hydrogen on extended defects in GaN was observed in [12, 13]. Oxygen acts as a donor in the GaN bulk, but it induces deep acceptor levels on the dislocations in GaN, where it forms complexes with the Ga vacancies [14]. As is well known, oxygen–hydrogen centers in the bulk and on the internal and external surfaces of solids can trap holes at low temperatures. This fact serves as the impetus for the stepwise temperature behavior of the surface band bending and work function in semiconductors. For example, general trends are observed in the temperature behavior of the surface band bending at about 200–250 and 150 K in Ge [15], Si [16], and GaAs [17], the positive built-in charge in the oxide in Si/SiO_2 FETs [18], and the work function of metals [19].

It is noteworthy that similar temperature behavior has been observed for capacitance in *p*-GaN Schottky diodes [20]. This behavior was attributed to the residual hydrogen after the activation annealing of the *p*-GaN layer. In an earlier study, we also observed similar temperature dependences of the capacitance in blue LEDs [8]. In addition, these general trends are observed in the temperature dependences of the LED current (Fig. 2). These facts allow us to attribute the temperature behavior of the current and quantum efficiency

$\eta_{ext}(T)$ to a change, at temperatures of about 150 and 250 K, in the charge state of the H- and O-containing complexes, which are responsible for the temperature shift of the Fermi level on the InGaN/GaN heterointerface.

4. CONCLUSION

It was found that the temperature behavior of the EL efficiency at low currents is opposite to that observed at high currents. An anomalous decrease in efficiency during cooling is observed for currents $J \gtrsim 1$ mA, whereas, at $J \lesssim 50$ μA, the efficiency increases at temperatures below 150 K. These results allow us to attribute the temperature and current dependences the of efficiency to a tunnel-recombination mechanism of the excess current, which involves electron tunneling through the potential barrier in *n*-GaN and the above-barrier thermal activation of holes in *p*-GaN. The study of transient currents shows that, at low forward biases, electron capture is the dominant process, whereas, at voltages above the trap-filling limit, an intense nonradiative recombination is dominant, which limits the increase in the hole density on the heterointerface as the bias increases. At room temperature, the rise in the recombination current is stronger than that of the injection current; therefore, the efficiency at small currents is low, but it increases during cooling. Since the density of free and trapped holes on the InGaN/GaN heterointerface decreases during cooling, a lower electron current is necessary to compensate the hole current; therefore, the tunnel-recombination current becomes the principal component of the total current, even at low currents in the LED, which reduces the quantum efficiency.

REFERENCES

1. T. Mukai, M. Yamada, and S. Nakamura, Jpn. J. Appl. Phys. **38**, 3976 (1999).
2. A. Hori, D. Yasunaga, A. Satake, and K. Fujiwara, Appl. Phys. Lett. **79**, 3723 (2001).
3. X. A. Cao, S. F. LeBoeuf, L. B. Rowland, *et al.*, Appl. Phys. Lett. **82**, 3614 (2003).
4. I. A. Pope, P. M. Smowton, P. Blood, *et al.*, Appl. Phys. Lett. **82**, 2755 (2003).
5. Y. T. Rebane, N. I. Bochkareva, V. E. Bougrov, *et al.*, Proc. SPIE **4996**, 113 (2003).
6. H. C. Casey, Jr., J. Muth, S. Krishnankutty, and J. M. Zavada, Appl. Phys. Lett. **68**, 2867 (1996).
7. P. Perlin, M. Osinski, P. G. Eliseev, *et al.*, Appl. Phys. Lett. **69**, 1680 (1996).
8. H. Morkoc, *Nitride Semiconductors and Devices* (Springer, Berlin, 1999).
9. J. A. DelAlamo and R. M. Swanson, IEEE Electron Device Lett. **7**, 629 (1986).
10. J. S. Im, A. Moritz, F. Steuber, *et al.*, Appl. Phys. Lett. **70**, 631 (1997).
11. G. E. Pikus, *Fundamentals of the Theory of Semiconductor Devices* (Nauka, Moscow, 1965) [in Russian].
12. K. S. A. Butcher, H. Timmers, Afifuddin, *et al.*, J. Appl. Phys. **92**, 3397 (2002).
13. I. Arslan and N. D. Browning, Phys. Rev. Lett. **91**, 165501 (2003).
14. J. Elsner, R. Jones, M. I. Heggie, *et al.*, Phys. Rev. B **58**, 12571 (1998).
15. A. V. Rzhanov, *Electronic Processes at Semiconductor Surfaces* (Nauka, Moscow, 1971) [in Russian].
16. S. I. Kirillova, M. D. Moin, V. E. Primachenko, *et al.*, Fiz. Tekh. Poluprovodn. (St. Petersburg) **26**, 1399 (1992) [Sov. Phys. Semicond. **26**, 784 (1992)].
17. Yu. V. Dubrovskiĭ and S. V. Morozov, Poverkhnost, No. 9, 143 (1987).
18. D. L. Griscom, Phys. Rev. B **40**, 4224 (1989).
19. A. Spitzer, A. Rotz, and H. Luth, Surf. Sci. **152–153**, 543 (1989).
20. J. W. Huang, T. F. Kuech, H. Lu, and I. Bhat, Appl. Phys. Lett. **68**, 2392 (1996).

Translated by D. Mashovets

Semiconductors, Vol. 39, No. 5, 2005, pp. 600–602. Translated from Fizika i Tekhnika Poluprovodnikov, Vol. 39, No. 5, 2005, pp. 633–635.

PHYSICS OF SEMICONDUCTOR DEVICES

Effect of Uniaxial Compression on the Photoconversion Parameters in a *p*-GaSe–*n*-InSe Optical Contact

S. I. Drapak^, M. O. Vorobets, and Z. D. Kovalyuk

Frantsevich Institute for Problems in Materials Science, Chernovtsy Branch, National Academy of Sciences of Ukraine, ul. Zhovteva 5, Chernovtsy, 58001 Ukraine

^e-mail: chimsp@unicom.cv.ua

Submitted August 3, 2004; accepted for publication September 9, 2004

Abstract—The effect of uniaxial pressure in the direction perpendicular to the localization plane of the interface for *n*-InSe–*p*-GaSe heterojunctions on a variation in the saturation photovoltage and short-circuit current is studied. It is shown that, in InSe/GaSe optical contacts subjected to a pressure $P = 35$–40 kPa, the open-circuit voltage increases almost twofold and the short-circuit current increases by more than a factor of 5 as compared to the values observed in the initial samples, which makes it possible to expect that the efficiency of photoconversion can be increased to 15–16% in the structures under consideration. © *2005 Pleiades Publishing, Inc.*

Photodiodes based on anisotropic *n*-InSe–*p*-GaSe heterojunctions (HJs), fabricated by bringing the surfaces of two semiconductors into direct optical contact [1], are analogues of silicon structures in their operation under exposure to intense radiation [2]. The photoconversion efficiency of these HJs is 0.7–3.2%, depending on the electrical parameters of the semiconductors in contact and on special features of the structures' design [3]. According to Drapak *et al.* [4], an InSe/GaSe heterocontact is equivalent to a semiconductor–insulator–semiconductor (SIS) structure. In spite of a widespread opinion that the surfaces of layered semiconductors cannot adsorb extraneous gases from the surrounding atmosphere [5], it is an oxygen layer that plays the role of the insulator in the SIS structures under consideration. This layer represents a nonequilibrium state of the system and exhibits a very long relaxation time. As has recently been shown [4], InSe and GaSe semiconductor wafers come into actual close contact in the course of long-term (10–14 years) storage as a result of the diffusive spread of oxygen. The area of this contact amounts to a mere ~10% of a HJ's geometric area. If the photoconversion efficiency of these structures is calculated taking into account the actual area (i.e., the area of the surfaces in close contact), this efficiency increases from 3.2 to 11–12% for an HJ based on InSe and GaSe with optimal electrical parameters. When the areas of close InSe/GaSe contact are obtained as a result of a partial displacement of a gaseous interlayer or the enveloping of clusters of adsorbed atoms under the effect of the weight of the semiconductors in contact, it seems expedient to study the effect of pressure on the photoconversion parameters of an InSe/GaSe contact.

In this paper, we report the results of studying for the first time the effect of uniaxial compression of an InSe–GaSe optical contact on the saturation photovoltage (the open-circuit voltage) V_{oc} and short-circuit current I_{sc}.

We studied structures whose series resistance R ranged from ~10^4 to ~10^5 Ω, depending on the charge-carrier concentration in the semiconductors in contact ($p_{GaSe} = 10^{14}$–10^{15} cm^{-3} and $n_{InSe} \approx 10^{15}$ cm^{-3} at $T = 300$ K). The HJs were subjected to a pressure directed perpendicularly to the interface plane (along the *c*-symmetry axis of the InSe and GaSe crystals).

In Fig. 1, we show dependences of the open-circuit voltage V_{oc}^P (curve *1*) and the short-circuit current I_{sc}^P (curve *2*) on the pressure P applied to the InSe–GaSe HJ under study. The initial values (in the absence of

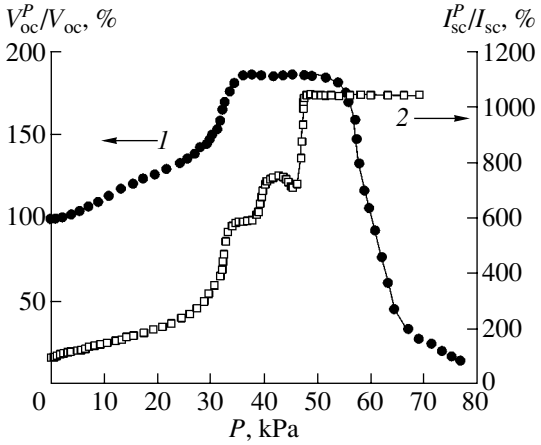

Fig. 1. Variations in the (*1*) open-circuit voltage V_{oc} and (*2*) short-circuit current I_{sc} in relation to the pressure P applied to the *n*-InSe–*p*-GaSe heterojunctions. Designations V_{oc}^P and I_{sc}^P correspond to the values of V_{oc} and I_{sc} for the structures exposed to pressure.

1063-7826/05/3905-0600$26.00

pressure) of the quantities V_{oc}^P/V_{oc} and I_{sc}^P/I_{sc} were taken to be equal to 100%. A study of the optical-absorption spectra for GaSe and InSe subjected to uniaxial compression at pressures as high as $P \approx 75$ kPa shows that the energy-band structure of these semiconductors is unaffected by pressure, which is in good agreement with the published data [6, 7]. For example, a decrease in the GaSe band gap E_g under the effect of pressure P becomes noticeable only at $P \approx 10^8$ Pa [6]. This circumstance makes it possible to relate variations in V_{oc}^P and I_{sc}^P for the *n*-InSe–*p*-GaSe HJ in the range of pressures under study to the changes that occur at the interface.

As can be seen from Fig. 1 (curve *1*), the value of V_{oc} increases almost twofold as P increases to ≈35 Pa and tends, as was predicted by Drapak *et al.* [4], to the value of the contact potential difference φ_0 calculated in the context of the Anderson model for ideal HJs. At the same time, measurements of the capacitance–voltage (*C–V*) characteristics for the structures exposed to pressure indicate that the contact potential difference φ_0^P still falls short of the value determined from the relation obtained for ideal HJs,

$$\varphi_0 = (\chi_p + E_{gp} - E_{Fp}) - (\chi_n + E_{Fn}), \qquad (1)$$

even if a possible variation in the position of the Fermi level E_F in InSe and GaSe is taken into account. This variation is indicated by an increase in the resistivity of these materials as the applied pressure increases to $P \approx$ 70 kPa (Fig. 2, curves *1*, *2*). In expression (1), χ_p and χ_n are the electron affinities for *p*- and *n*-type semiconductors, respectively; E_{gp} is the band gap of a *p*-type semiconductor; E_{Fp} is the energy spacing between the valence-band top and the Fermi level in a *p*-type semiconductor; and E_{Fn} is the energy spacing between the conduction-band bottom and the Fermi level in an *n*-type semiconductor. This circumstance, i.e., the discrepancy between the value of V_{oc}^P in the saturation region at $P > 35$ kPa and the value of φ_0^P,

$$eV_{oc}^P \le \varphi_0^P, \qquad (2)$$

indicates that it is impossible to completely eliminate the effect of the transitional layer formed of oxygen atoms adsorbed from the atmosphere on the value of V_{oc}^P, even in the presence of pressure. For the HJs that were not subjected to pressure, the open-circuit voltage far exceeds the contact potential difference, which is characteristic of structures that include an insulating layer at the interface [8]. Relation (2) indicates that the transitional-layer thickness decreases and eventually becomes negligible.

As the pressure applied to the HJs increases, not only does the resistivity of the semiconductors in contact increase (Fig. 2, curves *1*, *2*) but the contact potential difference φ_0^P determined from the *C–V* characteristics increases as well. An increase in φ_0^P brings about an increase in the width of the space-charge region. However, in spite of this circumstance, an appreciable increase in I_{sc}^P (by more than a factor of 5) is observed at $P > 35$ kPa. This observation indicates that the optical InSe–GaSe contact subjected to pressure can be considered as a close contact rather than an SIS structure. In the pressure range $P \approx$ 35–40 kPa, the quantities V_{oc}^P and I_{sc}^P attain a constant value, which may be a consequence of the fact that it is impossible to decrease the thickness of an insulating layer under the effect of applied pressure. A further increase in pressure leads to a steplike increase in I_{sc}^P while the value of V_{oc}^P remains constant, which can be related to an increase in the area of the HJs under study as a result of a more uniform distribution of the layer of oxygen atoms adsorbed from atmosphere at the interface. An increase in I_{sc}^P under pressure in the range $P \approx$ 40–50 kPa can be also caused by variations in the parameters of the semiconductors in contact under the effect of this pressure (these parameters include the lifetime of nonequilibrium charge carriers and the diffusion length). However, this assumption requires additional studies to be carried out. A drastic decrease in V_{oc}^P at $P >$ 55–60 kPa is apparently caused by the effect of the mismatch (~8%) between the crystal-lattice constants of the semiconductors in contact. This mismatch begins to manifest itself as the insulating-layer thickness decreases and becomes negligible, and it may be the cause of the

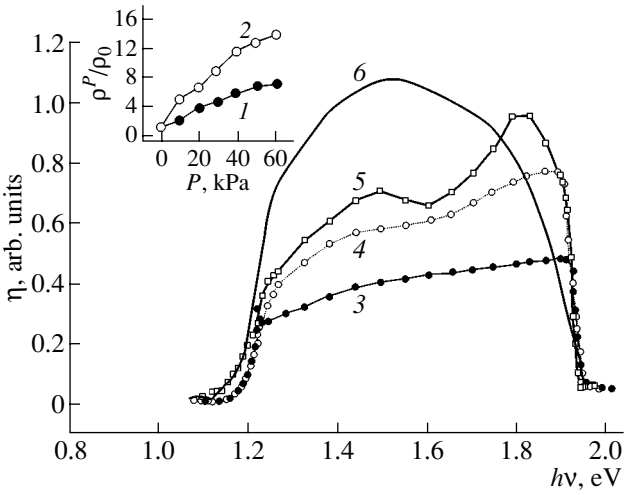

Fig. 2. Spectral dependences of the relative quantum efficiency η of the *n*-InSe–*p*-GaSe heterojunctions subjected to the pressure P = (*3*) 0, (*4*) 20, (*5*) 40, and (*6*) 60 kPa. T = 291 K. The effect of pressure on the resistivity of (*1*) InSe and (*2*) GaSe is illustrated in the inset.

appearance of photosensitivity for the HJ under study beyond the fundamental absorption edge of InSe (Fig. 2, curves *5*, *6*). As a consequence of an increase in the band-bending magnitude φ_0^P and an increase in the resistivity of the semiconductors in contact, the shape of the current–voltage (*I–V*) characteristics of the HJs subjected to pressure also changes: the forward *I–V* characteristics of the initial samples can be described by the expression $J \propto \exp(eV/nkT)$ (where the diode factor retains the value $n \approx 1$ in entire range of temperatures under consideration), whereas $n > 2$ at room temperature for the structures subjected to pressure.

In spite of the fact that the interpretation of the results obtained in the studies reported here is only tentative, these results indicate that it is possible to appreciably improve the photoconversion parameters of *n*-InSe–*p*-GaSe HJs. In conclusion, we should note that, if the filling factor of the *I–V* characteristic for heterojunctions subjected to uniaxial compression using a pressure of approximately 30–55 kPa is not decreased significantly, an increase in the photoconversion efficiency to 15–16% might be expected for these heterojunctions. The estimations were performed for structures with the following optimal parameters: the residual resistance ~10^3 Ω and the photoconversion efficiency ~3.2%. It is also worth noting that the area of *n*-InSe–*p*-GaSe HJs is restricted by the sizes of the quartz cells in which the indium and gallium monoselenides are grown and equals ~1 cm^2 for the structures under study. Encapsulation of the structures with the above sizes into cases under the pressure $P \approx 35$–50 kPa should not significantly affect the cost of photoconverters.

REFERENCES

1. V. L. Bakumenko and V. F. Chishko, Fiz. Tekh. Poluprovodn. (Leningrad) **11**, 2000 (1977) [Sov. Phys. Semicond. **11**, 1171 (1977)].
2. É. G. Ashirov, V. L. Bakumenko, A. K. Bonakov, *et al.*, in *Abstracts of All-Union Workshop on Radiation Effects in Semiconductors and Semiconductor Devices* (Azernesher, Baku, 1980), p. 91.
3. S. I. Drapak, V. N. Katerinchuk, Z. D. Kovalyuk, and V. A. Manasson, Fiz. Élektron., No. 41, 92 (1988).
4. S. I. Drapak, V. B. Orletskiĭ, and Z. D. Kovalyuk, Fiz. Tekh. Poluprovodn. (St. Petersburg) **38**, 566 (2004) [Semiconductors **38**, 546 (2004)].
5. R. H. Williams and A. J. McEvoy, J. Vac. Sci. Technol. **9**, 867 (1972).
6. *Landolt-Bornstein. Numerical Data and Functional Relationships in Science and Technology. New Ser. Group III: Crystal and Solid State Physics*, Ed. by O. Madelung (Springer, Berlin, 1983), Vol. 17.
7. C. Ulrich, D. Olguin, A. Cantarero, *et al.*, Phys. Status Solidi B **221**, 777 (2000).
8. S. I. Drapak, V. N. Katerinchyk, Z. D. Konalyuk, and V. A. Manasson, Phys. Status Solidi A **115**, K35 (1989).

Translated by A. Spitsyn

Semiconductors, Vol. 39, No. 5, 2005, pp. 603–607. Translated from Fizika i Tekhnika Poluprovodnikov, Vol. 39, No. 5, 2005, pp. 636–640.

PHYSICS OF SEMICONDUCTOR DEVICES

The Influence of Gain Saturation on the Output Power of Quantum-Well Semiconductor Lasers

G. G. Zegrya and I. Yu. Solov'ev^

Ioffe Physicotechnical Institute, Russian Academy of Sciences, St. Petersburg, 194021 Russia

^e-mail: igor@theory.ioffe.rssi.ru

Submitted October 7, 2004; accepted for publication October 12, 2004

Abstract—The light–power characteristic of a quantum-well semiconductor laser is theoretically studied taking into account the gain saturation effect. It is shown that, at high drive current densities, this light–current characteristic becomes nonlinear. The results obtained are in a good agreement with the experimental data.

1. INTRODUCTION

The use of semiconductor lasers is steadily increasing in various fields of science and technology, with the requirements being placed their characteristics becoming more and more stringent. One of these requirements is that their output power should be raised. It is well known that, as drive current increases, the output power of a semiconductor laser starts to grow sublinearly, and, occasionally, quenching of the lasing may be observed [1]. It is commonly believed that this output power "saturation" is due to carrier and lattice heating [1]. However, it has been reported that the saturation effect is observed even in the absence of lattice and carrier heating [2]. For example, in [3], the leveling-off of the light–current characteristics of quantum-well (QW) semiconductor lasers possessing various cavity lengths (with the laser temperature maintained at a constant level) was studied. The light–current characteristics of the lasers were simultaneously analyzed with the spectra of spontaneous emission. These spectra revealed that there was no lattice or carrier heating as the drive current was raised but that there was a leveling-off of the light–current characteristic. Therefore, they concluded that there must be other mechanisms responsible for the output power saturation.

Similarly to gas lasers, semiconductor lasers exhibit a gain saturation effect, which was first identified by O.N. Krokhin [4]. The gain saturation mechanism was analyzed in detail in [5]. To our knowledge, no analysis of this kind has been made for semiconductor heterostructure lasers.

At high excitation levels, the nonequilibrium carrier relaxation in heterostructures is more greatly enhanced than it is in homogeneous semiconductors. Carrier relaxation generally occurs via a Coulomb interaction that is, in particular, associated with the spatial localization of carriers. In bulk semiconductors, the main relaxation mechanism is commonly electron–phonon interaction. As is shown below, the relaxation processes strongly affect the gain and, consequently, the gain saturation mechanism in semiconductor lasers.

In this paper, the mechanism of gain saturation in QW semiconductor lasers is examined and its influence on the maximum output power is analyzed.

2. CALCULATION OF THE GAIN

In order to calculate the gain, we can use the density-matrix formalism [6]. Let us briefly describe the main points of this formalism as applied to the problem under consideration.

To calculate the gain, we need to know those components of the density matrix that describe the behavior of electrons in the valence and conduction bands. The equation for the density matrix components has the form

$$i\hbar\frac{\partial\rho_{ij}}{\partial t} = (E_i - E_j)\rho_{ij} + [H', \rho]_{ij} + \frac{i\hbar}{\tau_{ij}}(\rho^e_{ij} - \rho_{ij}). \quad (1)$$

Here, the indices $i, j = 1, 2$ correspond to the valence and conduction bands, respectively; E_i is the energy of an electron in the respective zone; $H' = -(e/m_c c)\mathbf{pA}$ is the Hamiltonian of interaction between electrons and the electromagnetic field; m_c is the effective electron mass; $\mathbf{p}$ is the momentum operator; $\mathbf{A}$ is the vector potential; and τ_{ij} is the relaxation time. At $i = j$, we have $\tau_{ii} = T_1$, which is the longitudinal relaxation time of the distribution function in each band; at $i \neq j$, we have $\tau_{ij} = T_2$, which is the transverse relaxation time. ρ^e_{ii} is the equilibrium distribution over momenta in the ith band.

A minor manipulation yields equations for the diagonal and off-diagonal components of the density matrix:

$$\frac{\partial\rho_{12}}{\partial t} = -\frac{i}{\hbar}(E_1 - E_2)\rho_{12} - \frac{\rho_{12}}{T_2} + \frac{ie}{\hbar}\mathbf{E}\mathbf{r}^{12}_p(\rho_{22} - \rho_{11}),$$

1063-7826/05/3905-0603$26.00 © 2005 Pleiades Publishing, Inc.

$$\frac{\partial \rho_{21}}{\partial t} = -\frac{i}{\hbar}(E_2 - E_1)\rho_{21} - \frac{\rho_{21}}{T_2} + \frac{ie}{\hbar}\mathbf{E}\mathbf{r}_p^{12}(\rho_{11} - \rho_{22}),$$
$$\frac{\partial \rho_{11}}{\partial t} = -\frac{1}{T_1}(\rho_{11} - \rho_{11}^e) + \frac{ie}{\hbar}\mathbf{E}(\mathbf{r}_p^{12}\rho_{21} - \rho_{12}\mathbf{r}_p^{21}), \quad (2)$$
$$\frac{\partial \rho_{22}}{\partial t} = -\frac{1}{T_1}(\rho_{22} - \rho_{22}^e) + \frac{ie}{\hbar}\mathbf{E}(\mathbf{r}_p^{21}\rho_{12} - \rho_{21}\mathbf{r}_p^{12}).$$

Here, $\mathbf{r}_p^{12}$ is the matrix element of the interband transition and $\mathbf{E}$ is the electric field of the wave.

In Eqs. (1) and (2), we used the relaxation-time approximation, which makes the calculation considerably simpler and yields analytical expressions for the density matrix components. Undoubtedly, an exact calculation requires that the collision integral should be considered accurately and integro-differential equations should be solved. However, we restrict our consideration to the relaxation-time approximation in a qualitative analysis of the gain saturation effect in QW semiconductor lasers and of the influence exerted by this effect on the maximum output power of a laser.

In addition, we use the resonance approximation; i.e., we retain, in the solution to Eqs. (2), only the terms with the same frequency ω as that of the external excitation and drop the contributions at doubled frequencies.

Let us introduce the difference of occupancies in the conduction and valence bands:

$$D(\mathbf{p}, t) = \rho_{22} - \rho_{11}. \quad (3)$$

From system of equations (2), we obtain the following expressions for the off-diagonal components of the density matrix:

$$\rho_{12}(\mathbf{p}, t) = -\frac{e}{\hbar}\mathbf{r}_p^{12}D(\mathbf{p})\frac{\mathbf{E}e^{i\omega t}}{\omega_{21} - \omega + \frac{i}{T_2}}, \quad (4)$$

$$\rho_{21}(\mathbf{p}, t) = -\frac{e}{\hbar}\mathbf{r}_p^{12}D(\mathbf{p})\frac{\mathbf{E}e^{-i\omega t}}{\omega_{21} - \omega + \frac{i}{T_2}}. \quad (5)$$

For the difference of occupancies, we have

$$D(\mathbf{p}) = D^e(\mathbf{p})\frac{(\omega_{21} - \omega)^2 + T_2^{-2}}{(\omega_{21} - \omega)^2 + T_2^{-2} + R}, \quad (6)$$

$$D^e(\mathbf{p}) = \frac{2}{n(2\pi)^2}[f_c(\mathbf{p}) - f_v(\mathbf{p})]. \quad (7)$$

Here,

$$\omega_{21} = \frac{E_2(\mathbf{p}) - E_1(\mathbf{p})}{\hbar}; \quad (8)$$

$$R = 4\frac{T_1}{T_2}\frac{e^2}{\hbar^2}|\mathbf{E}\mathbf{r}_p^{12}|^2; \quad (9)$$

$f_c(\mathbf{p})$ and $f_v(\mathbf{p})$ are the distribution functions of electrons in the conduction and valence bands, respectively; n is the two-dimensional (2D) carrier density; $E_1(\mathbf{p})$ and $E_2(\mathbf{p})$ are the energies of carriers with the momentum $\mathbf{p}$ in the valence and conduction bands, respectively; and ω_{12} is the transition frequency.

The polarization density vector of the system can be expressed in terms of the off-diagonal components of the density matrix:

$$\mathbf{P}(t) = \frac{en}{a}\int \mathbf{r}_p^{12}[\rho^{12}(\mathbf{p}, t) + \rho^{21}(\mathbf{p}, t)]d^2p. \quad (10)$$

Here, a is the QW width and $\mathbf{p}$ is the 2D carrier momentum. Substituting the solution to Eqs. (4) and (6) into (10), we obtain

$$\mathbf{P}(t) = -\frac{2e^2n}{a\hbar}$$
$$\times \int |\mathbf{r}_p^{12}|^2 \mathbf{E}D^e(\mathbf{p})\frac{(\omega_{21} - \omega)\cos\omega t + T_2^{-1}\sin\omega t}{(\omega_{21} - \omega)^2 + T_2^{-2} + R}d^2p. \quad (11)$$

For an isotropic medium, the polarization density vector can be represented as $\mathbf{P} = \chi(\omega)\mathbf{E}$, where χ is the complex susceptibility of the medium. The imaginary part of the susceptibility is related to the imaginary part of the relative permittivity of the medium by the expression $\varepsilon''(\omega) = 4\pi \mathrm{Im}\chi(\omega)$.

The gain is related to the imaginary part of the relative permittivity by

$$g(\omega) = -\frac{\omega}{c}\frac{\varepsilon''}{\sqrt{\varepsilon_0}}, \quad (12)$$

where ε_0 is the static relative permittivity of the medium. Substituting the explicit expression for the optical matrix element into (11) and using, instead, an integration over energy, we obtain the final expression for the gain [7]:

$$g(\hbar\omega) = I_{cv}^2\frac{\pi}{2}\frac{1}{a}\frac{\alpha}{\sqrt{\varepsilon_0}}\frac{E_g(E_g + \Delta_0)}{E_g + \frac{2}{3}\Delta_0}$$
$$\times \int_{E_0}^{\infty}\left(\frac{1}{1 + e^{A_n}} + \frac{1}{1 + e^{B_p}} - 1\right) \quad (13)$$
$$\times \left(1 + \frac{\varepsilon_n}{\varepsilon_n + \frac{M}{1 + M}(E_{cv} - E_0)}\right)F(E_{cv}, \hbar\omega, E)\frac{dE_{cv}}{E_{cv}}.$$

Here, symbols A_n and B_p denote the quantities

$$A_n = \frac{1}{T}\left[\frac{M}{1 + M}(E_{cv} - E_0) + \varepsilon_n - \mu_n\right],$$

$$B_p = \frac{1}{T}\left[\frac{1}{1+M}(E_{cv}-E_0)+\varepsilon_p-\mu_p\right];$$

α is the fine structure constant; I_{cv} is the overlap integral between the electron and hole wave functions ($I_{cv} < 1$); $M = m_h/m_c$; m_h is the effective hole mass; E_{cv} is the transition energy; E_g is the energy gap; Δ_0 is the spin–orbit splitting energy; $E_0 = E_g + \varepsilon_n + \varepsilon_p$, ε_n and ε_p are the energies of the quantum-well levels of an electron and a hole calculated from the corresponding band edge; μ_n and μ_p are the quasi-Fermi levels for electrons and holes, respectively; T is the temperature of the electron-hole plasma, expressed in energy units; and

$$F(E_{cv}, \hbar\omega, |E|^2) = \frac{1}{\pi}\frac{\hbar/T_2}{(E_{cv}-\hbar\omega)^2+(\hbar/T_2)^2+R}. \quad (14)$$

The function $F(E_{cv}, \hbar\omega, |E|^2)$ takes into account the dependence of the gain on the emission intensity.

As has already been mentioned, for an exact analysis of the problem of gain saturation, it is necessary to consider a collision integral that depends on the particle momentum in the sets of Eqs. (1) and (2) since the particle distribution function is deformed in a strong field. For the analysis to be more precise, it is also necessary to take into account the modification of the scattering processes that occur in a strong field. As we now intend to obtain only a qualitative explanation of the reasons for gain saturation, it is sufficient to use the relaxation-time approximation.

The lasing conditions, i.e., the equality of the gain and loss, give us an equation for determining the threshold carrier density of a laser:

$$\Gamma g^{\max} = \alpha, \quad (15)$$

$$\alpha = \alpha_{\text{int}} + \alpha_{\text{ext}}. \quad (16)$$

Here, α is the loss coefficient, Γ is the optical confinement factor, $g^{\max}$ is the maximum gain, α_{int} is the internal emission loss,

$$\alpha_{\text{ext}} = \frac{1}{L}\ln\frac{1}{R_r} \quad (17)$$

is mirror loss of the laser cavity, L is the cavity length, and R_r is the mirror reflectivity ($R_r = \sqrt{R_1, R_2}$, where R_1 and R_2 are the mirror reflectivities for the two mirrors).

Contributions to the threshold current density J_{th} of the laser are made by the radiative-recombination current J_{th}^R and the Auger-recombination current J_{th}^A [7]:

$$J_{\text{th}} = J_{\text{th}}^R + J_{\text{th}}^A. \quad (18)$$

Here, according to [7],

$$J_{\text{th}}^R = I_{cv}^2\frac{1}{3\pi}\alpha\frac{E_g(E_g+\Delta_0)}{E_g+\frac{2}{3}\Delta_0}\frac{\sqrt{\varepsilon_0}}{\hbar^3c^2}\int_{E_0}^{\infty}E\frac{1}{1+e^{A_n'}}\frac{1}{1+e^{B_p'}}dE,$$

$$A_n' = \frac{1}{T}\left[\frac{M}{1+M}(E-E_0)+\varepsilon_n-\mu_n\right],$$
$$B_p' = \frac{1}{T}\left[\frac{1}{1+M}(E-E_0)+\varepsilon_p-\mu_p\right], \quad (19)$$

$$J_{\text{th}}^A = e[C_1n^2p + C_2p^2n], \quad (20)$$

and C_i are the Auger recombination coefficients. The expression for the Auger recombination coefficients was reported in [8].

For simplicity, we disregard the carrier leakage from the active region.

Knowledge of the threshold current enables us to determine the light–current characteristic of the laser:

$$P_{\text{out}} = \frac{\hbar\omega}{e}(J - J_{\text{th}}). \quad (21)$$

Here, P_{out} is the output power of the laser and J is the drive current.

3. ANALYSIS OF THE RESULTS OBTAINED

Our study is concerned with the effect of the leveling-off of the light–current characteristic at high drive currents. At high excitation levels, the carrier energy distribution function is deformed due to the high-intensity processes involved in the relaxation of nonequilibrium carriers. Specifically, the distribution function shows a dip at an energy corresponding to the optical transition energy, which leads, eventually, to a decrease in the gain [5], with the density of the nonequilibrium carriers increasing as the drive current rises. As a result, the time T_1 of intraband relaxation decreases and the dip in the distribution function becomes deeper and wider. Consequently, the gain falls as the output power increases, and the threshold carrier density increases. Under theses circumstances, the dependence of the output power on the drive current becomes nonlinear and levels off.

Figure 1 shows the threshold carrier density as a function of the squared electric field of an electromagnetic wave. It is important to note that the threshold carrier density strongly depends on the laser output power and on the loss coefficient α. As α increases, the dependence of the threshold carrier density on the squared electric field of the electromagnetic wave becomes steeper (Fig. 1, curve *2*). The higher the loss, the larger the gain with which the lasing begins. At the same time, the gain depends nonlinearly on the carrier density, with a considerable increase in the carrier density required for the gain to increase. Because the gain falls as the electric field grows stronger, the carrier density needs to be raised in order to maintain lasing; moreover, due to the nonlinearity mentioned above, the higher the gain, the greater the extent to which the carrier density needs to be raised.

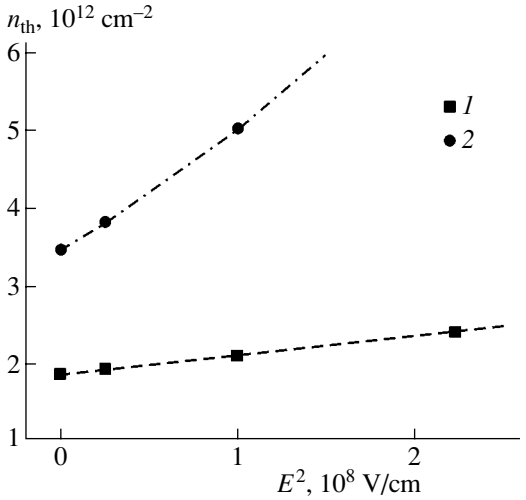

Fig. 1. Threshold carrier density n_{th} vs. the squared electric field of an electromagnetic wave E^2 for the relaxation time $\tau = 5 \times 10^{-13}$ s, optical confinement factor $\Gamma_0 = 0.03$, and loss coefficient α of (*1*) 13 and (*2*) 34 cm^{-1}.

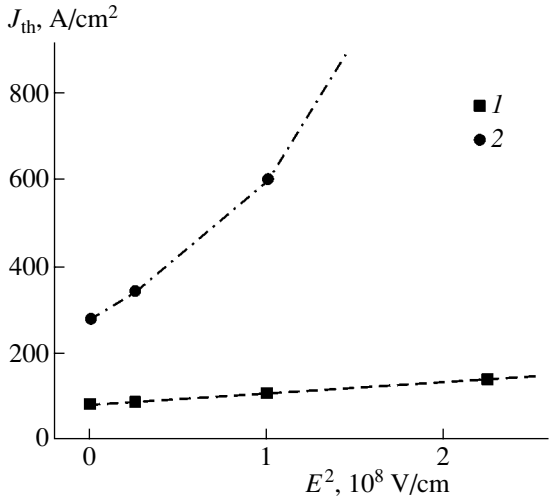

Fig. 2. Threshold current density J_{th} vs. the squared electric field of an electromagnetic wave E^2. The parameter values are the same as in Fig. 1.

Figure 2 shows the dependence of the threshold current density on the squared electric field for the same structure parameters as in Fig. 1. At a small loss coefficient (i.e., at low carrier densities), the main contribution to the threshold current density comes from the radiative current. Therefore, the dependence of the threshold current density on the squared electric field is weak (Fig. 2, curve *1*). As the loss coefficient α increases, the threshold carrier density also increases and the main contribution to the threshold current density is made by the Auger-recombination current (Fig. 2, curve *2*). It is important to note that the saturation effect is manifested to a greater extent in long-wavelength lasers. This circumstance is due to the fact that the Auger-recombination current is higher in long-wavelength lasers, and, consequently, the effects of gain saturation and leveling-off of the light–current characteristic are manifested at a lower output power.

Figure 3 shows the experimental and theoretical dependences of the output power P_{out} of a semiconductor laser on the drive current J for a relaxation time $T_2 = 5 \times 10^{-13}$ s and two values of the loss coefficient α.

The theoretical results shown in Fig. 3 are compared with the experimental data from [3]. In this experiment, the light-current characteristics of lasers with different cavity lengths were studied. It was found that, for a laser with a long cavity (low carrier densities), the light–current characteristic is linear in a wide range of drive currents (Fig. 3a, curve *1*). The linearity of the light–current characteristic for this laser means that the gain saturation effect is weak at a low threshold carrier density.

For a short-cavity laser (large α_{ext} and a high carrier density), the light–current characteristic is nonlinear and tends to level off (Fig. 3b, curve *1*). In this case, the

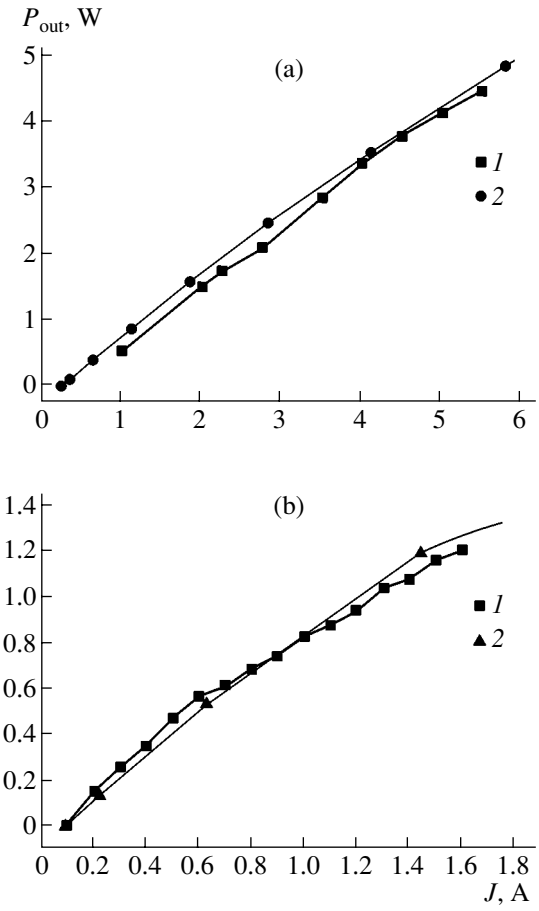

Fig. 3. Output power P_{out} vs. drive current J at the loss coefficients (a) $\alpha = 13$ cm^{-1} and (b) $\alpha = 34$ cm^{-1}. The parameters values are the same as in Fig. 1. Curves *1* show the experimental data [3] and curves *2*, the theoretical results.

threshold carrier density is higher than that of the long-cavity laser and the gain saturation effect is strong.

4. CONCLUSION

The gain was calculated in terms of the density-matrix formalism and in the relaxation-time approximation as a function of temperature, carrier density, and output power. The dependences of the threshold carrier density on the output power were found from the threshold condition. It was shown that, for short periods of intraband relaxation, the dependence of the threshold carrier density on the output power becomes strongly nonlinear. The light–current characteristic at high excitation levels was then calculated. It was demonstrated that the light–current characteristic is nonlinear for a short-cavity laser, with the threshold carrier density for this laser exceeding that of a long-cavity laser. Consequently, in comparison to a long-cavity laser, the relaxation processes in a short-cavity laser are more strongly enhanced and its gain is smaller. As the drive current increases, the gain falls. This leads to a nonlinear dependence of the output power of a laser of the drive current and, consequently, to a gain in saturation. The theoretical light–current characteristic of a semiconductor laser is in a good agreement with the experiment.

ACKNOWLEDGMENTS

The authors are grateful to V.P. Evtikhiev and E.Yu. Kotel'nikov for their helpful participation in discussions of the results.

The study was supported by the Russian Foundation for Basic Research (project nos. 02-02-17610, 04-02-16786, 04-07-90148), the research program of the Russian Academy of Sciences, and by the Presidium of the Russian Academy of Sciences.

REFERENCES

1. T. Makino, J. D. Evans, and G. Mak, Appl. Phys. Lett. **71**, 2871 (1997); L. V. Asryan, N. A. Gun'ko, A. S. Polkovnikov, *et al.*, Semicond. Sci. Technol. **14**, 1069 (1999).
2. J. G. Kim, L. Shterengas, R. U. Martinelli, *et al.*, Appl. Phys. Lett. **81**, 3146 (2002).
3. V. P. Evtikhiev, E. Yu. Kotelnikov, D. V. Dorofeyev, and G. G. Zegrya, in *Proceedings of 8th International Symposium on Nanostructures: Physics and Technology* (St. Petersburg, Russia, 2000), p. 407.
4. O. N. Kronin, Fiz. Tverd. Tela (Leningrad) **7**, 2612 (1966) [Sov. Phys. Solid State **7**, 2114 (1966)].
5. V. M. Galitskiĭ and V. F. Elesin, *Resonance Coupling of Electromagnetic Fields and Semiconductors* (Énergoatomizdat, Moscow, 1986) [in Russian].
6. K. Blum, *Density Matrix Theory and Its Applications* (Plenum, New York, 1981; Mir, Moscow, 1983).
7. L. V. Asryan, N. A. Gun'ko, A. S. Polkovnikov, *et al.*, Semicond. Sci. Technol. **15**, 1131 (2000).
8. A. S. Polkovnikov and G. G. Zegrya, Phys. Rev. B **58**, 4039 (1998).

Translated by M. Tagirdzhanov